Doctoral Dissertation

Doctoral Program in Materials Science and Technology (38^{th}cycle)

Effect of Process Gas Composition on the Characteristics of Atomized UNS S32760 Super Duplex Stainless Steel Powders and Their Properties After PBF-LB/M Processing

From Waste-Derived Powder Production to PBF-LB/M Components: Gas Atomization Optimization, Post-Processing Heat Treatment, Mechanical Characterization, and Corrosion Assessment

By

Antonio Pennacchio

******

Supervisor(s):

Prof. D. Manfredi, Supervisor

Prof. M. Actis Grande, Co-Supervisor

Doctoral Examination Committee:

Prof. Cinzia Menapace, University of Trento

Prof. Zbigniew Brytan, Silesian University of Technology

Politecnico di Torino

2026

Declaration

I hereby declare that, the contents and organization of this dissertation constitute my own original work and does not compromise in any way the rights of third parties, including those relating to the security of personal data.

Antonio Pennacchio
2026

* This dissertation is presented in partial fulfillment of the requirements for **Ph.D. degree** in the Graduate School of Politecnico di Torino (ScuDo).

Dedicata alla mia Zia Chiara

NNPPP

Acknowledgements

The present PhD thesis would not have been possible without the valuable contribution of all the people who supported me and shared their knowledge throughout my PhD journey.

I express my sincere gratitude to Matteo Turani and Dario Puccio of Inspire AG for giving me the opportunity to manufacture UNS S32760 super duplex stainless steel samples through the PBF-LB/M process, as well as for their patience, support and assistance throughout the related activities.

I would also like to thank Ilchat Sabirov and Pietro Martelli of the IMDEA Materials Institute for giving me the opportunity to spend a research period at their research center and for their valuable support during the fatigue characterization tests and the related analyzes.

My sincere thanks also go to Dario Pezzini for the valuable time dedicated to me during the mechanical testing activities and the SEM sessions carried out at the Alessandria campus of the Politecnico di Torino.

I would like to thank Enrico Pallavicini for his assistance during the gas atomization activities and for his help in solving the various issues related to the gas atomization plant.

I am also grateful to Emilio Bassini for his assistance during the numerous measurements performed using the LECO ONH 836 system.

Finally, I would like to express my deepest gratitude to Federico Gobber for all the valuable knowledge he shared with me, for the continuous support provided throughout this thesis work, and also for all the great moments and laughter along the way.

Abstract

This research develops an integrated sustainable route for producing and processing UNS S32760 super duplex stainless steel by Powder Bed Fusion - Laser Beam / Metal (PBF-LB/M), starting from gas-atomized powders produced from industrial waste. The originality of the work lies in the continuity of the investigated chain, from close-coupled gas atomization modelling and optimization to powder design, PBF-LB/M processing, heat treatment, mechanical and corrosion qualification testing.

Vacuum induction melting gas atomization was first investigated by CFD simulations and experimental trials to identify conditions suitable for maximizing the yield in the 20–63 μm particle-size range required for PBF-LB/M. The effect of inert gas pressure was correlated with jet morphology, atomization stability, particle size distribution, debris formation, and gas consumption. This approach enabled the selection of an optimized atomization condition and a physically grounded validation of the process window. In parallel, a carbon footprint evaluation quantified the environmental implications of converting UNS S32760 waste into additive manufacturing powder, highlighting the potential of a waste-to-powder strategy to reduce production impact.

The influence of process gas composition, specifically argon and nitrogen, on atomized UNS S32760 powder properties was then examined. Different combinations of melting-chamber atmosphere and atomizing gas were assessed in terms of particle size distribution, morphology, true density, light element content, nitrogen uptake, and ferrite-austenite phase balance. Nitrogen, when used as the melting-chamber atmosphere, increased the nitrogen content of the alloy, promoted a higher austenite fraction in the powders, and reduced intraparticle porosity compared with argon-based conditions. These results show that process gas selection is not only a fluid-dynamic variable, but also a metallurgical tool for tailoring the chemistry of super duplex powders before PBF-LB/M processing.

Powders were then used to optimize PBF-LB/M processing parameters for UNS S32760 components. A process window was identified to enable the fabrication of dense specimens with limited defectiveness and a relative density suitable for structural applications. The as-built material revealed the competing effects of nitrogen loss, solidification kinetics, cooling rate, and austenite formation, showing that nitrogen content decreased with increasing hatch energy density (HED) during PBF-LB/M. Although high-nitrogen powders promoted partial austenite formation, post-process heat treatment remained mandatory to restore a balanced duplex microstructure. Moreover, the comparison between low- and high-nitrogen powders demonstrated that nitrogen content plays a decisive role in the microstructural evolution of heat-treated PBF-LB/M components.

Heat treatment was carried out to control the ferrite-austenite ratio, limit detrimental secondary phases, and improve suitability for service conditions. The PBF-LB/M material was qualified through tensile, Charpy impact, and high-cycle fatigue testing. These analyses established relationships between powder chemistry, build orientation, process parameters, heat treatment, microstructure, and mechanical response. Localized corrosion resistance was assessed by ferric chloride testing according to ASTM G48 Methods A and E, comparing as-built and heat-treated PBF-LB/M conditions with conventionally processed reference materials. The discussion was framed according to NORSOK M-630 requirements, owing to the use of UNS S32760 in oil and gas applications exposed to chloride-containing environments and stringent acceptance criteria. Overall, this research demonstrates the feasibility of a circular manufacturing route for UNS S32760 components, from atomization modelling and waste-derived powder production to PBF-LB/M processing and performance assessment, contributing to lower-environmental-impact additive manufacturing pathways for super duplex stainless steels.

Contents

List of Figures

List of Tables

Chapter 1

The growing demand for metal powders: From Traditional Powder Metallurgy to Metal Additive Manufacturing

1.1 Overview of Metal Additive Manufacturing

1.1.1 The evolution of Powder Metallurgy

Powder metallurgy refers to a family of manufacturing routes that employ metallic powders as the starting feedstock to fabricate components in the desired geometry, often approaching near net shape [1]. Metal powders constitute only a minor share of the overall metal market when compared with cast and wrought products. The annual global production of metal powders is estimated to exceed 700,000 tonnes [2], whereas the worldwide production of crude steel amounted to approximately 1,000 million tonnes in 2024 [3]. Accordingly, metal powders account for less than 0.1% of the steel market in volumetric terms. This disparity emphasizes that powder metallurgy (PM) remains a highly specialized and niche technology, employed primarily when near-net-shape capability, complex geometries, or tailored material properties are required, advantages that are difficult to achieve with conventional casting or wrought processing.

Owing to their relatively high cost, however, powder-based materials are generally considered a deliberate choice for specialized applications rather than a competitive alternative to traditional metallic products [4].

With the advent of the 21st century, novel manufacturing technologies encompassed by the term Additive Manufacturing (AM) have transitioned to industrial-scale application [5]. Today, modern AM technologies enable the fabrication of components in diverse material systems, including metals, polymers, ceramics, and composite materials [6].

The AM processes represent a group of production technologies based on a layer-by-layer building strategy [7]. As described in the standard ISO/ASTM 52900 [8], additive manufacturing is defined as "*a method of the joining of materials to fabricate parts from 3D-model data, made layer upon layer. This process is opposed to formative manufacturing and subtractive manufacturing methodologies*".

This approach provides notable advantages, including enhanced design flexibility, improved efficiency through the reduction of material waste and energy consumption, and increased cost-effectiveness in the fabrication of complex geometries and customized components [6].

A distinctive advantage of additive processes is the direct CAD to machine workflow, whereby the digital part definition is sent to the equipment without intermediate tooling, mold fabrication, or auxiliary fixturing. Removing these steps markedly compresses the time from concept to production. The same digital pathway enables rapid, on demand prototyping, allowing frequent build, evaluate, and refine cycles that expand design space exploration, support deeper optimization, and facilitate early identification of potential design shortcomings [5].

Building on these advantages, the maturation of AM has added a second pillar to powder technologies. Alongside traditional PM, powder-based metal AM, over the past decade, has profoundly transformed the manufacturing landscape by enabling the realization of parts whose complexity would not be technically feasible or prohibitively expensive using traditional metallurgical technologies [9, 10].

These benefits have led to widespread adoption across multiple sectors, including aerospace, biomedical engineering, and high-performance motorsport applications [11].

1.1.2 Techniques in Powder-Based Additive Manufacturing

Being a relatively recent technology, AM processes were for many years characterized by a lack of standardization, to the extent that no formal categories existed to group similar technologies. This absence of a shared framework made the communication of information and the comparison of results particularly challenging. To address this issue, the International Organization for Standardization (ISO) and the American Society for Testing and Materials (ASTM) collaborated and, in 2015, published the standard ISO/ASTM 52900 [8], which introduced a unified classification and terminology for AM technologies [6]. According to this framework, current AM technologies are classified into seven main categories With just four of the seven categories pertaining to metals AM technologies [8].
As reported in the scheme shown in Figure 1.1, which illustrates all seven groups, three of them can be considered powder-based: Powder Bed Fusion (PBF), Directed Energy Deposition (DED), and Binder Jetting (BJT). Each category can in turn be subdivided into subclasses, representing the different commercial technologies currently available on the market.

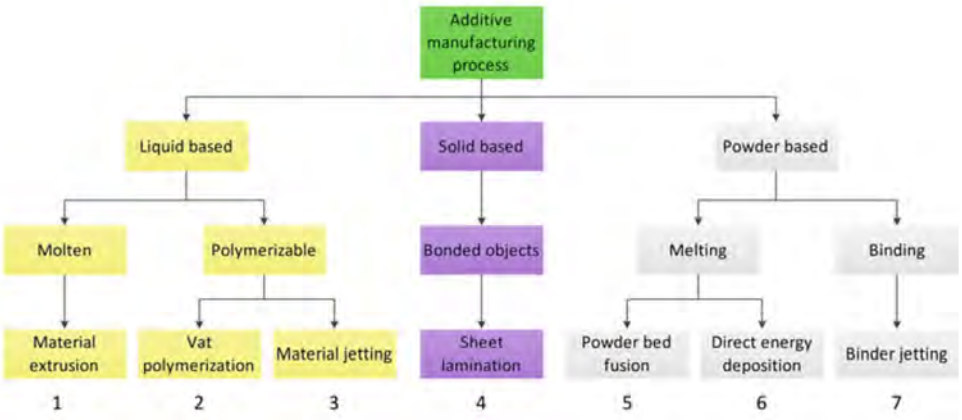

Fig. 1.1 Classification of AM technologies according to ISO/ASTM 52900 [6].

With reference to metal additive manufacturing techniques, Figure 1.2 presents a schematic summary, within the processes that use metal powders as feedstock can be distinguished.

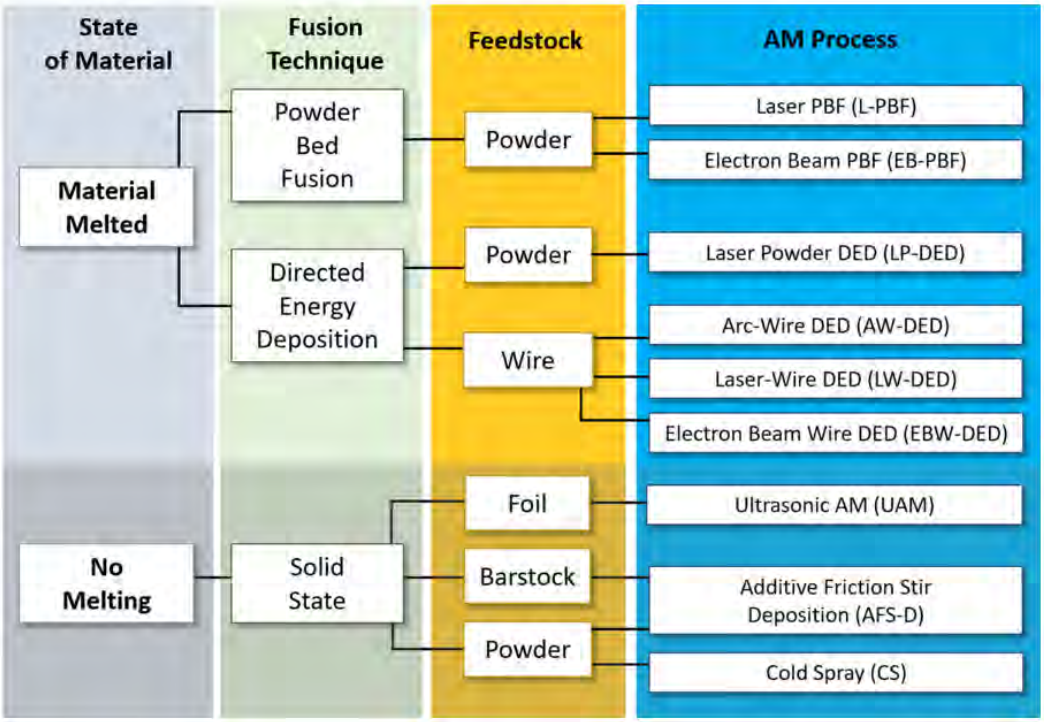

Fig. 1.2 A systematic classification of the major metal AM technologies [12].

Powder bed fusion is the most mature and widely used metal Additive Manufacturing technologies [11]. The most established and industrially applied process are laser powder bed fusion (PBF-LB/M) and electron beam powder bed fusion (EB-PBF) [13]. In both cases, a thin layer of powder is spread across the build plate, and a focused energy source (laser or electron beam) selectively melts or sinterizes the cross-section of the part within that layer.

Directed energy deposition (DED) is also widely employed in metal AM, particularly for repair and for adding features to existing parts. DED can process either powder or wire feedstock. As with powder bed fusion, lasers are frequently used, but in DED the feed delivery and energy source are usually integrated on the deposition head. Motion can be provided by a gantry, a robotic arm, or a trunnion table.

Within DED, laser powder DED (LP-DED) introduces powder into a melt pool to lay down beads, typically under a local purge or within an inert enclosure. Laser wire DED (LW-DED) feeds an off axis, and in some systems coaxial, wire into the

melt pool under similar shielding conditions. The Arc wire DED (AW-DED) uses an electric arc with wire feed to deposit beads under local shielding and is often referred to as wire arc additive manufacturing (WAAM). Instead, Electron beam wire DED (EBW-DED) operates in a vacuum with an electron beam and off axis wire feed; in this case the beam is stationary while the part moves on a Cartesian stage to create freeform structures [11].

The metal powder-based AM impose far more demanding requirements on feedstock powders, particularly in terms of particle size distribution, morphology, and the chemical composition to ensure high repeatability in the manufactured components. These properties are specific to each powder based AM technology and are determined not only by the production methods, but also by subsequent post-processing operations [14]. These include classification and screening, batch homogenization, surface passivation, and powder handling during packaging.

Due to their high surface area metal powders tend to be very sensitive to absorb moisture, oxygen and other elements present in the air. Furthermore, logistical aspects such as transport, which may induce segregation, and storage conditions, including atmospheric composition and moisture control, play a critical role in ensuring powder quality and performance. All these factors have a direct impact on the processability of the powders, as well as on the mechanical properties, surface finish, and overall quality of the final components [15].

Despite the advantages outlined above, a persistent limitation of metal powder-based AM is its overall cost structure, which often translates into higher unit prices. Major cost drivers include build duration, capital expenditure on equipment, the extent of post processing, typically surface finishing or, in sectors such as aerospace, hot isostatic pressing (HIP) [12], and the price of the feedstock powder. In particular, metal powder that meets AM grade specifications generally carries a price premium, with costs that usually exceed those of standard powders used in the powder metallurgy industry [1]. Additional limitations of powder-based AM include, for certain technology variants such as laser powder bed fusion (PBF-LB/M), the need for support structures to stabilize the build and mitigate thermal stresses during fabrication, as well as the generally restricted build volume of many systems, which constrains achievable component size and part orientation [6].

Given these considerations, it is not always straightforward to determine when powder-based AM delivers a clear advantage. In general terms, AM exhibits a near zero penalty for geometric complexity relative to conventional routes [16, 17]. By

comparing the unit cost of a part produced with each approach, a practical application window can be delineated. As geometric complexity increases, the cost of subtractive methods such as machining typically rises sharply due to longer toolpaths, additional setups, and increased scrap, whereas metal powder-based AM can accommodate intricate features with comparatively modest cost growth, provided build volume, support removal, and post processing remain within acceptable limits. In conventional manufacturing, setup and tooling costs are substantial, rendering small production runs economically unattractive [1]. In additive manufacturing, these setup burdens are largely absent, so limited batch sizes become viable. This capability also enables extensive product personalization, for example custom sports equipment and patient specific prostheses design and implants in the biomedical. Together, these attributes indicate that AM based on metal powders is particularly suited to sectors where maximizing quality and performance is prioritized over minimizing unit cost [11].

1.1.3 Laser powder bed fusion technique

The Powder Bed Fusion - Laser Beam / Metal (PBF-LB/M) is also referred to in the commercial literature as selective laser melting (SLM), direct metal laser sintering (DMLS), and direct metal laser melting (DMLM). More generally, this process is often known as Laser Powder Bed Fusion (PBF-LB/M).
The foundational intellectual property for this technology resides with the Fraunhofer Institute for Laser Technology (Fraunhofer ILT). In 1995, researchers at Fraunhofer ILT approached FS Stereolithografietechnik GmbH to develop a new three-dimensional printing technology. Research was carried out at both sites using FS software and hardware developed by Dieter Schwarze and Matthias Fockele. In 1996, ILT researchers secured the German patent DE 19649865 for the SLM process, with Schwarze and Fockele named co-inventors [18, 19].
A schematic representation of the hardware of a typical PBF-LB/M printing system is illustrated in Figure 1.3.

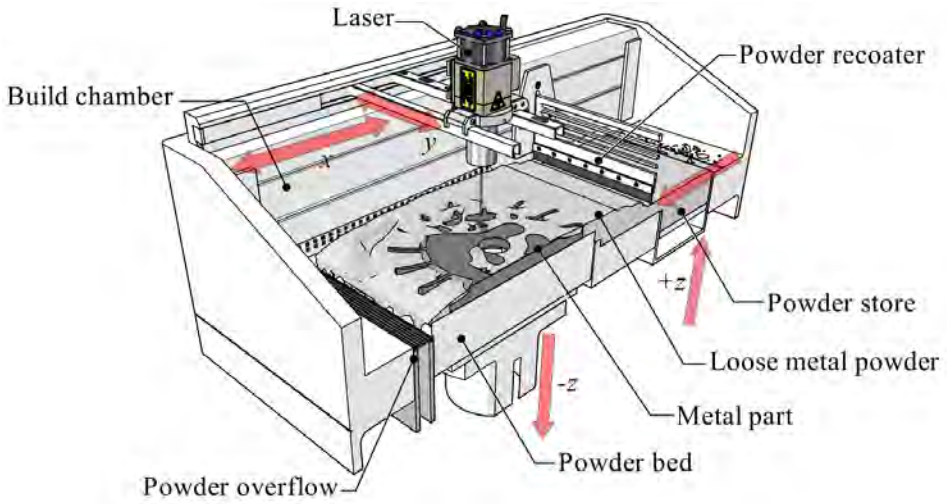

Fig. 1.3 Simplified schematic of a typical PBF-LB/M system [11].

In the PBF-LB/M systems the build chamber is purged with an inert atmosphere, typically argon or nitrogen, selected according to the reactivity of the metal powder. During the process, a slight chamber overpressure is maintained by a directed inert-gas cross-flow across the powder bed to minimize oxygen ingress and thereby suppress oxidation. The gas sweep simultaneously entrains and removes process by-products (metal vapor/plume and spatter) from the build region, limiting their redeposition on the powder layer and protecting the laser optics.
On the building platform (with maximum sizes typically in the range of 400 × 400 × 400 mm [18]) a thin layers of metal powder in the range of 10–60 µm (a parameter governed by the alloy processed and the required printing speed and also defines the tolerance and accuracy of the part) are spread over the powder bed and evenly leveled by a powder spreading unit, commonly referred to as a recoater [14].
After the first layer has been deposited and leveled, a high power laser (fibre-lasers Nd:YAG with a wavelength of 1.1 µm is normally used for processing the metals with a typical source power of 0.2 to 1 Kw [18]) spot melts the powder using a defined scan strategy along a toolpath derived from the STL data. At the same time, for components with complex geometries or for critical materials, support structures made from the same material are built to limit distortion caused by the high thermal gradients during melting. Once the initial layer has been scanned, the build platform moves downward along the z axis by one layer thickness, and the powder feed and recoater spread the next layer of loose powder. This cycle is repeated until the component reaches its final height. Upon build completion, the part is allowed to

equilibrate gradually to ambient temperature to prevent thermal shock and enable safe handling. Once thermally stabilized, the part is extracted from the powder bed, and the surrounding loose, unfused powder, which functions only as a temporary support during the build and remains fully reusable, is recovered and recycled for subsequent parts.

The EB-PBF is analogous to PBF-LB/M but employs an electron beam under vacuum. The beam is generated at a typical source power of about 6 kW by heating either a tungsten filament or a lanthanum hexaboride (LaB6) single-crystal cathode, thereby emitting electrons. The electrons are then accelerated to high voltage (60 kV) to form a focused beam that typically preheats each layer and, in turn, melts along the programmed toolpath [20]. Electron beam melting (EBM) is a commonly used synonym.

In the EBM system, the need to operate under vacuum necessitated by the electron beam affords strong oxidation control and also prevent the process of volatile elements like Mg or Al, yet it is constrained by the requirement for electrically conductive feedstock.

In general terms, PBF-LB/M is regarded as one of the most adaptable AM processes, partly because it can process a broad range of materials, including aluminum, titanium, iron, nickel, cobalt, and copper-based alloys, as well as various composite materials [7]. Furthermore, that PBF-LB/M can produce amorphous materials, due to the high cooling rates higher gradients of 10^5–10^7 °C/m in the molten pool and heat-affected zone (HAZ) together with cooling rates between 10^4 and 10^6 °C/s for melting processes [11]. A further advantage of PBF-LB/M is the ability to produce near-net-shaped parts, due to the high resolution of the process and surface finish that can be achieved. Resolution depends directly on the diameter of the laser beam (called "spot-size"), the layer thickness and the diameter of the largest particles present in the metal powder. PBF-LB/M has a beam spot size of 20–100 µm [7], whereas EMB's is 100–300 µm [20].

In general, both PBF-LB/M and EBM use fine spherical powders to improve flowability; however, PBF-LB/M ends to have more stringent requirements regarding the powder particle size and overall granulometry, with commonly used particle size distributions around 15–45 µm or 20–53/20–63 µm [21, 13], whereas EBM generally employs coarser powders, typically around 45–105 µm [22]. The larger beam spot and coarser feedstock used in EBM generally lead to a higher as-built

surface roughness than PBF-LB/M, with representative values around Ra 20–25 µm for EBM and $R_a \approx$ 5–10 µm for optimized PBF-LB/M/SLM conditions [11].

PBF-LB/M has, nevertheless, notable drawbacks, namely a low process speed (due to the mechanical laser-focusing system) and a high cooling rate. The latter is particularly significant, because it can result in distortion and residual stresses due to the heat differentials within the build. Consequently, PBF-LB/M systems can typically only use a resistive heating mechanism to heat the chamber, whereas EBM systems can preheat the powder bed to elevated temperatures by completely scanning each layer with the electron beam prior to melting, so they are regarded as a preferred route for certain crack-sensitive materials [20]. Because the electron beam is applied multiple times on each layer, the overall build time is significantly longer than PBF-LB/M. This leads to bed temperatures of 200–500 °C for PBF-LB/M [18] and 700–1100 °C for EBM [14]. The required cooldown before parts can be removed from the build plate further extends the cycle time.
Furthermore, the heating system in PBF-LB/M is often only applied to the build platform rather than the whole chamber, as a result the final printed layers will experience lower preheating temperatures and thus higher cooling rates.
Overall, this issue limits the feasibility of using PBF-LB/M for very brittle materials, like Ti-Al intermetallics, due to the high risk of cracking during solidification [23, 24].
Although conventional metalworking has long delivered consistent properties and a mature metallurgical knowledge base, this experience translates only partially to PBF-LB/M. The relationships among process, microstructure, and properties in PBF-LB/M remain incompletely understood, which makes their elucidation a central research priority. In particular, key gaps concern in situ monitoring during the build and physics-based process simulation to accelerate parameter selection and reduce empirical trial and error, reflecting distinctive attributes of printed components that conventional frameworks do not capture.

1.1.4 Economic perspective on metal powder-based additive manufacturing

The purpose of a market report is to deliver comprehensive, reliable insights and analysis on the current landscape, prevailing trends, and emerging opportunities, thereby supporting well informed business decisions [25].
According to the Wohlers Report 2025, as highlighted in the graph shown in Figure 1.4 the global additive manufacturing (AM) industry expanded by 9.1 %, reaching a market value of USD 21.9 billion. This growth was largely driven by the rapid expansion of the AM sector in Asia, particularly in China, whereas markets in Europe, the Middle East, and Africa, as well as in the Americas, showed only marginal growth or even slight contraction [26].

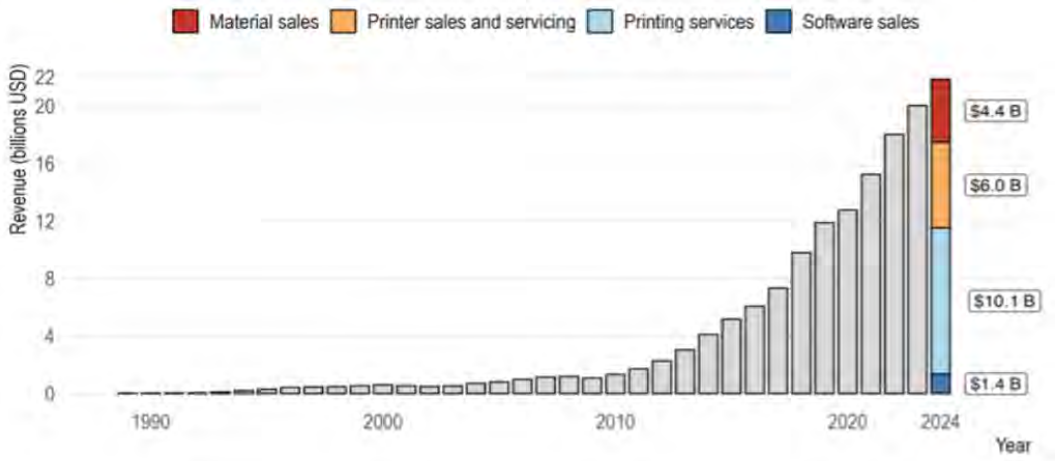

Fig. 1.4 AM market revenue per year, segmented by revenue type [26].

The report indicates continued growth in the service provider, software, and material sectors. By implementing precise optimization of process design, the economic viability of AM technologies can be significantly enhanced, thereby promoting wider industrial adoption.

In particular, during the past three decades, metal additive manufacturing has experienced substantial growth, driven by disruptive expectations about the possibility of extensively replacing or integrating traditional subtractive technologies. The entry into the market of direct metal Additive Manufacturing systems and the expiration of the first patents in the polymer sector have fueled extremely optimistic projections and attracted capital towards new operators and platforms [5]. Today, however, the empirical evidence presents a more differentiated view: growth persists, but along trajectories lower than many of the forecasts formulated in the past decade [27].
Although the sector has expanded markedly over recent decades, several indicators suggest that the market may be approaching an early saturation phase, with many suppliers competing over technologies, materials, services, and software. Annual sales of metal AM equipment are currently on the order of two thousand units distributed over roughly twenty process variants and supplied by nearly two hundred original equipment manufacturers, a profile more comparable to a specialised machinery market than to a rapidly scalable machine business [27].
However, most reporting bodies anticipate continued expansion of metal AM, with double-digit growth expected over the next five years [28, 29], a consistently supported by user feedback from major industrial adopters. Beyond this headline consensus, however, the numbers diverge substantially [30–32] both in estimates of the present metal powder AM market size and in the medium-term projections.
An essential preliminary step in constructing any market model is to delineate its boundaries, since changes to these can materially influence the results of market analyses [25]. Metal additive manufacturing, in particular, is best characterized as a specialized segment of the broader manufacturing industry and operates predominantly as a business to business market [32].
It is important to emphasize that the misalignment between forecasts and reality stems from structural factors within the sector and from methodological difficulties in measurement and prediction [27]. The main methodological issues concern the definition of boundaries. In quantifying the metal additive market, it is not trivial to determine what to include. Machines and materials clearly fall within scope, whereas gray areas persist for contract manufacturing services, general purpose software also used for AM, and the value of the finished product in the application sectors, with the attendant risk of estimates that are not comparable and exaggerated. Added to this are informational biases, since suppliers tend to communicate more expansive trajectories and startups anchor forecasts to very large potential markets, only weakly

tempered by implementation experience, triggering self-referential cycles in which optimistic reports and commercial plans reinforce one another. In addition, the limited visibility of high value applications, especially in domains protected by confidentiality such as aerospace and medical, deprives forecasting models of reliable public signals and compromises their calibration. All of these aspects taken together, along with the combination of uncertain and non unique boundaries, information asymmetries, and application opacity, lead to market assessments that are fragile and difficult to compare [27].

The way end users have adopted metal additive manufacturing has changed profoundly over the past decades. In the 2000s, early users purchased machines mainly for exploratory studies and research and development activities aimed at assessing the technology's potential. In the 2010s, by contrast, there was a wave of installations of metal AM systems, driven by curiosity and the fear of missing the next major innovation, with many actors eager to move directly into serial production [27].

At that time, the prevailing view, later shown to be incorrect, was that PBF would directly replace CNC machining across a wide range of products. In reality, PBF components often require lengthy redesign cycles, including a complete revision of parts and assemblies, in order to fully exploit the advantages of the technology[5].

Today, the experimental phase has largely been surpassed, and adoption is based on strategic investments by industries with concrete business cases for specific applications. Machines are purchased only based on rigorous calculations demonstrating their economic sustainability in the specific field of use.

The introduction of metal AM in several highly regulated sectors, such as aerospace and biomedical, has further supported the transition to serial production [5]. The increasing sharing of standards and qualification procedures within the metal additive sector has helped reduce uncertainty and stimulate adoption, supported as well by the increasingly active role of regulatory and certification authorities [33–35].

In contrast with the early phase, when media coverage routinely hyped alleged breakthroughs, much of today's progress in metal AM takes place out of the public eye, particularly in the defense and aerospace sectors [31]. The technology often functions as an essential enabling technology for high-performance components that have a substantial influence on larger-scale products. For this reason, concerns over intellectual property are a primary driver of the confidentiality surrounding the most significant projects.

Industry participants across the Additive Manufacturing ecosystem, including both buyers and suppliers, report a generally positive outlook, with many expecting a Compound Annual Growth Rate (CAGR) on the order of 20% [27], shown in Figure 1.5. They anticipate substantial expansion in the coming years and more extensive penetration into additional industrially relevant applications beyond those where AM is already well established. Against a backdrop of geopolitical tension, AM may further benefit from increased defense expenditures and from rising demand in other sectors for complex solutions and more resilient manufacturing capabilities.

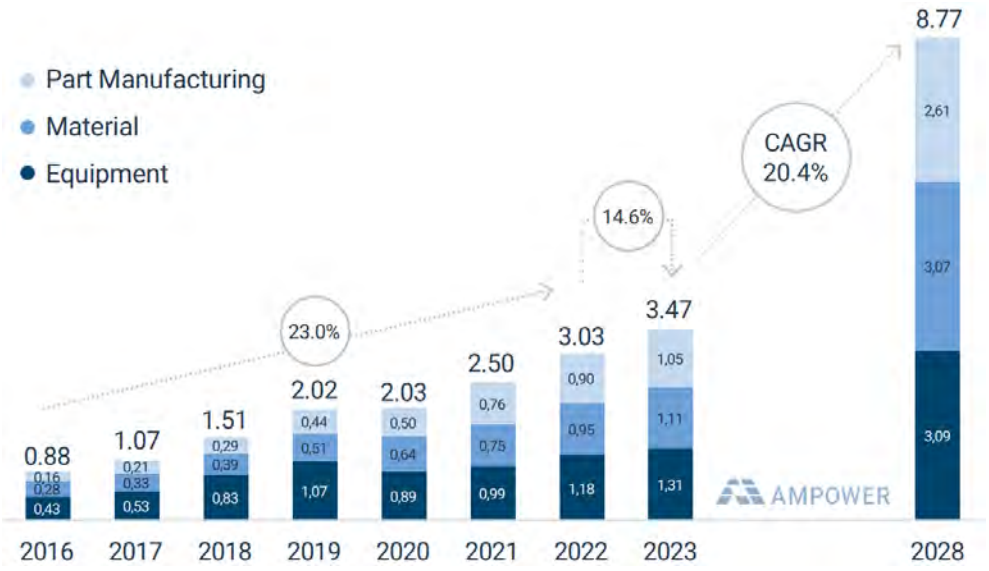

Fig. 1.5 The global metal Additive Manufacturing market from 2016 to 2023 and forecast 2028 (EUR billion) [27].

Over the past few years, industry surveys consistently indicate that powder-bed–based metal AM has consolidated its leading position in the metal AM segment, both in installed base and annual unit sales; within this family, laser powder bed fusion (PBF-LB/M) remains one of the principal growth driver of metal AM adoption across high-value sectors, underscoring the sustained industrialisation of PBF-LB/M solutions [36].

Within the PBF-LB/M materials portfolio, converging technical reviews and industrial practice point to a well defined ranking of alloy families [32]. Titanium based alloys, especially Ti6Al4V, continue to dominate applications in medical devices and in the aerospace sector, where nickel based superalloys (Inconel 718 and Inconel 625) also find applications [37]. Where high specific strength and biocompatibility are decisive; titanium based alloys are routinely described as among the most widely used in PBF-LB/M, and remain the focus of extensive process–structure–property optimisation [38]. Fe-based stainless steels (notably 316L and 17-4PH) constitute the second major class by breadth of use across general engineering and tooling, reflecting their processability and cost–performance balance [13]. Al Si foundry alloys are widely regarded as the third most widely deployed PBF-LB/M powder family for industrial production. Especially AlSi10Mg, they remain the workhorse for lightweight structures, combining broad process windows with robust weldability and favorable as-built strength-to-weight ratios. Their rapid solidification yields a fine cellular Al/Si network that can be tuned by direct aging or T6-type heat treatments to balance strength, ductility and fracture toughness, while also influencing corrosion behavior; these post-build routes are nowadays well documented for PBF-LB/M AlSi10Mg and related Al–Si compositions [39].

Within this framework, metal powders remain among the most critical cost drivers for AM part production [26]. The long-term sustainability of the metal AM market therefore depends on reducing powder production costs [40].

Chapter 2

The Metal Gas Atomization Process

2.1 Overview on metal atomization for AM

The production of metal powders has historically been characterized by a conservative approach. Methods for producing metal powders can be grouped into three principal categories: chemical, mechanical, and physical, each of which includes several subgroups [1]. Chemical routes produce powders by decomposition or reduction of metal compounds, or by precipitation from solution. Mechanical routes yield powders through comminution processes such as milling and grinding, and may also generate chips from machining operations that are subsequently crushed and classified.

Physical atomization entails the breakup of the molten metal stream into fine droplets, followed by rapid cooling and solidification. The most widely used mechanisms for atomizing metals at the industrial scale are water atomization (WA) and gas atomization (GA) [1]. These belong to the category called two fluid atomization, where the perturbation of the molten metal is induced by interaction with a high velocity fluid jet, either water or gas, resulting in powder formation usually spanning from a few tens of micrometres to about hundred microns in diameter.

Water atomization is generally associated with lower production costs compared to gas atomization and is widely adopted for alloys whose surface oxides can be easily reduced [41]. In this process, the molten stream is disrupted and subjected to rapid quenching; the resulting powders are collected at the bottom of the atomization chamber, followed by dewatering and drying operations. The extremely high cooling

rates, typically in the range of 10^4–10^6 °C s^{-1} [42], lead to irregular particle morphologies and a broad particle size distribution, usually spanning from approximately 10 to 1000 μm. In contrast, gas atomization is characterized by lower quench rates 10^3–10^5 °C s^{-1} (dependent on the process gas employed and on its temperature), which provide the droplets with sufficient time to achieve spheroidization prior to solidification [42].

Metal throughputs in gas atomization are generally lower than in water atomization. In batch GA, typical melt flow rates range from about 1 to 70 kg per minute, corresponding to melt stream diameters of approximately 2 to 15 mm. By contrast, water atomization lines can achieve throughputs on the order of 400 kg per minute [42].

The selected route strongly influences powder characteristics, particularly particle morphology, particle size distribution, and particle density. At the same time, each downstream metal powder-based AM technology imposes specific requirements on powder processability [14]. Consequently, the powder production method must be adapted to the process to satisfy the processability window of the equipment while also allowing the desired alloy to be produced.

Gas atomization, like other powder production methods, does not deliver one hundred percent yield within the target particle size fraction, so size classification by sieving is effectively mandatory. In particular, oversize particles and atomization debris that produce very large diameters must be removed. The off specification powder is generally recovered and recycled [43].

In contrast to press and sinter (P&S), both metal injection molding (MIM) and additive manufacturing (AM) typically require powders produced by gas atomization (GA) [4]. The primary constraint is flowability, because the feedstock must flow consistently through hoppers, feed screws, nozzles, and recoaters without blockage, a requirement that is especially critical in metal powder-based AM.

GA of metal powders exhibit high sphericity and relatively narrow particle size distributions, which promote superior flow and packing behavior. By comparison, water atomized powders, characterized by irregular morphology and higher surface roughness, generally display poorer flowability and are therefore unsuitable for MIM and metal powder-based AM [1].

However, P&S benefits from the angular morphology of water-atomized powders, which improves mechanical interlocking and green strength during compaction; highly spherical GA powders tend to compress less effectively and develop insufficient interparticle bonding under pressure, making them not applicable to P&S [4].

For the reasons outlined above, gas atomization represents the predominant method for the industrial production of powders intended for metal AM. It offers a favorable balance of production throughput, control of particle size distribution, and particle morphology. The process reliably yields highly spherical powders and is readily applicable to a wide range of alloy systems under robust process control [1].
Even though the objective in gas atomization is to obtain smooth, near spherical powders, substantial departures from ideal morphology are frequently observed in practice, especially for aluminum alloys, zinc, and copper zinc alloys [41]. These deviations arise principally from droplet cooling and solidification. Fine satellites adhering to coarser particles form through inter droplet collisions within the turbulent gas and melt spray. This agglomeration inhibits the effective separation of fine and coarse fractions and degrades downstream microstructure and properties by blending powders with markedly different dendritic scales and phase distributions. A further concern is the entrapment and dissolution of the atomizing gas in the liquid droplets, which can be retained in the solidified powders [42].
Most industrial gas atomization facilities still rely on technologies originally developed during the early decades of the twentieth century [1]. Several factors explain this persistence.
Firstly, the establishment of powder production plants requires substantial capital investment (often amounting to several million euros), which discourages industry participants to assume technological risks. Secondly, new plants are frequently designed to address the immediate and highly specific requirements of customers demanding tailored powder characteristics, leaving limited scope for extensive industrial research and development.
Finally, the stringent and highly sensitive nature of the powder specifications further discourages process modification [14, 15]. Even minor alterations in the production parameters of particles can significantly affect powder properties, such as particle size distribution and morphology [42]. Consequently, producers are often reluctant to modify established production routes, as the potential impacts on customers accustomed.

2.1.1 Gas Atomization technology

The principle of gas atomization is to transfer kinetic energy from a high speed gas jet to a liquid metal stream. The rapidly accelerated metal liquid becomes unstable and breaks into ligaments that are successively atomized in the jet wake by aerodynamic forces arising from the velocity difference between the gas and the metal droplets [42]. The particles produced in this process solidify in flight and are collected as metal powder. To ensure that all droplets are fully solidified and cooled below a specified temperature, the atomization tower must be sufficiently tall, in some cases higher than 10 m, to avoid agglomeration due to sintering at the base of the chamber [42]. At the industrial scale, the two most common gas atomization methods to produce spherical metal powders are Vacuum Induction Melting Gas Atomization (VIGA) and Electrode Induction Melting Gas Atomization (EIGA) [1]. Although the atomization mechanism is essentially the same (in particular in the case of free fall VIGA) and both processes operate in a inert atmosphere, the methods differ in how the molten stream is generated. In VIGA, the charge is melted in a crucible and then transferred to the gas nozzle through feed arrangements that depend on whether the system is configured for free fall or close coupled atomization. In EIGA, a prealloyed rod acts as a consumable electrode heated by an induction coil; liquid metal forms at the rod tip and then drains under gravity, in a free fall configuration, through an orifice located beneath it [43].

VIGA is generally more versatile because the crucible based melting practice is comparatively straightforward to regulate, enabling the production of powders from pure metals and from many alloys with melting points below about 1700 °C, including iron, nickel, cobalt, aluminum, and copper systems [43]. EIGA is more demanding to control due to the sensitivity of the rod melting rate, but the absence of contact with ceramic refractories greatly reduces the risk of contamination, which makes it well suited for reactive alloys, such as titanium alloys, and for materials with very high melting points [43].

In modern practice, a central challenge in gas atomization is to identify operating and geometric parameter windows that maximizes powder yield within the target particle size range while counteracting the inherent tendency toward broad particle size distributions and minimizing satellite formation and particle agglomeration.

Through appropriate control of atomization operating parameters, the particle size distribution can be shifted in a targeted manner, increasing the yield of powder within

the specification window required for the designed powder based AM technologies. To produce high density, defect free parts, PBF-LB/M requires powder feedstock with high sphericity, typically at least 0.85, and particle sizes distribution with a D10 of 20 μm and a D90 of 63 μm [14].

2.2 Vacuum induction melting Close-Coupled Gas Atomization

In vacuum induction melting gas atomization (VIGA) the charge is melted in an induction furnace under an inert atmosphere, which enables precise control of the chemical composition. The molten metal, from the bottom of a heated tundish, is then directed into a feed tube and discharged through a calibrated nozzle orifice to form a melt stream [41].
The processes setup most commonly used in VIGA gas atomization are close-coupled (CCGA) and free-fall (FFGA). The difference between these two technologies is the location where the gas jet meets the melt stream. Figure 2.1 summarizes the main characteristics of the two arrangements.

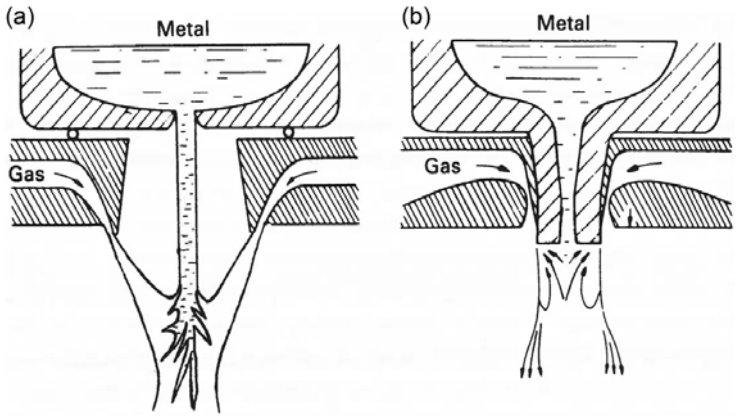

Fig. 2.1 Simplified schematic representation of a) free-fall (FFGA) and b) close-coupled gas atomization (CCGA) set up [44].

In the closed-coupled setup, the melt feed from a ceramic tube terminates in a metal melt nozzle that is inserted concentrically within the gas nozzle, whereas in free-fall atomization the gas orifices are repositioned, leaving a separation distance of about 5 to 10 cm between the outlet of the melt tube and the gas exit [41].

This allows the liquid stream to descend through the quiescent atomizing chamber's atmosphere before the high velocity gas strikes and disrupts it. As a result, FFGA exhibits greater operational stability and reliability than CCGA. For both types of atomizers, atomization can occur in the subsonic or supersonic regime, depending on the geometry of the gas nozzle (convergent or convergent-divergent) and the applied gas pressure [42].

The short separation between the jet and the melt in the CCGA configuration promotes stronger gas liquid interaction within the two phase flow, by minimizing kinetic energy loss and maintaining a high gas velocity and therefore achieves more effective break up of the liquid phase.

Close coupled atomization is generally favored for producing fine powders, achieving higher yields in the dimensional range needed for metal AM applications, and it permits a more compact layout, but it is prone to backflow and freeze off [45–47], phenomena that do not occur in FFGA systems. This behavior arises from the pronounced temperature drop during gas expansion: under near isentropic conditions the gas temperature can fall well below 0 °C (when no liquid metal stream is present), particularly when the atomizing gas is not preheated [43]. Furthermore, in accordance with the way in which the operating parameters are optimized, a suction effect may arise, increasing the metal flow and thereby altering the gas-to-metal flow ratio and the resulting particle size distribution. Nonetheless, it can be advantageous to configure the gas jets to induce a modest degree of suction, since the higher metal velocity helps mitigate the nozzle freeze-off issues highlighted above.

In summary, although free fall gas atomization is simpler to operate, it is less effective at producing fine powder fractions than the close coupled variant and therefore tends to yield a broader particle size distribution. Accordingly, the close coupled gas atomization configuration is the preferred route for manufacturing powders that meet PBF-LB/M feedstock specifications.

2.3 Physics of the close-coupled gas atomization

Gas atomization is governed by coupled fluid mechanical and thermal phenomena that evolve over very short length and time scales. Close-coupled gas atomization features a gas recirculation zone that forms a reverse conical structure directly beneath the melt, as illustrated schematically in the Figure 2.2. The apex of this cone coincides with a centerline stagnation point where the axial gas velocity approaches zero and the static pressure reaches a maximum. Gas from the outer stream is entrained into the recirculation zone across the stagnation front at subsonic speed. Near the melt orifice the flow turns radially toward the circumferential edge; upon reaching the periphery it encounters a sonic boundary that redirects the stream downstream. The recirculating core is therefore confined within the cone and separated from the surrounding supersonic jet, which produces a highly non-uniform velocity field throughout the atomization region.
For the purposes of analysis, from a theoretical standpoint, it is useful to partition the process into two conceptual stages that occur in rapid succession:

1. Primary atomization or primary breakup;
2. Secondary atomization or secondary breakup;

Although these stages overlap in space and time, treating them separately provides a practical framework for linking cause and effect in an otherwise complex multiphase flow. A schematic summarizing the two stages is shown in Figure 2.2.

Adopting this stage-based view also provides an interpretive lens for the high-speed image sequences analyzed later in this work. Observable quantities such as jet deflection angle, instability wavelength, plume envelope, and droplet trajectory can be mapped to underlying control parameters, including gas pressure, gas flow rate, and in particular the gas-to-metal ratio (GMR). This mapping enables a direct connection between optically accessible measurements and metrics of industrial relevance, including yield, particle size distribution, and powder morphology. The approach is therefore not merely didactic; it supplies the conceptual scaffolding required to explain how specific design choices and parameter settings propagate into measurable outcomes.

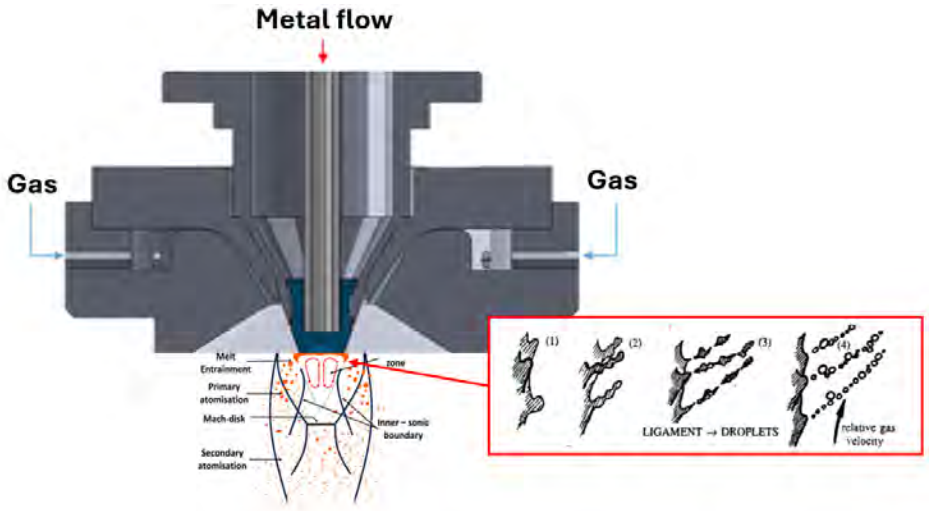

Fig. 2.2 Schematic of melt breakup during close-coupled gas atomization, showing the interaction between the descending molten metal stream and the high-velocity gas jets. The recirculation zone beneath the melt delivery tube promotes primary atomization through melt destabilization, ligament formation, and initial fragmentation. The resulting ligaments and coarse droplets are then further disintegrated during secondary atomization, as illustrated by the inset showing the transition from liquid ligaments to droplets with increasing relative gas velocity.

2.3.1 Primary atomization

Downstream of the nozzle, the shape of the molten metal column is governed by the competition between cohesive effects, primarily surface tension and viscosity, that tend to restore a minimum surface area and damp motion, and disruptive forcing from the external field. According to the model introduced by Dombrowski and Johns [48], primary atomization (or primary breakup) in close-coupled gas atomization can be decomposed into three sequential stages, a schematic illustration of which is shown in Figure 2.3:

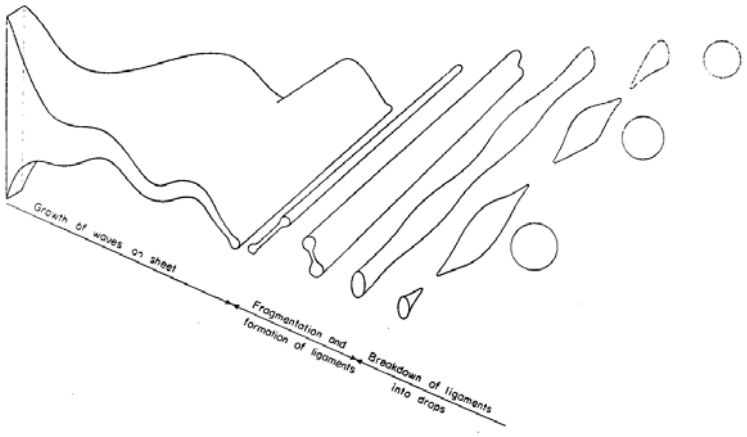

Fig. 2.3 Primary atomization pathway: (a) Formation and growth of a liquid film; (b) Ligament development; (c) Droplets formation; adapted from [48].

1. **Film formation.** As the melt column emerges from the delivery tube and enters the recirculating gas zone, it is subjected to two opposing actions: a stagnation pressure acting upstream and a sub-ambient suction acting downstream. Together these effects spread the column laterally into a thin sheet, which preconditions the liquid for subsequent fragmentation. During formation of the liquid sheet at the nozzle exit, the film thickness H is governed by the wetting behavior at the melt–orifice interface (contact angle θ) and cannot be reduced below a lower bound $H_{\min}$ (with H and $H_{\min}$ in mm) [49, 50]:

$$H_{\min} = (1 - \cos\theta)^{0.22} \tag{2.1}$$

2. **Ligament development.** The the high gas–liquid slip velocity imposes interfacial perturbations on the film that amplify through hydrodynamic instabilities (Kelvin–Helmholtz type) which induces strong aerodynamic loading through pressure gradients in the gas flow acting on the corrugated interface of the melt stream [48]. When the aerodynamic forcing is sufficien, the waves grow and the film locally thickens and thins until it ruptures, producing ligaments with a characteristic spacing related to approximately half the dominant interfacial wavelength.

Before introducing an operational scaling for the ligament diameter, it is useful to distinguish the two sheet-breakup regimes, long-wave and short-wave, derived from linear stability analysis as a function of the sheet Weber number (We_{sheet}) and illustrated in Figure 2.4:

$$\mathrm{We}_{\mathrm{sheet}} = \frac{\rho_{\mathrm{g}} (\Delta U)^2 h_F}{\sigma_{\mathrm{melt}}} \tag{2.2}$$

where ρ_g is the gas density, ΔU is the gas–melt slip velocity at the interaction zone, σ_{melt} is the melt surface tension and h_F is the half-thickness of the sheet at the breakup location [51].

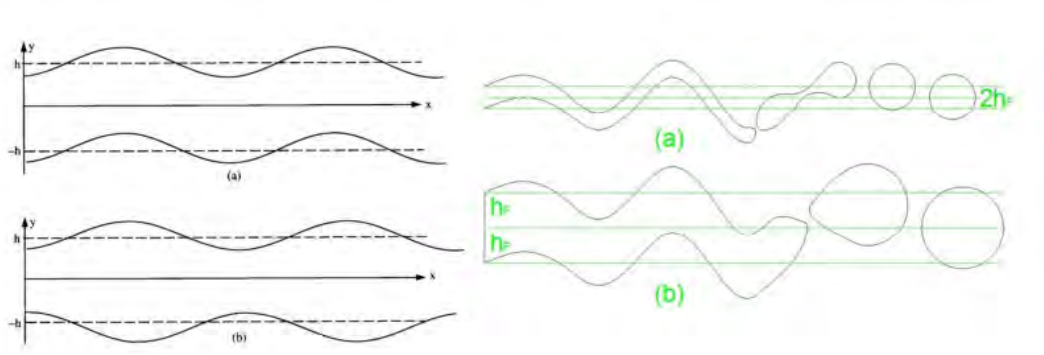

Fig. 2.4 On the left: sinuous (a) and varicose (b) instabilities triggered on a two-dimensional liquid sheet by imposed perturbations (adapted from [51]); on the right: long-wave (a) versus short-wave (b) breakup.

1) Long-wavelength breakup (low We_{sheet}): The disturbance wavelength λ is much longer than the half-thickness of the sheet h_F ($\lambda > 2\pi\, h_F$). Each wavelength produces two ligaments, since two pinch-off locations develop, as highlighted in Figure 2.4 (a). In this regime, the ligament diameter $d_{L,LW}$ is defined by the equation [51]:

$$d_{L,\mathrm{LW}} = \sqrt{\frac{8\, h_{\mathrm{F}}}{K_{max}}} \tag{2.3}$$

2) Short-wavelength breakup (high We_{sheet}): The disturbance wavelength λ is shorter than the half-thickness of the sheet h_F ($\lambda < 2\pi\, h_F$). Each wavelength produces one ligament (one pinch-off site per period), as highlighted in Figure 2.4 (b). In this regime, the ligament diameter $d_{L,SW}$ is defined by the equation [51]:

$$d_{L,\mathrm{SW}} = \sqrt{\frac{16\, h_{\mathrm{F}}}{K_{max}}} \tag{2.4}$$

For the specific case of a VIGA-CCGA atomizer with an annular converging–diverging (De Laval) nozzle, the operating conditions almost always favor the short-wavelength regime with a sinuous mode (the varicose mode remains secondary because ρ_g / ρ_l « 1), as highlighted in Figure 2.4. The physical reason is that the nozzle operates under choked/supersonic conditions: the gas jet is supersonic or nearly so, ΔU is very high, and, even with thin sheets, the sheet Weber number lies well above the transition threshold ($We_{sheet} > 1.69$). Representative values in the interaction zone for CCGA with Ar/N_2 as atomizing gas and a conergent-divergent nozzle are: $\rho_g \approx 2$–$6\,\mathrm{kg\,m^{-3}}$, $v_{rel} \approx 250$–$500\,\mathrm{m\,s^{-1}}$, $h_F \approx 20$–$100\,\mu\mathrm{m}$ and $\sigma_{melt} \approx 0.9$–$1.6\,\mathrm{N\,m^{-1}}$ [52].
For these ranges, We_{sheet} falls approximately between 1.6 and 170; therefore, in the vast majority of cases it exceeds 1.69 and the dominant regime is short-wavelength. Borderline cases (We_{sheet} close to 1.7) occur only when a low-density, low-pressure gas (small ΔU) is combined with extremely small h_F and high σ_{melt}, conditions that are not typical of VIGA–CCGA systems with annular slit nozzles [52].

In practice, when breakup occurs very near the orifice and h_F is not directly accessible, a common engineering approximation consistent with the short-wavelength regime is to replace h_F with the local film thickness H [49, 51] leading to:

$$d_L = \sqrt{\frac{16H}{K_{max}}} \qquad (2.5)$$

$$k_{\max}^{\mathrm{SW}} \approx \frac{2}{3}\frac{\rho_g\,(\Delta U)^2}{\sigma_{melt}} \qquad (2.6)$$

This links naturally to high-speed imaging through the dominant interfacial wavelength measured on the sheet, $\lambda_{\max}$, gives the most unstable wavenumber via $K_{\max} = 2\pi/\lambda_{\max}$. Substituting this into d_L Eq. 2.5 yields a direct, image-based estimate of the ligament diameter d_L . From a fluid-dynamic standpoint, a high gas–liquid relative velocity ΔU excites Kelvin–Helmholtz corrugations whose growth produces local thickening and thinning and ultimately sheet rupture into ligaments.

Alternatively, a practical first-order estimate of the most unstable wavenumber is given by Eq.2.6, which is appropriate for the short-wavelength regime in the sinuous mode and in the inviscid limit (Oh $\ll$ 1) [51]. When viscous effects are non-negligible, or when the dynamics deviate from the sinuous mode, $k_{\max}$ should be obtained from the full viscous dispersion relation of Senecal et. al [51] or directly from the measured $\lambda_{\max}$ from high-speed imaging.

In the Eq.2.6 the melt surface tension σ_{melt} is a function of the melt temperature T:

$$\sigma_{\text{melt}} = \sigma_{T_{\text{m}}} - k\,(T - T_{\text{m}}) \tag{2.7}$$

where σ_{T_m} is the melt surface tension at the melting point T_m, and k is a material-dependent constant [49, 51].

3. **Droplet generation.** The newly formed ligaments are highly unstable under the combined action of capillarity and aerodynamic forcing. Rayleigh–Plateau breakup governs their disintegration into droplet chains, while aerodynamic drag and shock–expansion wave oscillations further accelerate the process, yielding fine droplets and completing the primary breakup stage [48]. The diameter of these droplets d_{p} can be estimated using the following relation, where Oh is the Ohnesorge number [51]:

$$d_{\text{p}} = 1.88\,d_{\text{L}}\,(1 + 3\,\text{Oh})^{1/6} \tag{2.8a}$$

$$\text{Oh} = \frac{\mu_{\text{melt}}}{\sqrt{d_{\text{L}}\,\rho_{\text{melt}}\,\sigma_{\text{melt}}}} \tag{2.8b}$$

Where μ_{melt} is viscosity of the liquid droplet, ρ_{melt} is the density of the molten metal and d_L is the diameter of the ligaments defined by the equation 2.5.
Direct visualization of atomization is extremely challenging owing to the chaotic flow, elevated melt temperatures, and very high jet velocities; consequently, the mechanisms governing primary breakup remain only partially understood.
Nonetheless, reduced-order models and scaling relations, expressed through simplified governing equations that link operating parameters to gas and melt properties, are indispensable for quantifying the relative influence of these factors on gas atomization.

2.3.2 Secondary atomization

Primary atomization establishes the initial spray configuration. If the nascent droplets remain immersed in a high velocity gas stream, they undergo a coupled sequence of processes that interact with one another: additional droplet breakup driven by aerodynamic loading, acceleration governed by drag, spheroidization under the action of surface tension, cooling–solidification and oxidation. Taken together, this downstream evolution constitutes secondary atomization (or secondary breakup) and is the stage that ultimately determines the final particle size distribution [53]. In this regime, the relative motion between droplet and gas imposes destabilizing aerodynamic stresses; when these exceed capillary restoring forces, the droplet becomes unstable and fragments further by mechanisms analogous to those operative during primary breakup, although at shorter length and time scales.
Faeth et al. [54] systematically varied the droplet Weber number (We_{d_p}) and Ohnesorge number (Oh) 2.8b in breakup experiments:

$$\mathrm{We_{d_p}} = \frac{\rho_\mathrm{g}\,(\Delta U)^2\,d_p}{\sigma_\mathrm{melt}} \tag{2.9}$$

They found that for low-viscosity conditions ($Oh < 0.1$) the breakup regime is governed predominantly by We_{d_p}, with viscous effects being negligible. As Oh increases, viscous damping becomes significant and the threshold We_{d_p} required to trigger breakup increases [54]. Combining the equations from 2.1 to 2.9 and using Eq. 2.5 to evaluate the ligament diameter, replacing the superheat ΔT (the temperature of the melt minus the melting-point temperature T_m), neglecting Ohnesorge-number effects ($Oh \ll 1$), and accounting for the temperature drop during primary breakup ΔT_PB, we obtain the following expression:

$$\mathrm{We_{d_p}} = 9.18\,\Delta U\,\rho_\mathrm{g}\left[\frac{(1-\cos\theta)^{0.22}}{\sigma_{T_\mathrm{m}} - k(\Delta T - \Delta T_\mathrm{PB})}\right]^{0.5} \tag{2.10}$$

In general, only droplets with a Weber number exceeding a critical value ($We_\mathrm{crit} \approx 11-13$) [41, 49] undergo substantive secondary breakup, transitioning through modes such as twins, bag, film stripping, and catastrophic as We_{d_p} increases, which are showed in Figure 2.5. Droplets with $We_{d_p} < \mathrm{We_{crit}}$ primarily deform and then re-stabilize without fragmenting.

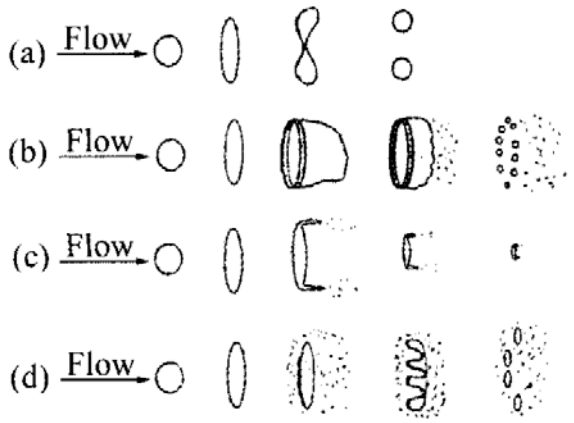

Fig. 2.5 Secondary breakup regimes for droplets: (a) Twins, 11< We < 12; (b) Bag, 12< We <100; (c) Film stripping, 100< We < 350; (d) Catastropic, 350< We; adapted from [49].

It follows that Weber numbers satisfying the breakup criterion are achieved only within a narrow region adjacent to the atomizer, consequently the effective atomization zone is very limited in extent. Beyond this zone, aerodynamic loading falls below the threshold for further fragmentation, even though the droplets may still be molten.

Different breakup modes impose distinct deformation histories on the droplets; consequently, the resulting powders exhibit variability in both particle size and microstructure. Because the cooling rate of a droplet depends on its diameter, and the final powder microstructure is governed by the initial cooling history of the droplet, the breakup mode indirectly controls microstructural results [42]. In the twins mode (10.7< We_{d_p} < 12), the droplet diameter produced by secondary breakup d_s is given by the following relation [49, 55], where d_p denotes the diameter of the drop at the end of the primary break-up stage (Eq. 2.8a):

$$d_\mathrm{s} = \frac{d_\mathrm{p}}{\sqrt[3]{2}} \tag{2.11}$$

In bag-mode breakup (12< We_{d_p} <100), fragmentation of the ring edge produces comparatively larger droplets with mean diameter denoted d_sr, whereas rupture of the bag membrane yields smaller droplets with mean diameter d_sb [56]:

$$d_{\mathrm{sr}} = 0.3\, d_{\mathrm{p}} \qquad \text{(2.12a)} \qquad\qquad d_{\mathrm{sb}} = 0.042\, d_{\mathrm{p}} \qquad \text{(2.12b)}$$

Under film-stripping conditions (100< We_{d_p} < 350) Faeth et al.[54], drawing on single-droplet experiments, proposed a semi-empirical correlation for the resulting particle size; in this regime, the mean droplet diameter d is given by the relation shown in the following equation [49, 54]:

$$d_{\mathrm{s}} = 7.44\, d_{\mathrm{p}} \left(\frac{\rho_{\mathrm{melt}}}{\rho_{\mathrm{g}}} \right)^{-0.25} \left[\frac{\mu_{\mathrm{melt}}}{\rho_{\mathrm{melt}}\, d_{\mathrm{p}}\, \Delta U} \right]^{0.5} \tag{2.13}$$

Catastrophic breakup (We_{d_p} >350) denotes an extreme, highly energetic fragmentation regime whose physics is not yet fully resolved, and that is rarely achieved under standard atomization settings. When it does occur, it is commonly associated with the formation of very fine powders and with comparatively narrow size distributions. Empirically, the characteristic droplet size after secondary breakup decreases with increasing Weber number; thus, to obtain finer powders, operating conditions should be adjusted to elevate the pre-breakup Weber number (e.g., by increasing the gas–melt slip velocity or using a higher-density atomizing gas), subject to stability and materials constraints.

According to Eq. 2.10, the droplet's Weber number depends on four primary quantities, the gas–melt slip velocity ΔU, the gas density ρ_g, the contact angle θ of the liquid to delivery tube orifice interface, and the melt surface tension σ_{melt}.

Holding the other variables fixed, We_{d_p} increases with both ΔU and ρ_g; thus, measures that raise these two terms, such as optimizing nozzle geometry, increasing gas supply pressure, selecting a more suitable atomizing gas, or adjusting melt flow rate, generally shift the spray toward finer particles [41]. In practice, the reverse-cone recirculation zone beneath the melt exit produces a strongly non-uniform velocity field. As a result, droplets experience different local slip velocities ΔU, leading to a spectrum of We_{d_p} values across the plume and, consequently, to different secondary breakup modes coexisting in space and time. Moreover, the rupture of the liquid sheet and ligaments, governed by capillary (Rayleigh–Plateau type) instabilities [48], is inherently stochastic, so the resulting droplet diameters typically follow a log-normal distribution. For these reasons, powders produced by close-coupled atomization inevitably exhibit particle-size variability that is well described by a log-normal law [43].

2.3.2.1 Spheroidization

Spheroidization is the terminal stage of powders formation. Its progression can be characterized by the dimensionless ratio:

$$\tau = \frac{t_{\mathrm{sp}}}{t_{\mathrm{th}}} \tag{2.14}$$

where t_{sp} is the spheroidization time required to dissipate internal mechanical energy within the droplet and t_{th} is the characteristic time for thermal energy removal leading to solidification.

If $\tau < 1$, capillary forces have sufficient time to smooth residual distortions and the droplets approach a spherical shape before solidification. If $\tau > 1$, solidification precedes complete capillary relaxation, and the resulting particles retain irregular morphologies, frequently in the form of ligaments [41].

Within the commonly adopted single–fluid description of atomization, models in the literature [41] indicate that the spheroidization time scales as:

$$t_{\mathrm{sp}} \propto \frac{\rho_{\mathrm{melt}} D^2}{\mu_{\mathrm{melt}}} \tag{2.15}$$

since spheroidization is governed by the viscous damping of interfacial oscillations in a droplet of diameter D and the molten alloy properties density ρ_{melt} and viscosity μ_{melt}.
In the final stages of the process, satellites may also form, producing defective powder when smaller droplets collide with and adhere to larger ones during flight [41].

2.4 Gas nozzle design

Gas nozzle design is a primary driver of atomization efficiency because it establishes the jet flow field and governs momentum transfer from the high-velocity gas to the melt stream; two main classes of nozzle geometry can be distinguished: purely converging nozzles and converging–diverging (De Laval) nozzles [42].
The expansion regime of a gas jet is governed by nozzle geometry and by the nozzle pressure ratio $PR = \frac{P_g}{P_a}$.
The pressure differential between a gas reservoir at stagnation pressure P_g and the atmosphere inside the atomizing chamber at pressure P_a, connected by a nozzle, results in a gas flow from high to low pressure.
When the PR ratio exceeds the critical value, define by the equation [52]:

$$\frac{P_{g,\text{crit}}}{P_a} = \left(1 + \frac{\kappa - 1}{2}\right)^{\frac{\kappa}{\kappa - 1}} \tag{2.16}$$

The flow becomes choked, and sonic conditions are reached at the narrowest cross-section of the gas nozzle (Mach number M = 1).
The critical pressure ratio for the typical gases used is reported in the Table 2.1.

Table 2.1 Critical pressure ratio for the gases used in the gas atomization process [52].

Type of gas	κ	$P_{g,\text{crit}}/P_a$
Helium, Argon	1,67	2,055
Air, Nitrogen	1,4	1,893

Depending on the nozzle geometry, convergent or converging–diverging, and the pressure ratio $PR = \frac{P_g}{P_a}$, three regimes of gas flow are distinguished: underexpanded, ideally expanded, and overexpanded. In practice, purely convergent nozzles produce underexpanded jets across most operating conditions, whereas convergent–divergent nozzles can be ideally expanded at a specific PR but, under typical atomization settings, discharge overexpanded or at most only weakly underexpanded jets [41].
In a convergent nozzle, the absence of a diverging section limits the exit Mach number to one, so at high chamber pressure the gas leaves before completing its expansion [57]. The remaining pressure expansion occurs outside the nozzle through the rapid expansion of fans and the formation of shock cells, with associated losses in

directed momentum. In contrast, a convergent-divergent contour enables acceleration to supersonic gas speed and accommodates most of the isentropic expansion within the nozzle, reducing external adjustment and the related energy losses. Consequently, convergent divergent nozzles generally achieve higher efficiency than purely convergent designs. Furthermore, for convergent–divergent nozzles, atomization is not confined to the fluid–fluid collision zone; secondary breakup persists downstream within the supersonic core [57].
The contrasting flow fields produced by different nozzle types are shown in Figure 2.6.

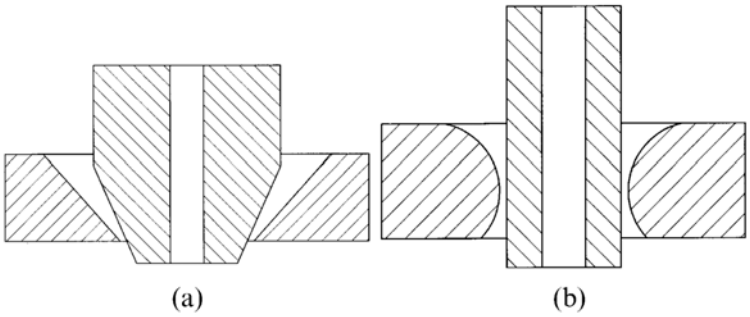

Fig. 2.6 Schematic representation of a) convergent nozzle and b) convergent–divergent nozzle, adapted from [43].

Optimal nozzle design must also address throat width. Analogous to raising the supply pressure, increasing throat width elevates gas mass flow and exit velocity and sustains a longer supersonic plume, thereby enhancing liquid disintegration [42].
In close coupled configurations, two nozzle archetypes are widely employed as shown in Figure 2.7: the annular slit nozzle, which features a continuous circumferential slot surrounding the melt delivery tube, and the discrete jet nozzle, which consists of an array of individual orifices.

In industrial practice, annular slit designs are preferred because they generally deliver superior performance relative to discrete jet configurations. In line with this, multiple studies have shown that annular nozzles tend to produce finer powders than discrete jet designs [58, 59]. The prevailing explanation is that annular geometries sustain longer supersonic core regions in the gas jet, extending the distance over which aerodynamic forces and instabilities act on the liquid; secondary breakup therefore continues well downstream of the impingement zone, leading to smaller droplets and, ultimately, smaller powders [42].

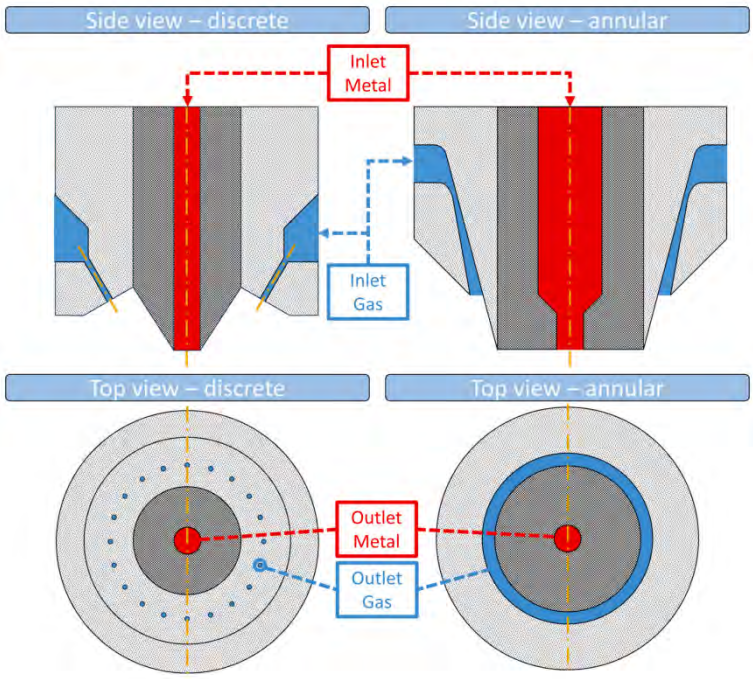

Fig. 2.7 Simplified schematic representation of discrete jet and convergent–divergent annular slit nozzle configurations [58].

The atomizer used in this study is a PSI Hermiga 100/10 system configured in a close coupled arrangement and equipped with an annular slit convergent divergent nozzle.

The angle of the gas nozzle in relation to the melt delivery nozzle is a key parameter in gas atomization. In concentric annular designs, shallow jets with a large impingement angle relative to the melt stream tend to produce a wide spray cone and elevate back pressure on the melt. By contrast, steep jets with a small impingement angle may require a longer stand off for the gas to engage the stream, which promotes turbulence and lowers gas utilization. Practical impingement angles span roughly 15° to 80°, with the optimum depending on the melt system and the atomizing gas [42].

2.5 Main process parameters

Gas atomization (GA) is a complex process governed by multiple interdependent physical phenomena. Consequently, the final outcome is influenced by various parameters, ranging from geometric and physical conditions to material properties. Direct relationships among melt flow rate, gas-only nozzle aspiration, and gas pressure are difficult to disentangle because the variables are mutually coupled; nevertheless, clarifying their interplay is essential for the efficient production of metal powder.

2.5.1 Gas properties

2.5.1.1 Gas type

A variety of atomizing gases are employed, including nitrogen, argon, helium, air, and tailored blends [43]. Inert gases such as argon and helium are preferred for the atomization of reactive alloys like titanium and superalloys or whenever a low oxygen content is required. Reactive gases can be selected to promote in situ formation of oxides, nitrides, or carbides. Gas mixtures allow tuning of jet properties and interfacial chemistry to obtain desired powder characteristics at lower cost. Additives or dopants may be introduced into the atomizing stream to passivate the surfaces of active droplets and powders [42].
Gases composed of smaller, lighter molecules generally exhibit higher thermal conductivity, since higher molecular speeds enhance energy transport between collisions. As a result, hydrogen and helium have greater thermal conductivity than nitrogen and argon. The choice of atomization gas therefore affects droplet cooling rates: lighter gases such as helium, with higher specific heat capacity, thermal conductivity, and thermal diffusivity, tend to yield higher convective heat transfer coefficients under comparable flow conditions and thus promote faster cooling. The gas chemistry also influences the particle morphology due to the formation of an oxide layer stabilizes ligaments and suppresses further breakup [42]. Oxidation of molten metals typically proceeds on timescales shorter than the spheroidization time t_{sp} (Eq. 2.15). When the resulting oxide is strong and adherent, it can arrest capillary relaxation, causing droplets to solidify with ligament-like geometries [41].
The process gas is commonly recirculated through a recovery loop, or else discharged

to the atmosphere, and the purge gas used for the chamber is usually the same as the atomizing gas. Moreover, some VIGA installations separate the gas used in the melt chamber from the high pressure atomizing gas. In practice, two independent gas circuits are employed: a low pressure line for the melt and atomising chamber atmosphere and a high pressure line for atomization, which enables the use of different gas combinations to tailor process conditions.

2.5.1.2 Gas pressure

The atomizing gas supply pressure P_g is a key control variable because it sets the gas mass flow rate $\dot{G}$, its velocity v_g and, through the the aspiration field established ahead of the melt orifice by the high speed jets, also influences the molten melt mass flow $\dot{M}$ [42]. Increasing P_g generally reduces the median particle size (D_{50}) by enhancing primary breakup efficiency. Part of this response arises because, as P_g rises, $\dot{G}$ increases while $\dot{M}$ often decreases due to a deeper subambient pressure region at the melt exit. Urionabarrenetxea et al. [57] linked the decrease in $\dot{M}$ at higher P_g is due to the formation of a recirculation zone and a stagnation point near the melt nozzle that restrict the incoming melt flow, thereby favoring finer powders. To mitigate this effect and avoid flow obstruction, in VIGA atomizer a positive overpressure is typically applied to the melt chamber with the aim of maintaining $\dot{M}$ approximately constant [42, 57]. Nevertheless, P_g must be maintained within an optimal window: excessively high values can depress melt velocity to the point of freeze-off before the stream reaches the atomization zone, whereas too low a pressure yields coarser powders because the gas imparts insufficient momentum to the liquid [42].

2.5.1.3 Gas Temperature

As observed for gas pressure, and as previously highlighted in the discussion of the atomizing gas nozzle design, several parameters indirectly affect particle size distribution via their impact on gas velocity.
In particular, the gas temperature T_g influences key attributes of the atomizing stream, including gas velocity, viscosity, and its interaction with the melt flow rate. In high-pressure gas atomization the use of hot gas, whose temperature is selected primarily according to the alloy being processed (approximately 100 °C of nitrogen gas for

aluminum alloys [60], 200 °C of nitrogen gas for NiCu-based alloy [61] and 300 °C of argon or nitrogen gas for steels [62]), has been reported to improve specification yield by enhancing kinetic-energy transfer from the gas phase and extending the effective breakup pathway [42]. Multiple studies report that increasing T_g markedly decreases the median particle size [62, 63]. In particular, Wang et al. [63] observed that a higher T_g (300°C) of argon reduces the median diameter of the primary atomization droplets of AISI 316L, an effect attributed to increased jet momentum and enhanced interfacial shear, which promotes a more effective breakup of the molten metal. Elevated T_g also prolongs convective heat transfer to the droplets and delays their solidification, allowing both primary disruption and secondary breakup to proceed further. As a result, the final particles become smaller, and the particle size distribution narrows, although accompanied by a possible concomitant rise in satellite particles that can degrade flowability and increase recoating defects [58].
The principal drawback of hot gas atomization is cost, since the adoption of this approach requires dedicated sections for recirculation and heating that increase capital demand, energy use, and process complexity. However, using heated gas can lower operating expenses because, at a given supply pressure, the higher gas velocity reduces the gas mass flow needed to reach the target atomization conditions, thereby decreasing overall gas consumption. Since gas usage is an important contributor to operating cost in high-pressure gas atomization, achieving lower consumption for the same or greater jet momentum is particularly advantageous on the commercial scale, improving cost efficiency without sacrificing atomization performance [53].

2.5.2 Molten metal properties

Atomization efficiency is governed not only by the properties of the atomizing gas but also by those of the molten metal.
Metal superheat denotes the temperature excess of the melt above its melting point, more precisely, the difference between the measured melt temperature prior to atomization and the liquidus temperature for an alloy. This parameter governs key thermophysical and rheological properties of the melt and therefore affects the powder particle size distribution, with a significant influence on the median size D_{50} [51, 64]. In general, increasing superheat reduces the viscosity μ_{melt} and the surface tension σ_{melt} of the melt, which promotes primary separation of the jet and subsequent secondary atomization, producing finer particles [42].

However, excessive superheat introduces disadvantages, including higher energy demand, volatilization of alloying elements, unfavorable reactions between crucible materials and the melt, with possible contamination of the melt itself, and potential damage to equipment. Furthermore, excessive melt flow rates can exceed the atomizing capacity of the gas, degrading primary breakup and leading to a broader particle size distribution.
An intermediate, optimized superheat is therefore required to prevent premature solidification in the melt transfer system from the crucible to the nozzle or at the nozzle itself, while limiting these side effects and minimizing particle size. The usual superheat levels vary between 100 °C up to 200-250 °C, depending on the alloy system and on the atomizing gas used [43].
In addition, the chemical composition of the melt influences the particle size distribution by modifying its physicochemical properties, particularly surface tension and viscosity. Overall, lower surface tension and lower viscosity promote primary melt breakup, reducing the energy required from the droplet formation, analogous to the effect of increased superheat. However, it should also be considered that higher surface tension can improve atomization efficiency because it lowers the probability of droplet coalescence after breakup [41].

2.5.3 Gas-to-Metal flow Ratio

Within the variables governing gas atomization, the gas to metal mass flow ratio (GMR_m) demonstrates a particularly strong influence on the final particle size. It is defined as:

$$GMR_m = \frac{\dot{G}}{\dot{M}} \tag{2.17}$$

where $\dot{G}$ and $\dot{M}$ denote the gas and melt mass flow rates, respectively.
Many operating and geometric settings impact the median size and the particle size distribution primarily through their effect on $\dot{G}$ and $\dot{M}$, and thus on GMR_m. A substantial body of work reports tight correlations between GMR_m and both D_{50} and PSD breadth [65]. As a rule, higher GMR_m values yield finer powders and narrower distributions, a trend documented for nickel, tin, aluminum, copper, and iron based alloys [66]. Conversely, if GMR_m is too low, the gas jet supplies insufficient momentum for effective disruption of the liquid stream, leading to

larger droplets, increased spatter, and a shift toward coarser powders. GMR_m is not, however, a complete descriptor of breakup physics. Several studies identify the gas–melt slip velocity at the interaction zone, $\Delta U = U_g - U_m$, as the dominant control during primary breakup [41, 42]. Urionabarrenetxea et al. [66] showed that identical GMR_m values achieved with different gas flow rates produced distinct PSDs, highlighting the direct role of gas velocity.

Building on this point, Urionabarrenetxea et al. [66] proposed that particle size correlates more strongly with a gas to metal ratio defined on volumetric flow rates rather than on mass flow rates. They introduced the volumetric metric (GMR_V) and observed robust relationships between particle size distributions and (GMR_V) for powders produced under varied operating conditions, including different atomizing gases. A plausible reason for the improved correlation is that (GMR_V) implicitly captures the influence of gas velocity, since the mean gas volumetric flow can be approximated as the nozzle cross sectional area multiplied by the average gas velocity

Despite these constraints, GMR_m remains widely used in industrial practice to benchmark atomizer performance because it is simple to determine and shows a strong, even if not exclusive, correlation with particle size metrics.

2.5.4 Optimal operating conditions for VIGA close-coupled gas atomization

In close-coupled gas atomization (CCGA), a primary objective is to maximize the yield within the target particle-size window while preserving spherical morphology and a narrow distribution. The operating window is set by the interaction between the jet flow field established by the gas nozzle and the melt discharge at the orifice. In the CCGA process, the wake closure pressure denotes the critical atomization gas pressure at which the gas flow transitions from an open wake to a closed wake regime. This shift modifies the gas melt interaction, with significant consequences for the breakup efficiency and particle sizes [41].

As illustrated in Figure 2.8 in an open-wake operation, the annular jets create a recirculation cavity with a narrow throat ahead of the melt orifice, still connected to the surrounding flow. The aspiration at the lip is only mildly sub-ambient, and the gas structures are characterized by internal and recompression shocks without a stable central Mach disk. Primary breakup is weaker once fragments are advected

out of the near field, which tends to broaden the size distribution. In addition, an internal shear surface that extends from the melt delivery tip bounds the primary atomization region; this is the first point of gas–melt contact and the location of the maximum shear-driven forces. If partially fragmented packets are carried beyond this near field, they enter in the secondary breakup regime characterized by lower-specific-momentum gas streams, producing coarser droplets and broadening the distribution [41].

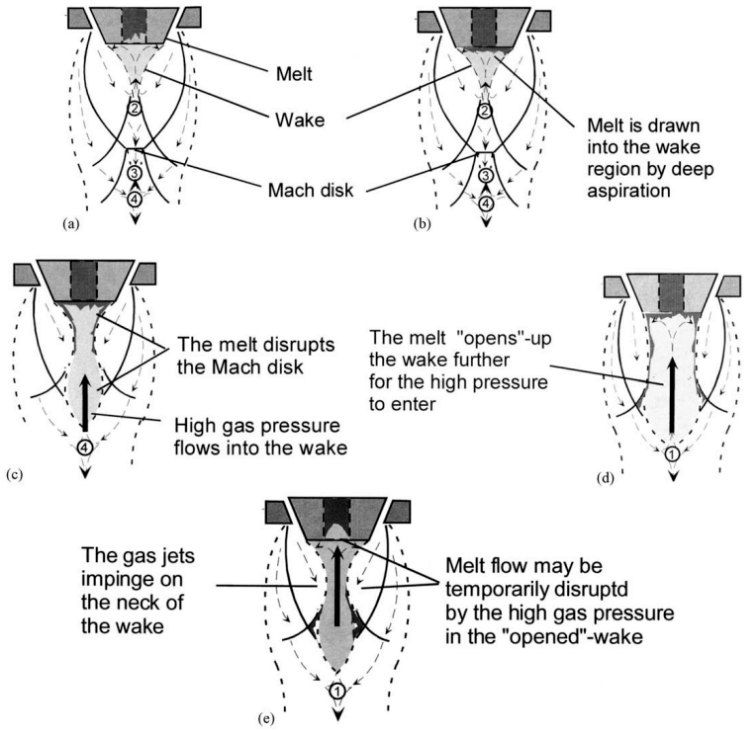

Fig. 2.8 Schematic representation of melt–gas interaction and wake-topology evolution in close-coupled gas atomization, illustrating the recirculation cavity beneath the melt orifice, the formation of the Mach disk, and the transition between open-wake and closed-wake conditions as a function of atomization pressure; adapted from [67].

At a critical wake-closure pressure (WCP), the topology switches to a closed-wake regime in which the wake neck collapses, a normal shock (Mach disk) forms on the centerline, and the local pressure field changes abruptly. This state produces a deeper subambient aspiration at the melt lip that can induce suction of additional melt from the tundish and a stronger, more focused shear field for primary breakup. Experiments on industrial CCGA dies show that atomizing slightly above WCP yields markedly finer powders and a narrower distribution. However, the same con-

ditions also raise the likelihood of unstable melt delivery, intermittent back-pressure, and freeze-off when the local melt velocity is depressed below a safe value [67].
The WCP regime is strongly governed by geometric design variables, including melt-tip protrusion length, the diameter at the melt delivery tip, and the angle of the gas nozzle in relation to the melt delivery nozzle; shortening the protrusion or reducing this diameter lowers the critical pressure, thereby improving atomization efficiency [67]. For VIGA–CCGA used to maximize yield in the 20–63 µm interval useful for PBF-LB/M additive manufacturing technique, the closed-wake regime at or just above WCP is generally the most efficient if the melt delivery remains stable and freeze-off is avoided [67]. The finer median size achieved above WCP is accompanied by a higher GMR because the effective recirculation pressure can slow the melt (in contrast to suction-driven draw-in from the tundish), so active control of flow balance is required. Control actions should therefore be concentrated within the primary breakup zone, where gas velocity is maximal and the melt is nearly stationary with respect to the jets; the thickness of the preformed melt film can be tuned via pour-tube orifice design, directly influencing primary fragmentation and the resulting distribution.
Through preliminary CFD simulations, together with direct observation of the atomization plume, the wake-closure regime is indicated by a visible contraction of the near-field plume; analysis of high-speed camera recordings corroborates this signature and enables identification of the parameter set required to operate at or just above the wake-closure pressure. In summary, for a VIGA–CCGA atomization system, in order to maximize process yields together with powder quality, it is necessary to operate at or slightly above the wake-closure pressure and maintain this state by coordinating the gas pressure, the melt-side overpressure tuned in the melt chamber during atomization, and appropriate metal superheat, while selecting a melt-tip diameter and nozzle geometry that promote closure. This approach concentrates breakup in the primary shear zone and delivers the highest fine-fraction yield with a tighter particle size distribution.

Chapter 3

Duplex Stainless steel

3.1 Duplex and Super Duplex stainless steel an overview

Duplex stainless steels are stainless alloys with mainly a two phase microstructure composed of austenite and ferrite, with both phases meeting the chromium stainless criterion in solid solution exceeding 12 wt.%; the designation “duplex” reflects the coexistence at ambient temperature of these two phases [68]. By appropriately balancing austenite-stabilizing and ferrite-stabilizing elements, primarily chromium and nickel, compositions can be tailored to yield approximately equal fractions of ferrite and austenite. Typical grades are iron-based materials containing chromium between 22 and 25 wt.% and nickel between 4 and 7 wt.%, often supplemented with molybdenum between 3 and 4 wt.% and nitrogen between 0.10 and 0.25 wt.% [69].

A representative Fe–Cr–Ni phase diagram section provides a useful framework for describing the solidification path and the subsequent phase evolution of duplex stainless steels. As shown in Figure 3.1, solidification initiates in the ferritic field; upon cooling, austenite progressively forms from the ferritic matrix, producing the characteristic dual-phase microstructure that is largely retained down to room temperature.

Due to their dual-phase architecture, duplex stainless steels combine high strength, comparable to or only slightly lower than that of martensitic or ferritic stainless steels, and the stress-corrosion-cracking resistance typical of ferritic grades, which is comparable to or superior to that of fully austenitic stainless steels, together with the fracture toughness associated with austenitic alloys. These materials were devel-

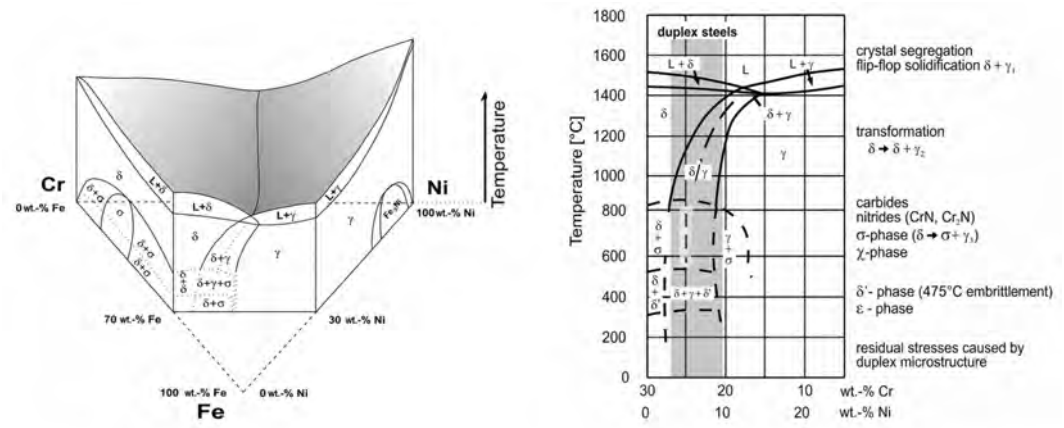

Fig. 3.1 Section of the Fe–Cr–Ni ternary phase diagram at 70 wt.% Fe and corresponding schematic representation of the phase evolution in duplex stainless steels. The diagram highlights solidification in the ferritic field, followed by austenite formation during cooling and retention of the ferrite-austenite duplex microstructure at lower temperatures. Adapted from [70].

oped for service in corrosive environments over the range -100 °C to 250 °C [69]. This property set is governed not only by the specific levels of alloying elements in solid solution but also by the balance between the and phases; extensive literature indicates that a near-equiatomic distribution, approximately 50% austenite and 50% ferrite, offers the most favorable compromise.

Their elevated chromium content yields a favorable corrosion-resistance-to-cost ratio, making these grades attractive substitutes for more traditional stainless steels or specialty alloys. Beyond their mechanical performance, the principal advantage of duplex and superduplex grades lies in their exceptional resistance to localized corrosion, particularly in chloride-containing environments; as a result, they are extensively employed in petrochemical processing and in oil and gas applications in marine service.

The sustained interest in these alloys stems from their resistance to stress corrosion cracking (SCC), achieved with a comparatively low nickel content of 4–7 wt.% when contrasted with austenitic stainless steels (ASS). Historically, the adoption of duplex stainless steels (DSS) has intensified during periods of nickel scarcity [71]. More recently, nickel's designation as a strategic raw material in 2023 [72] and the 2024 adoption of the EU Critical Raw Materials Act [73] have renewed interest in duplex stainless steels. Although the global share of duplex stainless

steels remains approximately 1–3 % of total stainless steel production [74], recent sources indicate renewed interest and steady market growth for duplex stainless steels, with the global market estimated at USD 4.4 billion in 2024 and projected to reach USD 6.0 billion by 2030 (CAGR 5.4%) [74, 75]. A pivotal milestone in duplex stainless steel development was the recognition that interstitial nitrogen acts as a potent austenite stabilizer. Incorporating nitrogen enabled a reduction in nickel content, thereby improving cost efficiency without compromising corrosion performance. Elevated nitrogen levels also accelerate austenite re-formation in the heat-affected zone during welding, which permits higher travel speeds and mitigates susceptibility to solidification cracking. In addition, nitrogen provides solid-solution strengthening that elevates the yield strength while preserving toughness [71].

3.1.1 Classification of duplex stainless steel

The localized corrosion resistance of duplex stainless steels is commonly assessed through the Pitting Resistance Equivalent Number (PREN), defined by Eq. 3.1a, or by Eq. 3.1b in the presence of tungsten, with all alloying element contents given in weight percent. In these formulations, the coefficient k is conventionally set to 16, although values within the interval 10–30 are also employed [76]. A larger PREN generally corresponds to improved resistance to pitting and crevice attack. It should be emphasized that PREN is a descriptor based on bulk composition and therefore operates at a macroscopic level; it does not account for microstructural discontinuities or heterogeneities, for example non-uniform partitioning of alloying elements between the austenite and ferrite phases. The practical advantage of this qualitative classification is the ability to estimate corrosion performance directly from the nominal chemical composition without recourse to dedicated experiments, with a marked dependence on the contents of chromium, nickel, and nitrogen that promote an expanded passive domain.
The PREN, together with the chemical composition, makes it possible to classify the different types of duplex steels into lean duplex, duplex, super duplex, and hyper duplex based, as summarized in the accompanying Table 3.1 [76].

$$\mathrm{PREN} = \%\mathrm{Cr} + 3.3\,\%\mathrm{Mo} + k\,\%\mathrm{N} \tag{3.1a}$$

$$\mathrm{PREN}_W = \%\mathrm{Cr} + 3.3\big(\%\mathrm{Mo} + 0.5\,\%\mathrm{W}\big) + k\,\%\mathrm{N} \tag{3.1b}$$

Table 3.1 Classification of duplex stainless steels by PREN and typical nominal composition [wt.%].

PREN range	Definition	Typical nominal composition [wt.%]
≤ 35	Lean duplex (LDSS)	Cr 25, Ni 4, N 0.10; Mo not intentionally added.
$35 < \mathrm{PREN} < 40$	Standard duplex (DSS)	Cr 22, Ni 5, Mo 3, N 0.17.
$40 \leq \mathrm{PREN} < 45$	Super duplex (SDSS)	Cr 25, Ni 7, Mo 4, N 0.30.
≥ 45	Hyper duplex (HDSS)	Cr > 30; other elements are grade-dependent.

In duplex and super duplex stainless steels, chromium is the main ferrite-stabilizing element, promoting the body-centered cubic structure and contributing to corrosion resistance through passive film formation. The chromium equivalent and nickel equivalent are empirical parameters adopted to describe the overall ferritizing and austenitizing contributions of the main alloying elements, respectively. Their expressions are reported below [77], with all alloying element contents expressed in weight percent:

$$\mathrm{Cr}_{eq} = \%\mathrm{Cr} + \%\mathrm{Mo} + 1.5\,\%\mathrm{Si} + 0.72\,\%\mathrm{W} \tag{3.2a}$$

$$\mathrm{Ni}_{eq} = \%\mathrm{Ni} + 0.44\,\%\mathrm{Cu} + 0.5\,\%\mathrm{Mn} + 30\,(\%\mathrm{C} + \%\mathrm{N}) \tag{3.2b}$$

While chromium mainly promotes ferrite formation, nickel acts as the principal austenite stabilizer, favoring the face-centered cubic structure and improving ductility, toughness, and repassivation capability.

3.1.2 Mechanical properties of duplex and super duplex stainless steels

Compared with the widely used austenitic stainless steels, duplex grades exhibit markedly higher yield strength, typically about twice as high, together with increased ultimate tensile strength [78]. In structural design, this strength advantage permits equivalent load-bearing capacity with reduced section thickness, enabling lighter components.

An additional salient mechanical attribute of duplex stainless steels is their excellent impact toughness, evidenced by a low ductile-to-brittle transition temperature of approximately -80 °C. However, the mechanical response is strongly influenced by microstructural transformations activated near 800 °C and 475 °C [79, 80]. The relatively high alloy content and the substantial fraction of body-centred cubic ferrite render these steels susceptible to embrittlement with a consequent degradation of properties, most notably a decline in impact toughness, which in practice confines recommended service to temperatures below about 300 °C. Accordingly, processing routes that involve elevated temperatures, including hot working, welding, and heat treatments, must be carefully optimised [79, 80].

3.1.3 Microstructural constituents of duplex stainless steels

Duplex stainless steels are characterized by a dual-phase microstructure mainly consisting of ferrite and austenite. However, depending on chemical composition and thermal history, additional microstructural constituents may form, including intermetallic phases, carbides and nitrides. These secondary phases are generally undesirable, since they can strongly affect toughness, ductility and corrosion resistance. A summary of the main phases and precipitates that may be observed in duplex stainless steels is reported in Table 3.2 at the end of this section.

3.1.4 Carbides and nitrides

Within the temperature range of approximately 600–1000 °C, duplex stainless steels may undergo precipitation of carbides and nitrides, mainly in the form of $M_{23}C_6$, CrN and Cr_2N. Their formation is related to the limited solubility of carbon and nitrogen in the alloy, which further decreases during cooling [76]. Due to the higher number of tetrahedral interstitial sites in the FCC lattice, austenite can accommodate larger amounts of these interstitial elements compared with ferrite, where their solubility is considerably lower. As a consequence, carbides and nitrides are preferentially observed within ferritic regions or along γ/δ interfaces. The occurrence of these precipitates is generally detrimental, as it may reduce both toughness and corrosion resistance [71].

3.1.4.1 $M_{23}C_6$ carbides

The presence of carbon together with carbide-forming elements, such as Cr and Mo, may promote carbide precipitation in duplex stainless steels. This phenomenon has been reported in duplex grades with carbon contents higher than approximately 0.05 wt.%, even after annealing followed by rapid cooling. For this reason, 0.05 wt.% is commonly regarded as the upper acceptable carbon limit for low-carbon duplex stainless steels [76].

In duplex stainless steels, carbides are most frequently observed as $M_{23}C_6$ precipitates, characterized by an FCC crystal structure. Their chemical composition is mainly governed by carbon and chromium, although other carbide-forming or

substitutional elements, including Mo, V, Mn, Si and Ni, may also contribute to the carbide chemistry.

$M_{23}C_6$ carbides typically precipitate within the temperature range of about 550–1050 °C, with the fastest precipitation kinetics occurring near 850 °C. Owing to their rapid formation, these carbides may be detected after holding times as short as 60 s within this temperature interval. Their precipitation is commonly described by the transformation [71]:

$$\alpha \rightarrow \gamma_3 + M_{23}C_6 \tag{3.3}$$

This reaction involves chromium diffusion from ferrite towards the growing carbide. As a consequence of the local chromium depletion, the surrounding ferrite may transform into secondary austenite, leading to the development of a lamellar microstructure. The reduction in chromium content within the ferritic matrix is particularly detrimental from a corrosion standpoint, since it may significantly impair the local corrosion resistance of the alloy [79, 80].

3.1.4.2 CrN and Cr_2N nitrides

Nitrogen addition as an alloying element provides several advantages in duplex stainless steels, particularly through the stabilization of the austenitic phase. Its solubility can be enhanced by increasing the chromium content; however, nitrogen exhibits a strong chemical affinity for Cr, which may promote nitride precipitation. The formation of these precipitates is generally detrimental to the overall performance of the material [71].

Although the solubility of nitrogen in the ferritic lattice is considerably higher than that of carbon, it remains significantly lower than in austenite. Consequently, nitride precipitation mainly occurs within ferritic regions or along γ/δ interfaces. Two main types of chromium nitrides are commonly reported, which can be distinguished on the basis of their precipitation mechanism and crystal structure: CrN, characterized by a cubic lattice, and Cr_2N, characterized by a hexagonal lattice.
CrN precipitation is associated with the variation in nitrogen solubility within ferrite. Since above approximately 1100 °C nitrogen solubility in austenite increases markedly, even rapid cooling may be insufficient to retain such a high nitrogen

content in solid solution without promoting lattice instability. The formation of Cr_2N nitrides is instead closely comparable to the precipitation behaviour of $M_{23}C_6$ carbides. Cr_2N generally forms within the temperature range of about 550–1000 °C, with the highest precipitation rate typically observed between 700 and 900 °C [71].

As for most of the secondary phases described above, chromium nitrides adversely affect the mechanical response of duplex stainless steels, leading to a reduction in toughness and favouring brittle fracture mechanisms. Since nitride precipitation cannot be effectively suppressed solely by rapid cooling, its formation in significant amounts may be limited either by reducing the nitrogen content of the alloy or by applying suitable heat treatments that, during cooling, allow nitrogen initially present in ferrite to diffuse towards the austenitic phase [69].

3.1.5 Secondary phases

Below approximately 1000 °C, duplex stainless steels are generally prone to phase transformations involving the precipitation of deleterious intermetallic phases [71]. Among the most relevant secondary phases, σ and χ are typically formed within the temperature range of about 650–970 °C, whereas α' precipitation occurs at lower temperatures, approximately between 300 and 500 °C [71]. This precipitation behaviour is schematically represented in the semi-quantitative TTT diagram shown in Figure 3.2.

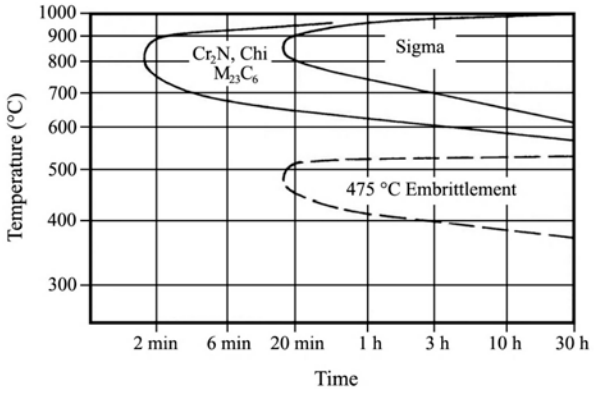

Fig. 3.2 Semi-quantitative time–temperature–transformation diagram showing the typical precipitation ranges of secondary phases in duplex stainless steels [81].

3.1.5.1 Sigma phase σ

The σ phase is one of the most extensively investigated secondary phases in duplex and austenitic stainless steels. This attention is mainly related to its detrimental influence on both mechanical performance and corrosion resistance, as well as to the fact that it can be relatively easily detected by conventional microstructural characterization techniques. Owing to its high hardness and brittle nature, the precipitation of σ promotes material embrittlement, with particularly critical effects in welded joints.

This behaviour has been reported, for instance, for Zeron 100, a commercial designation of UNS S32760. In that study, the presence of σ was associated with a slight increase in yield strength and ultimate tensile strength, while a severe loss of ductility was observed, with the elongation to failure decreasing from approximately 40% in the sigma-free condition to about 7% in the sigma-containing material [82].

From the corrosion standpoint, a further study carried out on the same alloy showed that σ can promote the anodic reaction. In addition, its precipitation induces a local depletion of chromium and molybdenum in the ferritic matrix adjacent to the σ-phase domains. Since Cr and Mo are key alloying elements for passivity and resistance to localized corrosion, their local impoverishment may lead to a marked reduction in corrosion resistance [69].

For these reasons, considerable research effort has been devoted to the identification of processing and heat-treatment conditions capable of suppressing or limiting σ precipitation. Its formation is generally sluggish and is therefore typically observed after thermal exposure within its stability range, approximately 700–1000 °C, or after heat treatments performed above this range followed by slow cooling. Increasing the alloy content of Cr, Mo and W enhances the tendency for σ formation, broadening the corresponding precipitation domain in the TTT diagram [82], as shown in Figure 3.3.

Since super duplex stainless steels are intrinsically characterized by high contents of these alloying elements, they are particularly susceptible to σ-phase precipitation. This phase is commonly observed at grain boundaries, preferentially along γ/δ and δ/δ interfaces. Suppression of σ formation, or its removal from the microstructure when already present, can be achieved by solution annealing above the stability range of the phase, followed by rapid water quenching [69].

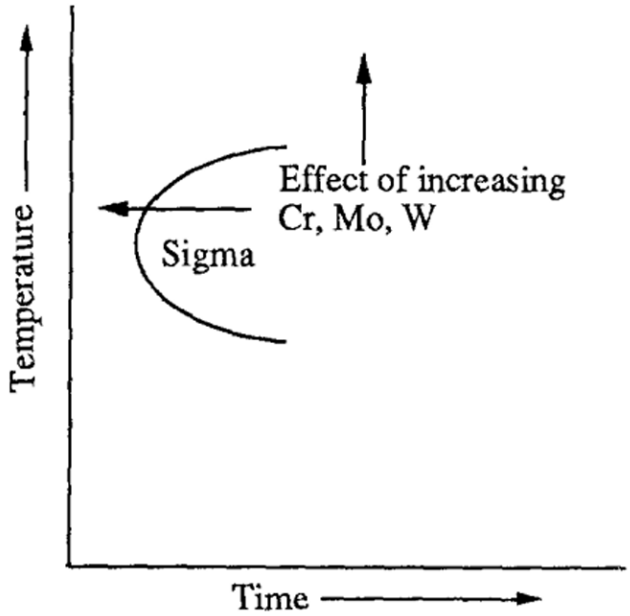

Fig. 3.3 Schematic representation of the effect of Cr, Mo and W additions on the σ-phase precipitation domain in the TTT diagram of duplex stainless steels [82].

3.1.5.2 Chi phase χ

The χ phase may occur in ferritic, austenitic and duplex stainless steels. Similarly to the σ phase, its precipitation is associated with a significant deterioration of both mechanical properties and corrosion resistance. The formation of χ is generally favoured only when the molybdenum content reaches a minimum level of approximately 2 wt.% or higher. As observed for σ, this phase preferentially nucleates at γ/δ and δ/δ grain boundaries; however, its stability domain is narrower and is typically located within the temperature interval of about 600–900 °C. Although χ has received comparatively less attention in the literature, mainly because of its sluggish precipitation kinetics, its occurrence is nevertheless regarded as highly detrimental to the performance of duplex stainless steels [71].

3.1.5.3 Alpha-prime phase α'

The α' phase is mainly enriched in Fe and Cr and exhibits a BCC crystal structure coherent with the ferritic matrix. It generally appears as very fine precipitates, with typical dimensions in the range of 20–200 Å. This phase is widely recognized as the main cause of ferrite embrittlement after exposure at approximately 475 °C. At this temperature, α' forms through spinodal decomposition [71].

Its influence on the material response is comparable to that of σ and χ phases. In particular, α' precipitation leads to a pronounced decrease in elongation to failure and toughness, accompanied by an increase in both yield strength and ultimate tensile strength. This strengthening and embrittlement effect is mainly related to the ability of the fine precipitates to hinder dislocation motion within the ferritic phase. The presence of α' also adversely affects corrosion behaviour, causing a significant reduction in pitting resistance [71].

Table 3.2 Summary of the microstructural constituents that may be observed in duplex stainless steels [81].

Phase	Unit cell	Atoms per cell	Space group	Lattice parameters (nm)	Composition
Main phases					
Austenite (γ)	fcc	4	Fm3m	$a = 0.358$–0.362	(Fe,Cr,Ni,Mo,N)
Ferrite (δ or α)	bcc	2	Im3m	$a = 0.285$–0.289	(Fe,Cr,Ni,Mo)
Martensite (α')	bcc	2	Im3m	$a = 0.285$–0.289	(Fe,Cr,Ni,Mo,N)
Martensite (ε)	hcp	2 (6)	$P6_3/mmc$	$a = 0.250$–0.255; $c = 0.410$–0.420	(Fe,Cr,Ni,Mo,N)
Carbides					
$M_{23}C_6$	fcc	116	Fm3m	$a = 1.057$–1.068	$(Cr,Fe,Mo)_{23}C_6$; $(Cr_{16}Fe_5Mo_2)C_6$
MC	ord fcc	8	Fm3m	$a = 0.4131$–0.4698	(Ti,Nb,V)C
M_6C	fcc	112	Fd3m	$a = 1.085$–1.128	$(Fe,Mo,Nb,Cr)_6C$
M_7C_3	pseudo hex.	40	Pnma	$a = 1.395$–1.400; $c = 0.452$–0.453	$(Cr,Fe)_7C_3$
Nitrides					
MN	ord fcc	8	Fm3m	$a = 0.4097$–0.4577	CrN; ZrN; TiN; NbN; VN
M_2N	hexagonal	9	P31m	$a = 0.475$–0.480; $c = 0.443$–0.447	$(Cr,Fe)_2N$
Z-phase	tetragonal	6	$P4/nmm$	$a = 0.303$–0.306; $c = 0.738$–0.740	CrNNb
Intermetallic phases					
Sigma (σ)	bct	30	$P4_2/mnm$	$a = 0.87$–0.92; $c = 0.4554$–0.48	$(Fe,Ni)_x(Cr,Mo)_y$
Chi (χ)	bcc	58	$I4_3m$	$a = 0.881$–0.895	$Fe_{36}Cr_{12}Mo_{10}$; $(Fe,Ni)_{36}Cr_{18}Mo_4$
Laves (η)	hex.	12	$P6_3/mmc$	$a = 0.473$–0.483; $c = 0.772$–0.786	Fe_2Mo; Fe_2Nb; Fe_2Ta; Fe_2Ti; Fe_2W
G	fcc	116	Fd3m	$a = 1.115$–1.120	$Ni_{16}Nb_6Si_7$; $Ni_{16}Ti_6Si_7$; $(Ni,Fe,Cr)_{16}(Nb,Ti)_6Si_7$
R	hex.	53 (159)	R3	$a = 1.08$–1.10; $c = 1.92$–1.94	$Fe_{22}Mo_{19}Cr_{13}$; $(Fe,Ni)_{10}Cr_{15}Mo_3Si_2$

3.2 Additive manufacturing of duplex and super duplex stainless steels: current state of the art in PBF-LB/M processing

3.2.1 Applied heat treatments and their influence on properties

Solution annealing is the heat treatment most widely adopted for duplex stainless steels and, in also, for components produced by laser powder bed fusion (PBF-LB/M). In the latter case, an alternative stress-relief anneal, as proposed by Gargalis et al. [83] for duplex and super-duplex references, was found to have negligible microstructural impact. Solution annealing, followed by rapid quenching (typically in water), allows the dissolution of intermetallic phases, carbides, and nitrides, thereby reducing or preventing their presence in the final microstructure. For duplex grades, these cycles are generally carried out above 1000 °C to move outside the stability field of embrittling phases, as discussed in Section 3.1.5.

Table 3.3 summarizes the mechanical properties reported for duplex and super duplex stainless steels, with particular emphasis on the as-built condition, together with the corresponding bibliographic references.

Table 3.3 Overview of PBF-LB/M processing conditions and selected properties reported in the literature for duplex and super duplex stainless steels. In the table, A.B. refers to the as-built state.

Steel grade	Ref.	HED [J/mm^3]	Atm.	N in powders [wt.%]	N in A.B. [wt.%]	Austenite [%]	Hardness [HV]	Relative density	R_m	A_r
UNS31803	[84]	–	Ar	–	0.12%	–	–	99.6%	865	8%
UNS32750	[84]	–	Ar	–	0.25%	–	–	99.6%	1031	14%
UNS31803	[85]	300	N_2	0.21%	0.2%	1%	–	99.98%	>1200	–
UNS32750	[85]	300	N_2	0.3%	0.3%	2%	–	99.98%	>1200	–
UNS32750	[86]	112.8	Ar	0.31%	–	30%	408.4	89–93%	–	–
UNS32750	[87]	–	Ar	0.3%	–	2%	450	99%	1320	8%
UNS32707	[88]	–	–	0.36%	0.24%	0.2%	530	–	1391	13.2%
UNS32760	[62]	–	N_2	0.38%	0.393%	–	–	99.92%	–	–
UNS31803	[83]	65	Ar	0.13%	–	0%	–	99.98%	–	–
UNS32750	[83]	59	Ar	0.29%	–	0%	–	99.95%	–	–
UNS32750	[89]	97.69	Ar	0.26–0.31%	–	10%	–	99.96%	1256	10%

When properly executed, solution treatment yields improved mechanical and corrosion properties. This improvement arises from a substantial re-balancing of

the austenite-to-ferrite ratio during the thermal cycle, from the redistribution of solute elements between the two phases (for example, chromium and molybdenum in ferrite, and nitrogen in austenite), and from the dissolution of any embrittling constituents [90].

For PBF-LB/M-processed material, heat treatment provides an effective route to restore the phase balance by increasing the austenite fraction, which is initially close to zero in the as-built state. Temperatures reported in the literature typically fall within 1000–1250 °C. The variation in the austenite (γ) content with solution-treatment temperature is closely related to the competition between the reactivation of the transformation of metastable ferrite (δ) into austenite, commonly referred to as secondary austenite, since it forms from metastable ferrite, and the thermodynamically driven transformation of austenite into ferrite. For temperatures above the thermodynamic equilibrium between austenite and ferrite, a decrease in the austenite fraction is expected with increasing heat-treatment temperature, because under these conditions the ferritic phase is thermodynamically more stable.

The kinetics of these transformations differ in PBF-LB/M-produced components compared with cast or forged duplex and super duplex stainless steels; consequently, the heat-treatment schedules and holding times must be re-evaluated accordingly. Figure 3.4a reports the predicted equilibrium austenite fraction as a function of temperature, as calculated by Thermo-Calc software for a duplex stainless steel [91]. Figure 3.4b shows the austenite fraction as a function of the solution-treatment temperature after a 15 min holding time in the electron-beam welded zone of an AISI F51 duplex stainless steel [91].

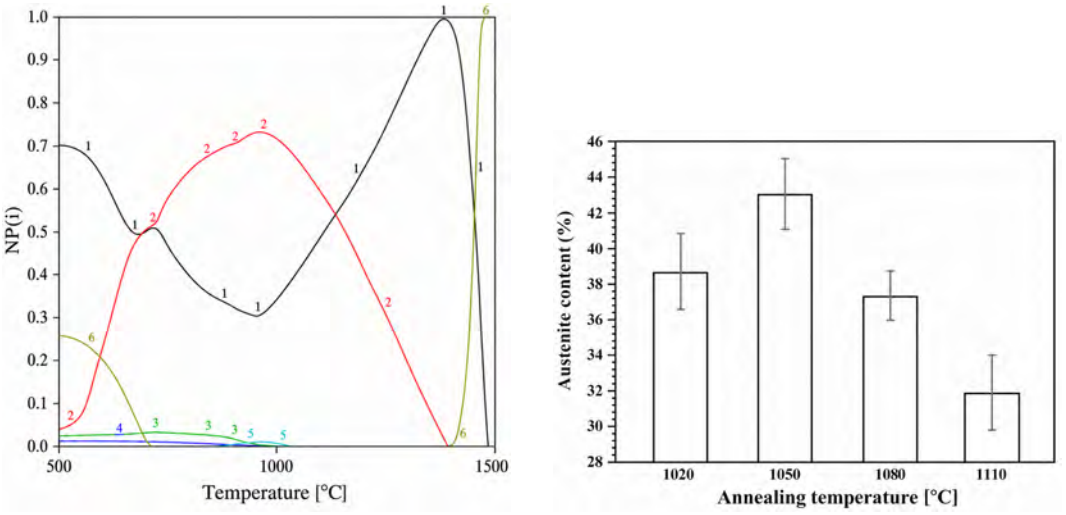

a) Thermo-Calc prediction of the equilibrium austenite content as a function of temperature for a duplex stainless steel. The black curve indicates ferrite (δ), while the red curve indicates austenite (γ).

b) Austenite content as a function of the solution-treatment temperature after a 15 min holding time in the electron-beam welded zone of an AISI F51 duplex stainless steel.

Fig. 3.4 Austenite fraction as a function of temperature in duplex stainless steels: (a) Thermo-Calc prediction of the equilibrium phase fraction, with ferrite (δ) shown in black and austenite (γ) shown in red [91]; (b) experimentally determined austenite content as a function of solution-treatment temperature after a 15 min holding time in the electron-beam welded zone of an AISI F51 duplex stainless steel [92].

Post-treatment microstructures consist of a ferritic matrix with austenite appearing in amounts and morphologies that depend on both alloy chemistry and thermal schedule. At equivalent heat-treatment conditions, super-duplex alloys exhibit a higher austenite fraction than standard duplex grades due to their greater nickel and nitrogen contents. Distinct austenite morphologies have been reported, including domains tracing melt-pool boundaries that arise from the growth of sparsely precipitated grains during cooling, as well as intergranular austenite with an acicular morphology and intragranular austenite [83, 93, 94].

Table 3.4 summarizes representative solution heat treatments and the resulting properties for duplex and super duplex stainless steels reported in the literature. In comparison with the as-built data in Table 3.3, solution treatment typically lowers the ultimate tensile strength while increasing elongation at fracture. A further observation is a marked reduction in hardness after heat treatment to levels comparable with wrought counterparts [95]. This trend does not hold if sigma phase precipitates

during the thermal cycle, a possibility under slow-cooling conditions; in that case hardness rises substantially and toughness deteriorates markedly [96].

Table 3.4 Representative solution heat treatments and the resulting properties reported in the literature for duplex and super duplex stainless steels.

Steel grade	Ref.	T [°C]	Soaking time	Austenite [%]	Secondary phases	R_m [MPa]	A_t [%]	Hardness [HV]
UNS S31803	[84]	1050	3 h	36%	–	750	19%	–
UNS S32750	[84]	1050	3 h	43%	–	859	21%	–
UNS S31803	[62]	1100	5 min	45%	–	–	–	–
UNS S32750	[62]	1170	5 min	52%	–	–	–	–
UNS S32750	[96]	1200	5 min / slow cooling	71%	Sigma and Chi	920	1.8%	400
UNS S32707	[88]	1100–1200	1 h	40.5–36.6%	–	941–851	24.6–29.2%	321–285
UNS S31803	[83]	1100	1 h	34%	–	–	–	–
UNS S32750	[83]	1100	1 h	65%	–	–	–	–

Chapter 4

From Gas Atomization to PBF-LB/M Components: Materials, Processing Conditions, and Characterization Procedures

4.1 Schematic Overview of the Research Activities

For an easier consultation and to provide a rapid overview of the experimental activities described in Chapter 4, the main stages of the present work are schematically summarized in Figure 4.1. The diagram highlights the overall sequence of the experimental activities workflow and the principal characterization steps carried out throughout the this research.

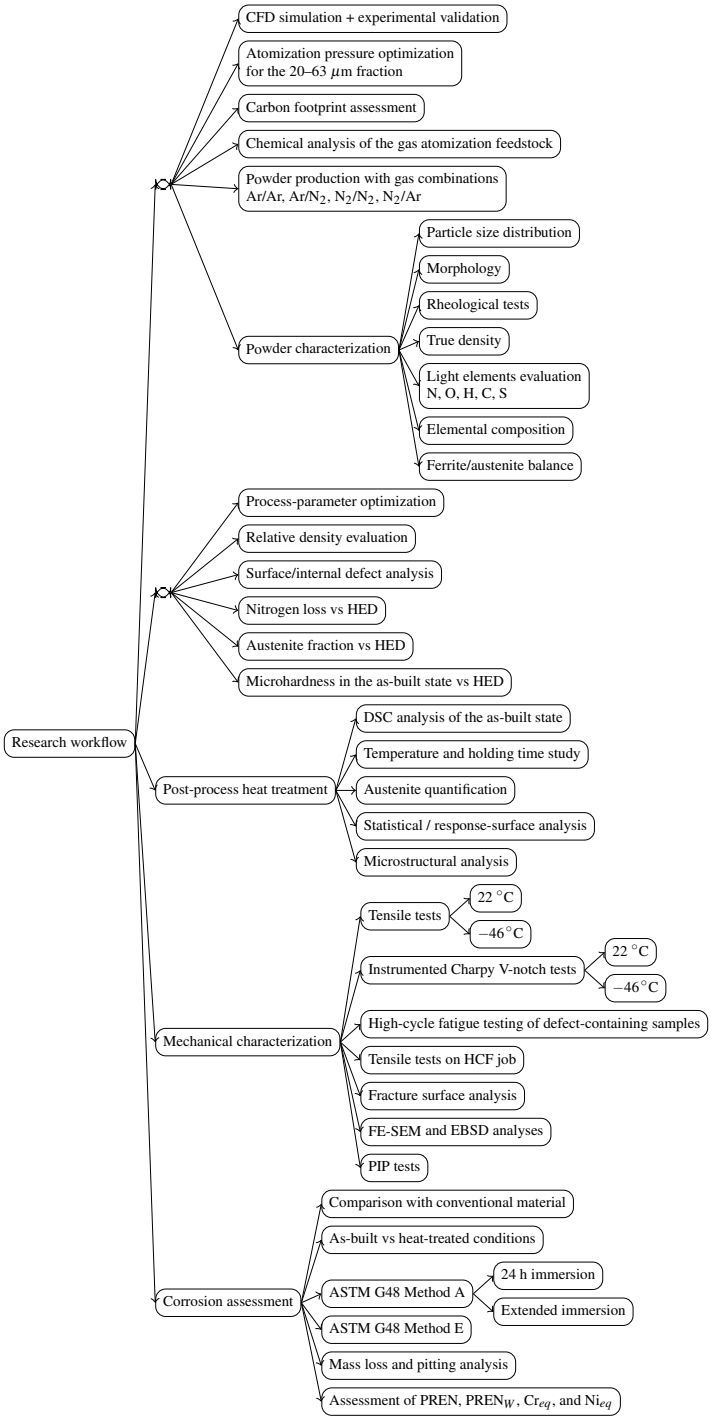

Fig. 4.1 Schematic summary of the research activities carried out in the present PhD work.

4.2 Influence of inert gas pressure on the properties of UNS S32760 super duplex stainless steel powders obtained from waste materials via gas atomization

4.2.1 Introduction

There is a large literature on how the principal operating parameters in gas atomization influence the resulting powder attributes. In general, investigations fall into two streams: experimental studies and numerical modelling. Historically, limited computing resources and immature models constrained researchers to empirical approaches. With modern increases in computational power, computational fluid dynamics (CFD) has become a compelling tool for analysing gas atomization, offering access to flow features that cannot be measured directly yet impact on powder formation [66].

The most advanced approach is the Volume of Fluid (VOF) method, which treats the gas and the melt as immiscible phases, solves a single momentum equation for the shared velocity field, and advects the phase volume fraction to track the interface throughout the computational domain [53].

Nevertheless, high fidelity simulation of multiphase breakup remains challenging owing to pronounced contrasts in density, viscosity, and interfacial physics between the gas and the molten metal. Even when both phases are explicitly resolved, computational constraints often necessitate two dimensional formulations rather than fully three dimensional non-axisymmetric calculations, and further idealizations are commonly introduced [53, 97]. These limitations are compounded by the scarce availability of reliable thermophysical data for specific melts, including temperature dependent viscosity and surface tension, which restricts model calibration and validation. For this reason, many contemporary studies isolate the gas phase and characterize the atomizing jet in the absence of the metal stream [57, 98].

The fluid-dynamic mechanisms governing gas atomization, even in the absence of a melt stream, are inherently complex and strongly dependent on the specific gas atomization configuration. In fact, within a given atomization route, such as the close-coupled method, key design parameters, including nozzle geometry, play a decisive role in determining process behaviour.

4.2.2 Materials and Methods

4.2.2.1 Single-Phase CFD model and simulation Setup

A steady, single-phase computational fluid dynamics framework was established to characterize the carrier-gas flow in the close-coupled atomization zone of the PSI Hermiga 100/10 system installed at the Alessandria campus of Politecnico di Torino. The calculation was conducted in an axisymmetric, two-dimensional setting that resolves the meridional section of the nozzle–chamber assembly, illustrated in Figure 4.2, a choice that concentrates resolution where gas expansion, shock formation, and stagnation features govern primary melt disintegration.

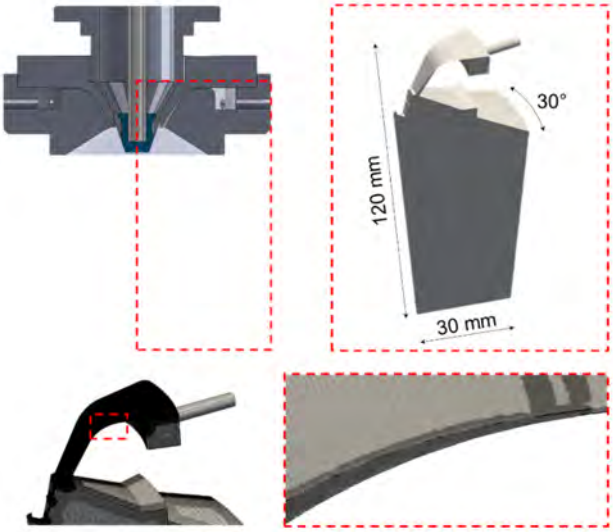

Fig. 4.2 Numerical modeling setup: Axisymmetric wedge-sector domain for the PSI Hermiga 100/10 close-coupled, annular-slit convergent–divergent nozzle: 30° sector, 120 mm axial extent, 30 mm radial extent. Bottom left: isometric view of the computational domain. Bottom right: mesh detail with targeted refinement at the annular slit and nozzle lip. Total mesh size 16 million finite-volume cells.

Unlike many prior studies that adopt surrogate or simplified nozzle surrogates, the present model reproduces the annular-slit, convergent–divergent gas nozzle with high geometric fidelity, retaining those details whose omission can distort the near-field flow. The computational mesh comprised approximately sixteen million finite-volume control volumes to secure adequate spatial resolution across steep gradients. Turbulence closure employed a Reynolds-Averaged Navier–Stokes (RANS) formulation with the $\kappa - \varepsilon$ model [99], and the governing equations were

advanced to a steady solution with the compressible solver rhoSimpleFoam in OpenFOAM v9. This configuration was designed to resolve velocity and pressure fields and to map streamline topology in the immediate vicinity of the nozzle exit. Boundary and operating conditions were selected to represent argon operation at room temperature upstream of the nozzle and to span plant-relevant inlet pressure levels.

Specifically, simulations were carried out for inlet total pressures of 30, 40, and 45 bar, with a supply temperature fixed at 298 K. These operating points were chosen to quantify how increasing driving pressure modulates the local gas dynamics that control ligament inception and, ultimately, the efficiency of secondary atomization in close-coupled configurations. It is important to note that the CFD campaign was conducted in the absence of a molten metal stream, as a single-phase gas calculation. The results should therefore be interpreted with explicit reference to the atomization die geometry of the PSI Hermiga 100/10 (a CCGA equipped with an annular slit and a convergent–divergent nozzle) since the predicted flow features are conditioned by this specific layout. Within this defined scope, the model provides a physically consistent description of the gas-phase field that underpins primary breakup in the PSI system and offers a robust basis for subsequent geometry–process optimization and for coupling to two-phase atomization analyses.

4.2.3 CFD-based analysis of the gas atomization process with experimental comparison

4.2.3.1 Pressure-dependent Gas-Jet flow field and Near-nozzle dynamics

The simulation results, as shown in Figure 4.4 (a), indicate the emergence of a stable supersonic core already at 30 bar. In agreement with the CFD study reported in [57] for a comparable close-coupled unit, the gas in the breakup region attains supersonic speeds, exceeding the acoustic velocity of argon at 1 bar $\approx 320\,\mathrm{m\,s^{-1}}$, as illustrated in Figure 4.4. As reported in Figure 4.3 a static pressure greater than 2 bar is established near the base of the atomization nozzle, coincident with the first shock in the supersonic jet's shock-cell structure generated by the high-speed flow [57].

The operating conditions explored through the simulation were subsequently reproduced in full-scale atomization trials conducted using UNS S32760 super duplex stainless steel (X2CrNiMoCuWN25-7-4, *AISI* F55, Werkstoff No. 1.4501)

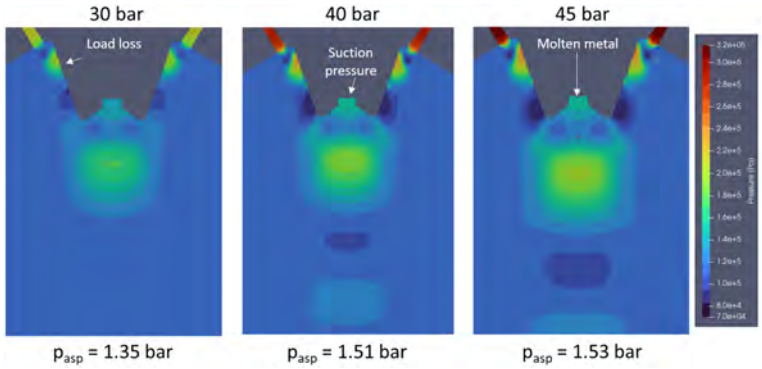

Fig. 4.3 Static pressure field around the tip–nozzle region from compressible RANS ($\kappa-\varepsilon$) CFD under argon at 30, 40, and 45 bar. The aspiration pressure p_{asp} in the melt feed tube increases with supply pressure. Colour scale: static pressure [Pa].

derived from industrial waste materials, and the corresponding results are reported in [65]. As shown in Figure 4.4 (a), increasing the atomization gas pressure raises the gas exit velocity at the nozzle tip and produces a narrower and more collimated atomization plume. The near-nozzle topology is characterized by oblique shock structures and a well-defined axial stagnation point a short distance downstream of the tip, consistent with close-coupled gas atomization under in-chamber expansion. As shown in Figure 4.4 (a), increasing the inlet argon pressure from 30 to 40 and 45 bar strengthens the acceleration in the throat region and extends the length of the supersonic plume. In parallel, as shown by the plot in Figure 4.5, the peak axial velocity of the argon gas increases from about 371 $\mathrm{m\,s^{-1}}$ at 30 bar to approximately 427 $\mathrm{m\,s^{-1}}$ to 443 $\mathrm{m\,s^{-1}}$ across 40 bar to 45 bar, with a sub-linear increase typical of choked expansion. Streamline analysis, proposed in Figure 4.4 (b), reveals a confined recirculation pocket beneath the melt delivery orifice that narrows laterally as pressure rises, which enhances momentum transfer to the emerging melt but also intensifies suction in the feed tube. Consistently, the static pressure in the feed line grows from roughly 1.35 bar at 30 bar inlet to 1.51 bar at 40 bar and 1.53 bar at 45 bar. Given the facility limit of 1.5 bar for aspiration pressure, the 40 bar setting is already marginal, whereas 45 bar is not feasible without adjustments to the die or to the operating strategy. Replacing Ar with N_2 lowers the jet-induced aspiration by $\sim 10\%$ under identical input conditions; thus, the 1.5 bar aspiration limit would be approached only around $\sim$44 bar (rather than $\sim$40 bar with Ar), making operation at slightly higher pressures feasible.

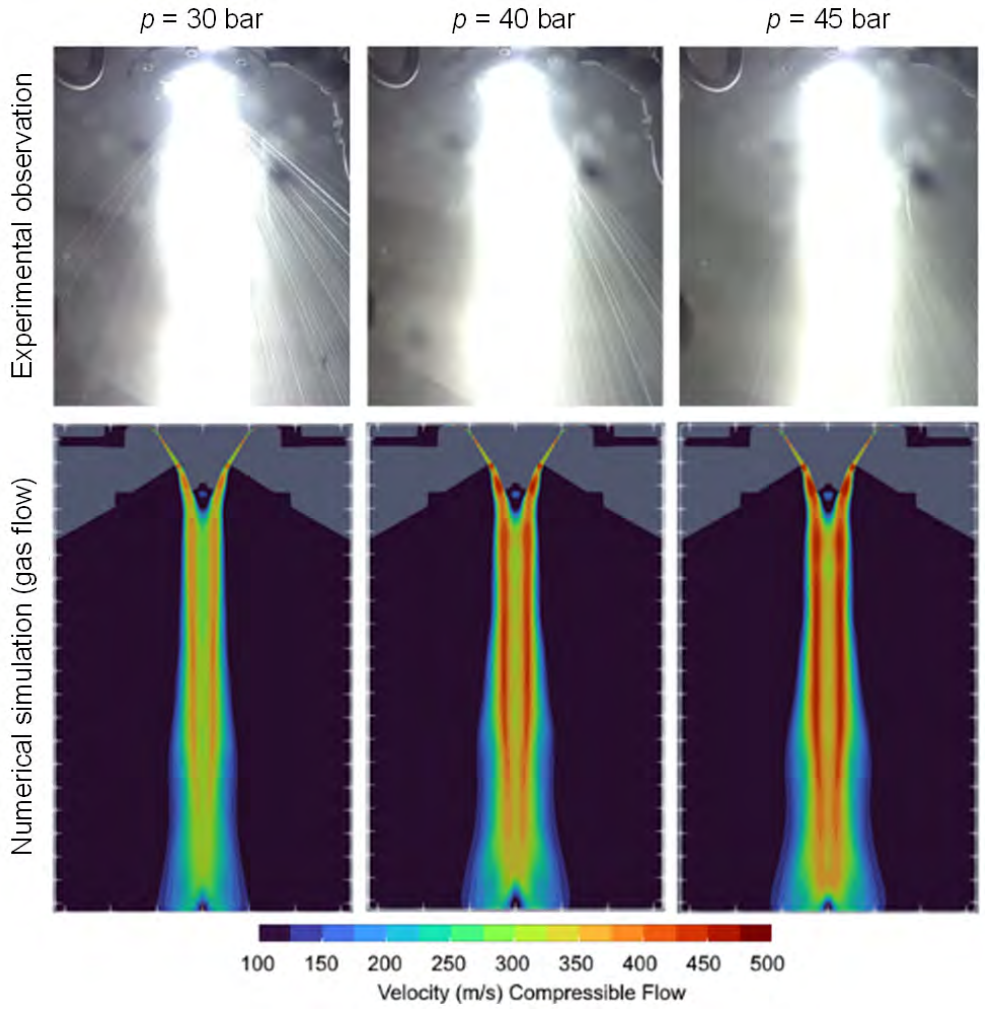

(a) Experimental observation (above) and CFD simulation (below) of the atomization plume as the gas pressure (p) is varied.

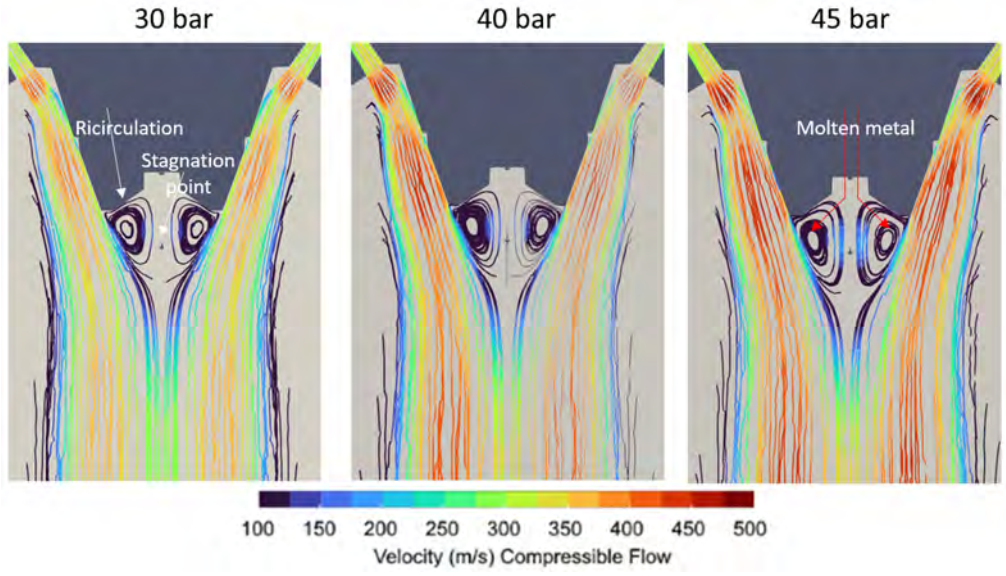

(b) Streamline gas velocity maps for argon at 30, 40, and 45 bar.

Fig. 4.4 Comparison between experimental observations and CFD simulations of the atomization jet under argon at 30, 40, and 45 bar atomizing pressure.

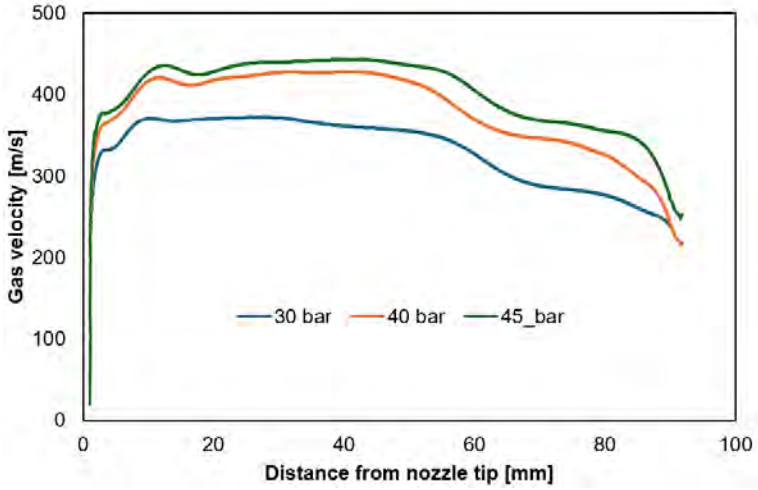

Fig. 4.5 Center-line gas velocity versus axial distance from the nozzle tip during argon "gas-only" runs at three inlet pressures (30, 40, 45 bar). The jet accelerates over the first millimetres, reaches a supersonic plateau that increases and extends with pressure (371 $\mathrm{m\,s^{-1}}$ at 30 bar to approximately 427 $\mathrm{m\,s^{-1}}$ to 443 $\mathrm{m\,s^{-1}}$ across 40 bar to 45 bar), and then decays downstream.

4.2.3.2 Experimental validation and Jet thermal behaviour

During the "gas-only" trials, the jet temperature was measured with a K-type thermocouple positioned 5 mm downstream of the nozzle exit, aligned with the flow axis. In parallel, chamber pressure sensors indicated a post-expansion pressure of approximately 1.04 bar, consistent with expansion through a de Laval nozzle. The gas flow rate was also recorded with an inline flow-meter (Platon GMTX), installed on the high-pressure gas line, to enable comparison with the CFD predictions; the results are reported in the graph of Figure 4.6, show close agreement between simulated and experimentally measured values across all investigated pressures.

The temperature–time plot in Figure 4.7 shows a rapid initial transient over the first few seconds, followed by a quasi-monotonic cooling toward a steady regime. As the supply pressure increases from 30 to 45 bar, the jet temperature progressively decreases, in line with the stronger expansion and higher gas velocity. After 6 min, representative values are about $-4\,^{\circ}\mathrm{C}$ (30 bar), $-10\,^{\circ}\mathrm{C}$ (40 bar), and approximately $-20\,^{\circ}\mathrm{C}$ (45 bar).

This behavior is physically expected: argon expansion in the atomization nozzle is essentially adiabatic, so raising the upstream pressure intensifies the downstream

temperature drop. From an operational standpoint, jet cooling has two main implications: (i) total gas consumption tends to increase as the jet temperature falls (higher density and mass flow are required), and (ii) the melt exit region can experience partial solidification, with the risk of blockage or, in less severe cases, periodic plume instabilities. These observations complement the velocity trends: higher pressures produce a faster, more collimated core, but at the cost of stronger jet cooling and a narrower practical operating window.

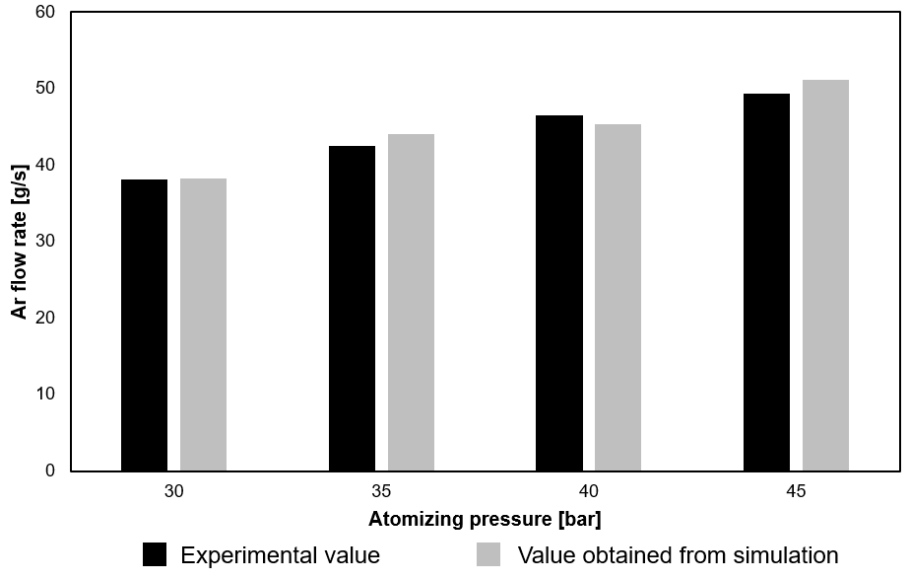

Fig. 4.6 Argon flow rate as a function of atomizing pressure: comparison between experimental measurements (black bars) and CFD simulation (gray bars) at 30, 40, and 45 bar.

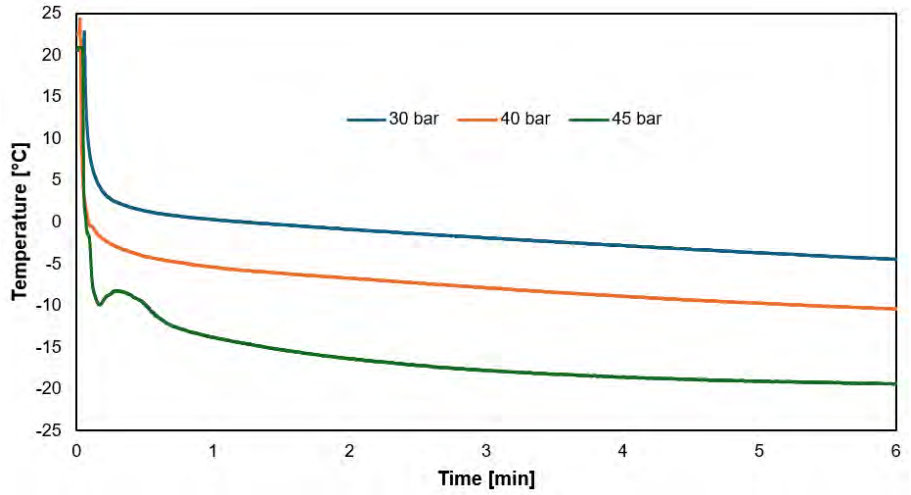

Fig. 4.7 Gas jet temperature vs. time measured with a K-type thermocouple positioned 5 mm downstream of the nozzle exit during argon "gas-only" runs at three inlet pressures (30, 40, 45 bar).

4.2.3.3 CFD-based definition of the Practical Operating Window

Even a single phase CFD simulation can provide a rigorous framework for defining the safe and effective operating envelope of the gas atomization process. In this work, CFD simulations were employed to delineate the practical operating limits of the process parameters. The simulation was useful to identified the maximum atomization pressure beyond which undesirable phenomena arise, including excessive cooling at the orifice and the development of nozzle back pressure sufficient to induce melt backflow into the atomization chamber.
Establishing these bounds improved equipment protection and operational safety by reducing the risk of malfunctions during startup and under transient conditions.
Moreover, also from an economic standpoint, CFD makes it possible to perform a virtual screening of parameter sets prior to any test on the atomizer, thus reducing the number of physical tests required, limiting the use of feedstock and utilities and lowering process gas consumption. The use of simulation enabled a design of experiments approach that directed laboratory efforts toward the most informative regions of the parameter space and thereby reducing development time and cost.
After calibration against targeted measurements, the combined use of simulation and focused experimentation enhanced process understanding, defined parameter limits with greater confidence, and accelerated the production of powders meeting

specification.
Further insights into the influence of process parameters, assessed through two phase Volume of Fluid (VOF) simulations on the PSI Hermiga 100/10 gas atomization system, can be found in the article [100].

4.2.3.4 Full-Scale atomization performance and Operating-pressure selection

Under the operating window reproduced in full-scale atomization trials, atomization at 30 to 40 bar yielded a continuous, stable plume. Raising the pressure to 45 bar introduced a periodic loss of coherence, with recurrent interruptions of the molten stream. These events are mirrored in the mass fraction of atomization debris: the fraction decreases as the pressure increases from 30 to 40 bar, but shows a slight rise at 45 bar, as shown in Figure 4.8 (a). Particle transport to the primary hopper is driven by the high-velocity flow of inert argon. As breakup becomes more efficient, the generation of fine particles increases; a larger portion is therefore separated by the cyclone upstream of the absolute filter and collected in the secondary hopper, while the share captured in the primary hopper correspondingly decreases with increasing atomization gas pressure (Figure 4.8 (b)). In these cases, we additionally observed that higher gas velocity correlates with longer atomization cycles, increasing from less than three minutes at 30 bar to more than five minutes at 45 bar. This trend is consistent with a concurrent rise in pressure at the melt delivery nozzle, as reported in [57]. Such a pressure buildup can plausibly explain the pronounced increase in argon consumption during atomization, despite only a modest rise in the measured gas flow rate, as shown in Table 4.1.

Table 4.1 Argon flow rate and argon consumption as a function of atomization pressure. Argon consumption is subdivided into the contribution associated with the atomization stage and that related to chamber backfilling.

Atomization gas pressure, p	**Argon flow rate**	**Argon consumption**		
		Atomization	**Backfilling**	**Total**
30 bar	2.29 kg/min	6.5 kg	1.0 kg	7.5 kg
35 bar	2.78 kg/min	13.9 kg	0.8 kg	14.7 kg
40 bar	2.79 kg/min	15.5 kg	0.9 kg	16.4 kg
45 bar	3.07 kg/min	17.0 kg	1.1 kg	18.1 kg

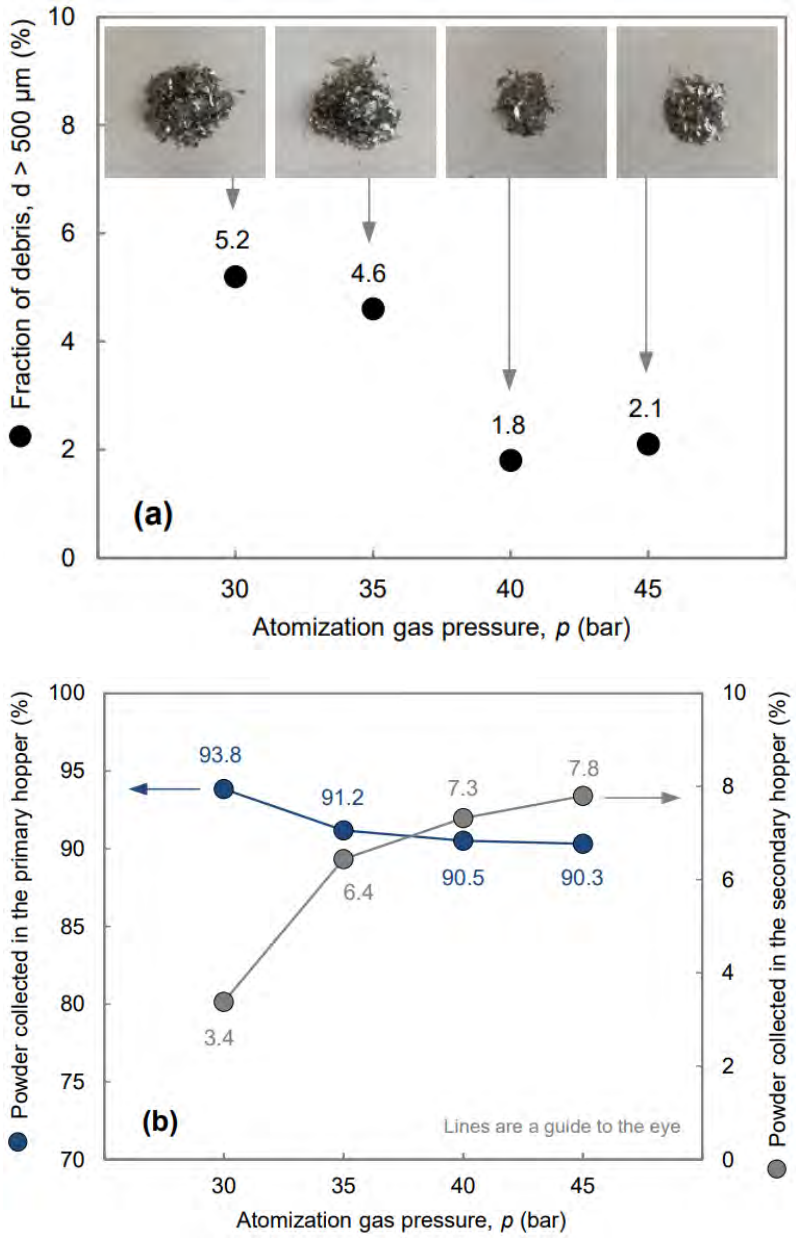

Fig. 4.8 Mass fraction of atomization debris (>500 µm) collected in the primary hopper as a function of argon atomizing pressure (a), and total powder mass collected in the primary and secondary hoppers (b). Plots as reported in [65].

The powder size distribution (PSD) shifts toward finer particles as the atomizing-gas pressure increases, as shown in Figure 4.9, as anticipated (2.5.1.2). The effect is most pronounced between 30 and 40 bar, where the median size (D50) decreases approximately linearly. Further raising the pressure to 45 bar does not yield an additional refinement: the 40 and 45 bar trials produce very similar PSDs, with a slight increase in D50 and D90 as reported in the table included in Figure 4.9.

Two mechanisms likely explain this departure from the expected monotonic trend. First, as discussed earlier, higher atomizing pressure should, in principle, reduce particle size; however, plume instabilities can introduce a pulsating regime that perturbs primary and secondary breakup, producing larger particles than expected [47]. Second, even when breakup dynamics are not substantially altered, system capacity limits can prevent significant size reductions with each incremental pressure increase [101]. In particular, higher gas velocities intensify internal recirculation within the upper region of the atomizing chamber, which is known to promote satellite formation; as the chamber flow rate rises, these recirculation zones can become more severe [102]. Consequently, increasing pressure from 40 to 45 bar consumes more gas without materially decreasing the final PSD. Considering also the yields for the PBF-LB/M-relevant size class (20–63 µm) obtained after sieving and reported in Table 4.2, 40 bar emerges as the most effective pressure for PSD reduction in this setup.

Table 4.2 Volume fraction by powder size at different atomization gas pressures.

Powder size	**Volume fraction [vol. %]**			
	30 bar	**35 bar**	**40 bar**	**45 bar**
$< 20\,\mu m$	4.2	6.4	8.1	8.3
20–63 µm	28.8	38.6	39.9	43.7
63–150 µm	49.0	41.0	42.0	38.2
$> 150\,\mu m$	18.0	14.0	10.0	9.8

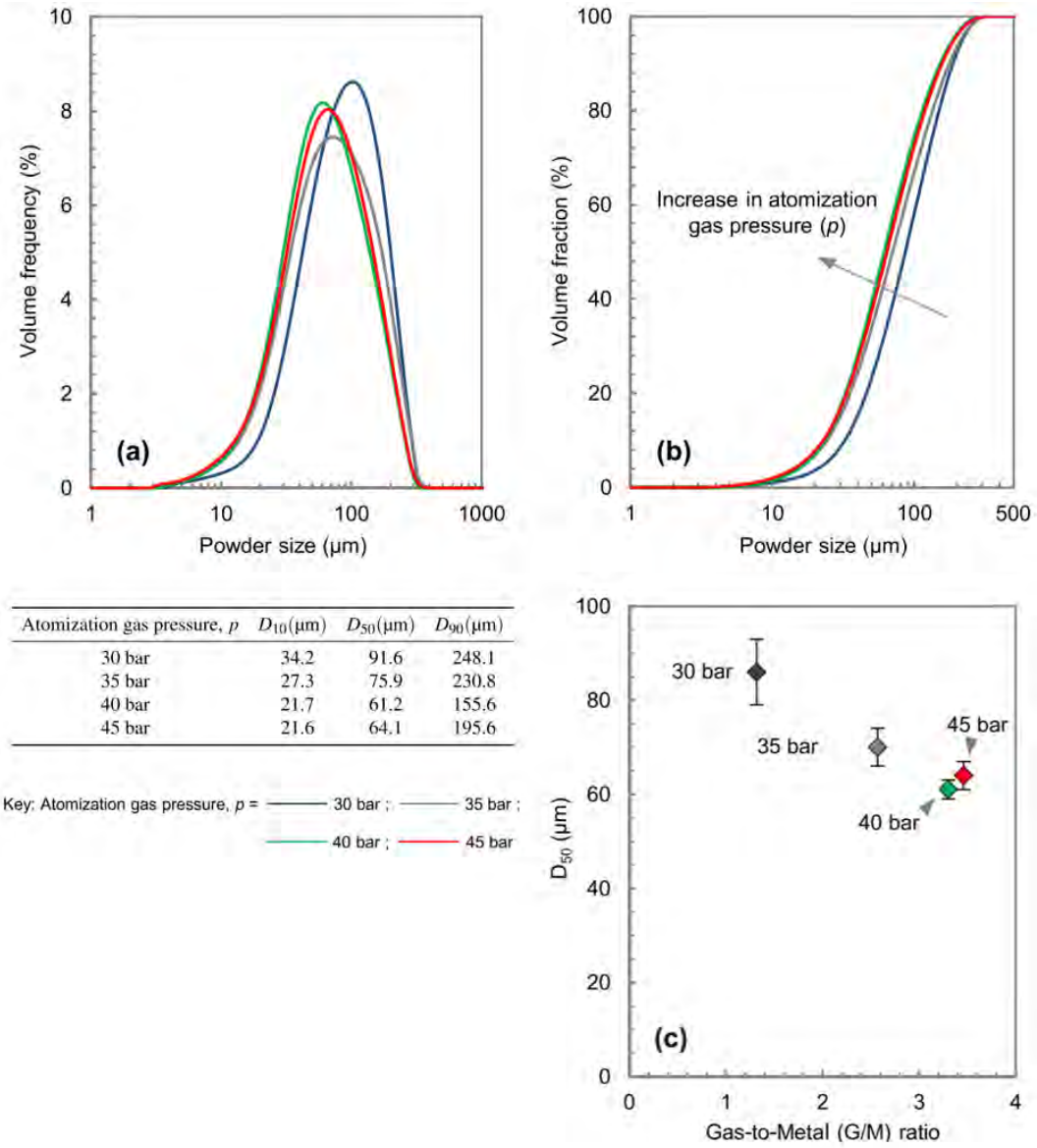

Atomization gas pressure, p	D_{10}(μm)	D_{50}(μm)	D_{90}(μm)
30 bar	34.2	91.6	248.1
35 bar	27.3	75.9	230.8
40 bar	21.7	61.2	155.6
45 bar	21.6	64.1	195.6

Fig. 4.9 After sieving the large atomized debris over 250 μm in size: Volume particle size distribution (a), cumulative particle size distribution (b), and correlation between median particle diameter (D50) and the gas-to-metal (G/M) ratio (c). The figure also includes a table summarizing the granulometric metrics (D10, D50, D90) obtained at various atomization gas pressures. Plots as reported in [65].

4.2.4 Carbon footprint evaluation of UNS S32760 powders from waste materials produced via gas atomization

4.2.4.1 Life-Cycle Assessment framework and Inventory data

Direct conversion of industrial waste into powder feedstock provides a technically robust alternative to conventional recycling routes, strengthening the closed-loop material cycles that support sustainable manufacturing and remaining consistent with the principles of industrial synergy [103, 104]. Due to the elevated cradle-to-gate footprint of superduplex stainless steel feedstock, exceeding that of austenitic and martensitic grades, there is a clear need to develop and adopt lower-impact powder manufacturing pathways. The results related to the carbon-footprint evaluation of UNS S32760 powders produced from waste materials via gas atomization, using argon as the atomizing gas, are briefly summarized below and reported in detail in [65]. Primary energy demand and CO_2-equivalent emissions were quantified for tests performed at argon atomization pressures of 20, 35, 40, and 45 bar. The carbon footprint per kilogram of powder was subsequently evaluated for the following particle-size fractions: $< 20\,\mu$m (MIM, BJ); 20–63 μm (PBF-LB/M); and 63–150 μm (EBM, DED). In this investigation, the atomization of recovered UNS S32760 industrial waste was modeled under system boundary "A" shown in Figure 4.10.

The life-cycle inventory accounted for energy and resource use associated with (i) preliminary waste preparation, (ii) inert-gas atomization, and (iii) post-atomization sieving. In the present case, waste preparation was limited to cleaning only: no cutting was required because the recovered parts already matched the crucible dimensions, allowing a full charge without prior fractionation. To evaluate the potential impact reduction of a direct waste-to-powder route, the resulting carbon footprint was benchmarked against an alternative scenario in which the same gas-atomization pathway is supplied with feedstock from primary and/or secondary production, This comparison corresponds to system boundary "B" in Figure 4.10. The analysis was based primarily on laboratory-acquired measurements, supplemented by secondary sources when primary measurements were unavailable. Parameter ranges were assigned, where necessary, to reflect input uncertainty. Electrical energy consumption was recorded using a Schneider PM3250 power analyzer, and argon consumption during atomization was quantified with a Platon GMTX flowmeter installed on the

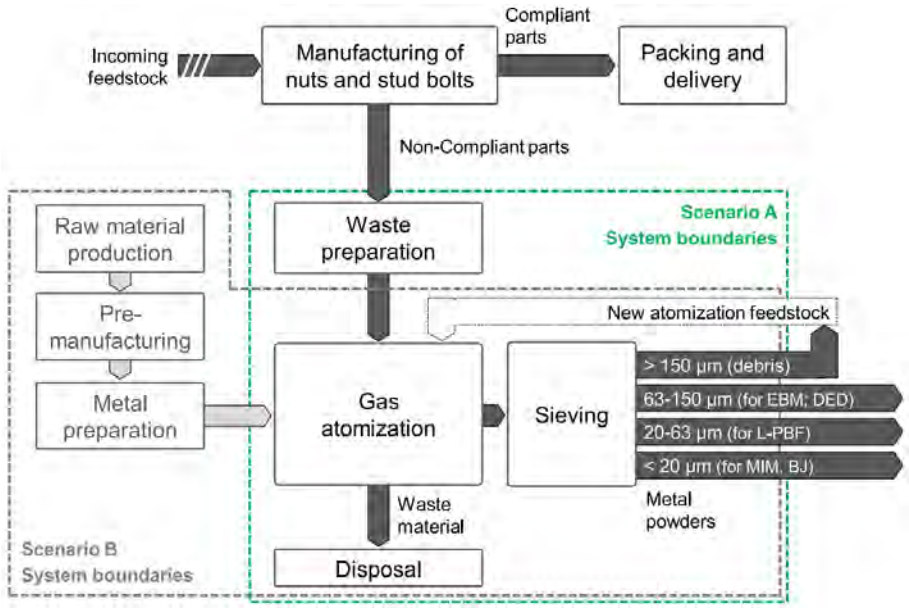

Fig. 4.10 System boundary definition for the environmental impact assessment; Scheme as reported in [65].

high-pressure gas line. For each test, the crucible was charged with 5.2 ± 0.3 kg of a mixture of non-compliant nuts and bolts made of UNS S32760 duplex stainless steel.

4.2.4.2 Carbon-Footprint results and Implications for process optimisation

Figures 4.11a and 4.11b report, respectively, the batch primary energy demand E_{Batch} and the CO_2 equivalent emissions $CO_{2,\text{Batch}}$ associated with processing a 5.2 ± 0.3 kg batch (cleaning, atomizing, and sieving). Figure 4.11c presents the specific CO_2 emissions per unit mass of powder for a given size class, obtained from the batch emissions in Figure 4.11b according to Equation 4.1 [65]:

$$\text{CO}_{2,\text{Batch}} = CE_{<20\,\mu\text{m}} \cdot m_{<20\,\mu\text{m}} + CE_{20\text{–}63\,\mu\text{m}} \cdot m_{20\text{–}63\,\mu\text{m}} + CE_{63\text{–}150\,\mu\text{m}} \cdot m_{63\text{–}150\,\mu\text{m}} \tag{4.1}$$

where

- $CO_{2,\text{Batch}}$ [kg CO_2] denotes the total CO_2 emitted per atomized-and-sieved batch (see Fig.4.11b);
- CE_i [kg CO_2 kg^{-1}] is the specific CO_2 emission per unit mass of powder in particle-size class i (see Fig.4.11c);

- m_i [kg] is the mass of powder in particle-size class i obtained from atomization and sieving of each batch.

Here, the index i takes one of the following size classes: $< 20\,\mu$m, 20 to 63 μm, or 63 to 150 μm.

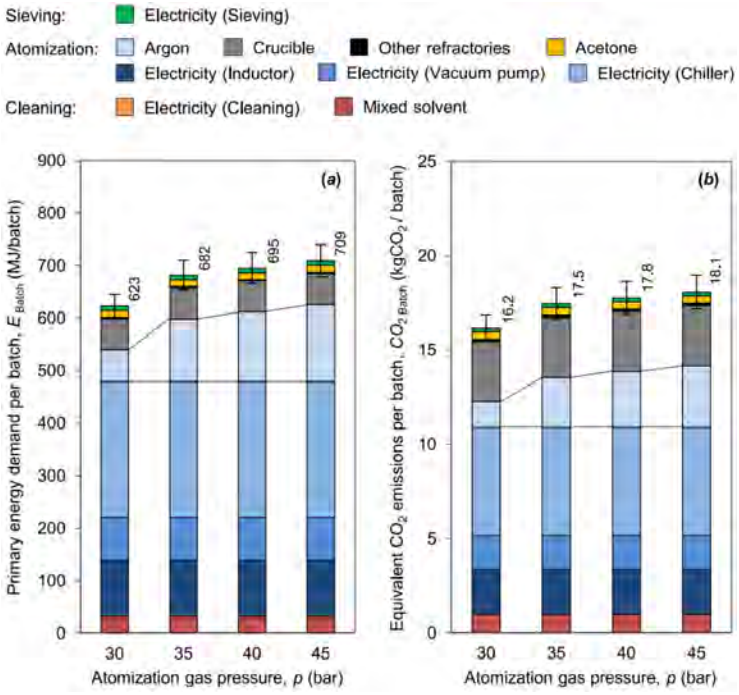

(a) Primary energy demand per batch. (b) Equivalent CO_2 emissions per batch.

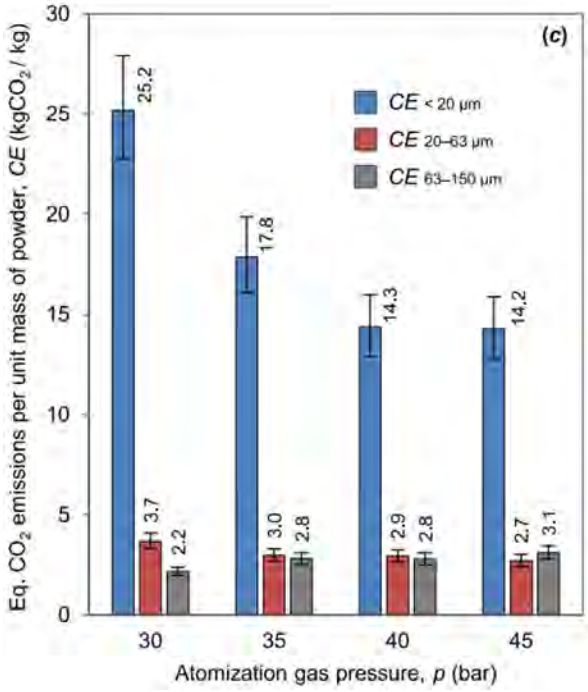

(c) Specific CO_2 emissions per unit mass of powder as a function of particle size class.

Fig. 4.11 Overview of the primary energy consumption and CO_2 equivalent emissions linked to processing a 5.2 ± 0.3 kg batch, and resulting specific carbon footprint for different powder size classes; graphs as reported in [65].

Compared with powders produced by atomizing primary and/or secondary feedstocks (Scenario 'B' in Fig. 4.10), direct waste-to-powder conversion (Scenario 'A'in Fig. 4.10) yields substantially lower CO_2 emissions. For UNS S32760 duplex stainless steel in the solution-annealed condition, the average carbon footprint is $5.4 \pm 5\%$ $kgCO_2/kg$ for primary production and $1.3 \pm 7\%$ $kgCO_2/kg$ for secondary production [105]. Assuming a recycled content of $0.37 \pm 5\%$ in the current supply [105] and adopting the recycled-content method of Hammond and Jones [106], the effective burden becomes $3.9 \pm 7\%$ $kgCO_2$ per kilogram of raw material. Under Scenario "B" (Fig. 4.10), this upstream material term is added to the process results in Fig. 4.11c when the same gas-atomization route is employed. Even neglecting pre-manufacturing and feedstock-conditioning contributions, this addition alone would more than double the carbon footprint for the coarser fractions (20–63 μm and 63–150 μm) and would increase the footprint of powders finer than 20 μm by approximately 15%–28%.

Drawing on convergent evidence from CFD simulations and full-scale atomization tests under the present equipment and operating conditions, a 40 bar atomizing-argon pressure was selected as the optimal setpoint. This choice balanced performance and sustainability by delivering favorable yields in the PBF-LB/M-relevant 20–63 µm fraction, meeting powder quality targets, and containing CO_2 emissions; it was therefore adopted for the subsequent campaign producing UNS S32760 powders with different process-gas combinations. Note, however, that this value is configuration-dependent: changes in atomizer geometry, gas/melt flow rates, or nozzle designs can shift the optimal pressure.

4.3 Properties of UNS S32760 powders as function of different processing gases

4.3.1 Introduction

The primary aim of this part of the research activity is to investigate how the melt-chamber atmosphere (Ar versus N_2) influences nitrogen uptake in super duplex stainless steel UNS S32760 powders produced from metal scrap by VIGA-CCGA manufacturing route. Additionally, the study aims to evaluate the effect of the atomization gas (Ar or N_2) on powder characteristics, including particle-size distribution, morphology, microstructure, chemical composition with specific attention to light elements (N, O, H, C, S), and powder rheology. The ultimate goal is to identify gas-process parameters that yield powders with the correct composition, particularly the target nitrogen content, since this strongly affects pitting resistance and governs the -ferrite/-austenite phase balance, which is critical for the mechanical performance of components produced by PBF-LB/M.

4.3.2 Materials and Methods

4.3.2.1 Atomization setup

In this study, four batches of UNS S32760 super duplex stainless steel forging scraps, each weighing 6.5 $\pm$ 0.1 kg, were prepared as feedstock for melting and gas atomization. The starting material, consisting of non-compliant UNS S32760 (X2CrNiMoCuWN25-7-4, *AISI* F55, Werkstoff No. 1.4501) stud bolts and nuts, was loaded into the crucible, as shown in Figure 4.12, and subsequently melted until a homogeneous molten bath was obtained.

Powder production was then carried out using a vacuum inert gas atomizer (VIGA see paragraph 2.1.1) in a close-coupled configuration (model PSI Hermiga 100/10 see paragraph 2.2), equipped with an annular slit convergent divergent nozzle (see paragraph 2.4), as schematically illustrated in Figure 4.13.
Melting was provided by an Ambrell EKOHEAT 20/25 induction power unit, with thermal management by a Hitema ENR 022 cooling unit. The principal atomization parameters adopted in this work are summarized in Table 4.3.

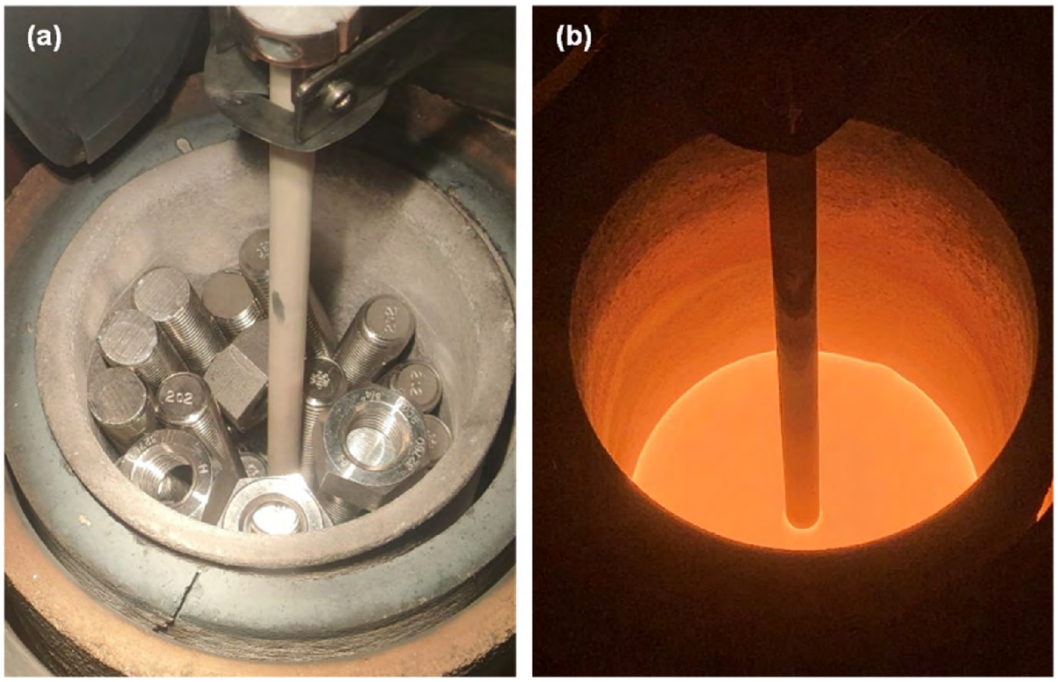

Fig. 4.12 (a) Crucible loading with non-compliant UNS S32760 stud bolts and nuts used as feedstock for gas atomization. (b) Melting and temperature homogenization phase prior to atomization.

After emptying the atomizer vessel atmosphere to 6×10^{-3} mbar, the charge was induction heated at a nominal ramp of 18 ± 4 °C min^{-1} in order to mitigate thermal shock to the alumina crucible. To maintain a stable heating rate as the temperature increase, the induction settings were progressively manually raised (power 3–12 kW, frequency 6–7 kHz, and voltage 110–200 V).

Upon reaching 1000°C, both the melting and atomizing chambers were backfilled to suppress volatilization from the molten pool. The process atmospheres were assigned according to the test matrix, yielding four configurations: Ar/Ar, N_2/ N_2, Ar/ N_2, and N_2/Ar, where the first term denotes the melt-chamber gas and the second the atomization gas. During the test the added gas in each chamber was pure and never mixed together. Also the gas feeder was not equipped with heating system for an accurate temperature control.

Following emptying and heating phases, the atomization chamber was returned to ambient pressure, while the melt chamber was maintained at a slight overpressure of 0.05 barg under a fluxing atmosphere.

A homogeneous molten pool was found to be 1440 ± 10 °C, after which an additional

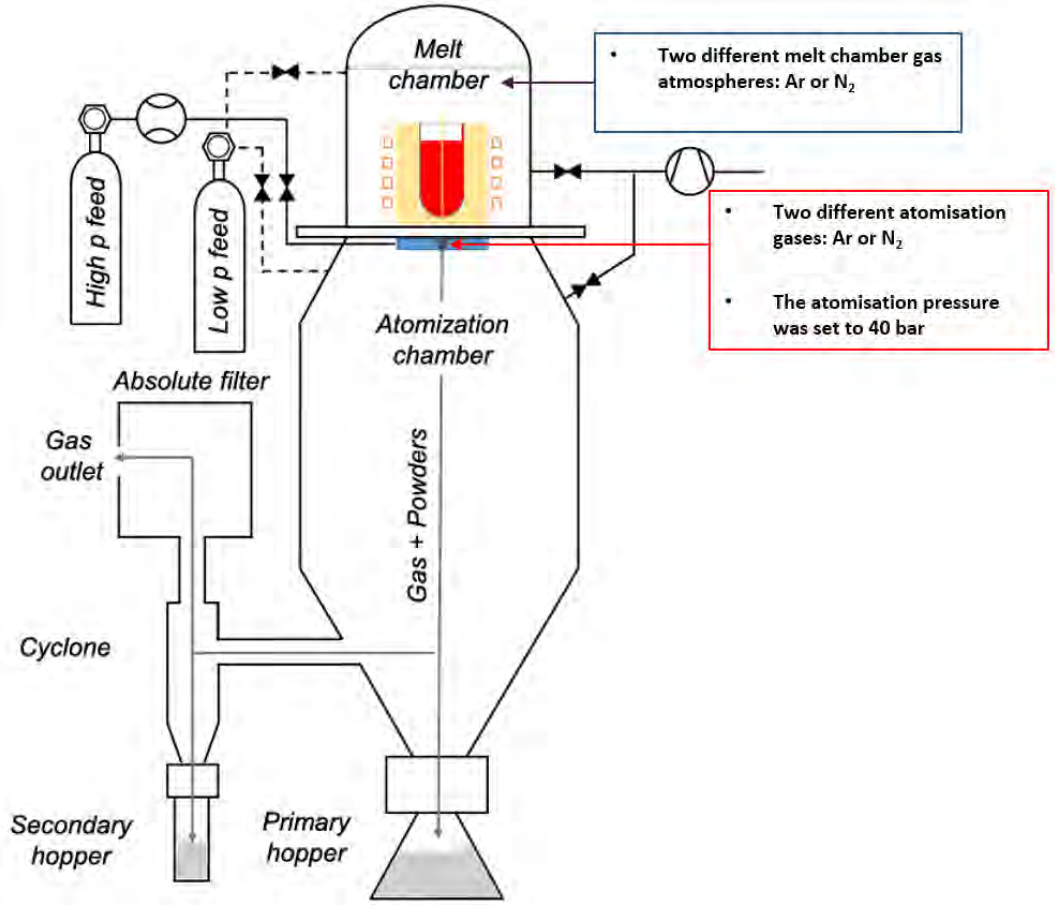

Fig. 4.13 Schematic diagram of the CC-VIGA unit (PSI Hermiga 100/10).

200 °C overheat was applied. Immediately before initiating atomization, the melt-chamber pressure was increased to 0.25 barg to promote metal transfer into the atomization chamber through an 88 mm feed tube connected to a 2.4 mm-diameter delivery nozzle. The atomization-chamber pressure was held constant for all trials, and a tower pressure of 0.04 – 0.05 barg was recorded throughout each run.

During atomization phase, the oxygen content in the atomization chamber was monitored in situ on continuous basis and verified to remain below 5 ppm trought a Cambridge Sensotec Rapidox 1100 Zr analyzer.

Independently from the atomisation gas used, Ar or N_2, the atomisation pressure was set to 40 bar as per the results presented previously in Section 4.2.

The bulk of the atomized powder was recovered in the primary hopper, yielding 6.1 – 6.4 kg per run (approx 98% yield). A smaller fraction was stripped from the argon or nitrogen exhaust stream by a cyclone and collected in a secondary hopper

Table 4.3 Main process parameters for the atomization of UNS S32760 SDSS.

Parameter	**Atomization gas**	**Value**
Loaded material	–	6.5 ± 0.1 kg
Liquidus temperature	–	1440 ± 10 °C
Overheating	–	200 °C
Melting chamber atmosphere	–	Ar or N_2
Melting chamber pressure	–	0.25 barg
Oxygen level in the atomisation chamber	–	< 5 ppm
Atomization gas	–	Ar or N_2
Atomization gas pressure, p	–	40 bar
Average atomization gas mass flow	Ar	2.79 kg/min
Average metal mass flow	Ar	0.84 kg/min
Gas-to-metal ratio, GMR	Ar	3.32
Average atomization gas mass flow	N_2	2.62 kg/min
Average metal mass flow	N_2	0.86 kg/min
Gas-to-metal ratio, GMR	N_2	3.05

(see scheme of Figure 4.13), amounting to 0.15 – 0.30 kg. The atomization yield was computed as the ratio of the total powder mass collected from both hoppers to the initial charge loaded into the alumina crucible. Powders from each run were then thoroughly blended to ensure homogeneity and minimize segregation, and subsequently sieved with a 250 μm mesh to remove debris generated during atomization.

4.3.2.2 Feedstock chemical composition evalutation

The chemical composition of the wrought feedstock was characterized by optical emission spectroscopy (GNR Metal Lab Plus), with carbon and sulfur level quantified by combustion with non-dispersive infrared detection (LECO CS 744), oxygen, nitrogen and hydrogen content was measured by inert-gas fusion with infrared detection (LECO ONH 836) according to ASTM E1019 standard [107]. Sampling was performed for each batch of feedstock used.

4.3.2.3 Particle size distribution

The powder size distributions (PSD) were determined by laser technique (Mastersizer 3000 instrument by Malvern) on dried samples. Measurements were conducted with a 15% sample feed and a 3.0 bar carrier-gas pressure, adopting an optical model that assumes spherical particles and uses the stainless-steel coefficient of reflectivity provided in the Malvern database. For each atomization run, the PSD was evaluated over the full powder lot, using multiple sub-samplings (at least five per batch) after removal of coarse atomization debris by sieving at 250 μm.

4.3.2.4 Rheological and Flowability test

Powder rheometry tests provide quantitative information on the behaviour of powders when subjected to shear stresses. These data are generally used to compare different powders or powders with different particle size distributions. The rheometer used for the measurements was a Freeman Technology FT4. After instrument calibration and warm-up, three tests were performed for each sample on virgin powders previously dried in a vacuum oven at 60 °C for 2 h, in order to minimise the influence of moisture and reduce possible segregation effects during subsequent tests. The testing programme used was Stability & Variable Flow Rate, which provides information on the stability of powder behaviour during flow, Stability, and on the response of the powder to variations in blade rotational speed, Variable Flow Rate. In this programme, the two measurements are performed sequentially on the same powder sample.

The flowability analyses were carried out using standard Hall and Carney funnels. The adopted procedures are described in detail in ASTM B213 [108] for the Hall funnel and ASTM B964 [109] for the Carney funnel.

4.3.2.5 Powder morphology and True density

Powder morphology was characterized using two complementary approaches. Qualitative features were examined by a scanning electron microscopy (Zeiss EVO 15) equipped with secondary-electron (SE) and backscattered-electron (BSE) detectors, while quantitative descriptors were obtained by automated optical image analyser (Malvern Morphologi 4). All analyses were performed on powder fractions

with particle sizes lower than 150/250 µm.
The true (skeletal) density was measured by helium pycnometry (Anton Paar Ultrapyc 3000) on the powder fraction sieved to < 250 µm.

4.3.2.6 Powder Light Elements determination

Following atomization, three sets of samples were collected from each of the four gas-process configurations (Ar/Ar, N/N, Ar/N, N/Ar) for quantification of the interstitial and light elements (O, N, H, C, S). To account for surface-area effects associated with particle size, the bulk PSD was further fractionated into three classes by additional sieving: < 20 µm, 53–63 µm, and 106–125 µm. Carbon and sulfur were measured by non-dispersive infrared (NDIR) detection following powder combustion using a LECO CS 744 analyzer, whereas oxygen, nitrogen, and hydrogen were measured by NDIR after inert-gas fusion with helium as the carrier using a LECO ONH 836 analyzer. The procedures for C, S, O, and N was according to ASTM E1019 standard [107]; hydrogen determination, while not standardized, follows a widely adopted practice in steelmaking and research. For each size class and production route, five replicates were analyzed to determine the mean composition, each test was performed on samples of approximately 1.00 ± 0.01 g.

4.3.2.7 Elemental composition of the powders

The elemental composition of the powders was determined by energy-dispersive X-ray spectroscopy (EDS; Oxford Ultim Max) on polished cross-sections of resin-mounted specimens. Metallographic preparation employed a sequence of diamond suspensions of 6, 3, and 1 µm followed by a colloidal-silica finish compound. Quantification was carried out by AZtecLive software, constraining the concentrations of light elements to the mean values obtained with the analytical procedures described previously 4.3.2.6.

4.3.2.8 Quantification of Austenite/Ferrite Phase Fractions

Phase fractions of austenite and ferrite were quantified by X-ray diffraction (XRD) on powders and on the wrought material. Measurements were performed with a Pulstec μ-X360s diffractometer designed for residual-stress/retained-austenite analysis, equipped with a two-dimensional detector and a Cr anode operated at 30 kV and 1.5 mA. The scan range was restricted to $2\theta = 120$–175°, which contains diffraction peaks from both austenite and ferrite.

4.3.3 Characterization of UNS S32760 steel powder

In Table 4.4, the average chemical composition of the starting feedstock, measured by OES prior to charging the SDSS into the crucible, is reported to assess compliance with the chemical requirements specified by BS EN 10088-2:2014 for grade UNS S32760. In addition, the mean contents of N, O, C, and S, determined by LECO analysis, are also presented. The obtained results indicate that the chemical composition of the starting material is fully consistent with the specification limits prescribed for UNS S32760. In particular, the major alloying elements determined by OES fall within the required compositional ranges, while the contents of the light elements are likewise in agreement with the corresponding standard limits. Overall, these findings confirm that the selected feedstock is chemically suitable for the subsequent atomization stage and fully representative of the nominal composition expected for a UNS S32760 super duplex stainless steel.

4.3.3.1 Chemical composition of the powders determined by EDS analysis

The chemical composition of the UNS S32760 powder particles was investigated by EDS analysis on polished cross sections, in order to evaluate the average concentration of the main alloying elements. The results are reported in Table 4.5.

Table 4.4 Average chemical composition of the starting feedstock, measured prior to charging into the crucible, and comparison with the chemical requirements specified by BS EN 10088-2:2014 for grade UNS S32760. The feedstock composition measured by optical emission spectroscopy is reported together with the contents of selected light elements measured separately by LECO ONH836 and LECO CS744. All values are reported in wt.%.

BS EN 10088-2:2014 requirements for UNS S32760					
Element	**Requirement**	**Element**	**Requirement**	**Element**	**Requirement**
C	≤ 0.030	Si	≤ 1	Mn	≤ 1
Cr	24.0 to 26.0	Mo	3.0 to 4.0	Ni	6.0 to 8.0
Cu	0.50 to 1.0	Co	–	Nb	–
Ti	–	V	–	W	0.50 to 1.0
N	0.20 to 0.30	P	≤ 0.035	S	≤ 0.015
Fe	Bal.				

UNS S32760 feedstock measured by optical emission spectroscopy (GNR Metal Lab Plus)					
Element	**Content**	**Element**	**Content**	**Element**	**Content**
C	0.015 ± 0.001	Si	0.406 ± 0.001	Mn	0.628 ± 0.003
Cr	25.8 ± 0.03	Mo	3.6 ± 0.01	Ni	7.15 ± 0.03
Cu	0.65 ± 0.01	Co	0.065 ± 0.001	Nb	0.02 ± 0.001
Ti	< 0.001	V	0.06 ± 0.008	W	0.65 ± 0.025
N	0.20 ± 0.007	Fe	Bal.	P	< 0.02
S	< 0.004				

Light elements measured by LECO ONH836 and LECO CS744				
	O	**N**	**C**	**S**
Content	0.0074 ± 0.0027	0.268 ± 0.004	0.0267 ± 0.0067	0.001034 ± 0.000076

Table 4.5 Average chemical composition measured by EDS on cross sections of UNS S32760 powder particles. All values are reported in wt.%. The concentrations were determined by EDS analysis on polished powder cross sections. Values are reported as mean $\pm$ standard deviation.

Sample	**Si**	**Cr**	**Mn**	**Fe**	**Ni**	**Cu**	**Mo**	**W**
UNS S32760 powder cross section	0.43 ± 0.06	26.67 ± 0.06	0.69 ± 0.05	60.63 ± 0.59	6.55 ± 0.60	0.90 ± 0.07	3.28 ± 0.14	0.84 ± 0.08

4.3.3.2 Particle size distribution and Morphology

The particle size distribution results reported in Table 4.6 show that the different combinations of shielding gas and atomization gas do not produce significant variations in the granulometric characteristics of the as-atomized powders. The PSD curves are substantially overlapping, and the corresponding D10, D50 and D90 values remain within a narrow range for all the investigated conditions. In particular, D50 values close to 65 μm and D10 values around 25 μm confirm that the selected atomization conditions are suitable for the production of powders for PBF-LB/M applications. This result is consistent with the selection of an atomization pressure of 40 bar, previously identified as the optimal setpoint for the present equipment and operating conditions (Section 4.2). It should also be noted that particle size distribution is strongly dependent not only on atomization pressure, but also on atomizer geometry, nozzle design, and gas and melt flow conditions. Since all these parameters were kept constant throughout the experimental campaign, the absence of appreciable differences in PSD indicates that, under the present conditions, the process gas combination has only a limited effect on powder size distribution.

Consistently, the the quantitative morphological descriptors reported in Table 4.7 and in the graphs of Figure 4.14, together with the SEM observations shown in Figure 4.15, indicate that the different process-gas combinations do not significantly affect powder morphology.

Morphological analyses were also performed on powder batches in which the shielding gas, was varied. Although this parameter is not expected to directly affect particle morphology, its inclusion strengthened the statistical robustness of the assessment of process-gas effects.

Overall, the results confirm that powder morphology is primarily governed by the atomization gas, whereas the shielding gas in the melt chamber has no appreciable direct influence. In all cases, the powders exhibit a predominantly spherical shape, high values of circularity, convexity and aspect ratio, and a limited presence of satellites. Overall, these results indicate that, once the atomization pressure and the main geometrical and fluid-dynamic parameters are fixed, the variation of shielding gas and atomization gas within the investigated combinations does not significantly modify either the PSD or the morphological quality of the produced UNS S32760 powders.

Table 4.6 Particle size distribution curves and characteristic particle size distribution parameters of powders produced using different combinations of shielding gas and atomization gas, corresponding to the powder batches shown in Figure 4.15. The plot reports the volume-based and cumulative particle size distributions, while the table summarizes the corresponding D10, D50, and D90 values, expressed in μm.

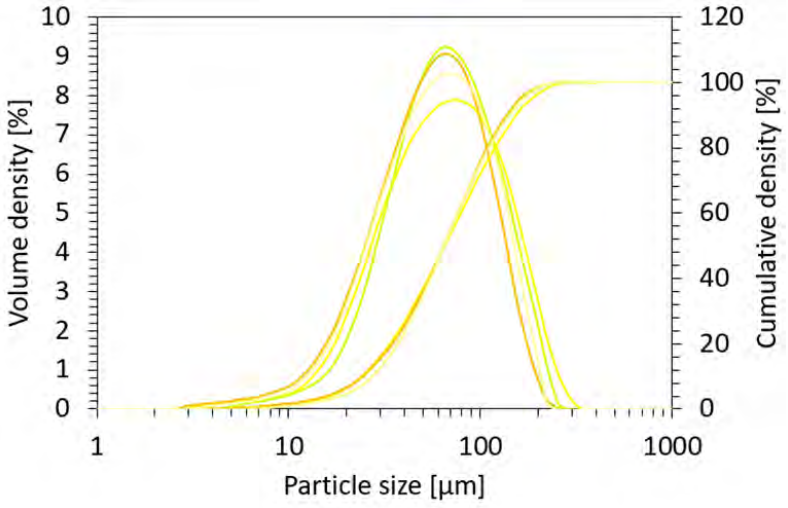

Image	Process gases		Particle size distribution parameters		
	Shielding gas	Atomization gas	D10 [μm]	D50 [μm]	D90 [μm]
a)	Ar	Ar	26.0	67.8	148.3
b)	Ar	N_2	24.4	64.5	137.3
c)	N_2	N_2	27.2	64.7	141.0
d)	N_2	Ar	24.1	65.2	154.4

Table 4.7 Morphological descriptors of powders produced using different combinations of shielding gas and atomization gas, corresponding to the SEM images reported in Figure 4.15. Morphological data were obtained by automated optical image analyser (Malvern Morphologi 4). All analyses were performed on powder fractions with particle sizes lower than 250 μm.

Image	Process gases		Morphological descriptors		
	Shielding gas	Atomization gas	Circularity	Convexity	Aspect ratio
a)	Ar	Ar	0.984 ± 0.027	0.996 ± 0.012	0.949 ± 0.084
b)	Ar	N_2	0.985 ± 0.022	0.997 ± 0.008	0.944 ± 0.079
c)	N_2	N_2	0.987 ± 0.018	0.996 ± 0.005	0.941 ± 0.077
d)	N_2	Ar	0.983 ± 0.028	0.995 ± 0.010	0.948 ± 0.088

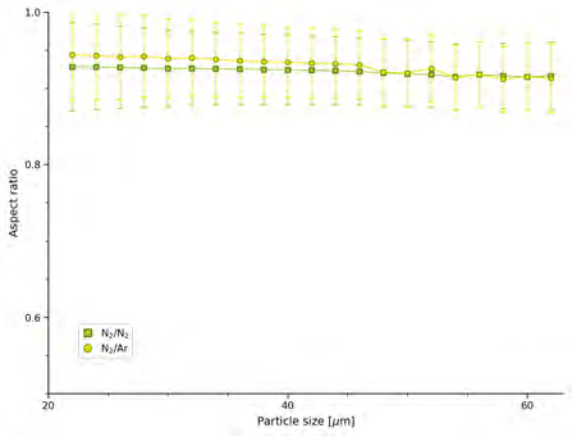

(a) Aspect ratio.

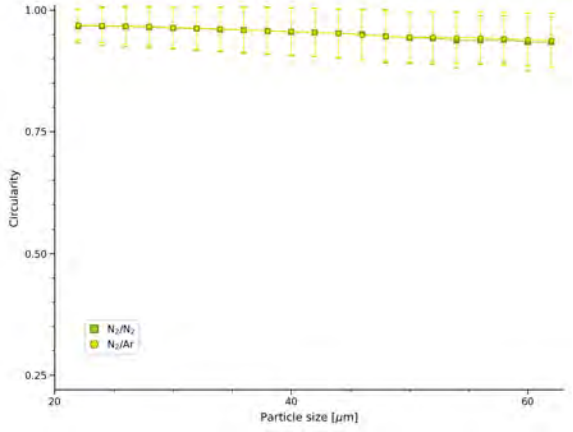

(b) Circularity.

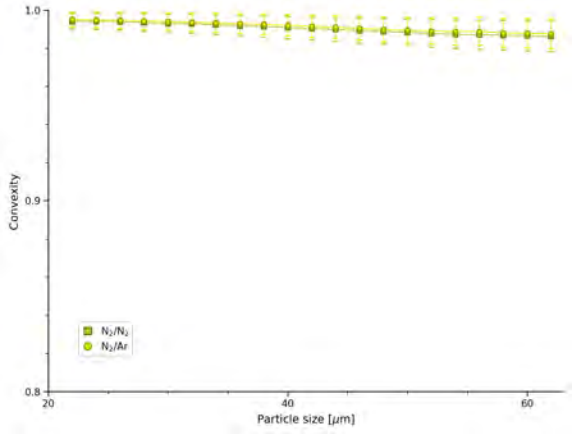

(c) Convexity.

Fig. 4.14 Morphological descriptors obtained by 2D image analysis for the high-nitrogen powders produced under N_2/N_2 and N_2/Ar processing conditions, considering the particle size range of interest for PBF-LB/M (20–63 μm): a) Aspect ratio, b) Circularity, and c) Convexity. The reported data are average values calculated from a large number of particles for each size class. Each experimental point is representative of a granulometric class defined as particle diameter $\pm$ 1 μm, where the particle size was defined on the basis of the CE diameter. Error bars represent the corresponding standard deviation.

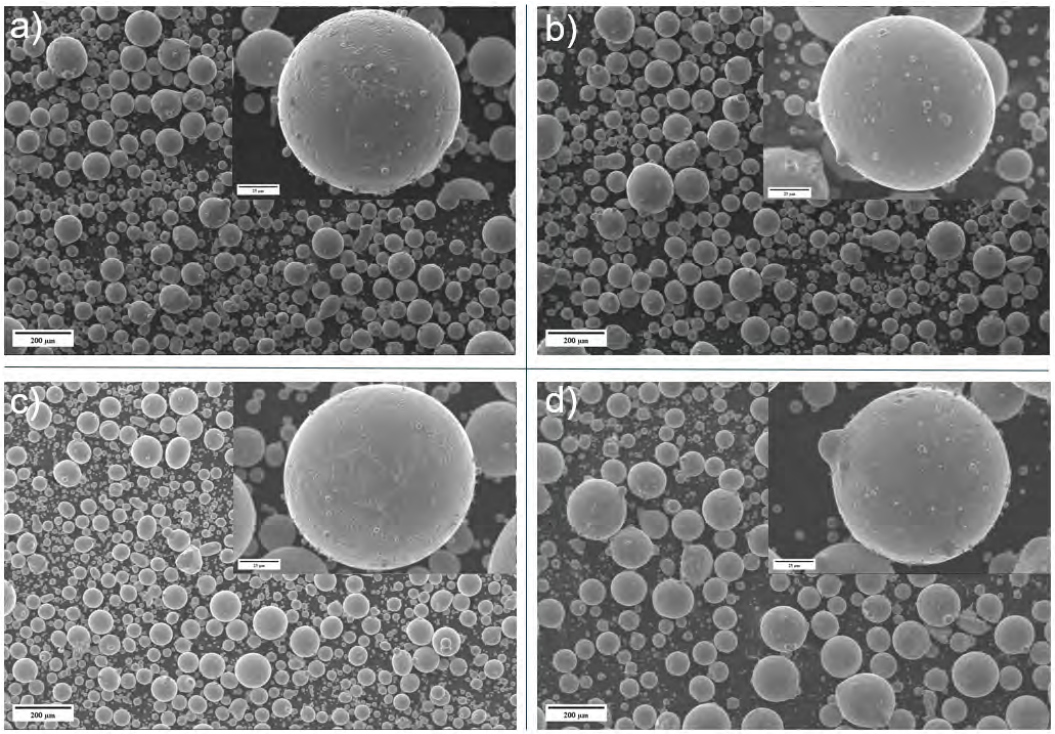

Fig. 4.15 SEM micrographs of powders produced using different combinations of shielding gas and atomization gas: (a) Ar/Ar, (b) Ar/N_2, (c) N_2/N_2, and (d) N_2/Ar. The insert in each micrograph reports a higher-magnification image of a representative particle.

4.3.3.3 Particle size distribution of the powder blend used for PBF-LB/M parameter optimization and Rheological tests

The powder rheometry and funnel flow tests were carried out on the 20–63 μm sieved UNS S32760 powder, whose particle size distribution is reported in Table 4.8, and on commercial SS316L powder. Before testing, both powders were dried and analysed under the same humidity conditions, in order to ensure a consistent comparison of their flowability behaviour.

Table 4.8 Particle size distribution of the powder blend employed for the optimization of the PBF-LB/M process parameters on the Aconity Mini 3D system. The powder consisted of a mixture of the high-nitrogen powders produced under N_2/N_2 and N_2/Ar atomization conditions. The graph reports the frequency and cumulative volume distributions, while the table summarizes the corresponding particle size distribution parameters (D10, D50, and D90) together with the cumulative volume fractions within selected particle-size intervals.

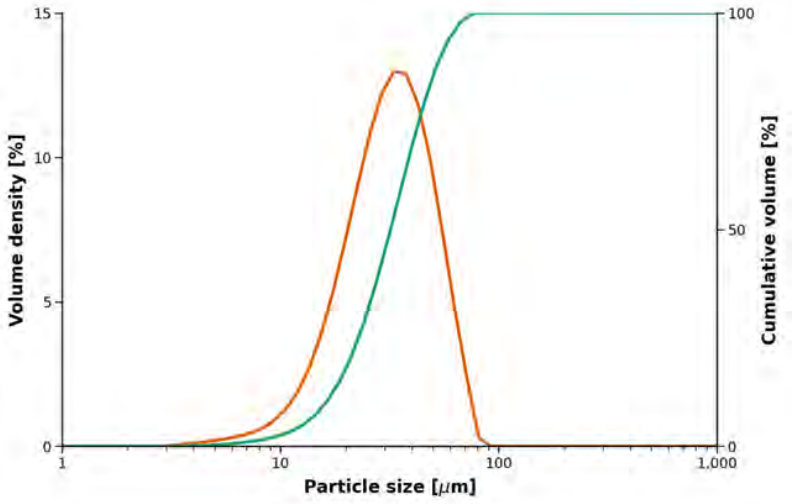

Particle size distribution parameters			Selected size ranges	
D10 [μm]	**D50 [μm]**	**D90 [μm]**	**Range [μm]**	**Volume fraction [%]**
16.1	31.9	54.3	0–20	18.21
			20–63	77.80
			20–75	81.49

Rheological tests were performed on the high-nitrogen powder blend, characterized by the particle size distribution reported in Table 4.8, which was subsequently used for the optimization of the PBF-LB/M process parameters.

The rheological indices used to interpret the data obtained from the Stability and Variable Flow Rate tests were the Stability Index (SI) 4.2, the Flow Rate Index (FRI) 4.3 and the Basic Flowability Energy (BFE) 4.4. These parameters are defined as follows:

$$SI = \frac{\text{Energy Test 7}}{\text{Energy Test 1}} \tag{4.2}$$

$$FRI = \frac{\text{Energy Test 11}}{\text{Energy Test 8}} \tag{4.3}$$

$$BFE = \text{Energy Test 7} \tag{4.4}$$

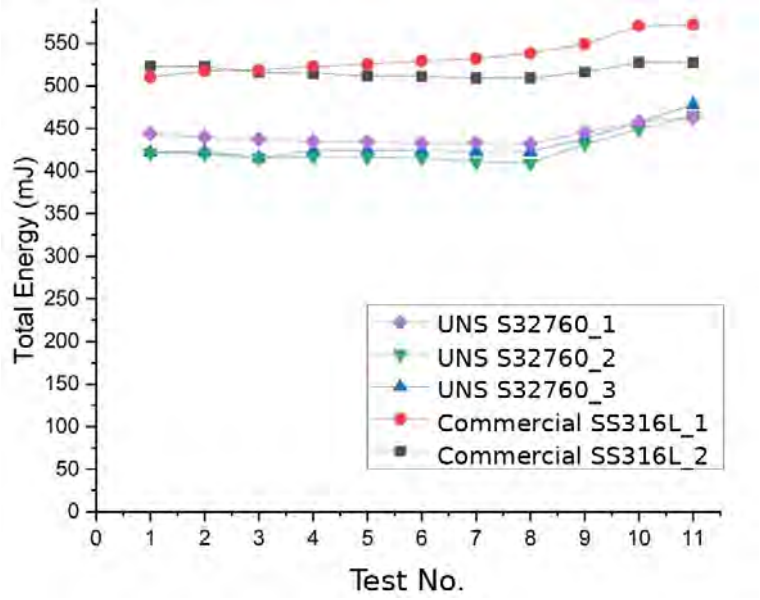

Fig. 4.16 Total energy measured during repeated powder rheometry tests on UNS S32760 powder and commercial SS316L powder. The UNS S32760 powder shows lower total energy values than the commercial SS316L reference powder, indicating a more favourable flow response under the investigated testing conditions.

The Stability Index values obtained for the UNS S32760 powders were all within the range of 0.9–1.1, indicating that the powder can be considered rheologically

stable and not significantly affected by flow-induced variations in behaviour. This can be observed in Figure 4.16 from tests 1–7.

The Flow Rate Index values were slightly higher than 1 in all cases, suggesting a mildly flow-rate-dependent behaviour, as shown in Table 4.9 from tests 8–11. A direct comparison with a commercial SS316L powder revealed a very similar trend, with a difference of approximately 100 mJ between the BFE values of the commercial powder and those measured for the UNS S32760 powder.

Table 4.9 Flowability parameters of UNS S32760 powder compared with commercial SS316L powder. The table reports the Stability Index, Flow Rate Index and Basic Flowability Energy for each test.

Test	**Stability Index**	**Flow Rate Index**	**Basic Flowability Energy [mJ]**
UNS S32760_1	0.97	1.07	434
UNS S32760_2	0.97	1.13	416
UNS S32760_3	1.00	1.13	423
Commercial SS316L_1	1.04	1.06	522
Commercial SS316L_2	0.97	1.03	514

The flow-rate values obtained using the Hall and Carney funnels are reported in Table 4.10. The UNS S32760 powders did not flow during the Hall funnel test, indicating limited flowability under these testing conditions. Conversely, a flow rate of 12.8 s/150 g was measured when the Carney funnel was used.

Table 4.10 Hall and Carney flow rate values measured for UNS S32760 powder and commercial SS316L powder.

Sample	**FR_H [s/50g]**	**FR_C [s/150g]**
UNS S32760	–	12.8
Commercial SS316L	13.28	–

In comparison, the commercial SS316L powder exhibited better flowability, since flow was achieved during the Hall funnel test, with a measured flow rate of 13.28 s/50 g. This difference can be mainly attributed to the relatively high fraction of fine particles in the UNS S32760 powder, equal to approximately 18 vol.%, which promotes stronger cohesive interactions, primarily associated with van der Waals forces.

4.3.3.4 True density of powders as a function of different processing gases

The true density results reported in Figure 4.17 show a clear effect of the atomization gas on the internal integrity of the produced powders. In particular, the highest true density values were measured for the powders atomized with nitrogen, namely in the Ar/N_2 and N_2/N_2 conditions, whereas the lowest value was obtained for the Ar/Ar condition. The N_2/Ar powder batch exhibited an intermediate true density. This trend indicates that the nature of the atomization gas plays a more relevant role than the shielding gas in determining the final compactness of the particles.

This interpretation is consistent with the cross-sectional SEM observations reported in Figure 4.18. In the N_2/Ar powders, internal pores are clearly visible, as shown in the higher-magnification micrograph in Figure 4.18 b), with an estimated average diameter of approximately 183.7 ± 33.8 nm. By contrast, no evident internal porosity was observed in the N_2/N_2 powders, as shown in Figure 4.18 c). This behavior can be reasonably attributed to the insolubility of Ar in liquid and solid steel: when argon is used as atomization gas, gas entrapment within the droplets is promoted, leading to the formation of intraparticle porosity that is retained after solidification. As a consequence, the presence of pre-existing intraparticle porosity in the feedstock may contribute to an increased porosity level in PBF-LB/M components produced from the same powder. Conversely, the use of nitrogen as atomization gas suppresses this effect, resulting in denser particles and, consequently, in higher measured true density values [110].

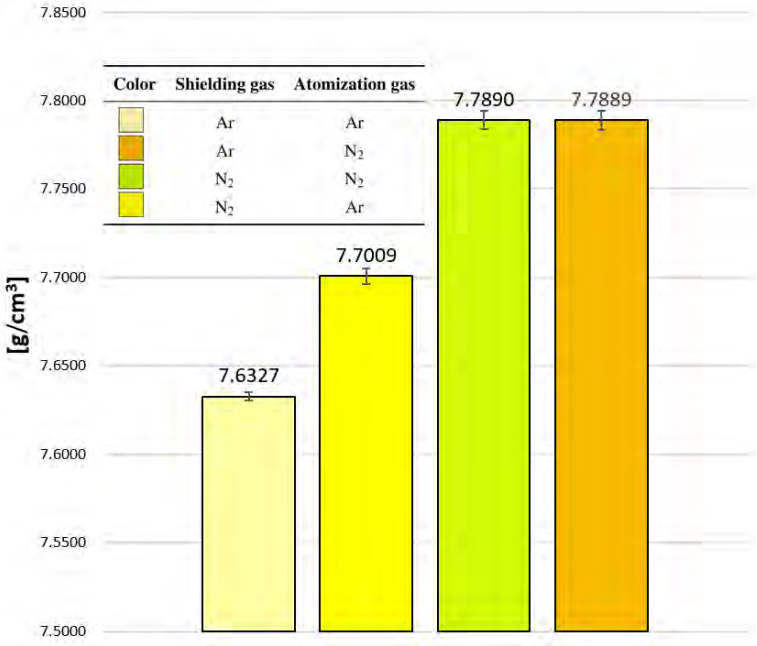

Fig. 4.17 Density-related results of powders produced using different combinations of shielding gas and atomization gas. The plot shows the measured true density values, expressed in g/cm^3.

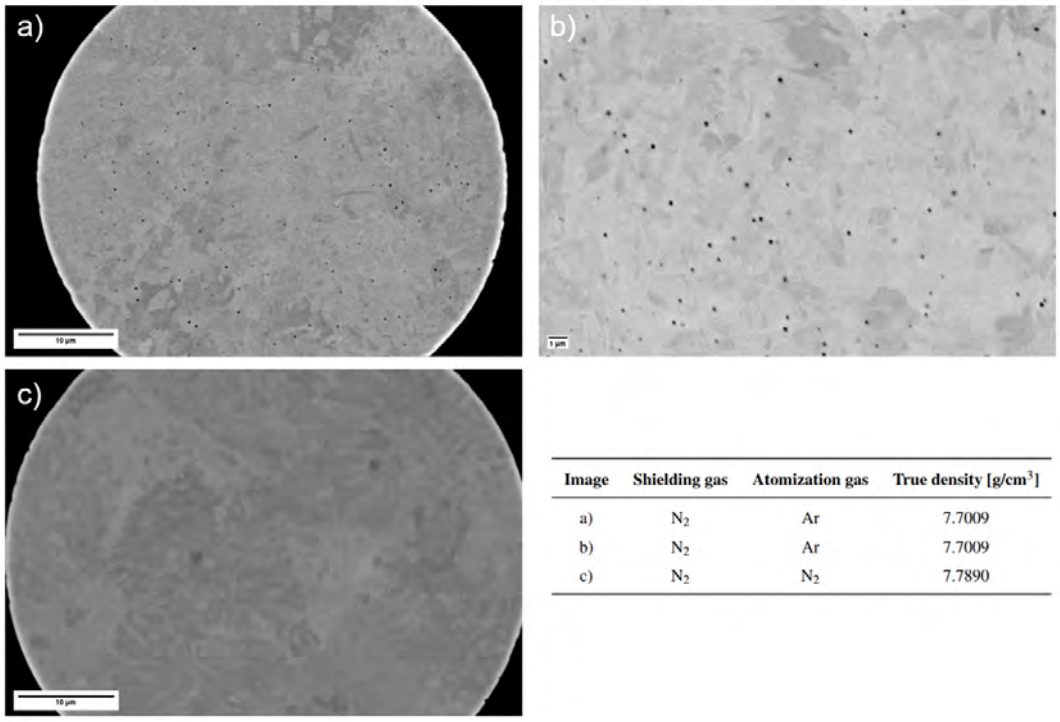

Image	Shielding gas	Atomization gas	True density [g/cm^3]
a)	N_2	Ar	7.7009
b)	N_2	Ar	7.7009
c)	N_2	N_2	7.7890

Fig. 4.18 Cross-sectional micrographs of powders produced under nitrogen-based process-gas combinations: (a,b) N_2/Ar and (c) N_2/N_2. Images (a) and (c) show representative polished powder cross-sections, while image (b) provides a higher-magnification view of the N_2/Ar condition, in which pores attributable to the insolubility of Ar in steel can be observed.

4.3.3.5 Nitrogen content as a function of different processing gases

The overpressure value in the melting chamber plays a crucial role, as shown in Figure 4.19, because nitrogen solubility changes significantly with both melt temperature and nitrogen partial pressure, according to Sieverts' law [111]. The equilibrium between the gas phase in the melting chamber and the nitrogen dissolved in the melt is described by Equation 4.5 [111]. Under ideal conditions and at thermodynamic equilibrium, the solubility of nitrogen in the melt is proportional to the square root of the nitrogen partial pressure, as expressed by Sieverts' law in Equation 4.6 [111].

$$\frac{1}{2}N_2 \leftrightarrow [N]_{\text{melt}} \tag{4.5}$$

$$[N]_{\text{melt}} \propto \sqrt{P_{N_2}} \tag{4.6}$$

In both atomizations conducted with N_2 in the melt chamber, once the temperature reached approximately 1000 °C the chamber was maintained at 0.11 MPa under a fluxing atmosphere. Immediately before initiating atomization, the melt-chamber pressure was raised to 0.13 MPa. The charge mass and dwell times were kept essentially identical for the two runs, thereby exposing the melt to the nitrogen atmosphere for the same residence time and ensuring the same level of electromagnetic stirring by applying identical induction parameters. In addition, the literature indicates that this phenomenon does not show any significant dependence on gas temperature [62].

The data presented in the graph of Figure 4.20 show how the nitrogen content varies depending on the combinations of argon or nitrogen as process gas:

- Using argon in the melt chamber and as atomising gas decreased the nitrogen content in the atomised powders compared to the feedstock material (Table 4.4), while using nitrogen in atomisation is sufficient to hinder such decrease.
- The application of nitrogen as both the cover gas in the atomisation chamber and the atomising gas led to an increase in the nitrogen content of ~ 0.210 wt% compared to the average value 0.268 ± 0.004 wt% of the feedstock material. A slightly lower increment was observed when nitrogen was used as the cover gas and argon was employed as the atomising gas.

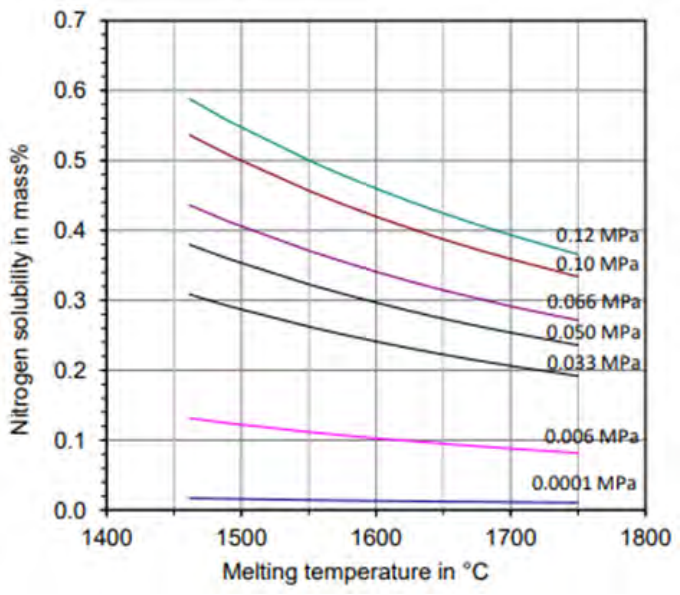

Fig. 4.19 Predicted nitrogen solubility in molten UNS S32760 super duplex stainless steel as a function of melt temperature and nitrogen gas pressure, according to Sieverts' law. Adapted from [62].

- No significant differences in nitrogen content were found in relation to the three different particle size ranges examined for each combination of process gases used.

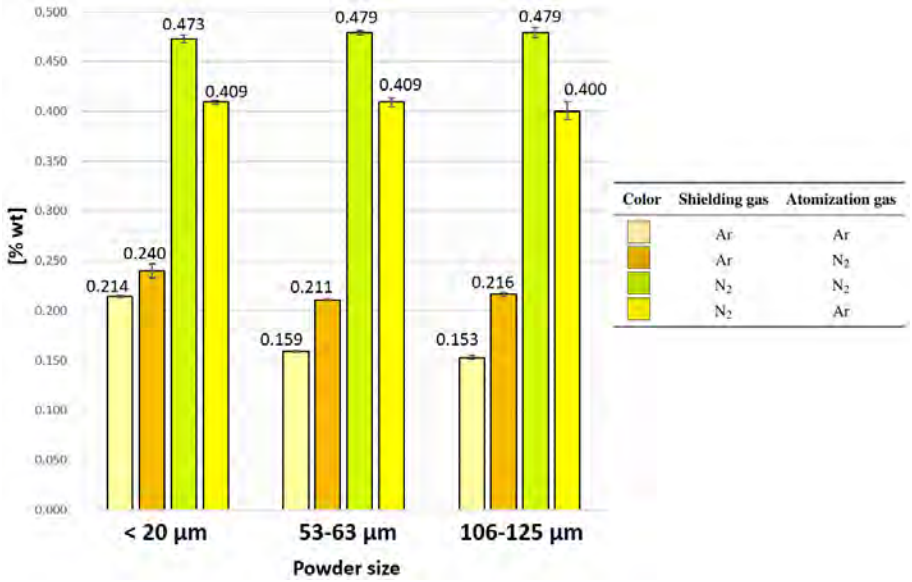

Fig. 4.20 Nitrogen content (wt.%) in UNS S32760 powders as a function of powder size and process-gas configuration. Bars report the mean nitrogen concentration measured for three size fractions produced under different combinations of shielding and atomization gases. Nitrogen was quantified by LECO ONH836, with five replicates analyzed for each size class to determine the average composition.

4.3.3.6 Austenite/Ferrite phase fractions as a function of different processing gases

The XRD analysis of the feedstock (Figure 4.21) indicates an approximately balanced phase distribution, with a mean austenite content of 56.3%. Results for the atomised powders are shown in Fig. 4.22. Because residual austenite values below 5% are generally considered unreliable [112, 113], those measurements are reported as "< 5%" rather than as specific numerical estimates.

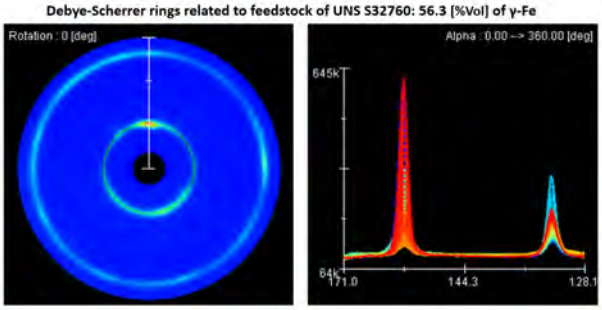

Fig. 4.21 Austenite phase fraction of the UNS S32760 feedstock determined by XRD

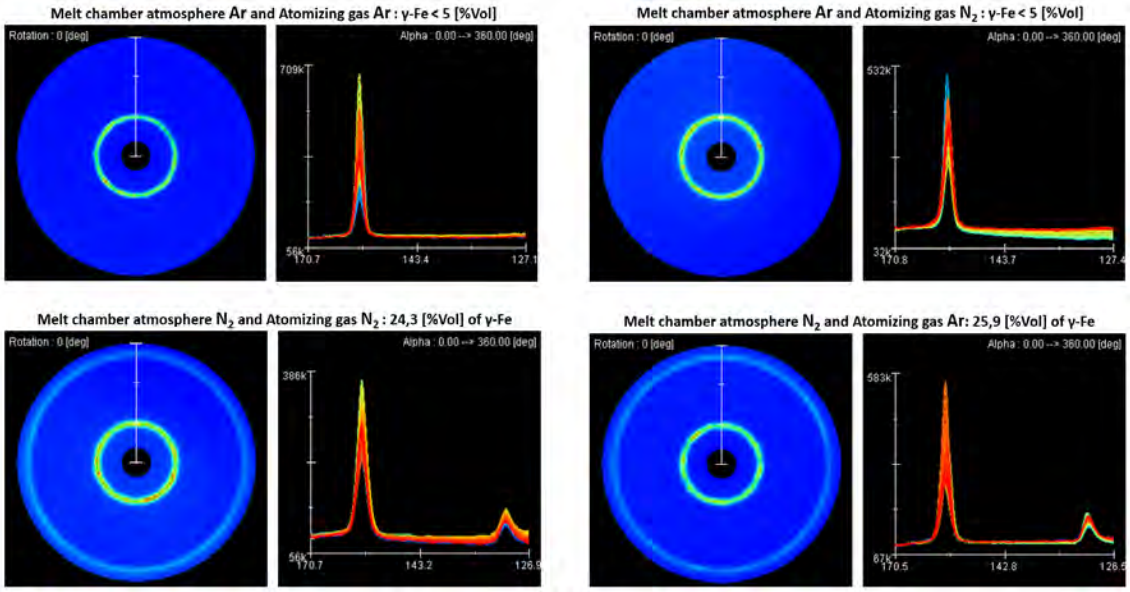

Fig. 4.22 Austenite phase fraction of as-atomized UNS S32760 powders produced under different combinations of shielding gas and atomization gas, as determined by XRD analysis. Austenite contents below 5 vol.% are reported as "< 5 vol.%" owing to the limited reliability of lower quantitative estimates.

Comparing the four argon–nitrogen process-gas combinations reveals that:

- Argon in the melting chamber yields powders with nitrogen contents consistent with a fully ferritic microstructure after rapid solidification (< 5% austenite).
- Nitrogen in the melting chamber and argon as the atomisation gas produces powders with an average austenite fraction of 25.9%. In contrast, argon in the melting chamber and nitrogen as the atomisation gas again results in fully ferritic powders. In line with the chemical analyses, the increase in nitrogen, an austenite stabiliser [111, 114], is attributed to its use as a cover gas during melting; when nitrogen is used only as the atomisation gas, its effect is negligible because the very rapid cooling limits diffusion into the metallic matrix [115].
- When both the melting-chamber atmosphere and the atomisation gas are nitrogen (N_2/ N_2), the austenite fraction is comparable to the N_2/Ar case. Although the nitrogen content in the N_2/N_2-atomized powders is nearly twice that of the feedstock (see Table 4.4 and Figure 4.20), and although a higher nitrogen concentration is known to accelerate the $\delta \rightarrow \gamma$ transformation [116], the austenite fraction reaches only about 25%, which is still far below the 56.3% measured in the feedstock material (Figure 4.21). This behavior is attributed to the rapid quenching conditions inherent to gas atomization, which generate pronounced undercooling and strongly hinder the kinetics of austenite formation [117, 118].

The bar chart in Figure 4.23 shows a clear particle-size dependence of the austenite fraction for both the N_2/N_2 and N_2/Ar powders. In both cases, the austenite content increases with increasing particle size, consistent with the lower cooling rates and longer high-temperature residence times experienced by coarser droplets, which promote nitrogen partitioning and the $\delta \rightarrow \gamma$ transformation. By contrast, the rapid quench affecting finer particles suppresses γ-phase formation and favors ferrite retention [115].

This interpretation is supported by the etched cross-sections of N_2/N_2 powders shown in Figure 4.24. The 106–125 μm particle exhibits a more extensive and continuous austenitic network, whereas the 53–63 μm particle shows finer and more discontinuous γ regions within a predominantly ferritic matrix. These results also

highlight the importance of maintaining a consistent PSD when selecting powders for PBF-LB/M. Since nitrogen content and phase balance vary with particle size, changes in the powder size range may alter the average nitrogen level of the feedstock supplied to the process. As a consequence, shifting, for instance, from a 20–63 μm fraction to a 15–45 μm fraction may lead to measurable differences in the nitrogen content and, therefore, in the microstructural features of the final PBF-LB/M components. It should also be noted that increasing the austenite fraction can be advantageous in applications such as cold spray: the fcc γ phase provides more active slip systems and higher room-temperature ductility than δ-ferrite, enhancing particle deformability on impact, flattening and bonding, and thereby improving deposition efficiency with reduced cracking or rebound.

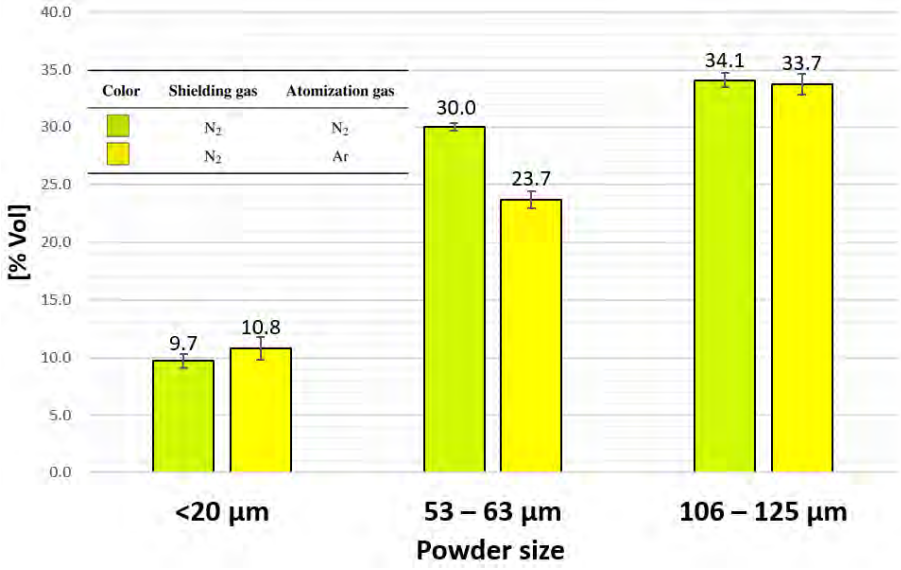

Fig. 4.23 Austenite phase fraction as a function of powder size for UNS S32760 powders produced under nitrogen-containing process-gas combinations. In both the N_2/Ar and N_2/N_2 conditions, the austenite content increases with increasing particle size, reflecting the lower cooling rates experienced by coarser droplets during solidification.

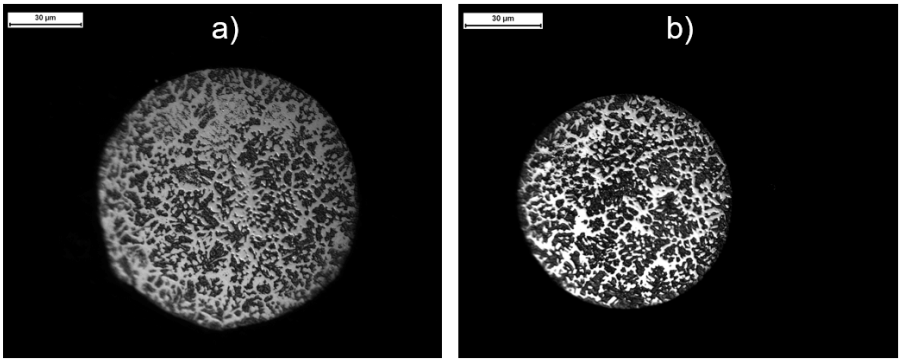

Fig. 4.24 Representative optical micrographs of etched cross-sections of N_2/N_2 powders belonging to different particle-size classes: (a) 106–125 μm and (b) 53–63 μm. Metallographic etching was performed using Beraha II reagent.

4.4 Optimization of PBF-LB/M process parameters for UNS S32760

4.4.1 Introduction

At the time of writing, the application of super duplex stainless steels in PBF-LB/M process technique remains a relatively early-stage research field. As a result, the available literature is still limited to a comparatively small number of studies. In this context, the present work should be regarded as exploratory and is therefore grounded, where necessary, on considerations and experimental evidence derived from alloys closely related to UNS S32760 (AISI F55). Among these, UNS S32750 (AISI F53) has received the greatest attention, and a sufficiently developed body of literature is currently available for this grade. Within this framework, the present section aims to examine selected aspects of PBF-LB/M process-parameter optimization, with particular emphasis on their influence on material quality and microstructural development. A further objective is to provide an overview of the optimization of post-processing heat-treatment routes for these alloys.

4.4.2 Materials and Methods

4.4.2.1 PBF-LB/M experimental setup

For the optimization of the PBF-LB/M process parameters on the Aconity Mini 3D system [119], a powder blend composed of the high-nitrogen powders produced under N_2/N_2 and N_2/Ar atomization conditions was employed. The complete characterization of this powder system is reported in Section 4.3, while its particle size distribution is shown in Table 4.8. Cubic samples with nominal dimensions of 8 $\times$ 8 $\times$ 8 mm, excluding support structures, were manufactured. For clarity and to ensure an unambiguous interpretation of the specimen geometry and observation directions, the reference coordinate system adopted in the present work is schematically illustrated in Figure 4.25. The description is based on an orthogonal reference system in which the Z axis identifies the vertical build direction, consistently with the machine coordinate system, while the X and Y axes define the build plane and are parallel to the faces of the specimens.

4.4.2.2 Densification-based Process-parameter Optimisation

The optimization procedure was carried out through two successive iterations, during which only hatch laser power and hatch laser speed were varied, whereas all the remaining process parameters were kept constant, as summarized in Table 4.11. Archimedes density was adopted as the main optimization criterion, allowing the gradual refinement of the processing window up to the definition of the final parameter set used to produce the test specimens . The variation of hatch laser power and hatch laser speed was specifically intended to identify the optimal hatch energy density (HED), also commonly referred to as volumetric energy density (VED), as defined in Equation 4.7, in terms of maximum attainable densification.

$$\mathrm{HED\,(VED)} = \frac{\textit{Hatch Laser Power}}{\textit{(Hatch Laser Speed)} \cdot \textit{(Layer Thickness)} \cdot \textit{(Hatch Spacing)}} \quad \left[\frac{J}{mm^3}\right] \tag{4.7}$$

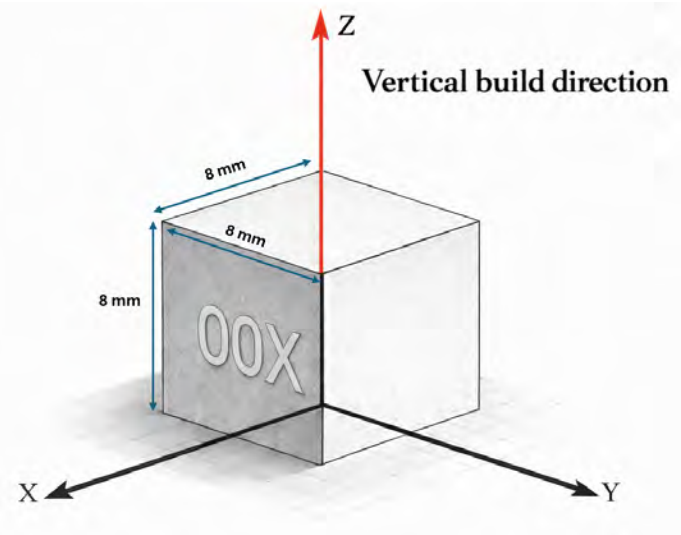

Fig. 4.25 Orthogonal reference coordinate system adopted for the description of the PBF-LB/M specimens. The Z axis corresponds to the vertical build direction, while the X and Y axes lie on the build plane and are parallel to the specimen faces.

Table 4.11 PBF-LB/M process parameters employed during the optimization stage. Only hatch laser speed and hatch laser power were varied, while the remaining parameters were kept constant.

Hatch laser speed [mm/s]	Hatch laser power [W]	Layer thickness [μm]	Spot size [mm]	Atmosphere	Scanning strategy
500–1100	200–300	50	0.07	Nitrogen	Rotation of 67°

4.4.3 Optimization of PBF-LB/M parameters using high-nitrogen UNS S32760 powder

The results of the densification-based optimization are presented in Figure 4.26, where the Archimedes density is plotted as a function of hatch laser speed for the first and second PBF-LB/M optimization iterations. The figure provides a direct comparison between the two stages and illustrates the progressive refinement of the processing window toward the conditions associated with the highest density.

In the first iteration, the most promising results were obtained for laser powers of 250 and 300 W and scan speeds ranging from 600 to 1100 mm/s. These results made it possible to restrict the experimental domain and to improve the densification response in the second iteration.

Stereomicroscopic examination of the as-built specimens revealed a clear dependence of surface finish on the adopted processing conditions, particularly on the XY plane (top view). Figure 4.27 provides a schematic overview of the external appearance of the specimens as a function of the PBF-LB/M parameters employed during the first and second iterations. The samples highlighted in green correspond to the conditions associated with the highest Archimedes density values, which were used to define the optimization window for the second iteration and, subsequently, to identify the final optimal parameter set.

A significant variability in the occurrence of surface-connected porosity was observed as a function of the printing parameters. In general, the samples associated with the highest density also exhibited the best surface quality and a lower occurrence of open porosity. Delamination was also observed in some non-optimized specimens, particularly in the samples produced under the lowest HED values experimentally investigated, specifically 42.1 and 36.4 J/mm^3. An example of this defect, occurring

on multiple planes within the same specimen, is shown in Figure 4.28. Although its origin was not investigated in further detail, the disappearance of this defect during the second optimization iteration suggests that the refinement of the processing window effectively suppressed its formation. In the PBF-LB/M literature, such defects are generally associated with the development of residual stresses during the repeated melting and solidification cycles, especially under low-HED conditions [120].

A further aspect concerns the position of the specimens on the build plate. For each parameter set, three specimens were manufactured, and in some cases marked differences in surface finish and density were observed even under nominally identical process conditions. An example is reported in Figure 4.29, where two specimens fabricated at 250 W and 950 mm/s exhibit a clear qualitative difference in terms of surface-connected porosity. This difference is also reflected in the Archimedes density, which decreases by 0.15 g/cm^3 for one of the three specimens with respect to the other two, thereby suggesting a higher internal porosity content. Such behavior can reasonably be attributed to the different exposure of the specimens to the shielding gas flow over the powder bed.

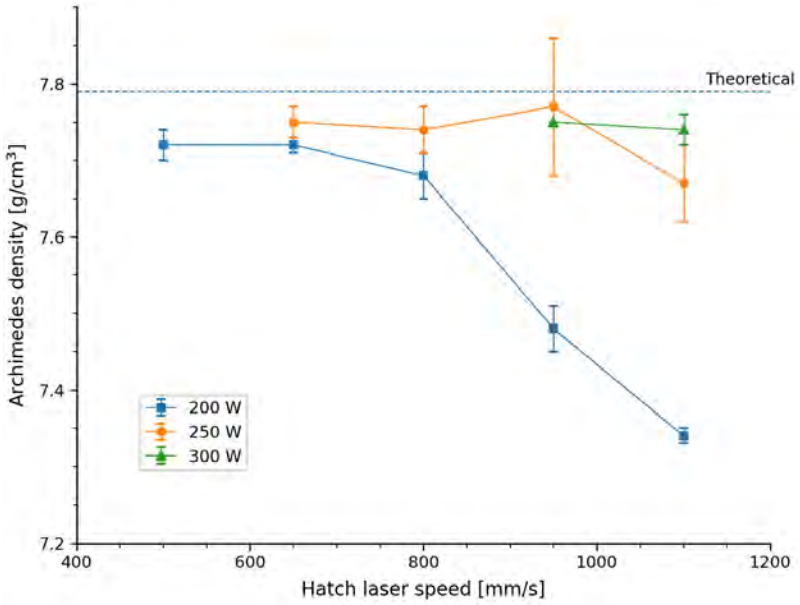

(a) First iteration.

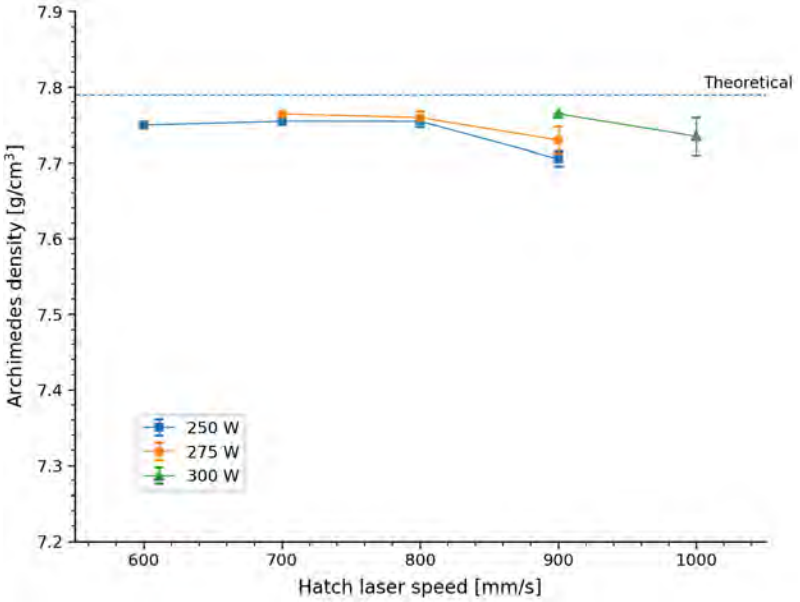

(b) Second iteration.

Fig. 4.26 Archimedes density as a function of hatch laser speed for the two PBF-LB/M process-parameter screening iterations: a) first iteration and b) second iteration. Each point represents the mean value obtained for a given processing condition, while the error bars denote the corresponding standard deviation. The different series refer to different laser power levels, and the dashed horizontal line indicates the theoretical density.

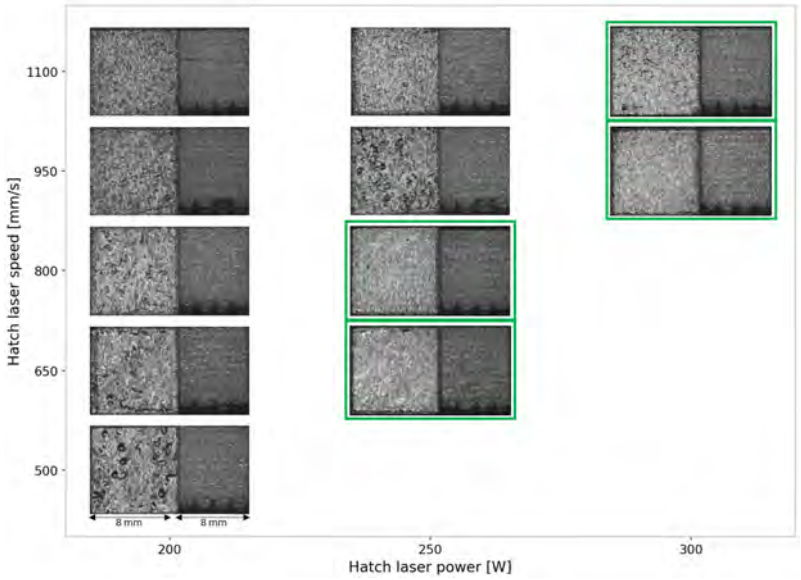

(a) First iteration.

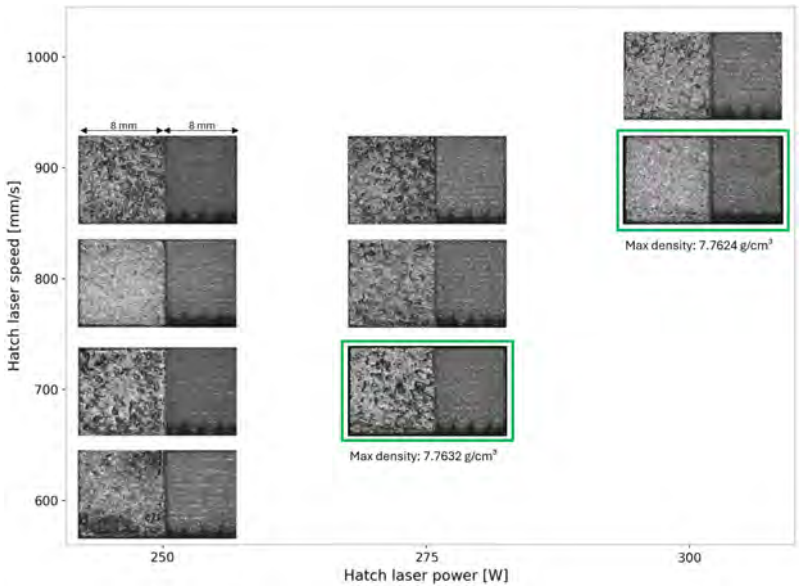

(b) Second iteration.

Fig. 4.27 Stereomicroscopic overview of the surface appearance of PBF-LB/M as-built samples as a function of the applied process parameters for the first iteration (top) and the second iteration (bottom). The green-highlighted samples correspond to the conditions associated with the highest Archimedes density, which defined the optimization window for the second iteration and the final optimal parameter set.

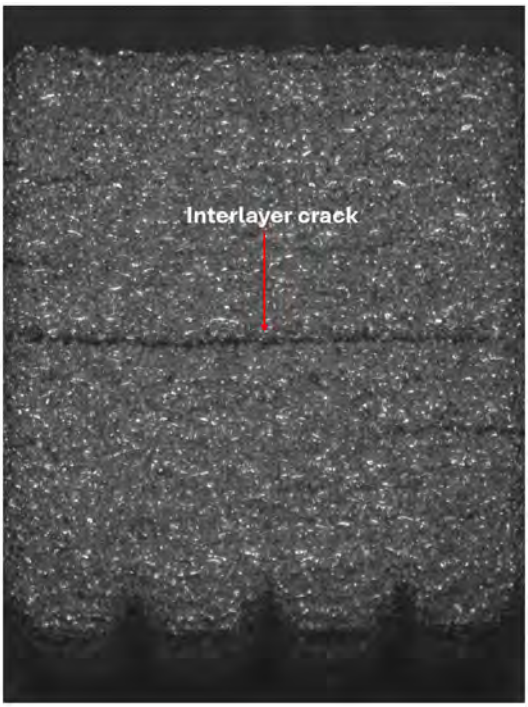

Fig. 4.28 Example of an interlayer crack observed in the PBF-LB/M specimen fabricated using a hatch laser power of 200 W and a hatch laser speed of 1100 mm/s.

In general, based on the results reported in Figure 4.26 and the stereomicroscopic observations shown in Figure 4.27, two parameter combinations, 275 W–700 mm/s and 300 W–900 mm / s, were identified as optimal, both ensuring a density of approximately 7.76 g/cm^3. Between these two conditions, the latter was selected as the final optimal parameter set because the higher scan speed led to a substantial reduction in printing time, while still maintaining the same density level. Indeed, the corresponding build rate increased from 12.6 to 16.2 cm^3/h, which represents a significant advantage in view of the possible future manufacturing of application-oriented components. By considering a theoretical density of 7.79 g/cm^3, determined by helium pycnometry on the powder condition, the relative density associated with the optimized PBF-LB/M parameters was calculated to be 99.6%. The corresponding binary image of the specimen cross-section is reported in Figure 4.30. This value is in good agreement with those commonly reported in the literature for duplex and super duplex stainless steels processed by PBF-LB/M, as summarized in Table 3.3, previously presented in Section 3.2.

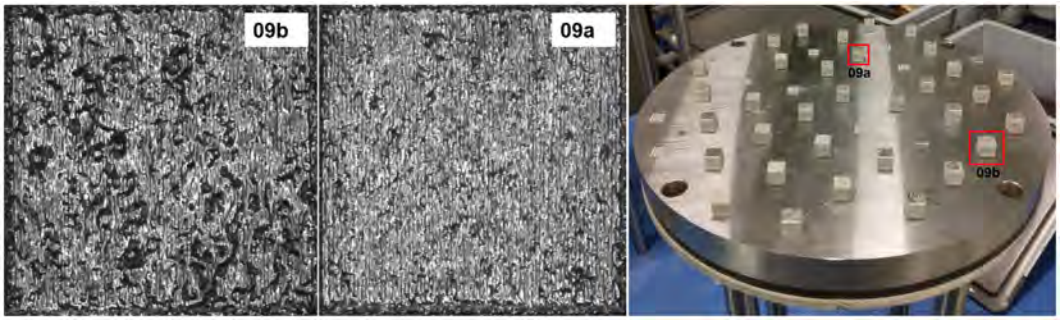

Fig. 4.29 Example of the effect of specimen position on build plate on the surface appearance of PBF-LB/M as-built samples fabricated during the first iteration using identical process parameters (250 W and 950 mm/s). Samples 09a and 09b exhibit a marked qualitative difference in terms of surface-connected porosity, which is also reflected in their measured Archimedes density, equal to 7.74 and 7.59 g/cm^3, respectively.

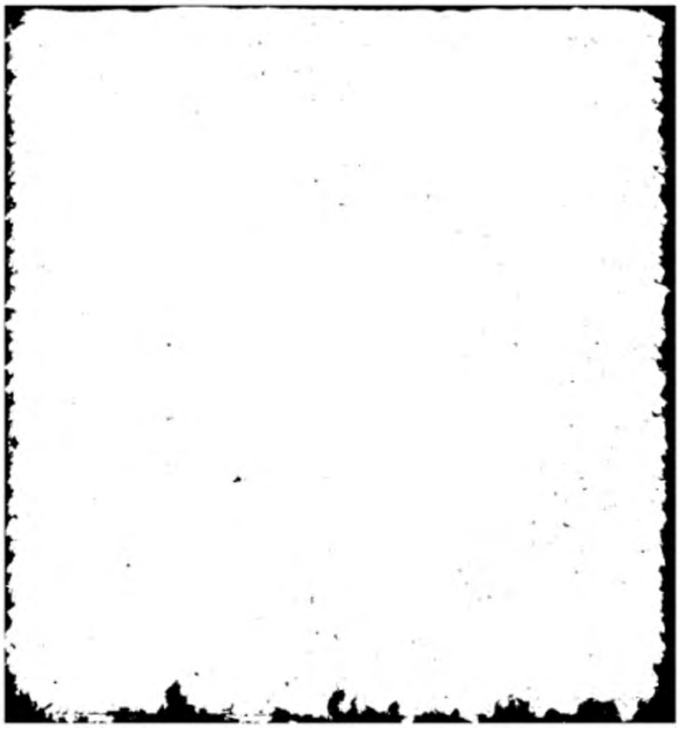

Fig. 4.30 Binary image of the cross-section of the PBF-LB/M specimen manufactured using the optimized process parameters, corresponding to a relative density of 99.6%, obtained with a hatch laser power of 300 W and a hatch laser speed of 900 mm/s (HED = 66.7 J/mm^3).

4.4.4 Influence of powders Nitrogen content on the properties of UNS S32760 PBF-LB/M as-built components

The analysis of the results reported in the graph of Figure 4.31 reveals a clear decrease in the nitrogen content of the PBF-LB/M as-built samples produced from the high-nitrogen powder mixture (N_2/N_2 and N_2/Ar, 20–63 μm) with increasing hatch energy density (HED). Cubic specimens with dimensions of 8 × 8 × 8 mm, excluding support structures, were manufactured using an Aconity Mini 3D PBF-LB/M system [119] in order to characterize their properties. The nitrogen content decreases from approximately 0.436 wt% at the lowest HED values to about 0.389–0.395 wt% at the highest HED levels, following an almost linear trend. This behavior indicates that a higher energy input, associated with deeper melt pools and longer residence times in the molten state, promotes nitrogen loss during processing, even though the PBF-LB/M process was carried out using nitrogen both as the protective atmosphere and as the shielding gas.

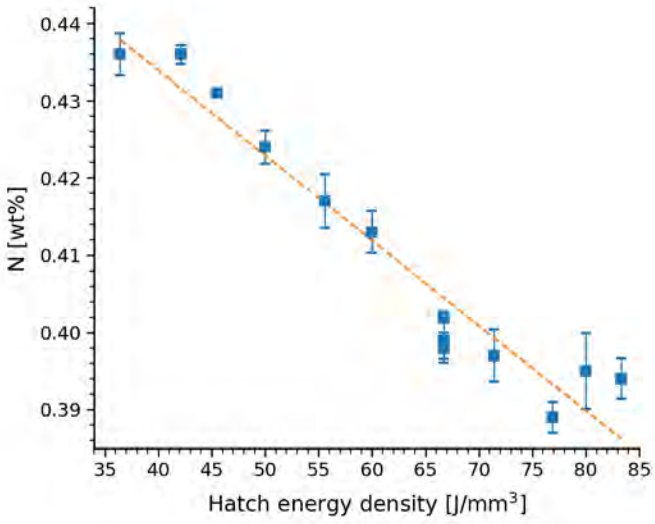

Fig. 4.31 Nitrogen content as a function of the hatch energy density (HED) of the PBF-LB/M process for the investigated conditions. Error bars denote the instrumental standard deviation associated with the nitrogen measurements.

The comparison with the average values reported in Table 4.12 further confirms that, although the PBF-LB/M process causes a reduction in nitrogen content with respect to the high-nitrogen powder feedstock, the consolidated material still retains a nitrogen level significantly higher than that of the initial atomization feedstock.

More specifically, while the high-nitrogen powder mixture exhibits an average nitrogen content of 0.479 ± 0.003 wt%, the PBF-LB/M as-built high-nitrogen sample produced using the optimized process parameters (HED = 66.7 J/mm^3) shows a nitrogen content of 0.400 ± 0.002 wt%, which remains markedly higher than that measured for the atomization feedstock, namely 0.268 ± 0.004 wt%.

It is worth emphasizing that the nitrogen content values reported in Figure 4.31 and in Table 4.12, obtained by LECO ONH836 analysis, correspond to the average of five measurements for each sample condition. In addition, all measurements were carried out on the same day in order to avoid repeated instrument shutdown and restart cycles, which could have introduced possible calibration variations. Instrument calibration was verified prior to testing by means of certified standards. For consistency, the nitrogen analysis of the atomization feedstock was also repeated under the same conditions, yielding a value consistent with that originally reported in Table 4.4.

Table 4.12 Comparison of the average Nitrogen content of UNS S32760 measured in the atomizing feedstock, in the High-Nitrogen powder mixture produced using N_2/N_2 and N_2/Ar atomization gas combinations, and in the PBF-LB/M as-built high-nitrogen sample manufactured from these powders using the optimized process parameters.

UNS S32760 nitrogen content measured by LECO ONH 836	
	N [wt%]
Atomizing feedstock	0.268 ± 0.004
High-nitrogen powder mixture, 20–63 μm	0.479 ± 0.003
PBF-LB/M as-built high nitrogen (HED = 66.7 J/mm^3)	0.400 ± 0.002

Additional nitrogen-content measurements were also performed on specimens produced from low-nitrogen powders using the optimized process parameters (HED = 66.7 J/mm^3). These measurements showed that, under comparable PBF-LB/M energy input conditions, the nitrogen depletion remains of the same order of magnitude for both low-nitrogen and high-nitrogen powder feedstocks. In particular, the low-nitrogen powders exhibited a decrease from approximately 0.206 wt.% to 0.140 wt.%, corresponding to a nitrogen loss of about 0.066 wt.%. By comparison, the high-nitrogen powder mixture decreased from 0.479 ± 0.003 wt.% in the powder state to 0.400 ± 0.002 wt.% in the as-built condition produced using the optimized process parameters, corresponding to a nitrogen loss of about 0.079 wt.%. Therefore,

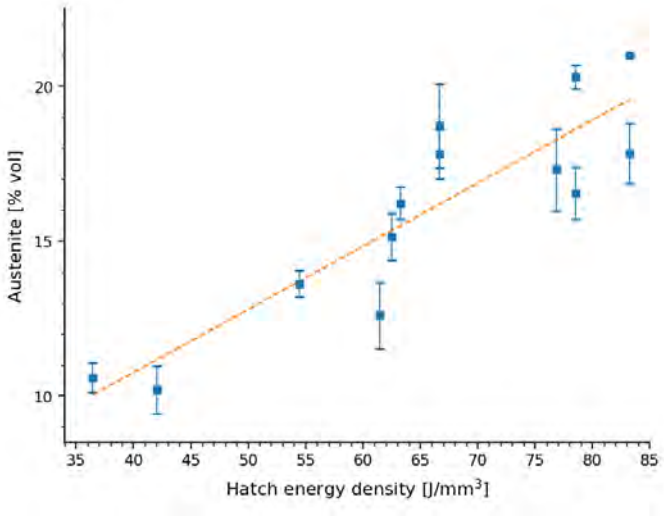

Fig. 4.32 Variation of austenite content determined by XRD, expressed as volume fraction, as a function of the hatch energy density (HED) applied during the PBF-LB/M process.

although the absolute nitrogen decrease occurred within the same order of magnitude for both powder blends, its relative impact was greater for the low-nitrogen material because of its lower initial nitrogen content. This indicates that nitrogen depletion is governed primarily by the thermal history associated with laser melting and solidification, while the initial powder composition remains decisive in determining the nitrogen level retained in the final component. Consequently, the use of high-nitrogen powders remains strategically advantageous, since it allows the final component to retain a significantly higher nitrogen level even after the depletion induced by the process.

With regard to the microstructural response, the results shown in Figure 4.32 indicate an increase in the austenite volume fraction with increasing HED, with values rising from approximately 10–11 vol% up to about 20–21 vol%. Such values markedly differ from those generally reported in the literature. Within the limited number of studies available on the as-built condition of similar alloys, such as UNS S32750, the microstructure is commonly reported to be fully ferritic or to contain only very limited amounts of austenite, typically on the order of 1% [121, 85], whereas higher austenite fractions have been achieved only in a few cases [86, 89]. This discrepancy may reasonably be ascribed to the higher nitrogen concentration attained in the present work relative to the studies cited above.

When considering the trend observed within the present dataset, however, the increase in austenite fraction with increasing HED may appear to contradict what would be expected on the basis of the nitrogen content evolution alone. This apparent inconsistency can be rationalized by considering the competition between chemical and thermal effects. On the one hand, the reduction in nitrogen content tends to hinder the stabilization of the austenitic phase, since nitrogen is a strong austenite stabilizer [71, 81]. However, higher HED values reduce the effective cooling rate, because the increase in melt pool depth lowers the efficiency of heat extraction toward both the surrounding material and the substrate [93, 83]. As a consequence, more time becomes available for the $\delta \rightarrow \gamma$ transformation, resulting in a higher austenite fraction due to the reduced undercooling of the liquid. This finding is in line with the observations reported in the previous section on powder atomization (Section 4.3.3.6), a process characterized by cooling rates several orders of magnitude lower than those achieved during PBF-LB/M. In fact, for the powders, austenite fractions of approximately 25% were obtained for particle sizes in the 20–63 μm range only in the two cases where the alloy nitrogen content was equal to or greater than 0.4 wt%.

A further noteworthy aspect is the dispersion of the experimental data, which also highlights a dependence on the specimen position across the build plate, as shown in Figure 4.33. Even under identical nominal processing parameters, samples fabricated at different locations exhibit appreciable variations in austenite fraction. This effect is particularly evident for the specimens produced at 250 W and 600 mm/s, corresponding to an HED of 83.3 J/mm^3, for which approximately 21% and 17% austenite were measured at positions b and c, respectively. Such a difference, amounting to 4 percentage points under the same nominal process conditions, indicates that the local thermal environment may not be fully uniform over the entire build plate. Localized heat accumulation, differences in heat extraction efficiency toward the substrate, thermal interactions with neighboring specimens, and possible variations in shielding gas flow conditions may all substantially alter the local thermal history, thereby affecting the final ferrite–austenite phase balance.

Overall, the results indicate that, within the investigated processing window, the thermal effect associated with increasing HED outweighs the adverse effect related to the the partial nitrogen depletion, thereby promoting a net increase in the as-built austenite fraction. At the same time, the results clearly show that a high initial nitrogen content in the starting powders is a key prerequisite for promoting

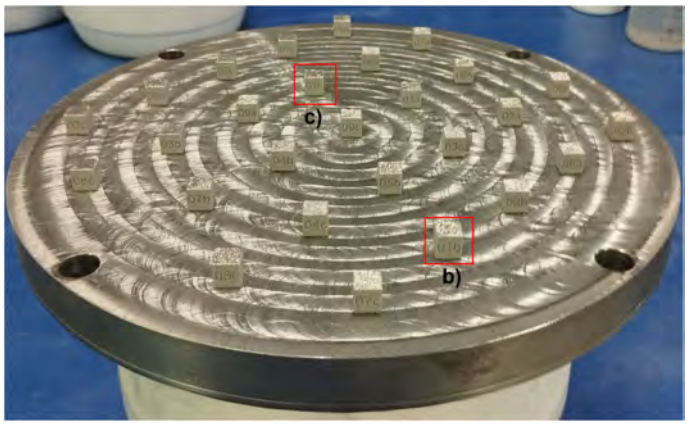

Laser power [W]	Scan speed [mm/s]	Position	Austenite [%]
250	600	b	21
		c	17

Fig. 4.33 Variation of austenite content determined by XRD, expressed as volume fraction, as a function of the hatch energy density (HED) applied during the PBF-LB/M process. The table reports the difference in austenite fraction as a function of specimen position over the build plate for samples manufactured using identical PBF-LB/M parameters.

austenite formation already during the PBF-LB/M process. Although the austenite fractions obtained in the present study are significantly higher than those commonly reported in the literature for PBF-LB/M as-built duplex and super duplex stainless steels [83], they remain insufficient to achieve a fully balanced duplex microstructure. In particular, the optimized PBF-LB/M parameter set, consisting of 300 W laser power and 900 mm/s scan speed, corresponding to an HED of 66.7 J/mm^3, yields an austenite content of approximately 18 vol%, associated with a nitrogen content of 0.400 wt%. This confirms that, while the adopted processing strategy is effective in enhancing austenite formation in the as-built condition, a subsequent post-process heat treatment is still strictly required to obtain the desired phase balance.

4.4.5 Microhardness evolution during PBF-LB/M parameter optimization using high-nitrogen UNS S32760 powder

Microhardness measurements were performed at the center of the *ZY* section of cubic specimens with dimensions of $8 \times 8 \times 8$ mm (scheme of Figure 4.25). Figure 4.34 reports the variation of the microhardness HV0.2 as a function of the hatch energy density (HED) for specimens produced during the second iteration of the PBF-LB/M parameter optimization campaign. The investigated processing conditions covered an HED range between approximately 55.6 and 83.3 J/mm^3.

The collected data highlight a progressive reduction in hardness with increasing hatch energy density. The highest hardness value was measured for the specimen processed at the lowest investigated HED, corresponding to approximately 460 ± 12 HV0.2 at 55.6 J/mm^3. Conversely, the lowest hardness values were observed at the highest HED conditions, where the hardness decreased to approximately 437 ± 10 HV0.2. The optimized process condition, corresponding to a hatch laser power of 300 W and a hatch laser speed of 900 mm/s (HED $= 66.7$ J/mm^3), exhibited an average hardness of approximately 440 ± 12 HV0.2.

The observed decrease in hardness with increasing HED can be primarily attributed to the different thermal histories experienced during solidification and subsequent cooling. An increase in HED generally promotes the formation of larger and more persistent melt pools, associated with lower cooling rates and longer thermal cycles. These conditions favor microstructural coarsening, particularly grain growth, which is known to reduce hardness according to the Hall–Petch relationship. Similar trends have been reported in the literature for duplex and super duplex stainless steels processed by PBF-LB/M, where increasing volumetric energy density results in a progressive increase in grain size accompanied by a reduction in hardness values [93, 86].

At lower HED values, the extremely high cooling rates characteristic of the PBF-LB/M process, typically in the order of 10^6–10^7 K/s, promote the formation of a very fine microstructure. Such refined microstructural features strongly contribute to the elevated hardness values measured in the low-HED specimens. In addition to grain refinement strengthening, another possible contribution to the high hardness values may derive from the precipitation of chromium nitrides, mainly CrN and Cr_2N. In duplex stainless steels, nitride precipitation is favored under extremely rapid

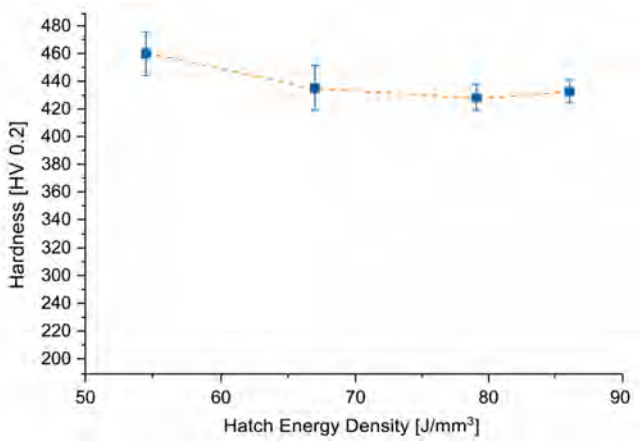

Fig. 4.34 Variation of microhardness HV0.2 as a function of hatch energy density (HED) for UNS S32760 specimens produced by PBF-LB/M in the as-built condition during the second iteration of the process-parameter optimization campaign. Each point represents the average hardness measured at the center of the *ZY* section of cubic specimens ($8 \times 8 \times 8$ mm), while the error bars indicate the corresponding standard deviation.

solidification and cooling conditions, where the diffusion of nitrogen from ferrite to austenite becomes kinetically limited. As a consequence, ferrite may remain locally supersaturated in nitrogen, promoting nitride formation [116].

Furthermore, as previously discussed in relation to Figure 4.32, the austenite fraction tends to increase with increasing HED. Since austenite generally exhibits lower hardness compared to ferrite, the progressive increase in austenite content may further contribute to the overall reduction in hardness observed at higher energy densities. Therefore, the hardness evolution appears to result from the combined effects of grain coarsening, phase balance variation, and possible differences in nitride precipitation behavior induced by the different thermal conditions associated with the investigated HED values.

Although rapid cooling during PBF-LB/M is beneficial for suppressing the precipitation of several detrimental intermetallic phases, it is generally insufficient to completely avoid nitride formation in nitrogen-alloyed duplex stainless steels. The mitigation of excessive nitride precipitation may therefore require either a reduction in nitrogen supersaturation or the application of suitable post-process heat treatments capable of promoting nitrogen diffusion from ferrite toward austenite during cooling [116].

4.4.6 Microstructural Analyses in the As-Built State

The as-built microstructures of the UNS S32760 specimens produced by PBF-LB/M were investigated after electrolytic metallographic etching with NaOH. This preparation allowed the main solidification-related features to be revealed, including the melt-pool morphology, the scan-track arrangement and the microstructural differences associated with the use of low- and high-nitrogen powder blends. Representative micrographs of the as-built conditions are reported in Figures 4.35 and 4.36.

For the specimens produced from the low-nitrogen powder blend, the microstructural features observed on the XY and ZY planes are shown in Figure 4.35. The etched microstructure highlights the characteristic layer-wise features induced by the PBF-LB/M process, including the scan-track morphology on the plane parallel to the build platform and the melt-pool profile on the section containing the build direction.

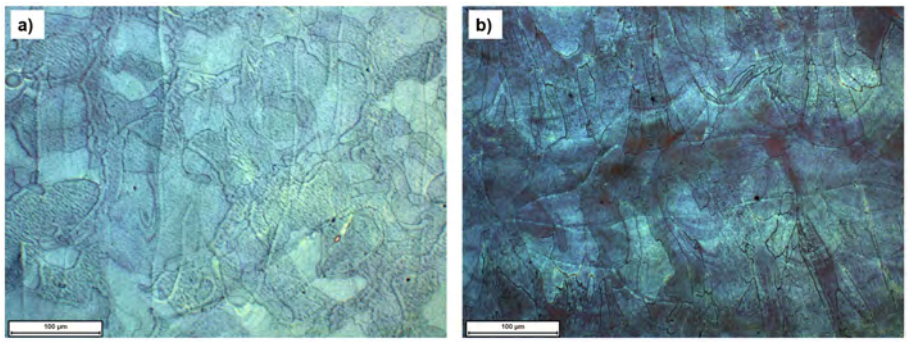

Fig. 4.35 Microstructural features of the as-built PBF-LB/M UNS S32760 specimen produced from the low-nitrogen powder blend after electrolytic metallographic etching with NaOH. (a) XY plane; (b) ZY plane.

For the specimens produced from the high-nitrogen powder blend, observations were performed on both the XZ and XY planes, as reported in Figure 4.36. The lower-magnification optical micrographs allow the melt-pool morphology and the variation in scan-track orientation between successive printed layers to be identified. At higher magnification, columnar ferritic grains preferentially oriented along the build direction, namely the Z-axis, can be observed. However, the presence and morphology of the austenitic phase could not be clearly resolved by optical microscopy in the as-built condition.

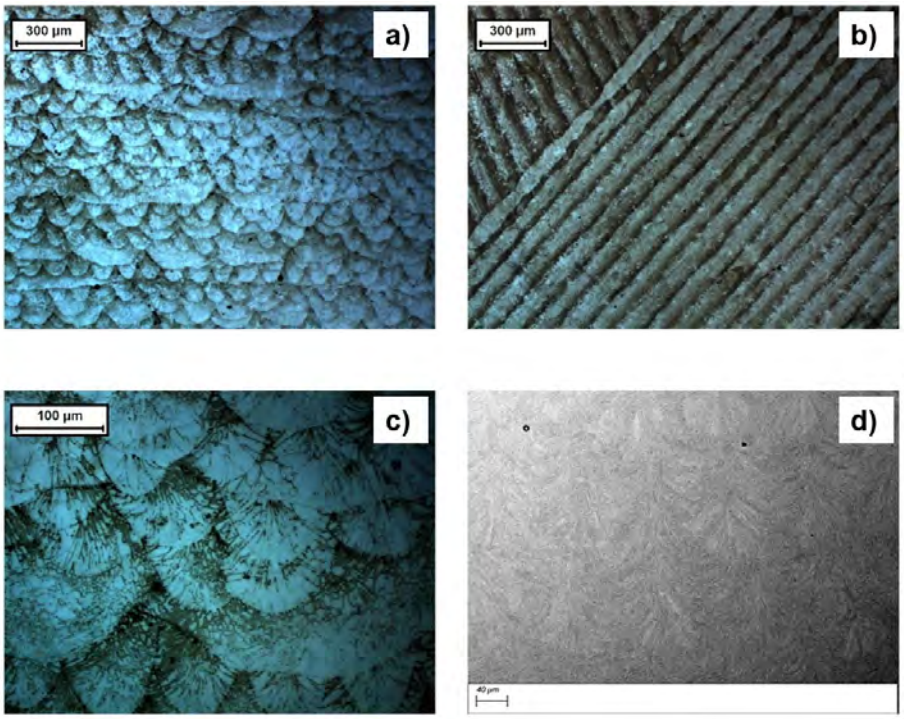

Fig. 4.36 Microstructural features of the as-built PBF-LB/M UNS S32760 specimen produced from the high-nitrogen powder blend after electrolytic metallographic etching with NaOH. (a) XZ plane observed by optical microscopy at 50× magnification; (b) XY plane observed by optical microscopy at 50× magnification; (c) XZ plane observed by optical microscopy at 500× magnification; (d) XZ plane observed by SEM-HDBSD at 500× magnification.

4.5 Heat treatment optimization for UNS S32760 PBF-LB/M components

4.5.1 Introduction

The main scope of this part of the experimental activity was to evaluate the influence of heat-treatment parameters on samples produced by the PBF-LB/M additive manufacturing technique using UNS S32760 powders characterized by a nitrogen content of $\sim 0.2\,\text{wt.}\%$ (obtained by a mix of Ar/Ar and Ar/N2 powders). Although the influence of these parameters during solution treatment is well documented in the literature for duplex steels produced by conventional routes (ingot melting/continuous casting followed by hot plastic deformation or simply casted components), a limited amount of data is available regarding their effect in duplex steel components manufactured by PBF-LB/M, quite none of which pertains to the UNS S32760 grade. Moreover, in "conventionally" produced components a certain fraction of austenite is always present prior to solution annealing, whereas in components manufactured by PBF-LB/M, due to the high cooling rate, austenite formation is inhibited and when starting from powders with low nitrogen content the resulting microstructure at the as-built PBF-LB/M state consists exclusively of ferrite.
The secondary objective is to identify the combination of heat-treatment parameters that achieves the target of 50% austenite in the microstructure. After providing an overview of the experiment and explaining how the factors under study were selected, attention will be focused on the outcomes of the experimental tests, on the statistical analysis of the results, and on the descriptive analysis of the data. Using the Johnson method [122], the graphical effects of the factorial parameters will be examined.

4.5.2 Materials and Methods

4.5.2.1 Preliminary description of the activity

The experiment aims to quantify the austenite fraction at the core of 10 × 10 x 10 mm UNS S32760 cubes produced by laser powder bed fusion (PBF-LB/M), before and after solution annealing performed at different temperatures and soaking times. All heat treatments were carried out in the same muffle furnace (Manfredi Warmy 9) as per the protocol detailed below.

4.5.2.2 Heat treating procedure

1. Empty Furnace stabilization for 30 minutes after reaching the target temperature;
2. Quick insertion of a single specimen into the furnace set to the target temperature, the soaking time was counted from specimen insertion until its extraction;
3. Removal of the specimen and rapid quenching in a water bath (approx 10 liters) at 20 °C .

4.5.2.3 Sectioning of samples and measurement planes

For each heat treatment, the austenite and ferrite fractions were measured on two sections extracted from each specimen 5 mm below the treated suface, the xy plane and the zy plane, both defined with respect to the PBF-LB/M build direction along the z axis, as illustrated in Figure 4.37. This design enables assessment of potential differences in austenite content associated with microstructural anisotropy induced by the laser scan strategy. Figure 4.38 shows, for a specimen treated at 1080 °C for 65 minutes, the austenite morphologies observed on the xy and zy planes.

4.5.2.4 Metallographic sample preparation and image analysis

Each specimen surface was prepared by standard metallography procedure, including polishing and electrolytic etching in NaOH solution. The austenite fraction was then evaluated by image analysis using ImageJ software, based on micrographs acquired

with an inverted optical microscope (LEICA MEF4M), at a magnification of 500X. As schematized in Figure 4.37 b), five micrographs were captured from the central region of the plane under examination. For each temperature–time combination and for each plane, the mean austenite percentage was computed from these fields of view.

For the low-nitrogen specimens heat treated at 1020°C for 35 min, the occurrence of a dark constituent was also assessed by optical microscopy after electrolytic etching in NaOH solution. The constituent was distinguished from the surrounding ferritic and austenitic phases on the basis of its optical contrast and morphology in the etched micrographs.

The estimated fraction of this dark constituent was obtained through manual image analysis in ImageJ, following the same general procedure adopted for the austenite quantification. Multiple optical micrographs were acquired from the investigated sections at 500X magnification, including five representative fields for each analysed plane and heat-treatment condition. The resulting value, estimated at approximately 1.5 vol%, should therefore be considered an image-based approximation derived from two-dimensional optical observations. On the basis of its morphology, thermal history, and the known precipitation behaviour of UNS S32760, the dark constituent was preliminarily attributed to sigma-phase precipitation.

Because the quantification relied on manual image analysis in ImageJ software, the measurement can be biased by underestimation or overestimation of the austenite fraction, as illustrated in Figure 4.39. Underestimation is most common, reflecting the resolution limits of image analysis that hinder accurate detection of very fine acicular austenite.

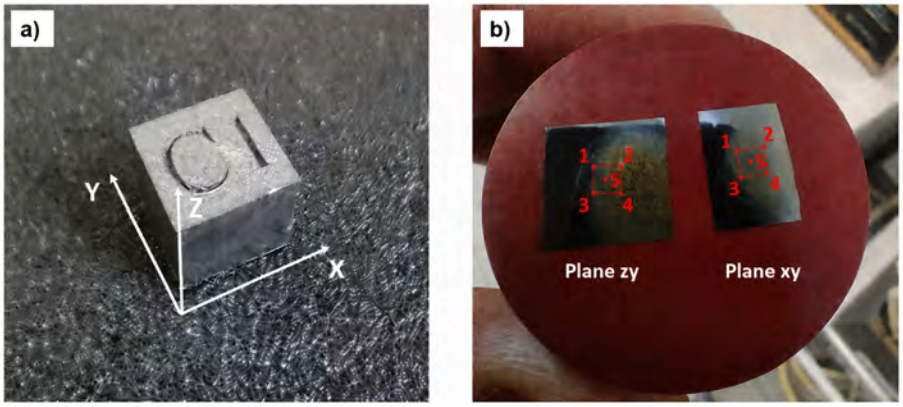

Fig. 4.37 a) 10 × 10 × 10 mm UNS S32760 specimen produced by PBF-LB/M with the build direction along the z-axis. b) The same specimen, sectioned after heat treatment to measure the percentage of austenite on both the zy and xy planes; in red are the locations where the five micrographs were acquired for each specimen.

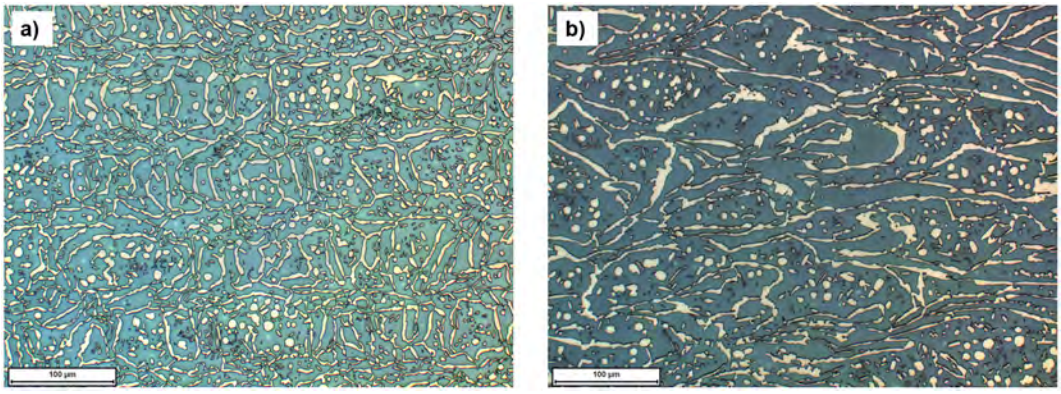

Fig. 4.38 a) Micrograph of the xy plane of the specimen treated at 1080 °C for 65 min. b) Micrograph of the zy plane of the specimen treated at 1080 °C for 65 min; the austenitic phase appears in white and the ferritic phase in light blue.

4.5.2.5 Experimental factors and levels

1. Furnace soaking temperature: 1020 °C, 1050 °C, 1080 °C;
2. Soaking time: 15 min, 35 min, 65 min;
3. Specimen plane: xy section, zy section.

The temperature levels were chosen to be equally spaced, whereas the soaking times were not. The latter were selected considering that approximately 5 minutes

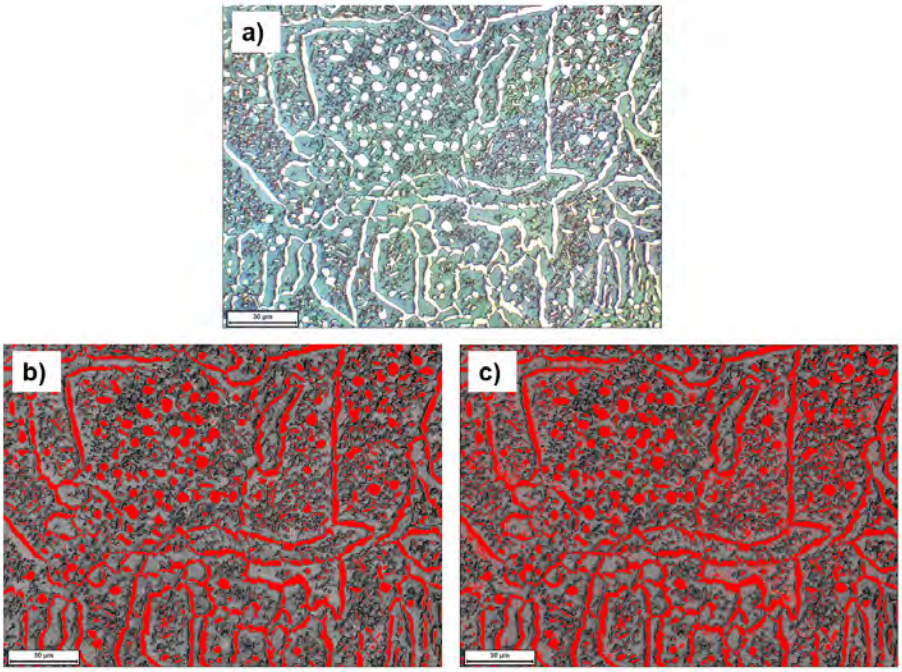

Fig. 4.39 (a) Micrograph of the xy-plane of the specimen heat treated at 1050 °C for 15 min; the austenitic phase appears in white, while the ferritic phase appears in light blue. (b) Micrograph of the same xy-plane processed with ImageJ, yielding an austenite underestimation error of 21.17%. (c) Micrograph of the same xy-plane processed with ImageJ, yielding an austenite overestimation error of 26.79%.

are required for the $10 \times 10 \times 10$ mm cubes to reach the target temperature at the core; the soaking time was defined as the interval from specimen insertion into the furnace to its extraction. A factorial plan of 2×3^2 was implemented, corresponding to 9 distinct temperature–time combinations, 18 total specimens when accounting for the two section planes (xy and zy), and 90 optical micrographs acquired overall (five per specimen). With regard to randomization, heat treatments were executed in randomized order with respect to both temperature and soaking time. In addition, not all treatments were performed on the same day, and the furnace was shut down and restarted between sessions.

4.5.2.6 Post-Processing Heat Treatment Route for PBF-LB/M UNS S32760 Specimens

Heat treatment was carried out on the PBF-LB/M UNS S32760 blanks and pillars from which the specimens for tensile, impact toughness, HCF fatigue, and fatigue-related mechanical characterization were subsequently obtained.
Except for the specimens intentionally tested in the as-built condition, the PBF-LB/M blanks were subjected to the selected post-processing heat-treatment route prior to final machining, in order to assess the mechanical response of the material after solution treatment and subsequent specimen preparation.

The solution heat treatment was performed in a muffle furnace (Manfredi Warmy 9). The thermal cycle was monitored using a type-K thermocouple positioned at the geometric centre of a representative PBF-LB/M UNS S32760 steel specimen with dimensions of 12 $\times$ 12 $\times$ 60 mm. Temperature data were recorded using a Sefram 9816B data logger with an acquisition frequency of 1 Hz. The PBF-LB/M components were introduced into the furnace only after the chamber had reached the prescribed solution heat-treatment temperature. Based on preliminary thermocouple measurements, the total holding time was set to 35 min in order to ensure an effective soaking time of 30 min at the selected treatment temperature.

A mean heating rate of 4 °C/s was recorded between 800 and 1000 °C, with a residence time of 51 s within this temperature interval. During quenching, the mean cooling rate between 1000 and 800 °C was 202 °C/s, corresponding to a residence time of approximately 1 s. On this basis, and particularly considering the very short residence time in the 1000–800 °C temperature range during quenching, the nucleation of the σ phase is considered unlikely under the adopted cooling conditions [123].

4.5.3 Preliminary DSC analysis of the as-built state

Heat-treatment temperatures and holding times were selected on the basis of differential scanning calorimetry (DSC) analyses, literature data, and previous experimental trials carried out on similar alloys. The DSC measurements were performed using a SETARAM TGA 92 instrument, applying a heating rate of 20 K/min over the temperature range from 200 °C to 1185 °C.

In particular, a comparison was performed between UNS S32760 specimens in the as-built condition, produced from powder blends with high and low nitrogen contents. The interpretation of the DSC curves and the identification of the thermal peaks were carried out with reference to the study reported by Khosnaw F. et al. [124]. In that work, the combined microstructural and thermoanalytical characterization of a specimen not obtained through a powder-metallurgy route provided useful information on the phase transformations occurring in the alloy and on their corresponding temperature ranges. The reported DSC curves were acquired using heating rates of 3 °C/min and 10 °C/min, whereas the analyses performed in the present study were carried out at 20 °C/min. Therefore, it should be considered that the transformation temperatures are affected by thermal lag, which is typical of DSC measurements performed at different heating rates. In the present case, as already highlighted in the reference study, this effect results in an apparent shift of the transformation temperatures towards higher values.

Particular attention was paid to the sharp decrease in the heat-flow signal detected at approximately 1300 K, corresponding to 1026 °C. This feature can be associated with the progressive reduction of σ-phase formation and the concurrent increase in secondary austenite γ_2 formation. This trend persists up to approximately 1500 K, where, according to the thermoanalytical interpretation, the σ phase is expected to be completely dissolved.

Figure 4.40 shows the DSC curves obtained for the investigated specimens. No significant shift in the peak temperature around 1300 K can be observed when comparing the samples produced from low-nitrogen and high-nitrogen powder blends. This evidence further supports the assumption that the same heat-treatment conditions identified for the low-nitrogen UNS S32760 condition can also be retained for the high-nitrogen UNS S32760 condition.

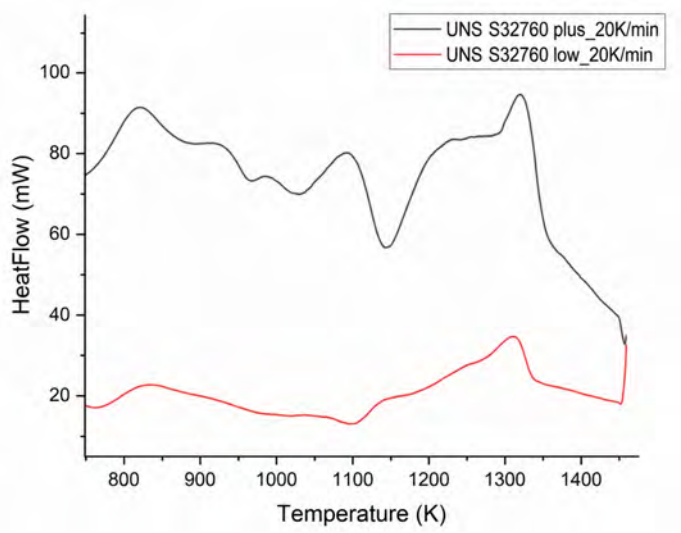

Fig. 4.40 Differential scanning calorimetry curves of as-built UNS S32760 specimens produced from low-nitrogen and high-nitrogen powder blends.

4.5.4 Influence of Heat-Treatment Parameters on the Austenite Fraction in PBF-LB/M UNS S32760 Produced from Low-Nitrogen Powders

4.5.4.1 Results of the Measurement Campaign and Data Analysis

The experimental campaign described in the previous section produce the dataset summarized in Table 4.13. These data were then subjected to statistical analysis using Minitab® software; the corresponding results are presented and discussed in the following pages.
Subsequently, for each specimen the maximum absolute deviation from the mean among the five measurements was computed and normalized by the specimen's standard deviation. By convention [122], any observation exceeding 3 σ from the mean is classified as an outlier. In the present dataset, all measurements for all specimens lay within the interval 1.2 σ to 1.8 σ.

4.5.4.2 Factorial Design Analysis: Aggregated Results

As outlined earlier, three factors were investigated. Furnace temperature took three levels: 1020 °C, 1050 °C, and 1080 °C. Soaking time also took three levels: 15,

Table 4.13 Austenite content [vol.%] measured by image analysis using ImageJ software. For each of the 18 experimental combinations described above, five measurements were performed; the corresponding mean value and standard deviation are also reported.

#	Heat Treatments	Measure 1	Measure 2	Measure 3	Measure 4	Measure 5	Mean	Std. dev.
1	1020°C, 15 min, XY plane	25.340	25.356	23.897	26.670	24.059	25.064	1.131
2	1020°C, 15 min, ZY plane	26.158	25.106	23.222	26.821	26.786	25.619	1.509
3	1020°C, 35 min, XY plane	27.382	26.599	26.453	26.645	25.355	26.487	0.728
4	1020°C, 35 min, ZY plane	27.993	27.791	27.273	27.594	27.694	27.669	0.266
5	1020°C, 65 min, XY plane	33.076	33.348	30.467	33.522	31.403	32.363	1.354
6	1020°C, 65 min, ZY plane	31.034	30.859	31.496	29.295	27.691	30.075	1.569
7	1050°C, 15 min, XY plane	22.477	24.878	22.943	21.086	22.370	22.751	1.374
8	1050°C, 15 min, ZY plane	18.747	19.482	18.830	18.652	23.103	19.763	1.895
9	1050°C, 35 min, XY plane	26.137	27.005	23.825	25.520	24.563	25.410	1.256
10	1050°C, 35 min, ZY plane	25.696	24.108	24.459	26.772	26.154	25.438	1.128
11	1050°C, 65 min, XY plane	27.603	25.604	25.283	24.318	26.206	25.803	1.216
12	1050°C, 65 min, ZY plane	26.847	23.687	25.086	26.156	23.211	24.997	1.556
13	1080°C, 15 min, XY plane	21.663	19.493	23.643	23.047	22.051	21.979	1.596
14	1080°C, 15 min, ZY plane	24.683	21.699	23.978	24.149	22.016	23.305	1.351
15	1080°C, 35 min, XY plane	26.533	23.981	24.701	23.853	24.635	24.741	1.071
16	1080°C, 35 min, ZY plane	25.587	22.935	21.213	21.652	20.570	22.391	1.985
17	1080°C, 65 min, XY plane	29.238	25.553	27.690	27.573	26.061	27.223	1.461
18	1080°C, 65 min, ZY plane	25.205	25.570	25.476	24.377	25.237	25.173	0.471

35, and 65 minutes. The measurement plane was a two-level categorical factor with sections xy and zy. The first two factors are quantitative, whereas the third is qualitative. Two alternative regression strategies were considered for modeling the factorial design:

1. Treating each individual field of view on a specimen as a replicate, yielding five replicates for each response;
2. Using the mean of the five fields of view, resulting in a single replicate for each factorial response.

The results reported below refer to the dataset aggregated by specimen, that is, using the mean across the five replicates.

4.5.4.3 ANOVA and Linear Regression on the aggregated dataset

The analysis of variance for the factorial design is presented in Table 4.14. Temperature (T) is statistically significant at the 98.4% confidence level, and the soaking time is significant at the 98.6% confidence level. The measurement plane does not exhibit a significant effect on the response. No statistically significant interaction terms were detected among the factors. An R^2 of 94.33% and an adjusted R^2_{adj} of 75.90% indicate that the fitted regression provides a reasonable approximation of the phenomena

The residual probability plot, shown in Figure 4.41, indicates that the errors are approximately normally distributed, suggesting no systematic departures from the model. The residuals-versus-fitted plot shows a random scatter with no discernible trend, consistent with homoscedastic and independent errors. Together, these diagnostics support the adequacy of the model and suggest that no additional statistically significant structure has been omitted.

Table 4.14 ANOVA of the factorial design based on aggregated data, and accuracy metrics of the fitted regression model.

Analysis of Variance

Source	DF	Adj SS	Adj MS	F-Value	P-Value
Model	13	136.640	10.5108	5.12	0.064
Linear	5	122.222	24.4445	11.90	0.016
T	2	57.745	28.8723	14.06	0.016
time	2	61.443	30.7215	14.96	0.014
plane	1	3.035	3.0348	1.48	0.291
2-Way Interactions	8	14.418	1.8023	0.88	0.596
T*time	4	11.669	2.9172	1.42	0.371
T*plane	2	0.954	0.4769	0.23	0.803
time*plane	2	1.796	0.8978	0.44	0.673
Error	4	8.214	2.0535		
Total	17	144.855			

Model Summary

S	R-sq	R-sq(adj)	R-sq(pred)
1.43302	94.33%	75.90%	0.00%

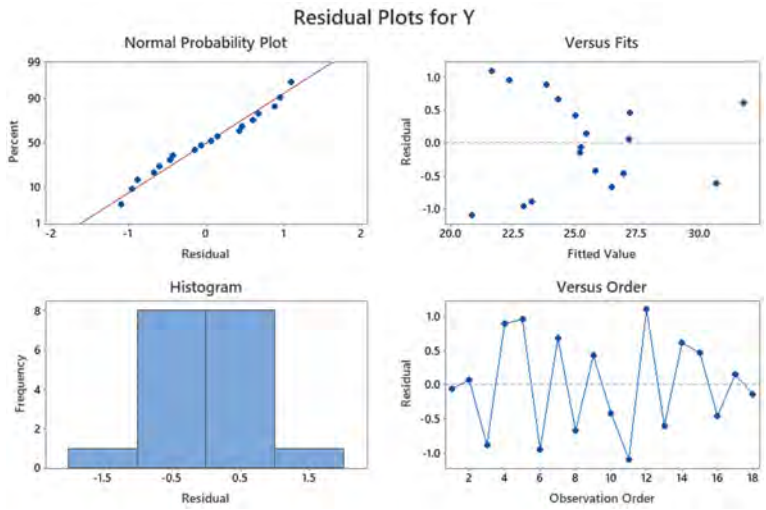

Fig. 4.41 Residual analysis of the regression model for the aggregated dataset.

From the factorial plot in Figure 4.42, the response varies approximately linearly with furnace soaking time. The measurement plane exhibits a negligible effect on the response, as evidenced by the near-zero slope. The temperature–response plot indicates that temperature is statistically significant between the lowest and intermediate levels, whereas the effect effectively vanishes above the intermediate level. In contrast, the interaction plot in Figure 4.43 hints at a possible temperature–time interaction, most apparent at the intermediate soakingtime; however, this interaction does not achieve significance at conventional confidence levels and should be regarded as tentative.

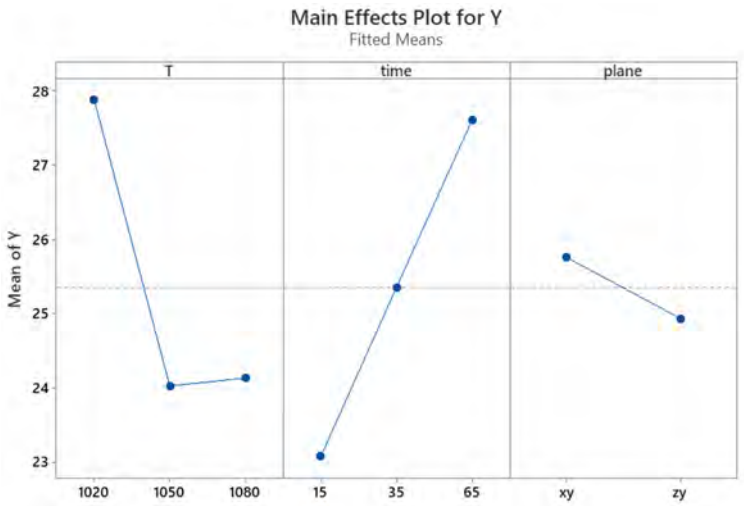

Fig. 4.42 Factorial plot of response Y (austenite fraction, %) for the aggregated dataset.

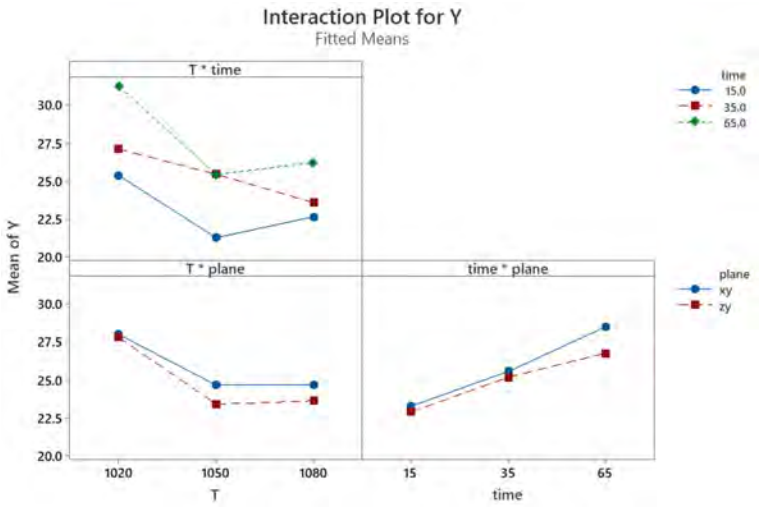

Fig. 4.43 Interaction plot of response Y (austenite fraction, %) for the aggregated dataset.

4.5.4.4 Response surface analysis based on the aggregated dataset

A response surface is introduced as a continuous tool to estimate the response within the sample space. The stepwise method was applied with the aim of minimizing the number of parameters. In Table 4.15, the parameters and the ANOVA analysis of the obtained response surface are reported. It is observed that the regression model approximates the phenomena with an adjusted R-squared of 77.77%, indicating a good approximation. From the regression equation it is also observed that it is linear with respect to time, whereas it depends quadratically on temperature. It is further observed that the plane factor is not retained by the stepwise model, a result expected in light of the analysis of variance presented previously.

Table 4.15 ANOVA of the response surface based on aggregated data, and accuracy metrics of the fitted regression model.

Coded Coefficients

Term	Coef	SE Coef	T-Value	P-Value	VIF
Constant	24.176	0.563	42.98	0.000	
T	-1.872	0.397	-4.71	0.000	1.00
time	2.232	0.395	5.66	0.000	1.00
T*T	1.981	0.688	2.88	0.012	1.00

Model Summary

S	R-sq	R-sq(adj)	R-sq(pred)
1.37640	81.69%	77.77%	69.68%

Analysis of Variance

Source	DF	Adj SS	Adj MS	F-Value	P-Value
Model	3	118.33	39.444	20.82	0.000
Linear	2	102.64	51.321	27.09	0.000
T	1	42.05	42.055	22.20	0.000
time	1	60.59	60.587	31.98	0.000
Square	1	15.69	15.690	8.28	0.012
T*T	1	15.69	15.690	8.28	0.012
Error	14	26.52	1.894		
Total	17	144.85			

Regression Equation in Uncoded Units

$$Y = 2512 - 4.68\,T + 0.0893\,time + 0.002201\,T * T$$

From the contour plot of the response surface shown in Figure 4.44, the austenite fraction in the specimen (Y), reaches a minimum for a treatment time of 15 minutes at a temperature of approximately 1065 °C, with a concentration below 22%. Conversely, the austenite content is maximized when the heat treatment is performed at the lowest temperature level and the longest soaking time, yielding a concentration greater than 30%. The surface plot in the design space is presented in Figure 4.45. It is observed that the phenomena is linear with respect to heat-treatment time, and that the maximum austenite concentration occurs at one extreme of the reference plane.

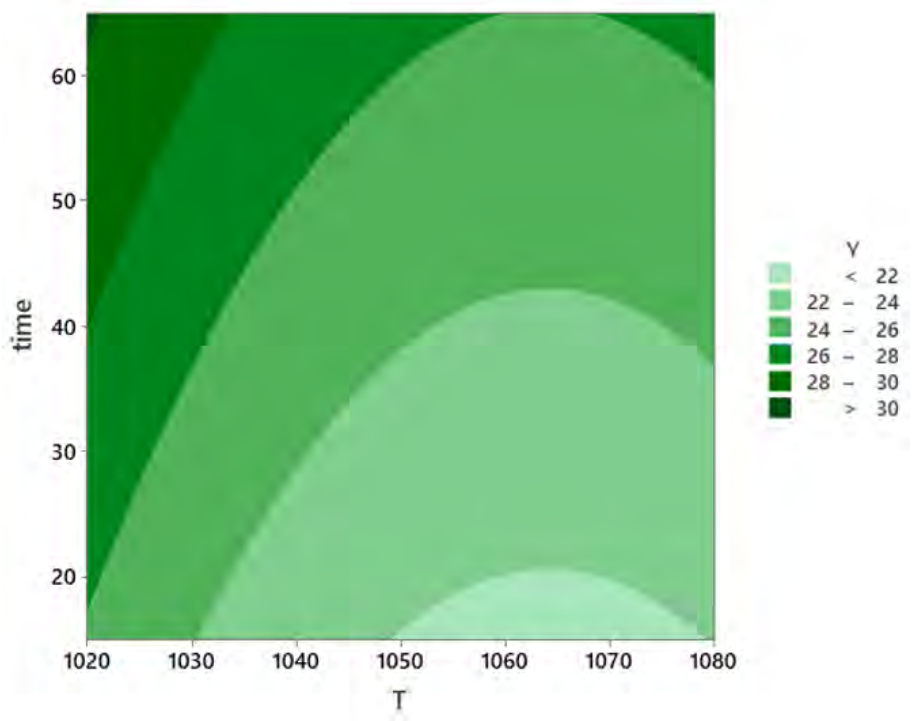

Fig. 4.44 Contour plot of the response surface for the aggregated dataset.

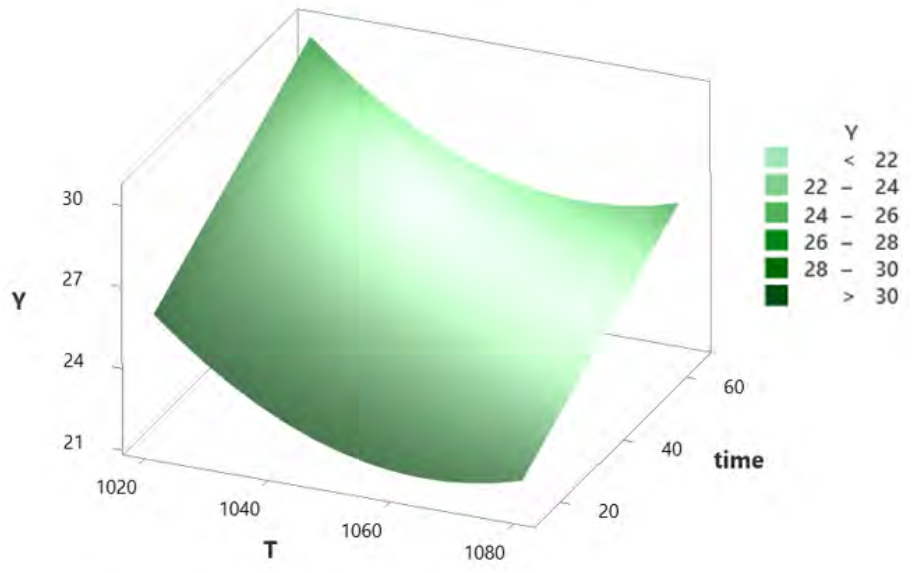

Fig. 4.45 Response surface of the investigated phenomena in the reference space, derived from the aggregated dataset.

4.5.4.5 Factorial Design Analysis: All individual data

Given the results obtained from the analysis of the averaged data, and considering that the interaction plots for the response suggest the possible presence of effects beyond those identified at this stage, the analysis of the factorial design and the response surface was repeated using the complete dataset of 90 observations (Table 4.13), treating the five measurements per specimen as five experimental replicates. The target is to determine whether additional contributions exist beyond those identified thus far.

Table 4.16 presents the ANOVA of the factorial design with replicates. In addition to the effects previously identified (Table 4.14), the measurement-plane factor emerges as significant at the 99.1% confidence level. A time–temperature interaction is also significant, with confidence exceeding 99.9%. The computed adjusted R^2_{adj} higher than in the preceding analysis (Table 4.14). In this case as well, as shown in Figure 4.46, the residuals are approximately normally distributed, and no underlying statistical structure not captured by the model is evident.

Table 4.16 ANOVA of the factorial design based on all single data, and accuracy metrics of the fitted regression model.

Analysis of Variance

Source	DF	Adj SS	Adj MS	F-Value	P-Value
Model	17	701.641	41.273	19.47	0.000
Blocks	4	18.438	4.610	2.17	0.080
Linear	5	611.112	122.220	57.65	0.000
T	2	288.723	144.362	68.10	0.000
time	2	307.215	153.607	72.46	0.000
plane	1	15.174	15.174	7.16	0.009
2-Way Interactions	8	72.090	9.011	4.25	0.000
T*time	4	58.344	14.586	6.88	0.000
T*plane	2	4.769	2.384	1.12	0.330
time*plane	2	8.978	4.489	2.12	0.128
Error	72	152.640	2.120		
Total	89	854.281			

Model Summary

S	R-sq	R-sq(adj)	R-sq(pred)
1.45602	82.13%	77.91%	72.08%

4.5.4.6 Response surface analysis based on all individual data

Analogously to the previous case, a response-surface model is introduced. Since the ANOVA revealed a significant effect of the measurement plane, a distinct surface is expected for each plane. The stepwise method was again applied with the aim of

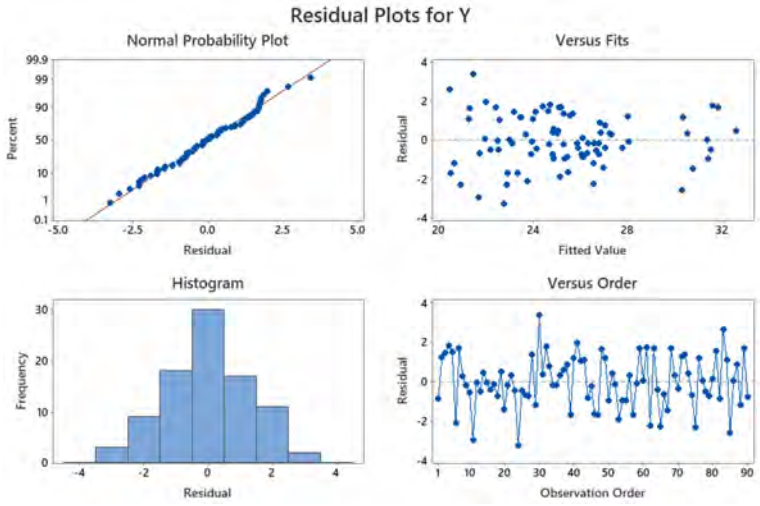

Fig. 4.46 Residual analysis of the regression model using all individual data.

minimizing the number of parameters. Table 4.17 reports the coefficients and the ANOVA for the fitted response surfaces. In addition to the quadratic contribution of temperature noted earlier, a second-order temperature–time term is present, together with a significant time–plane interaction. However, the adjusted R^2_{adj} is lower than in the preceding case, indicating that the model is not necessarily more accurate in approximating the phenomena, or that additional, unidentified effects may be operative, or that some acquired data may be misleading.

From the contour plots of the fitted response surfaces in Figure 4.47, the austenite content attained on the xy plane is generally higher than that on the zy plane, while the overall surface topology remains substantially similar between the two sections. The global trend of austenite content with respect to temperature and soaking time is consistent with the findings from the previous analysis. Figure 4.47 presents the corresponding response surfaces in the design space. In this case as well, the two surfaces exhibit essentially the same shape, with one appearing as an upward translation of the other.

Table 4.17 ANOVA of the response surface based on all individual data, and accuracy metrics of the fitted regression model.

Coded Coefficients

Term	Coef	SE Coef	T-Value	P-Value	VIF
Constant	24.176	0.296	81.60	0.000	
Blocks					
1	0.842	0.342	2.46	0.016	1.60
2	-0.178	0.342	-0.52	0.605	1.60
3	-0.351	0.342	-1.03	0.308	1.60
4	0.081	0.342	0.24	0.814	1.60
T	-1.911	0.210	-9.10	0.000	1.01
time	2.232	0.208	10.74	0.000	1.00
plane					
xy	0.434	0.171	2.53	0.013	1.01
T*T	1.981	0.362	5.46	0.000	1.00
T*time	-0.584	0.255	-2.29	0.024	1.01
time*plane					
xy	0.354	0.208	1.70	0.093	1.01

Analysis of Variance

Source	DF	Adj SS	Adj MS	F-Value	P-Value
Model	10	646.714	64.671	24.61	0.000
Blocks	4	18.438	4.610	1.75	0.146
Linear	3	537.476	179.159	68.19	0.000
T	1	217.683	217.683	82.85	0.000
time	1	302.937	302.937	115.30	0.000
plane	1	16.856	16.856	6.42	0.013
Square	1	78.449	78.449	29.86	0.000
T*T	1	78.449	78.449	29.86	0.000
2-Way Interaction	2	21.441	10.720	4.08	0.021
T*time	1	13.837	13.837	5.27	0.024
time*plane	1	7.604	7.604	2.89	0.093
Error	79	207.567	2.627		
Total	89	854.281			

Model Summary

S	R-sq	R-sq(adj)	R-sq(pred)
1.62094	75.70%	72.63%	68.78%

Regression Equation in Uncoded Units

plane	
xy	$Y = 2481 - 4.654\,T + 0.921\,time + 0.002201\,T*T - 0.000779\,T*time$
zy	$Y = 2481 - 4.654\,T + 0.893\,time + 0.002201\,T*T - 0.000779\,T*time$

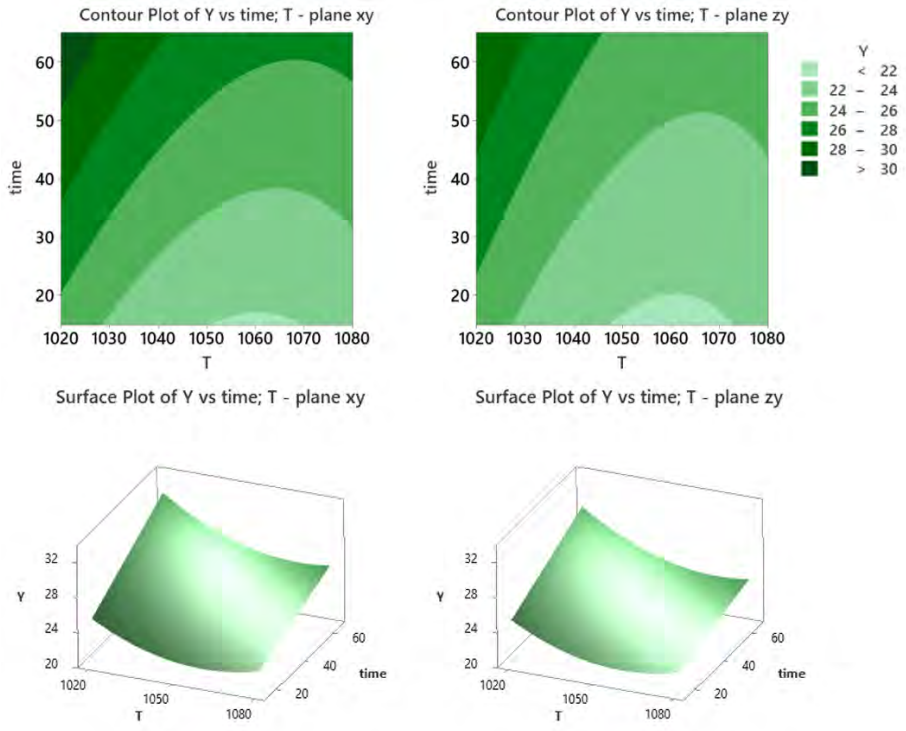

Fig. 4.47 Contour plot of the response surface obtained using all individual data and corresponding response surface of the investigated phenomena in the reference space. Y denotes the response, expressed as austenite content (%).

4.5.5 Conclusions on the Influence of Heat-Treatment Parameters on the Austenite Fraction in PBF-LB/M UNS S32760 Produced from Low-Nitrogen Powders

Analysis of the factorial design by ANOVA on averaged responses (mean values of Table 4.13) indicates that the austenite fraction is governed primarily by heat-treatment temperature and soaking time, whereas the sectioning plane does not exert a statistically significant effect on the measured austenite content.

Temperature exerts a measurable influence up to the intermediate level of 1050 °C; at higher temperatures the austenite fraction becomes effectively insensitive to further increases in temperature. This trend implies that, within the interval 1020–1050 °C, the transformation kinetics of austenite to ferrite become dominant over the reformation of secondary austenite from metastable ferrite, and the global austenite content decreases as a consequence. The monotonic increase of austenite with soaking time at each investigated solution-treatment temperature indicates that the ferrite-to-secondary-austenite reaction is markedly rate-limited; in the literature this kinetics has been associated with the elevated tungsten content characteristic of UNS S32760 super duplex steel [125].

A response-surface model was developed to provide a continuous approximation of the phenomena over the experimental domain. The dependence on time is well captured by a linear term, while temperature contributes quadratically. The model predicts that the maximum austenite fraction lies at the boundaries of the explored space. The analysis of averaged data nevertheless suggested the possible presence of additional effects; therefore, an ancillary analysis was performed on the unpooled measurements (Table 4.13), treating each micrograph as a replicate. This revealed statistically significant contributions from the sectioning plane and a temperature–time interaction. With regard to the plane effect, it should be noted that the yz plane entails greater measurement complexity, which can increase uncertainty; indeed, this significance vanishes when the data are averaged.

From the response-surface perspective, maximizing the austenite fraction would motivate extending the exploration toward lower treatment temperatures and longer soaking times, in order to localize the global maximum. However, temperatures below 1020 °C were not pursued, since preliminary trials at 1000 °C evidenced precipitation of intermetallic sigma phase, which is strongly embrittling and detrimental

to corrosion resistance [123, 82]. Extending the dwell time at 1020 °C beyond 65 minutes may represent a viable strategy to further increase the austenite content, but additional assessment of austenite morphology is required. Excessive soaking can coarsen the characteristically fine PBF-LB/M microstructure, leading to a competition between toughness gains due to a higher austenite fraction and toughness losses associated with microstructural coarsening.

4.6 Mechanical testing and characterization

4.6.1 Introduction

The mechanical behaviour of PBF-LB/M UNS S32760 super duplex stainless steel was investigated through tensile testing and Charpy V-notch impact testing. Both test campaigns were carried out at room temperature and at -46 °C, in order to evaluate the response of the material under standard and low-temperature service-relevant conditions. The investigated conditions included specimens produced from low- and high-nitrogen powder blends, different build orientations, and different post-process heat-treatment states, with the aim of correlating mechanical performance with microstructural evolution, phase balance, and process-induced anisotropy.

Room-temperature tensile tests were performed to assess the static mechanical properties of the material and to verify the compliance of the investigated conditions with the minimum requirements specified by NORSOK M-630 [126], a standard commonly adopted for duplex and super duplex stainless steels intended for Oil and Gas applications. Charpy V-notch impact tests at -46 °C were also carried out in relation to the same qualification framework, since low-temperature impact toughness represents a critical requirement for materials used in severe environments.

Additional tensile tests at -46 °C were performed to directly determine the mechanical parameters of the material, namely $R_{p0.2}$, R_m, and E, under the same thermal conditions envisaged for possible future low-temperature CTOD tests as an extension of the present research. These data are particularly relevant for the qualification of PBF-LB/M UNS S32760 in critical applications, where defect tolerance and fracture resistance are key design requirements, as commonly required in the Oil and Gas sector and in the emerging use of this class of materials for biomedical applications. The direct determination of tensile properties at low temperature also avoids relying on room-temperature data conversion, which may not be fully applicable to PBF-LB/M-processed UNS S32760 due to its specific microstructural condition and limited availability of consolidated temperature-dependent mechanical data.

4.6.2 Materials and Methods

4.6.2.1 PBF-LB/M Processing conditions and Applied Heat Treatment

The samples were manufactured using the Aconity Mini 3D PBF-LB/M system [119], adopting the optimized process parameters, consisting of a laser power of 300 W and a scanning speed of 900 mm/s, as discussed in Section 4.4 and summarized in Table 4.11.

Mechanical testing was performed on specimens produced from both low-nitrogen and high-nitrogen powder blends. For the low-nitrogen material, the investigated conditions included the as-built state and the solution-treated states obtained at 1020 °C for 35 min and 1080 °C for 35 min. The condition treated at 1020 °C for 35 min was specifically included to assess the influence of sigma-phase precipitation on the mechanical response of the PBF-LB/M material. In contrast, the condition treated at 1080 °C for 35 min was selected as the reference heat-treatment condition on the basis of the microstructural and corrosion results discussed in Section 4.8.

For the high-nitrogen powder blend, mechanical testing was performed in the as-built condition and after solution treatment at 1080 °C for 35 min. The latter condition was selected to evaluate the mechanical response of the nitrogen-enriched material after the heat treatment identified as the most favourable practical compromise within the investigated processing window.

4.6.2.2 Tensile specimen preparation and Testing procedure

Cylindrical tensile specimens were machined by turning from horizontal and vertical PBF-LB/M cylindrical blanks. Representative vertical blanks, built with their longitudinal axis parallel to the build-direction axis (Z) of the PBF-LB/M system, are shown in Figure 4.48. The final tensile specimen geometry, prepared in accordance with the reference standard [127] and based on the specific technical drawing adopted in this work [128], is reported in Figure 4.49. Except for those tested in the as-built condition, all blanks were heat treated according to the conditions reported in sub-section 4.5.2.6 prior to final machining, in order to evaluate the mechanical response of the material under the selected post-process conditions.

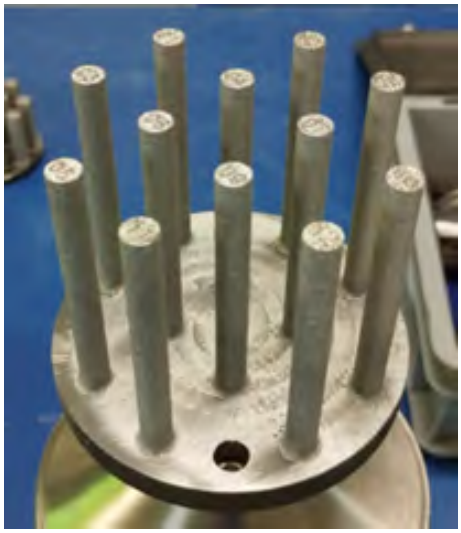

Fig. 4.48 PBF-LB/M cylindrical blanks used for the machining of tensile specimens. The blanks shown in the figure were produced in the vertical orientation, with their longitudinal axis parallel to the build-direction axis (Z) of the PBF-LB/M system. After heat treatment, when required, the final cylindrical tensile specimens were obtained by turning.

4.6.2.3 Charpy V-Notch specimen preparation and Impact-Testing procedure

Charpy V-notch specimens were machined from PBF-LB/M parallelepiped blanks produced in both build orientations. Representative vertical blanks, built with their longitudinal axis parallel to the build-direction axis (Z) of the PBF-LB/M system, are shown in Figure 4.50. The specimens were heat treated according to the conditions reported in sub-section 4.5.2.6 before final machining, except for those tested in the as-built condition, and prepared with a geometry in accordance with the reference standard [129]. The notch was produced by grinding rather than broaching, since broaching may introduce local alterations at the notch root, potentially affecting crack nucleation and reducing test repeatability [130]. For both tensile and Charpy impact tests, two repetitions were performed for each investigated condition.

Tensile tests were carried out using a Zwick/Roell Z100 universal testing machine equipped with a Zwick/Roell BTC-EXMACRO.001 macro-extensometer. The tests were performed by imposing a strain rate of 1 s^{-1} [131], as defined in the reference standard [132] for the specific tensile specimen geometry adopted in this study. Room-temperature tests were conducted at approximately 22 °C, whereas low-temperature tests were performed at −46 °C. For the latter, the specimens were first

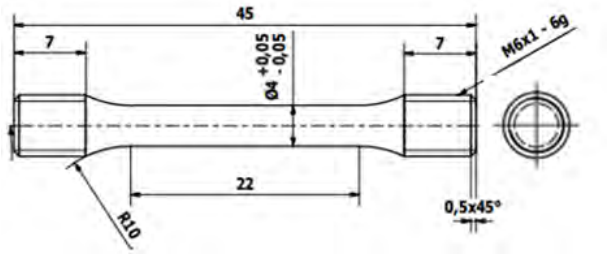

Fig. 4.49 Geometry of the cylindrical tensile specimens [128] used for the mechanical characterization of PBF-LB/M UNS S32760, prepared in accordance with the reference standard [127] . The specimens were machined by turning from cylindrical blanks produced in horizontal and vertical build orientations.

cooled using an Espec ARS-0390 climatic chamber and subsequently acclimatized for an additional 15 min in the climatic chamber integrated with the tensile testing machine before testing, as shown in Figure 4.51.

Charpy V-notch impact tests were performed using a Zwick/Roell RKP 450 instrumented Charpy pendulum operated in the 300 J configuration and equipped with an instrumented striker having a 2 mm tip radius, corresponding to the KV2 configuration. Tests were carried out at room temperature and at -46 °C. For low-temperature impact testing, the specimens were cooled to -46 °C using an Espec ARS-0390 climatic chamber. The transfer time between the climatic chamber and the Charpy pendulum was kept below 5 s, in accordance with the applicable standard requirements [133].

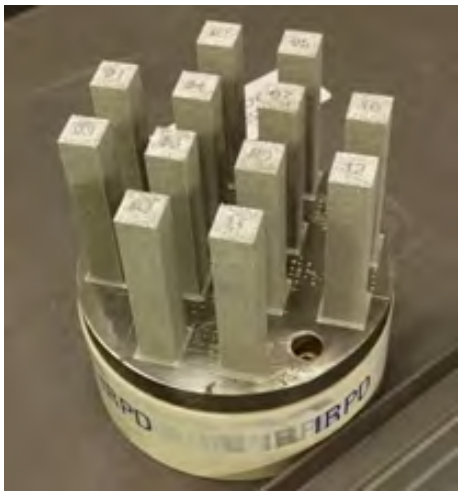

Fig. 4.50 PBF-LB/M parallelepiped blanks used for the machining of Charpy V-notch impact specimens. The blanks shown in the figure were produced in the vertical orientation, with their longitudinal axis parallel to the build-direction axis (Z) of the PBF-LB/M system. After heat treatment, when required, the final notched specimens were machined from these blanks.

Fig. 4.51 Low-temperature tensile test setup used for testing the PBF-LB/M UNS S32760 specimens at -46 °C. The specimen was mounted in the grips of the tensile testing machine inside the climatic chamber and acclimatized for an additional 15 min before testing, in order to ensure thermal stabilization under the selected test conditions. The specimen temperature was monitored throughout the entire test by means of a thermocouple.

4.6.3 Charpy Impact Test Results

4.6.3.1 Charpy impact test results of specimens produced from the low-nitrogen powder mixture

The Charpy impact tests highlight, as expected, a marked dependence of the absorbed energy not only on the heat-treatment condition but also on the manufacturing route. As shown by the results obtained on specimens produced from the low-nitrogen powder mixture and built in the horizontal orientation, reported in Table 4.18, the as-built condition exhibits an overall poor response, consistently with the absence of austenite observed in the analysed cross-sections.

At 22 °C, the as-built H1 and H2 specimens absorbed 49 and 62 J, respectively, with corresponding lateral expansion values of 0.59 and 0.78 mm. These values are markedly lower than those obtained after heat treatment at 1080 °C. The difference between H1 and H2 also suggests a certain sensitivity to the orientation of the notch plane, since the specimen notched on the zx plane exhibited a higher absorbed energy than that notched on the xy plane. This behaviour may be associated with the different interaction between the crack propagation front, the PBF-LB/M build direction, the melt-pool morphology, possible preferentially oriented defects, and the resulting microstructural anisotropy. On the basis of this evidence, it was decided to test the remaining specimens under the most severe testing condition, namely with the notch located on the xy plane.

The heat treatment performed at 1020 °C for 35 min increased the average austenite fraction to 27 vol.%; however, the improvement in toughness remained relatively limited due to the significant presence of the sigma intermetallic phase (1.5 vol.%). At 22 °C, specimens H3 and H4 exhibited absorbed energies of 70 and 83 J, respectively. The increase in performance with respect to the as-built condition indicates that the restoration of a duplex microstructure positively contributes to the energy absorption capability.

The heat treatment at 1080 °C represented the most effective condition for the horizontally built low-nitrogen specimens. At 22 °C, specimens H5 and H6 reached absorbed energies of 166 and 171 J, with lateral expansions of 1.70 and 1.80 mm, respectively. Compared with the as-built condition, the average absorbed energy increased by approximately three times, rising from a mean value of 56 J to 169 J. A very pronounced increase was also observed with respect to the treatment at 1020

°C. The high lateral expansion measured in these specimens indicates greater plastic deformation before and during crack propagation, consistently with a more ductile fracture mode.

The effect of the testing temperature is evident. In the horizontally built low-nitrogen specimens, decreasing the temperature from 22 °C to -46 °C resulted in a significant reduction in absorbed energy under all investigated conditions. The as-built condition showed the most critical behaviour, with absorbed energies of 14 and 25 J and very low lateral expansion values of 0.17 and 0.25 mm. These results indicate a strong tendency towards brittle fracture at low temperature, consistently with a microstructure lacking austenite and therefore dominated by a ferritic matrix, which is less effective in relaxing stress concentrations at the notch tip. The specimens heat-treated at 1020 °C also exhibited a limited response at -46 °C, with absorbed energies of 29 and 37 J.

Conversely, the specimens heat-treated at 1080 °C retained high impact toughness values even at -46 °C. Specimens H11 and H12 absorbed 130 and 134 J, respectively, with lateral expansions of 1.24 and 1.36 mm. Although a decrease with respect to the tests performed at 22 °C was observed, it remained relatively limited when compared with the other testing conditions. Indeed, the average absorbed energy decreased from 168 J to 132 J, corresponding to a reduction of approximately 22%. This result indicates that the microstructure obtained at 1080 °C is able to preserve good toughness even at -46 °C, limiting the transition towards brittle behaviour. The combination of high absorbed energy and lateral expansion above 1 mm confirms the significant contribution of plastic deformation to the fracture process.

The force–time traces acquired during the tests shown in Figure 4.52 for the low-nitrogen specimens confirm the trends observed from the data reported in Table 4.18. At 22 °C, the as-built specimens and those heat-treated at 1020 °C exhibit a response characterised by a force peak followed by a rapid load drop, indicating relatively unstable crack propagation and a limited ability to sustain further deformation after crack initiation. In contrast, the specimens heat-treated at 1080 °C show a more extended post-peak stage and a longer tail in the curve, highlighting a more progressive and energy-dissipative fracture process.

At -46 °C, this difference becomes even more pronounced. In the curves of the as-built specimens and of those treated at 1020 °C, the force decreases abruptly after the peak, whereas the specimens heat-treated at 1080 °C retain a more gradual load

decay, with a significantly longer impact event duration. This behaviour is consistent with the higher energy absorbed during crack propagation.

4.6.3.2 Charpy impact test results of specimens produced from the high-nitrogen powder mixture

With regard to the specimens produced from the high-nitrogen powder mixture and built in the vertical orientation, whose results are reported in Table 4.19, the absolute absorbed energy values are lower than those obtained for the low-nitrogen specimens built horizontally and heat-treated at 1080 °C. This comparison, however, must be interpreted with great caution, since the two series differ in terms of build orientation.

Vertical building is generally unfavourable for impact toughness, since it may promote a more critical crack propagation path with respect to the build direction, while also increasing the relevance of interlayer defects, lack-of-fusion discontinuities, track-boundary imperfections, and anisotropy associated with the layer-wise PBF-LB/M architecture [94]. In this case, therefore, the positive effect of the higher nitrogen content and the consequent enhanced austenite stabilisation is counterbalanced by the detrimental effect of the vertical orientation, further highlighting the fundamental importance of the initial PBF-LB/M layer deposition process.

In the as-built condition, the high-nitrogen vertically built specimens V01 and V02 both show an absorbed energy of 33 J at 22 °C, with lateral expansions of 0.19 and 0.21 mm, respectively. These values are lower than those measured for the low-nitrogen horizontally built as-built specimens. This result is not interpreted as a direct detrimental effect of nitrogen, but rather as a consequence of the different specimen architecture with respect to the build direction. The vertical orientation appears to prevail over the possible compositional benefit, leading to a more brittle impact response and to very limited lateral deformation.

The heat treatment at 1080 °C markedly improves the response of the high-nitrogen vertical specimens as well. Nevertheless, the absorbed energies remain considerably lower than those measured for the low-nitrogen horizontal specimens heat-treated at 1080 °C. This further confirms that build orientation and the direction of the notch plane play a fundamental role in the Charpy impact response of PBF-LB/M materials.

At -46 °C, the high-nitrogen vertical specimens heat-treated at 1080 °C show a decrease in absorbed energy, with values of 36 and 43 J, and lateral expansion ranging from 0.43 to 0.49 mm. The reduction with respect to 22 °C is significant, although it does not lead to a complete collapse of the mechanical response. The average absorbed energy decreases from 60 J to 40 J. However, the response is clearly less tough than that of the low-nitrogen horizontal specimens treated at the same temperature, for which the absorbed energy at -46 °C exceeds 130 J.

The force–time curves of the high-nitrogen specimens built in the vertical orientation are reported in Figure 4.53. At 22 °C, the as-built specimens exhibit a relatively high force peak, followed by a rapid load drop, indicating fracture with limited stable crack propagation.

After heat treatment at 1080 °C, curves V03 and V04 show a slightly more progressive load decay and a longer impact duration compared with the as-built condition. However, the extent of the post-peak stage remains markedly lower than that observed for the low-nitrogen horizontal specimens heat-treated at 1080 °C, reported in Figure 4.52. At -46 °C, curves V05 and V06 are characterised by short impact events, with rapid attainment of the peak load followed by a sharp load decrease, confirming the limited ability of the vertically built configuration to sustain ductile crack propagation.

Overall, the results indicate that the heat treatment at 1080 °C for 35 min proved to be, among the investigated conditions, the most effective one for increasing the impact toughness of PBF-LB/M UNS S32760 specimens. In the low-nitrogen specimens built horizontally, this treatment enabled the highest absorbed energy values to be achieved, both at room temperature and at -46 °C. This result is particularly relevant also with respect to the requirements specified by the NORSOK M-630 standard [126], which is commonly adopted for duplex and super duplex stainless steels intended for oil and gas applications. For forged components subjected to Charpy V-notch testing at -46 °C, this standard requires a minimum absorbed energy of 45 J as an average value and 35 J as the minimum individual value. The comparison between the experimental results and these threshold values shows that both the as-built condition and the condition treated at 1020 °C for 35 min do not meet the required specifications.

The best response was obtained for the low-nitrogen specimens built horizontally and heat-treated at 1080 °C for 35 min, which exhibited the highest absorbed energies

and the greatest lateral expansions. This condition is also the only one, among those evaluated for the horizontal specimens tested at -46 °C, that fully satisfies the toughness requirements prescribed by NORSOK M-630 [126].

The comparison with the high-nitrogen specimens built vertically suggests, instead, that the higher nitrogen content and the consequent stabilisation of austenite are not sufficient to compensate for the detrimental effect arising from the vertical build orientation. The higher nitrogen content promotes a greater austenite fraction and a finer, less anisotropic morphology, thereby favouring improved toughness, as highlighted by the comparison between the microstructures shown in Figure 4.58. However, in the experimental configuration analysed here, these potential benefits are impaired by the vertical build direction, which makes crack propagation much more sensitive to the layer-wise architecture and to the discontinuities characteristic of the PBF-LB/M process. Therefore, the direct comparison between the two series does not allow the effect of nitrogen content to be unambiguously isolated, but rather clearly demonstrates that the impact toughness of super duplex stainless steel components produced by PBF-LB/M results from the complex interaction among composition, heat treatment, phase morphology, the presence of intermetallic phases such as sigma, build orientation, and loading direction with respect to the PBF-LB/M build axis.

The high-nitrogen specimens built vertically show an improvement after heat treatment at 1080 °C, but still retain lower impact toughness values, confirming the dominant role of build orientation in the impact response. These results therefore underline the need to jointly optimise the build strategy and the post-processing heat treatment in order to achieve full compliance with the application requirements for severe service conditions, such as those specified by NORSOK M-630 for oil and gas applications [126].

Table 4.18 Summary of Charpy impact test results for PBF-LB/M UNS S32760 specimens produced from a blend of low-nitrogen powders, with the specimen longitudinal axis perpendicular to the growing Z axis (horizontal direction), and tested under different heat-treatment conditions and test temperatures. The reported average austenite values, determined by XRD, refer to the corresponding heat-treated condition. Lateral expansion values were determined according to ASTM E23 standard [129].

ID	Build direction	HT state	HT time	Austenite [vol.%] on plane	Test temp.	Notch plane	Energy [J]	Energy [J/cm^2]	Lateral expansion [mm]
H1	Horiz.	as-built	–	0	22°C	xy	49	64	0.59
H2		as-built	–	0		zx	62	79	0.78
H3		1020°C	35 min	plane xy: 26.5 ± 0.7		xy	70	89	0.90
H4		1020°C		plane zy: 27.7 ± 0.3			83	105	1.16
H5		1080°C		plane xy: 24.7 ± 1.1			166	208	1.70
H6		1080°C		plane zy: 22.4 ± 2.0			171	213	1.80
H7		as-built	–	0	-46°C	xy	14	18	0.17
H8		as-built	–	0			25	33	0.25
H9		1020°C	35 min	plane xy: 26.5 ± 0.7			29	37	0.33
H10		1020°C		plane zy: 27.7 ± 0.3			37	47	0.45
H11		1080°C		plane xy: 24.7 ± 1.1			130	163	1.24
H12		1080°C		plane zy: 22.4 ± 2.0			134	168	1.36

Table 4.19 Summary of Charpy impact test results for PBF-LB/M UNS S32760 specimens produced from a blend of high-nitrogen powders, with the specimen longitudinal axis parallel to the growing Z axis (vertical direction), and tested under different heat-treatment conditions and test temperatures. The reported average austenite values, determined by XRD, refer to the corresponding heat-treated condition. Lateral expansion values were determined according to ASTM E23 standard [129].

ID	Build direction	HT state	HT time	Austenite [vol.%] on plane	Test temp.	Notch plane	Energy [J]	Energy [J/cm^2]	Lateral expansion [mm]
V01	Vert.	as-built	–	plane xy: 21.1 ± 1.2		zx	33	42	0.19
V02		as-built	–	plane zy: 22.5 ± 1.6	22°C		33	42	0.21
V03		1080°C	35 min	plane xy: 61.7 ± 2.7 plane zy: 60.5 ± 2.7	22°C		58	73	0.79
V04		1080°C			22°C		61	76	0.80
V05		1080°C			-46°C		36	51	0.49
V06		1080°C			-46°C		43	54	0.43

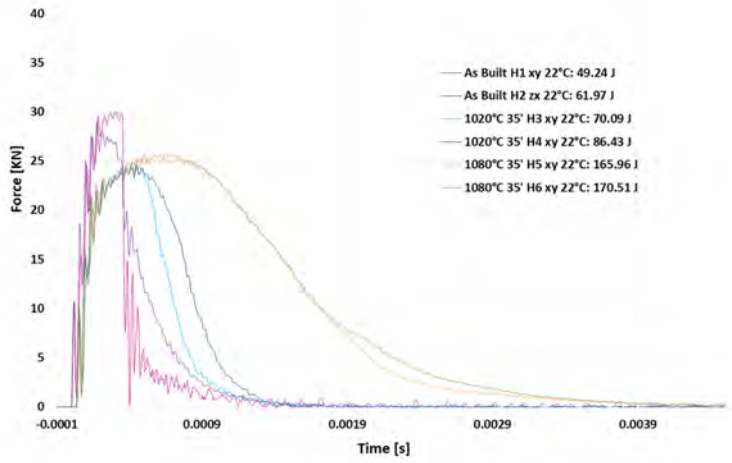

(a) Notched PBF-LB/M UNS S32760 specimens produced from a low-nitrogen powder blend. Specimens longitudinal axis perpendicular to growing Z axis (horizontal direction). Tested at 22°C.

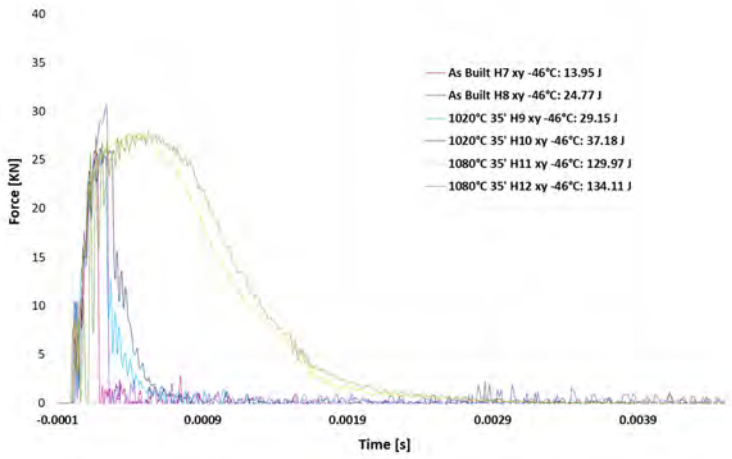

(b) Notched PBF-LB/M UNS S32760 specimens produced from a low-nitrogen powder blend. Specimens longitudinal axis perpendicular to growing Z axis (horizontal direction). Tested at -46°C.

Fig. 4.52 Force–time curves acquired using an instrumented Charpy pendulum equipped with a 2 mm radius striker during impact testing of notched PBF-LB/M UNS S32760 specimens produced from a low-nitrogen powder blend, specimens longitudinal axis perpendicular to growing Z axis (horizontal direction). Tested at 22°C and −46°C. The data corresponding to the individual curves are reported in Table 4.18.

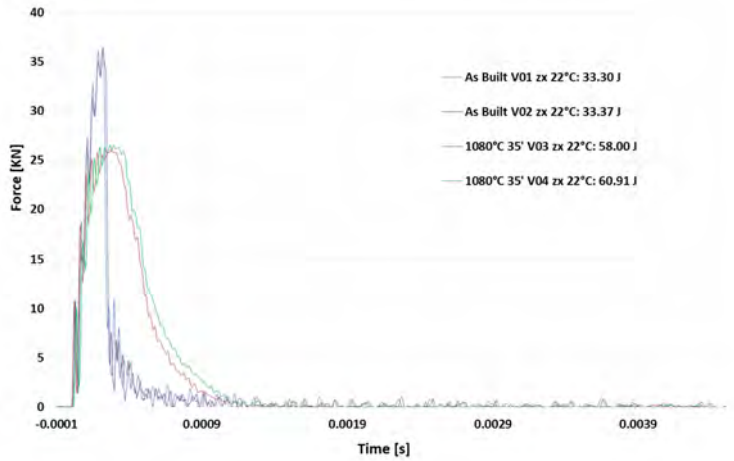

(a) Notched PBF-LB/M UNS S32760 specimens produced from a high-nitrogen powder blend. Specimens longitudinal axis parallel to grow- ing Z axis (vertical direction). Tested at 22°C.

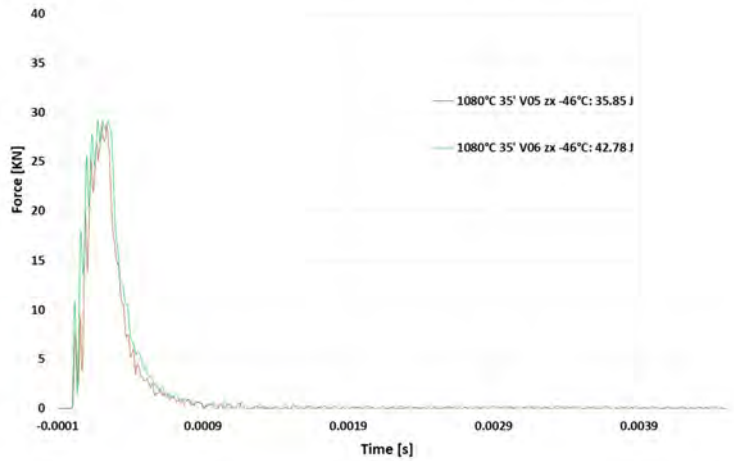

(b) Notched PBF-LB/M UNS S32760 specimens produced from a high-nitrogen powder blend. Specimens longitudinal axis parallel to growing Z axis (vertical direction). Tested at -46°C.

Fig. 4.53 Force–time curves acquired using an instrumented Charpy pendulum equipped with a 2 mm radius striker during impact testing of notched PBF-LB/M UNS S32760 specimens produced from a high-nitrogen powder blend, built in the vertical orientation, and tested at 22°C and −46°C. The data corresponding to the individual curves are reported in Table 4.19.

4.6.4 Fracture Surface and Microstructural Analysis of Charpy Impact-Tested Specimens and Correlation with Impact Behaviour

To better interpret the Charpy impact response of the PBF-LB/M UNS S32760 specimens, the fracture surfaces were analysed by SEM and correlated with the corresponding microstructural condition. This analysis was aimed at identifying the fracture micromechanisms activated after impact testing and at assessing whether the reduced absorbed energy observed in selected conditions could be associated with specific microstructural features, such as phase balance, heat-treatment condition, or process-induced defects.

4.6.4.1 Low-Nitrogen Material: Fractography and Microstructural analysis

Particular attention was given to the specimens produced from the low-nitrogen powder blend and tested at -46 °C in the horizontal direction, namely with the specimen longitudinal axis perpendicular to the build Z axis. Figure 4.54 compares the fracture surfaces of the as-built condition with two heat-treated conditions that exhibited the lowest impact response among the investigated states. The low-magnification views provide an overall assessment of the fracture surface morphology, whereas the higher-magnification images allow the local fracture micromechanisms to be evaluated.

To correlate the fracture behaviour with the corresponding microstructural condition, optical micrographs of the same Charpy impact specimens are reported in Figure 4.55. The as-built state is compared with the two heat-treated conditions at 1020 °C for 35 min and 1080 °C for 35 min. For each condition, both the *xy* and *zy* sections are shown, allowing the microstructural morphology to be assessed with respect to the build direction. The electrolytic NaOH etching highlights ferrite in blue and austenite in white, while the absorbed impact energy and the corresponding XRD-derived austenite fraction are reported together with the micrographs. In the specimen treated at 1020 °C for 35 min, the presence of a dark constituent associated with the embrittling σ phase, estimated at approximately 1.5 vol.%, provides a microstructural explanation for the marked decrease in impact toughness.

A more detailed comparison between the two heat-treated states is provided in Figure 4.56. The higher-magnification micrographs highlight the persistence of a pronounced anisotropy between the *xy* and *zy* sections, indicating that directional microstructural features inherited from the PBF-LB/M process are not fully removed by the investigated heat treatments. Compared with the 1020 °C condition, the treatment at 1080 °C promotes a higher fraction of globular secondary austenite and a thickening of grain-boundary austenite. Moreover, the intragranular acicular, Widmanstätten-like austenite observed after treatment at 1020 °C tends to evolve towards a more globular morphology when the heat-treatment temperature is increased to 1080 °C, contributing to the different impact behaviour observed between the two conditions.

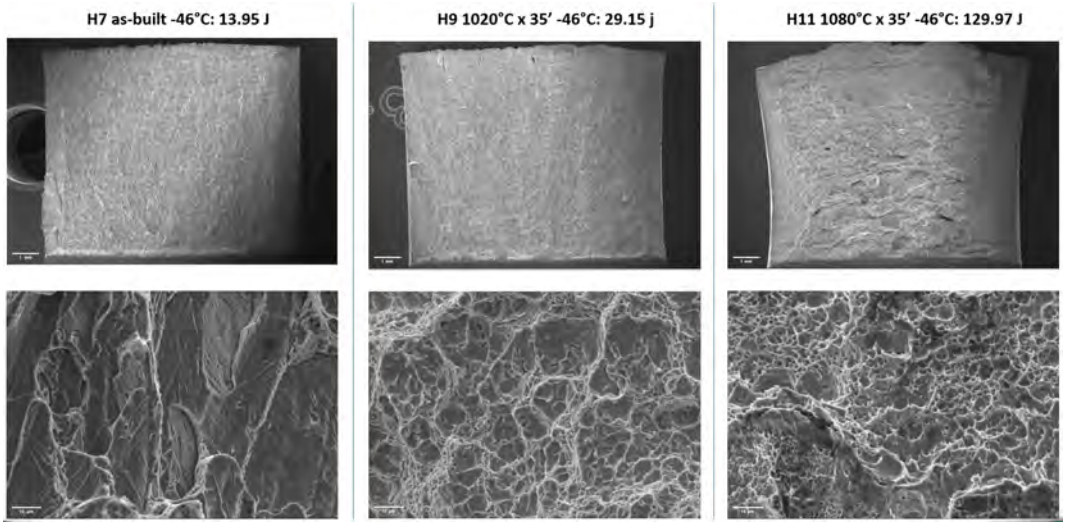

Fig. 4.54 SEM fractographs of PBF-LB/M UNS S32760 Charpy impact specimens produced from a blend of low-nitrogen powders and tested at −46 °C in the horizontal direction, with the specimen longitudinal axis perpendicular to the build *Z* axis. The images compare the as-built condition and two selected heat-treatment conditions that showed the lowest impact response among the investigated states. For each condition, the upper row shows a low-magnification overview of the fracture surface, whereas the lower row highlights the corresponding fracture micromechanisms. The absorbed impact energies measured are reported above each specimen. The complete Charpy impact results, including lateral expansion values determined according to ASTM E23 [129] and the corresponding XRD-derived austenite fractions, are reported in Table 4.18 and Figure 4.52.

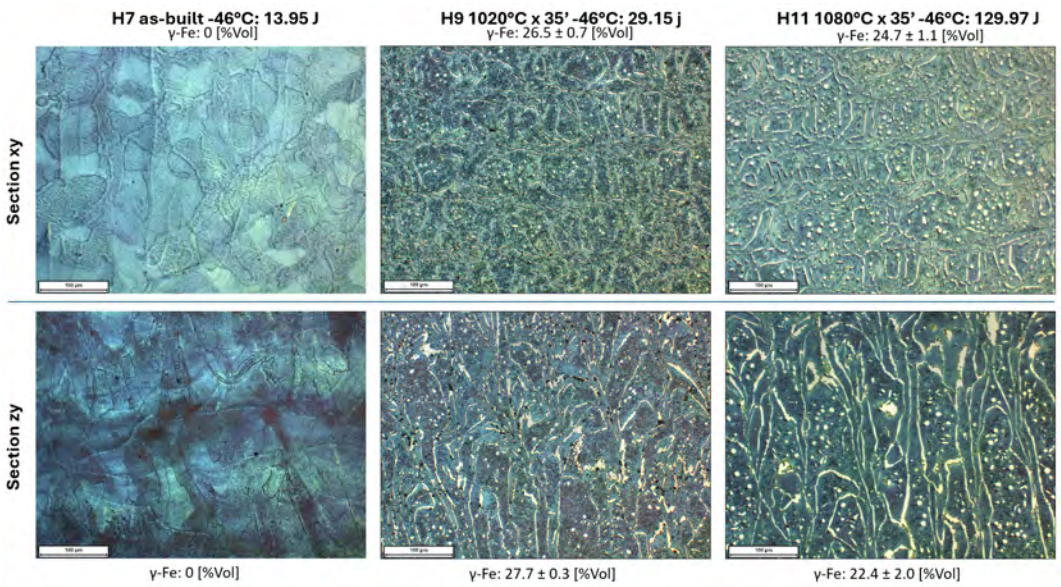

Fig. 4.55 Optical micrographs of PBF-LB/M UNS S32760 Charpy impact specimens produced from a blend of low-nitrogen powders and tested at -46 °C in the horizontal direction, corresponding to the same sample reported in the SEM fractographs of Figure 4.54. The microstructures were revealed by electrolytic etching in NaOH solution, which highlights ferrite in blue and austenite in white. The as-built condition is compared with the two heat-treated states at 1020 °C for 35 min and 1080 °C for 35 min. For each condition, both the *xy* and *zy* sections are shown in order to assess the microstructural morphology with respect to the build direction. For the specimens treated at 1020 °C for 35 min, the dark constituent is associated with the embrittling σ phase, with an estimated average value of 1.5 vol.%, whose formation is responsible for the marked reduction in impact toughness. The absorbed impact energy and the corresponding XRD-derived austenite fraction are reported above or below each micrograph. The complete Charpy impact data, including lateral expansion values determined according to ASTM E23 [129], are reported in Table 4.18 and Figure 4.52.

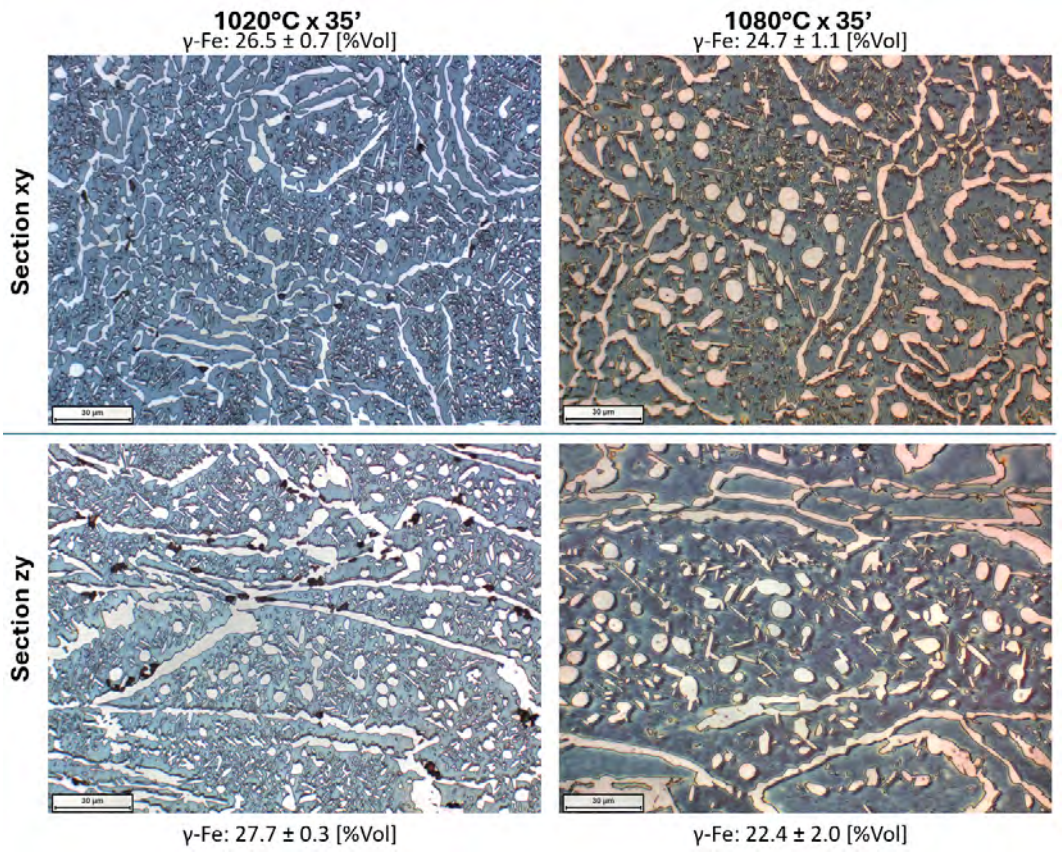

Fig. 4.56 Higher-magnification optical micrographs of PBF-LB/M UNS S32760 specimens produced from a blend of low-nitrogen powders in the horizontal direction. The microstructures were revealed by electrolytic etching in NaOH solution, where the ferritic phase appears in blue and the austenitic phase in white. For the specimens treated at 1020 °C for 35 min, the dark constituent is associated with the embrittling σ phase, with an estimated average value of 1.5 vol.%, whose formation is responsible for the marked reduction in impact toughness. Both heat-treated conditions show a pronounced anisotropy between the *xy* and *zy* sections, confirming the persistence of directional microstructural features inherited from the PBF-LB/M process. Compared with the 1020 °C condition, the treatment at 1080 °C promotes a higher fraction of globular secondary austenite and a thickening of grain-boundary austenite. The intragranular acicular, Widmanstätten-like austenite observed after treatment at 1020 °C tends to evolve toward a more globular morphology when the heat-treatment temperature is increased to 1080 °C. The corresponding XRD-derived austenite fractions are reported above or below the micrographs.

4.6.4.2 High-Nitrogen Material: Impact Fractography

The fracture behaviour of the specimens produced from the high-nitrogen powder blend and tested at −46 °C was further investigated by SEM, as reported in Figure 4.57. In this case, the analysed specimens were built in the vertical direction and heat-treated at 1080 °C for 35 min. The low-magnification fractographs show an overall fracture morphology still affected by the process-induced texture, with features that can be associated with the laser scanning tracks. However, the higher-magnification images reveal that these regions are mainly characterized by ductile fracture mechanisms, as indicated by the presence of numerous small dimples distributed over the fracture surface.

Compared with the low-nitrogen specimens built in the horizontal direction and reported in Figure 4.54, the fracture surfaces of the high-nitrogen vertically built specimens show a more evident texture associated with the laser scanning tracks. In the low-nitrogen horizontal specimens, this process-induced texture was not clearly highlighted by the fracture surface morphology. This difference suggests that the fracture path in the vertically built condition may be more affected by the directional features inherited from the PBF-LB/M process, although the higher-magnification observations still indicate a predominantly ductile fracture mode characterized by numerous small dimples.

The observation of the fracture surfaces of the Charpy impact specimens tested at 22 °C highlighted the same main features identified for the specimens tested at −46 °C.

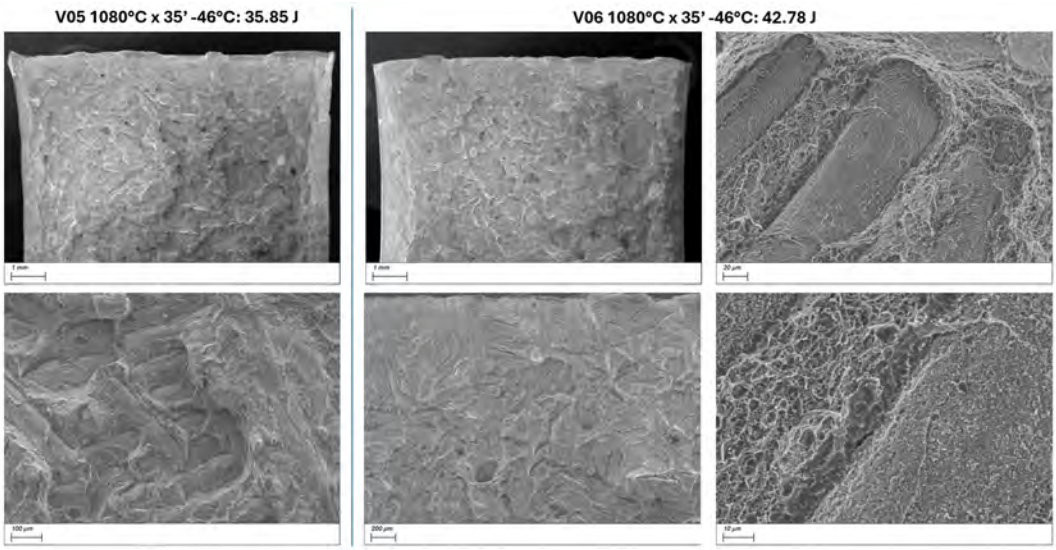

Fig. 4.57 SEM fractographs of PBF-LB/M UNS S32760 Charpy impact specimens produced from a blend of high-nitrogen powders and tested at -46 °C in the vertical direction, with the specimen longitudinal axis perpendicular to the build Z axis. The low-magnification images show the overall fracture surface morphology of the investigated specimens, for which absorbed energies of 35.85 J and 42.78 J were measured. In the vertically built specimens, the fracture surfaces reveal a texture associated with the laser scanning tracks, indicating the persistence of process-induced directional features. Nevertheless, the higher-magnification images show that these regions are still characterized by a predominantly ductile fracture morphology, with numerous small dimples distributed over the fracture surface. The complete Charpy impact results, including lateral expansion values determined according to ASTM E23 [129] and the corresponding XRD-derived austenite fractions, are reported in Table 4.19 and Figure 4.53.

4.6.4.3 Effect of powder Nitrogen content on Heat-Treated PBF-LB/M microstructures

The micrographs reported in Figure 4.58 and Figure 4.59 clearly show the strong influence of the powder nitrogen content on the microstructure obtained after heat treatment. This difference is directly related to the different atmospheres used during powder production, which resulted in different average nitrogen contents in the feedstocks and, consequently, in the components produced by PBF-LB/M. In particular, the Ar/Ar and Ar/N_2 powder blend exhibited an average nitrogen content of 0.206 ± 0.03393 wt.%, which decreased to 0.148 ± 0.00636 wt.% after PBF-LB/M processing, whereas the N_2/N_2 and N_2/Ar powder blend showed higher values, equal to 0.429 ± 0.00296 wt.% in the powder and 0.372 ± 0.00967 wt.% after PBF-LB/M. In the specimens produced from low-nitrogen powders, a ferritic-austenitic duplex microstructure is observed, still characterized by pronounced anisotropy. In particular, primary austenite can be identified mainly along the ferritic grain boundaries, together with secondary austenite with a more globular or discontinuous morphology within the matrix. The phase distribution appears heterogeneous and oriented, with a marked dependence on the observation plane, highlighting the microstructural inheritance of the PBF-LB/M process and of the directional solidification conditions.

By contrast, the specimens obtained from high-nitrogen powders exhibit a significantly finer, more homogeneous and more isotropic microstructure. The increased nitrogen content promotes a higher amount of austenite formation during heat treatment, leading to a more uniform distribution of the γ-Fe phase and reducing the pronounced anisotropy observed in the low-nitrogen specimens. For the same heat treatment, the difference in ferrite/austenite balance is therefore evident: the average austenite fraction increases from approximately 23 vol.% in the low-nitrogen specimens to approximately 55 vol.% in the high-nitrogen specimens. Overall, these observations confirm that the use of high-nitrogen powders is a key factor for obtaining PBF-LB/M UNS S32760 components with a finer, more isotropic microstructure and a higher austenite fraction. This aspect is particularly relevant because a more homogeneous austenite distribution may contribute to improving the overall mechanical response of the material, especially in terms of ductility and fracture toughness. For comparison, Figures 4.60 and 4.61 report the microstructures of a UNS S32760 threaded bar and a forged UNS S32760 component, respectively.

These reference materials are shown to better assess the degree of microstructural refinement achieved in the PBF-LB/M specimens after heat treatment at 1080 °C for 35 min. The same conventionally processed materials were also used as comparative references in the corrosion tests discussed in Section 4.8.

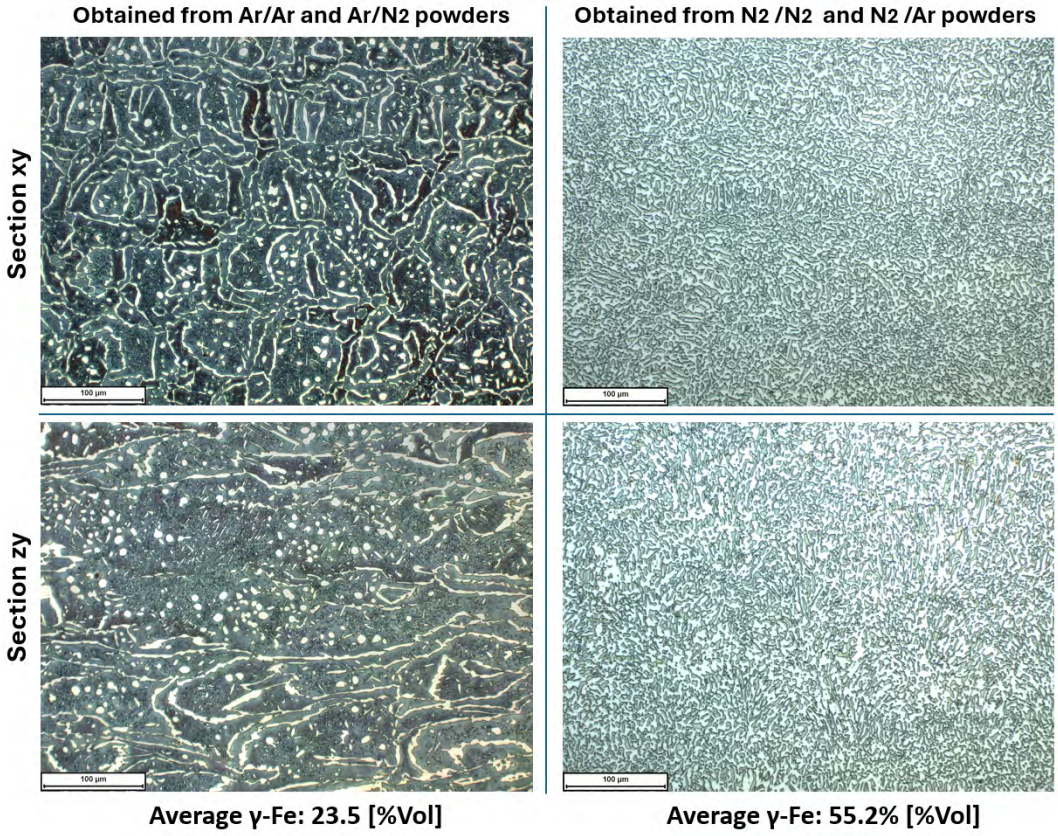

Fig. 4.58 Optical micrographs of heat-treated PBF-LB/M UNS S32760 specimens produced from powder blends with different nitrogen contents. The left column refers to specimens obtained from Ar/Ar and Ar/N_2 powders, characterized by a lower nitrogen content, whereas the right column refers to specimens produced from N_2/N_2 and N_2/Ar powders, characterized by a higher nitrogen content. For each condition, both *xy* and *zy* sections are reported. The low-nitrogen material exhibits a ferritic-austenitic duplex microstructure with pronounced anisotropy, with austenite (in white) mainly located along ferritic grain boundaries and as discontinuous secondary austenite within the matrix. Conversely, the high-nitrogen material shows a finer, more homogeneous and more isotropic microstructure, together with a markedly higher austenite fraction. The average γ-Fe content increases from 23.5 vol.% in the low-nitrogen specimens to 55.2 vol.% in the high-nitrogen specimens.

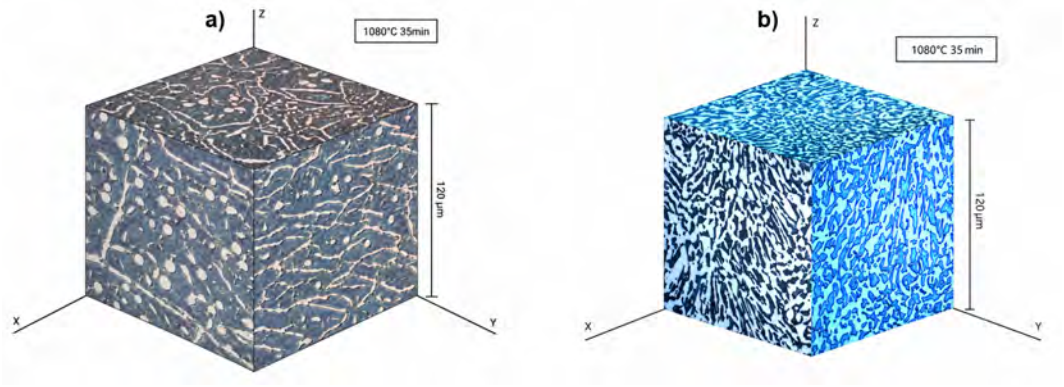

Fig. 4.59 3D reconstruction of the microstructures observed on the *XZ*, *YZ*, and *XY* planes of heat-treated PBF-LB/M UNS S32760 specimens produced from powder blends with different nitrogen contents. Image (a) refers to the specimen produced from low-nitrogen powders (Ar/Ar and Ar/N_2) and heat treated at 1080 °C for 35 min, whereas image (b) refers to the specimen produced from high-nitrogen powders (N_2/N_2 and N_2/Ar) and heat treated under the same conditions. The comparison highlights the more pronounced microstructural anisotropy of the low-nitrogen specimen and the higher microstructural isotropy achieved in the high-nitrogen specimen.

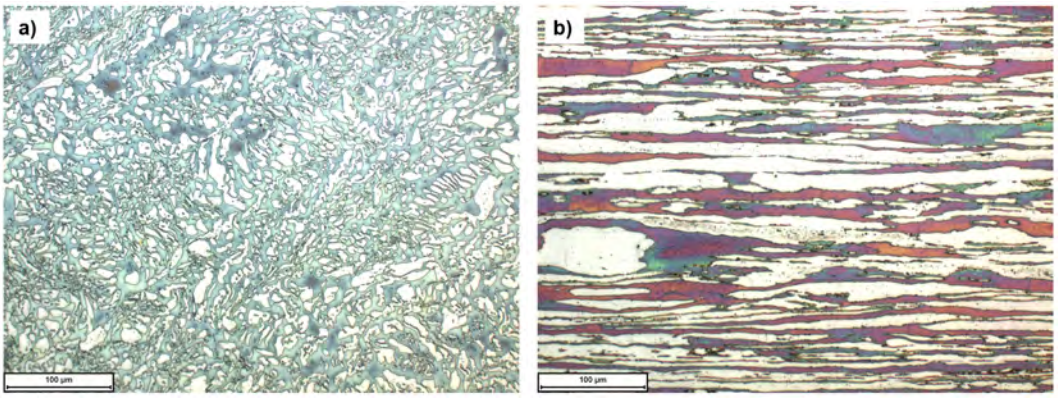

Fig. 4.60 Optical micrographs of the UNS S32760 threaded bar used as a reference conventionally processed material. Image (a) shows the transverse section, whereas image (b) shows the longitudinal section. The microstructure is characterized by a duplex ferritic-austenitic morphology, with austenite appearing in white and ferrite in light blue, with phase fractions close to 50% austenite and 50% ferrite. The longitudinal section highlights the marked elongation and alignment of the microstructural constituents along the bar axis, while the transverse section shows the corresponding cross-sectional phase distribution.

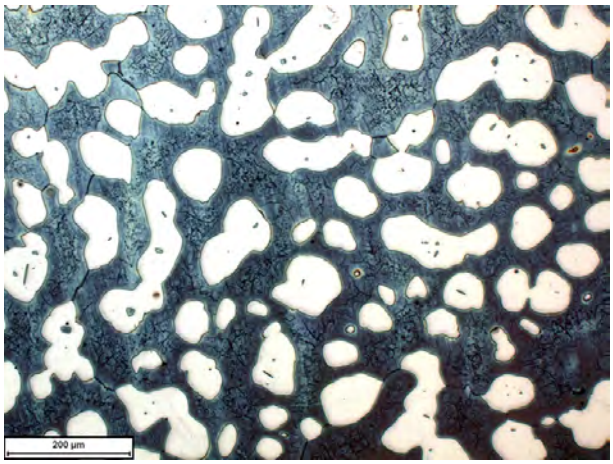

Fig. 4.61 Optical micrograph of the forged UNS S32760 component used as a reference conventionally processed material. The image shows a duplex ferritic-austenitic microstructure, with austenite appearing in white and ferrite in light blue, with phase fractions close to 50% austenite and 50% ferrite. Compared with the PBF-LB/M heat-treated condition, the forged material exhibits a coarser phase morphology, with relatively large austenitic regions embedded within the ferritic matrix.

4.6.5 Tensile Test Results

The results of the tensile tests performed on PBF-LB/M UNS S32760 specimens produced in the horizontal build orientation from a low-nitrogen powder mixture are reported in Table 4.20, while those obtained for vertically built specimens produced from a high-nitrogen powder mixture are reported in Table 4.21. The corresponding stress–strain curves are shown in Fig. 4.62 and Fig. 4.63.

Similarly to what was observed for the Charpy impact tests, the direct comparison between the two experimental series must be carried out with caution, since the specimens differ in terms of nitrogen content of the starting powder, build orientation, and microstructural condition. However, in tensile testing, the vertical orientation may be less detrimental than in impact testing and, in some cases, even favourable, since the loading axis may interact differently with the columnar structure, crystallographic texture, melt-pool directionality, and defect distribution compared with the conditions occurring during impact tests [94, 134].

4.6.5.1 Tensile test results of specimens produced from the low-nitrogen powder mixture

In the low-nitrogen specimens built in the horizontal orientation, the as-built condition is characterised by the highest mechanical strength values, but by a strongly limited ductility. At 22 °C, specimens H1 and H2 show $R_{p0.2}$ values of 969 and 927 MPa, respectively, and R_m values of 1038 and 1059 MPa. These values are markedly higher than those obtained after heat treatment, highlighting the strong strengthening effect associated with the PBF-LB/M as-built microstructure. This behaviour can be attributed to the predominantly ferritic matrix, as indicated by the absence of austenite reported in Table 4.20. However, the higher strength is accompanied by reduced elongation values: A_{gt} is equal to 4.9–5.3%, whereas A_t is equal to 15.1–15.5%. This response is consistent with a ferritic microstructure that is poorly suited to stable work hardening and plastic strain redistribution.

The heat treatment at 1020 °C for 35 min causes a significant reduction in strength, but a marked increase in ductility. At 22 °C, specimens H3 and H4 exhibit $R_{p0.2}$ values of 615 MPa and R_m values of 868 and 867 MPa, associated with A_{gt} values of 13.81 and 15.71% and A_t values of 24.4 and 31.4%. The decrease in strength with respect to the as-built condition can be ascribed to residual stress relaxation,

the reduction in the density of lattice defects, and the partial transformation of the ferritic matrix into a duplex microstructure containing an average austenite fraction of 27 vol.%. The increase in austenite fraction contributes to improving the plastic deformation capability, although this beneficial effect remains limited by the presence of the embrittling sigma intermetallic phase.

The treatment at 1080 °C for 35 min produces a similar mechanical response in terms of strength, but a further improvement in ductility and strain stability. At 22 °C, specimens H5 and H6 show $R_{p0.2}$ values of 620 and 637 MPa and R_m values of 855 and 858 MPa, therefore close to those measured for the specimens treated at 1020 °C. However, A_t reaches 30.5 and 30.9%, while the reduction of area Z increases up to 70.2 and 75.2%. This increase in necking capability suggests a greater ability of the material to sustain localised plastic deformation before fracture. Moreover, the energy absorbed up to A_{gt}, reported in the sub-table of Table 4.20, reaches values of 111.2 and 110.2 MJ/m^3, which are higher than those of the as-built condition and generally higher than those obtained after treatment at 1020 °C. This result is particularly relevant, since it indicates that the treatment at 1080 °C does not simply maximise the final elongation, but also improves the overall ability of the material to absorb energy during plastic deformation, as previously highlighted by the impact tests reported in Table 4.18.

The curves reported in Fig. 4.62 clearly confirm this evolution. At 22 °C, the as-built specimens show a rapid increase in load up to high stress values, followed by a relatively limited plastic deformation range. Conversely, the heat-treated specimens exhibit a lower yield strength and lower ultimate tensile strength, but a much more extended plastic region. The curves of the specimens treated at 1080 °C are characterised by a greater deformation capability after reaching the ultimate tensile strength, consistently with the high A_t and Z values. This behaviour confirms that the loss in strength induced by the heat treatment is compensated by a significant increase in elongation to fracture.

The effect of the testing temperature is evident in the horizontally built low-nitrogen specimens. At -46 °C, the as-built condition shows a further increase in strength compared with 22 °C: specimens H7 and H8 reach $R_{p0.2}$ values of 1080 and 1038 MPa and R_m values of 1158 and 1149 MPa. This increase is consistent with the typical behaviour of steels, in which decreasing temperature hinders dislocation mobility and increases the stress required to activate plastic deformation. However,

uniform deformation remains very limited, with A_{gt} values of 3.6–4.2%. The as-built condition at low temperature therefore retains a high-strength behaviour, but with a reduced uniform work-hardening capability, in agreement with the brittle response observed in the Charpy tests at -46 °C.

The heat-treated specimens also show an increase in strength at -46 °C compared with 22 °C. In the case of the treatment at 1020 °C, $R_{p0.2}$ increases up to 703 and 686 MPa, while R_m reaches 971 MPa for both specimens. For the treatment at 1080 °C, $R_{p0.2}$ is equal to 697 and 754 MPa, with R_m values of 946 and 956 MPa. Although ductility is slightly reduced compared with room temperature, the total elongation values remain significant, especially for the specimens treated at 1080 °C, which show A_t values of 28.6 and 26.9%. This result indicates that the microstructure obtained after treatment at 1080 °C maintains a good deformation capability even at low temperature, consistently with the results of the impact tests.

An important aspect concerns the different role of the austenite fraction in the specimens treated at 1020 °C and 1080 °C. Although the treatment at 1020 °C produces a slightly higher austenite fraction, with an average value of 27 vol.%, the presence of the embrittling sigma phase in this condition leads to a less favourable response. As a result, the treatment at 1080 °C provides a more advantageous behaviour in terms of final elongation, reduction of area, and energy absorbed during tensile deformation.

4.6.5.2 Tensile test results of specimens produced from the high-nitrogen powder mixture

The specimens produced from the high-nitrogen powder mixture and built in the vertical orientation, reported in Table 4.21, show a particularly interesting mechanical response. In the as-built condition, specimens V01, V02, and V03 exhibit very high $R_{p0.2}$ values, ranging from 1093 to 1119 MPa, and R_m values of 1357–1364 MPa. These values are higher than those measured for the low-nitrogen as-built specimens produced in the horizontal orientation, suggesting a combined contribution of the higher nitrogen content, the vertical build orientation, and the specific PBF-LB/M microstructure to the mechanical strength. Nitrogen, in addition to stabilising austenite, can contribute to solid-solution strengthening and modify the response of the matrix during deformation. Moreover, in tensile loading, the vertical orientation

may promote a stronger response depending on the loading direction with respect to the growth structure and the texture developed during the PBF-LB/M process.

However, also in this case, the high strength of the as-built condition is accompanied by limited uniform ductility. The A_{gt} values are equal to 3.6–3.7%, while A_t is approximately 13.9–14.3%. The reduction of area, ranging from 57.9 to 61.5%, is higher than that observed for the low-nitrogen horizontally built as-built specimens, suggesting that the high-nitrogen vertical specimens, despite showing low uniform deformation, retain a reasonable capacity for localised plastic deformation before fracture. Indeed, the curves reported in Fig. 4.63 show an as-built response characterised by very high strength, but also by rapid strain localisation after reaching the maximum load.

After heat treatment at 1080 °C for 35 min, the high-nitrogen vertical specimens show a significant reduction in strength, but a marked increase in ductility. The $R_{p0.2}$ values decrease to 646–660 MPa, while R_m stabilises around 976–979 MPa. At the same time, A_{gt} increases up to 19.0–19.6%, and A_t reaches 32.4–33.6%. These values are particularly relevant because they indicate a higher uniform deformation than that observed for the low-nitrogen specimens heat-treated at 1080 °C in the horizontal orientation. The energy values up to A_{gt}, equal to 71.6–86.2 MJ/m^3, also indicate a greater ability to sustain stable plastic deformation compared with the as-built condition, although the highest overall tensile energy values were observed in some low-nitrogen horizontal specimens treated at 1080 °C.

The comparison between the two series, Table 4.20 and Table 4.21, highlights a substantial difference with respect to what was observed in the impact tests. In the Charpy tests, the vertical orientation had a detrimental effect on impact toughness, even in the presence of a higher nitrogen content and a potentially more favourable microstructure. In tensile testing, instead, the vertical orientation is not penalising in the same way and may contribute to achieving very high strength values, especially in the as-built condition of the high-nitrogen specimens. This confirms that the sensitivity to build orientation strongly depends on the type of applied loading.

The Charpy test is governed by crack initiation and rapid crack propagation in the presence of a notch and is therefore strongly affected by defect distribution, PBF-LB/M layer-wise architecture, and the fracture propagation plane.
In contrast, the tensile test involves a more distributed deformation within the gauge volume of the specimen and may benefit, in specific configurations, from the

microstructural directionality and melt-pool orientation developed along the build axis.

From a standard-compliance perspective, the tensile test results are overall satisfactory with respect to the requirements specified by NORSOK M-630 [126] for forged duplex steel components. This standard prescribes minimum values of $R_{p0.2} = 550$ MPa, $R_m = 750$ MPa, and $A_t = 15\%$. Based on the data reported in Table 4.20 and Table 4.21, all the investigated conditions satisfy these requirements, with the exception of the as-built specimens produced from high-nitrogen powders and built in the vertical orientation. In this latter case, although the measured strength values are well above the minimum required limits, with $R_{p0.2}$ ranging from 1093 to 1119 MPa and R_m ranging from 1357 to 1364 MPa, the total elongation to fracture A_t is equal to 13.9–14.3%, and is therefore slightly below the standard requirement of 15%.

Considering instead the more stringent requirements specified by the same standard for studs and bolts, namely $R_{p0.2} = 725$ MPa, $R_m = 860$ MPa, $A_t = 16\%$, and $Z = 30\%$, the most critical parameter is the yield strength $R_{p0.2}$. Indeed, R_m, A_t, and Z are generally above the required limits for most of the heat-treated conditions, whereas $R_{p0.2}$ tends to decrease significantly after heat treatments at 1020 °C and 1080 °C, reaching values below 725 MPa in several specimens. This behaviour highlights the compromise introduced by post-process heat treatment: on the one hand, it promotes the recovery of ductility and increases the plastic deformation capability; on the other hand, it reduces the yield strength compared with the as-built condition. It is nevertheless necessary to distinguish the apparent mechanical response from the actual microstructural suitability of the different heat-treated conditions. In particular, although the specimens treated at 1020 °C for 35 min show strength and elongation values compatible with the minimum requirements for forged components, this condition must be considered less favourable due to the presence of the intermetallic σ phase.

In this regard, the treatment at 1080 °C for 35 min appears more promising than the treatment at 1020 °C, since it provides a more balanced combination of mechanical properties and microstructural quality. Although, in some cases, it leads to a reduction in $R_{p0.2}$ below the stricter limit required for studs and bolts, it ensures high R_m, A_t, and Z values, a greater plastic deformation capability, and, as demonstrated by the Charpy tests, a markedly superior impact toughness.

4.6.5.3 Analysis of the strain-hardening exponent n

The values of the strain-hardening exponent n of the Hollomon law, Eq. 4.8, reported in Table 4.20 and Table 4.21, highlight significant differences among the as-built condition, the heat-treated conditions, and the testing temperatures.

$$\sigma_t = H \cdot \varepsilon_t^n \tag{4.8}$$

where:

- σ_t is the true stress;
- ε_t is the true strain;
- H is the strength coefficient;
- n is the strain-hardening exponent.

4.6.5.4 Analysis of the strain-hardening exponent n for specimens produced from the low-nitrogen powder mixture

For the specimens produced from low-nitrogen powders and built in the horizontal orientation, the as-built condition exhibits relatively low n values. At 22 °C, specimens H1 and H2 show $n = 0.091$ and $n = 0.064$, respectively. These values are consistent with a microstructure characterised by the absence of detectable austenite and by a predominantly ferritic matrix, strongly affected by the peculiar features of the PBF-LB/M process. The presence of high residual stresses and microstructural anisotropy may promote high initial strength values, but limits the ability of the material to sustain progressive strain hardening during plastic deformation.

This behaviour is confirmed by the main mechanical data. The as-built specimens H1 and H2 show high $R_{p0.2}$ values, equal to 969 and 927 MPa, and R_m values of 1038 and 1059 MPa, respectively, but reduced elongation values, with A_{gt} equal to 4.9–5.3%. The combination of high strength and low n indicates that the material rapidly reaches the maximum load after yielding, showing a limited ability to redistribute strain before localisation. In other words, the as-built condition is highly resistant in terms of tensile strength, but poorly efficient from the standpoint of plastic strain hardening.

The heat treatment at 1020 °C for 35 min causes a clear increase in the strain-hardening exponent n. At 22 °C, specimens H3 and H4 both show a value of $n = 0.135$, higher than that of the as-built condition. This increase is consistent with the formation of a duplex microstructure containing approximately 27 vol.% austenite. The increase in austenite fraction enables a more effective partitioning of plastic deformation between the phases and contributes to delaying localisation. Indeed, compared with the as-built condition, the specimens treated at 1020 °C show a marked reduction in $R_{p0.2}$, which decreases to 615 MPa, but a significant increase in A_{gt}, equal to 13.81–15.71%, and in A_t, equal to 24.4–31.4%.

However, the n value of the specimens treated at 1020 °C must also be interpreted by considering the possible presence of the σ phase, already discussed as a critical microstructural feature.

The treatment at 1080 °C for 35 min provides n values comparable to, or slightly higher than, those obtained after treatment at 1020 °C. At 22 °C, specimens H5 and H6 show $n = 0.141$ and $n = 0.123$, respectively. The higher value observed for H5, equal to 0.141, is associated with one of the best combinations of ductility and energy absorbed during plastic deformation, with $A_t = 30.5\%$, $Z = 70.2\%$, and W up to A_{gt} equal to 111.2 MJ/m^3. Although H6 shows a slightly lower n value, it still retains a highly ductile response, with $A_t = 30.9\%$, $Z = 75.2\%$, and W up to A_{gt} equal to 110.2 MJ/m^3.

At -46 °C, the horizontally built low-nitrogen specimens show an interesting behaviour. In the as-built condition, the n values remain low, equal to 0.069 and 0.074 for H7 and H8, respectively. These values are slightly lower than, or comparable to, those measured at 22 °C and confirm the limited strain-hardening capability of the as-built condition even at low temperature. The decrease in testing temperature leads to an increase in strength, with $R_{p0.2}$ values of 1080 and 1038 MPa and R_m values of 1158 and 1149 MPa, but does not improve the ability of the material to deform uniformly. Indeed, A_{gt} remains very low, equal to 3.6–4.2%, indicating a rapid tendency towards plastic localisation.

For the specimens treated at 1080 °C and tested at -46 °C, the n values are equal to 0.126 and 0.106 for H11 and H12, respectively. Compared with the tests performed at 22 °C, a slight decrease in the strain-hardening exponent is therefore observed, more evident for H12. Nevertheless, these specimens retain high values of total elongation, equal to 28.6% and 26.9%, respectively, and reduction of area, equal

to 68.1% and 61.6%, respectively. This indicates that, although the uniform strain-hardening capability moderately decreases at low temperature, the microstructure obtained at 1080 °C preserves good overall ductility and a significant ability to sustain localised deformation before fracture.

4.6.5.5 Analysis of the strain-hardening exponent *n* for specimens produced from the high-nitrogen powder mixture

The comparison with the specimens produced from high-nitrogen powders and built vertically highlights the favourable role of nitrogen and vertical orientation in the tensile response. In the as-built condition, specimens V01, V02, and V03 show n values of 0.166, 0.183, and 0.173, respectively. These values are markedly higher than those of the low-nitrogen as-built specimens built horizontally, for which n ranges from 0.064 to 0.091 at 22 °C. This suggests that the high-nitrogen vertical specimens, despite being characterised by very high strength, possess a greater strain-hardening capability than the corresponding low-nitrogen horizontal condition.

This result is particularly significant because specimens V01–V03 exhibit very high $R_{p0.2}$ values, equal to 1093–1119 MPa, and R_m values of 1357–1364 MPa, but still limited A_{gt} values, equal to 3.6–3.7%, although in this case the as-built condition is characterised by the presence of an austenite fraction of 20 vol.%. Apparently, therefore, the high n value does not translate into a high measured uniform elongation. This apparent discrepancy may be related to the fact that n, calculated over the selected plastic region of the true tensile curve, describes the local slope of the strain-hardening behaviour, whereas A_{gt} is also affected by the geometrical stability of the specimen, by strain localisation, and by the defect distribution.

After treatment at 1080 °C for 35 min, the high-nitrogen vertical specimens show highly uniform n values, equal to 0.149, 0.149, and 0.147 for V04, V05, and V06, respectively. These values are slightly lower than those of the high-nitrogen as-built condition, but are associated with a marked increase in ductility. Indeed, A_{gt} increases up to 19.0–19.6%, while A_t reaches 32.4–33.6%. This behaviour indicates that the heat treatment reduces the excessive strength of the as-built condition and makes plastic deformation more extended and stable, while still maintaining a significant strain-hardening capability.

The decrease in n after heat treatment in the high-nitrogen specimens should therefore not be interpreted as a deterioration of the tensile properties. On the contrary, it probably reflects the transition from a strongly strengthened and metastable as-built microstructure to a more balanced and ductile microstructure. In this condition, the material exhibits a lower yield strength, but a greater extension of useful plastic deformation. The high uniform elongation of specimens V04–V06 indicates that the treatment at 1080 °C enables a more suitable response for structural applications than the as-built condition.

In the overall comparison between the two specimen families, the lowest n values were observed in the low-nitrogen as-built specimens built horizontally, whereas the highest values belonged to the high-nitrogen as-built specimens built vertically. This confirms that the strain-hardening capability does not depend exclusively on the heat treatment, but is strongly affected by nitrogen content, the microstructure generated by the PBF-LB/M process, and build orientation. Moreover, the vertical build orientation, which proved detrimental in the impact tests, appears instead favourable or at least not detrimental in the tensile response, in agreement with the different loading mechanism.

In conclusion, the parameter n provides complementary information with respect to $R_{p0.2}$, R_m, A_{gt}, A_t, and Z. It allows high-strength conditions with limited stable deformation capability, such as the low-nitrogen as-built specimens, to be distinguished from more balanced conditions, such as the specimens treated at 1080 °C. In the high-nitrogen vertical specimens, the high n value of the as-built condition highlights a marked local strain-hardening capability, whereas the best overall engineering response is obtained after treatment at 1080 °C, where the material combines a still significant n value, high uniform elongation, and pronounced ductility to fracture.

Table 4.20 Summary of tensile test results for PBF-LB/M UNS S32760 specimens produced from a blend of low-nitrogen powders, built in the horizontal direction and tested under different heat-treatment conditions and test temperatures. The reported average austenite values, determined by XRD, refer to the corresponding heat-treated condition. Additional tensile parameters, including the Hollomon strain-hardening exponent n (Eq. 4.8), derived from tensile-curve analysis, are reported in the lower sub-table.

ID	Build direction	HT state	HT time	Austenite [vol.%] on plane	Test temp.	d_0 [mm]	$R_{p0.2}$ [MPa]	R_m [MPa]	A_{gt} [%]	R_B [MPa]	A_t [%]	Z [%]
H1	Horiz.	as-built	–	0	22°C	4.03	969	1038	4.9	787	15.1	47.2
H2		as-built	–	0		4.03	927	1059	5.3	824	15.5	39.7
H3		1020°C	35	plane xy: 26.5 ± 0.7		4.00	615	868	13.81	607	24.4	59.6
H4		1020°C		plane zy: 27.7 ± 0.3		4.00	615	867	15.71	525	31.4	65.3
H5		1080°C		plane xy: 24.7 ± 1.1		4.01	620	855	14.8	475	30.5	70.2
H6		1080°C		plane zy: 22.4 ± 2.0		4.00	637	858	14.6	469	30.9	75.2
H7		as-built	–	0	-46°C	3.99	1080	1158	3.6	858	16.7	40.1
H8		as-built	–	0		4.02	1038	1149	4.2	882	17.1	40.3
H9		1020°C	35	plane xy: 26.5 ± 0.7		4.00	703	971	13.8	718	17.6	34.8
H10		1020°C		plane zy: 27.7 ± 0.3		4.00	686	971	13.5	678	26.9	57.3
H11		1080°C		plane xy: 24.7 ± 1.1		4.04	697	946	13.4	530	28.6	68.1
H12		1080°C		plane zy: 22.4 ± 2.0		3.96	754	956	12.2	584	26.9	61.6

ID	n	Poisson	W [MJ/m^3] up to $R_{p0.2}$	W [MJ/m^3] up to R_m	W [MJ/m^3] up to A_{gt}
H1	0.091	–	2.7	4.0	35.3
H2	0.064	–	2.5	4.5	34.9
H3	0.135	–	1.0	8.7	66.8
H4	0.135	–	1.1	9.4	104.7
H5	0.141	–	1.7	9.4	111.2
H6	0.123	–	1.0	7.9	110.2
H7	0.069	–	3.6	4.9	4.9
H8	0.074	–	2.9	4.6	42.7
H9	0.137	–	1.4	8.9	53.0
H10	0.141	–	1.3	9.3	79.4
H11	0.126	–	1.3	8.6	113.4
H12	0.106	–	1.4	7.2	94.8

Table 4.21 Summary of tensile test results for PBF-LB/M UNS S32760 specimens produced from a blend of high-nitrogen powders, built in the vertical direction and tested under different heat-treatment conditions and test temperatures. The reported average austenite values, determined by XRD, refer to the corresponding heat-treated condition. Additional tensile parameters, including the Hollomon strain-hardening exponent n (Eq. 4.8), derived from tensile-curve analysis, are reported in the lower sub-table.

ID	Build direction	HT state	HT time	Austenite [vol.%] on plane	Test temp.	d_0 [mm]	$R_{p0.2}$ [MPa]	R_m [MPa]	A_{gt} [%]	R_B [MPa]	A_t [%]	Z [%]
V01	Vert.	as-built	–	plane xy: 21.1 ± 1.2 plane zy: 22.5 ± 1.6	22°C	4.04	1093	1357	3.7	917	14.3	58
V02		as-built	–			4.03	1104	1364	3.6	847	14.3	61.5
V03		as-built	–			3.99	1119	1362	3.7	902	13.9	57.9
V04		1080°C	35	plane xy: 61.7 ± 2.7 plane zy: 60.5 ± 2.7		4.03	654	976	19.0	772	32.4	53.4
V05		1080°C				4.03	646	976	19.6	747	33.6	59.2
V06		1080°C				4.05	660	979	19.4	739	33.4	62.5

ID	n	Poisson	W [MJ/m^3] up to $R_{p0.2}$	W [MJ/m^3] up to R_m	W [MJ/m^3] up to A_{gt}
V01	0.166	–	3.2	6.5	54.6
V02	0.183	–	2.9	5.8	54.4
V03	0.173	–	3.3	6.2	51.2
V04	0.149	–	1.2	14.9	71.6
V05	0.149	–	1.1	15.0	80.8
V06	0.147	–	1.2	14.7	86.2

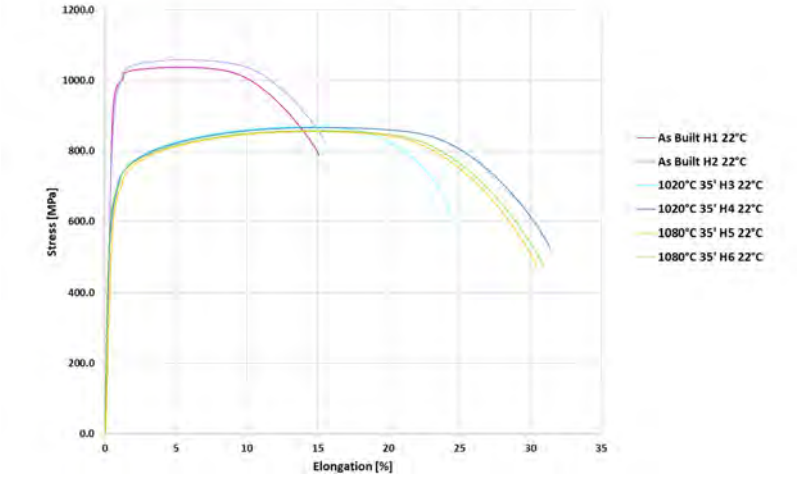

(a) PBF-LB/M UNS S32760 specimens produced from a low-nitrogen powder blend. The specimens were manufactured with horizontal orientation relative to the build-direction axis (Z) of the PBF-LB/M system and tested at 22°C.

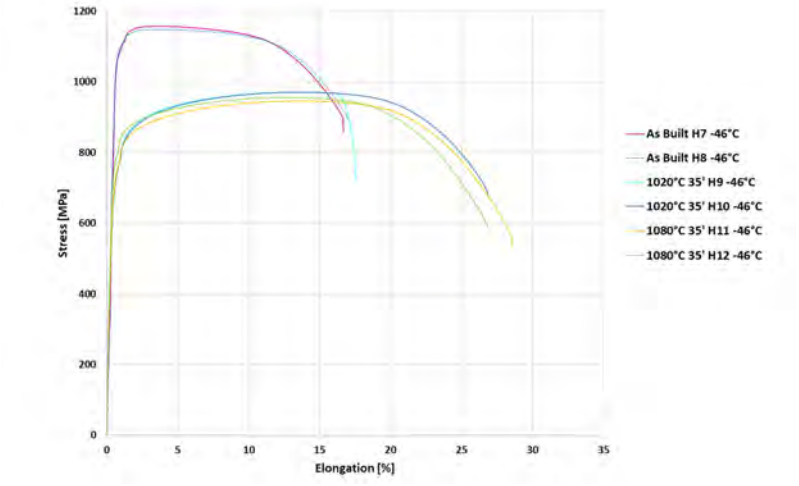

(b) PBF-LB/M UNS S32760 specimens produced from a low-nitrogen powder blend. The specimens were manufactured with horizontal orientation relative to the build-direction axis (Z) of the PBF-LB/M system and tested at -46°C.

Fig. 4.62 Tensile test of PBF-LB/M UNS S32760 specimens produced from a low-nitrogen powder blend, built in the horizontal orientation, and tested at 22°C and −46°C. The data corresponding to the individual curves are reported in Table 4.20.

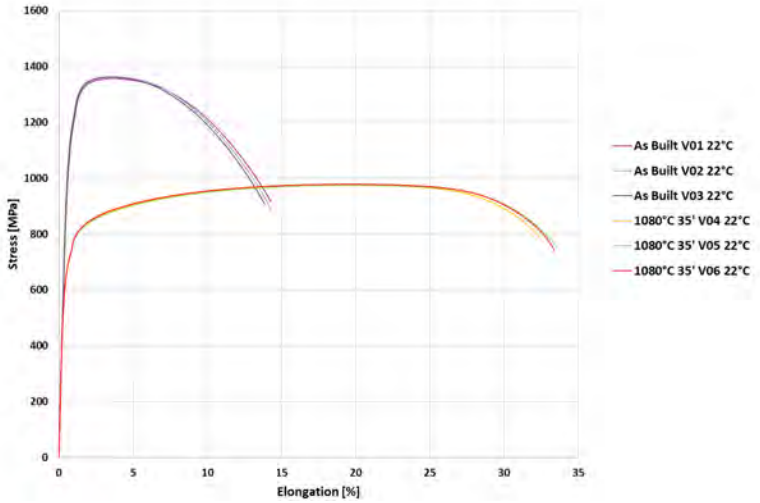

Fig. 4.63 Tensile test of PBF-LB/M UNS S32760 specimens produced from a high-nitrogen powder blend, built in the vertical orientation, and tested at 22°C. The data corresponding to the individual curves are reported in Table 4.21.

4.6.6 Fracture Surface analysis of tensile-tested specimens and correlation with tensile behaviour

To support the interpretation of the tensile behaviour of the PBF-LB/M UNS S32760 specimens, SEM analyses were performed on selected fracture surfaces after tensile testing. The aim of this investigation was to correlate the measured tensile properties with the corresponding fracture morphology, with particular attention to the effect of the as-built condition and subsequent heat treatments on the activation of ductile fracture mechanisms.

Figure 4.64 reports representative SEM fractographs of horizontally built specimens produced from the low-nitrogen powder blend and tested at 22 °C. The as-built condition is compared with the heat-treated states at 1020 °C for 35 min and 1080 °C for 35 min, selected among the least favourable tensile responses reported in Table 4.20 and Figure 4.62a. The low-magnification images provide an overview of the fracture surface morphology, whereas the higher-magnification details allow the local fracture micromechanisms to be assessed. In this comparison, the as-built specimen shows a mixed fracture morphology with limited local ductility, while the heat-treated conditions exhibit a more evident dimpled morphology, consistent with the improvement in elongation after heat treatment.

Figure 4.65 reports representative SEM fractographs of vertically built specimens produced from the high-nitrogen powder blend and tested at 22 °C. The figure compares the as-built condition with the heat-treated state at 1080 °C for 35 min, considering specimens selected among the least favourable tensile responses reported in Table 4.21 and Figure 4.63. As for the low-nitrogen horizontal specimens, the upper row provides low-magnification overviews of the fracture surfaces, whereas the lower row highlights the local fracture micromechanisms. The as-built specimen shows a mixed fracture morphology with limited evidence of local ductility, while the heat-treated specimens exhibit a more pronounced dimpled morphology, in agreement with the improvement in elongation after heat treatment.

Compared with the low-nitrogen specimens built in the horizontal direction and reported in Figure 4.64, the fracture surfaces of the high-nitrogen vertically built specimens show a more evident texture associated with the laser scanning tracks. In the low-nitrogen horizontal specimens, this process-induced texture was not clearly highlighted by the fracture surface morphology. This difference suggests that the fracture path in the vertically built condition may be more affected by the directional features inherited from the PBF-LB/M process. Nevertheless, the higher-magnification observations still indicate a predominantly ductile fracture mode, characterized by numerous small dimples.

The observation of the fracture surfaces of the tensile specimens tested at −46 °C highlighted the same main features identified for the specimens tested at 22 °C.

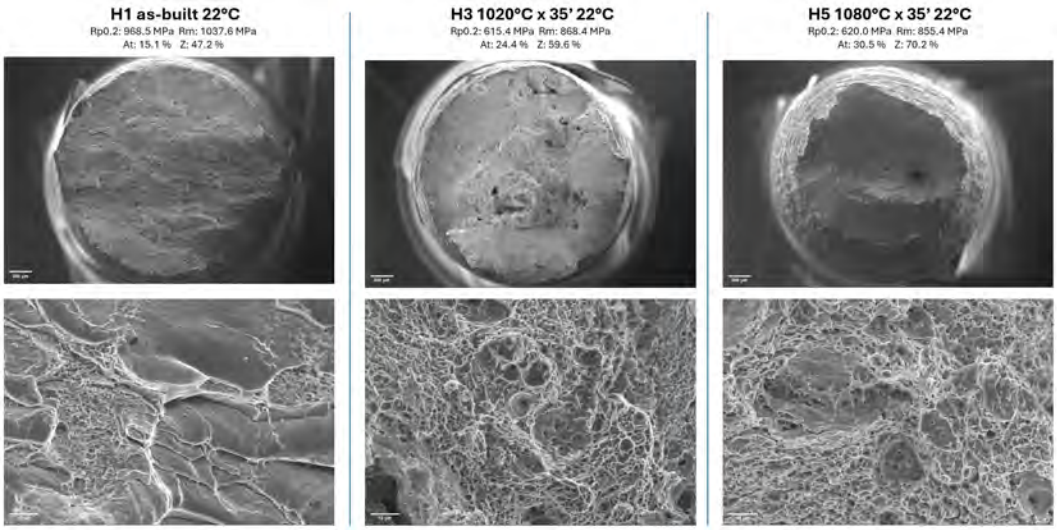

Fig. 4.64 SEM fractographs of PBF-LB/M UNS S32760 tensile specimens produced from a low-nitrogen powder blend, built in the horizontal direction with respect to the PBF-LB/M build axis Z, and tested at 22 °C. The figure compares the as-built condition with the heat-treated states at 1020 °C for 35 min and 1080 °C for 35 min, corresponding to representative specimens among the least favourable tensile responses reported in Table 4.20 and Figure 4.62a. For each condition, the upper row shows a low-magnification overview of the fracture surface, whereas the lower row highlights the corresponding fracture micromechanisms. The as-built specimen exhibits a mixed fracture morphology with limited local ductility, while the heat-treated conditions show a more pronounced dimpled fracture surface, consistent with the increased elongation after heat treatment. The main tensile properties measured for each specimen are reported above the corresponding fractograph.

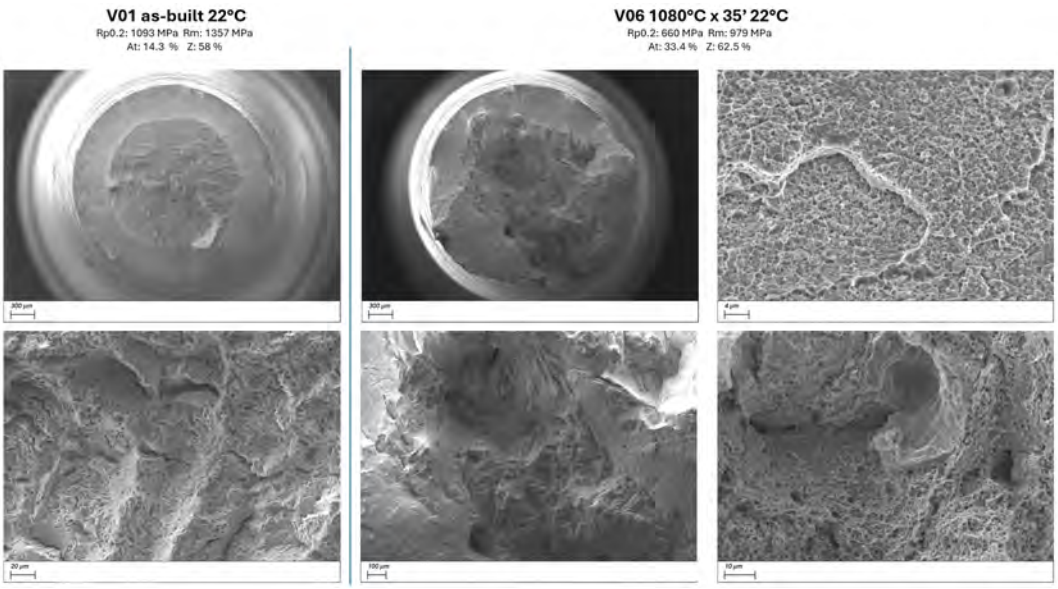

Fig. 4.65 SEM fractographs of PBF-LB/M UNS S32760 tensile specimens produced from a high-nitrogen powder blend, built in the vertical direction with respect to the PBF-LB/M build axis Z, and tested at 22 °C. The figure compares the as-built condition with the heat-treated states at 1080 °C for 35 min, corresponding to representative specimens among the least favourable tensile responses reported in Table 4.21 and Figure 4.63. For each condition, the upper row shows a low-magnification overview of the fracture surface, whereas the lower row highlights the corresponding fracture micromechanisms. The as-built specimen exhibits a mixed fracture morphology with limited local ductility, while the heat-treated conditions show a more pronounced dimpled fracture surface, consistent with the increased elongation after heat treatment. The main tensile properties measured for each specimen are reported above the corresponding fractograph.

4.7 Influence of Defects on the High-Cycle Fatigue Behaviour of PBF-LB/M UNS S32760 samples

4.7.1 Introduction

Since evident defects related to issues associated with the manufacturing technology were detected in the available samples, mainly attributable to lack-of-fusion regions, the main objective of the tests became the evaluation of the impact of these defects on fatigue resistance in the HCF regime. This defectiveness is documented by the SEM images reported later in this section.

4.7.2 Materials and Methods

4.7.2.1 High-Cycle Fatigue Testing Conditions

High-cycle fatigue tests were performed on PBF-LB/M UNS S32760 specimens produced from a high-nitrogen powder mixture, built in both vertical and horizontal orientations with respect to the Z-axis of the PBF-LB/M machine. The samples were manufactured using the Aconity Mini 3D PBF-LB/M system [119], adopting the optimized process parameters, consisting of a laser power of 300 W and a scanning speed of 900 mm/s, as discussed in Section 4.4. The tests were carried out at room temperature using an Instron 8802 machine equipped with a 25 kN load cell, adopting a sinusoidal waveform, a frequency of 50 Hz and a load ratio of $R = 0.1$. The run-out was set at 10 million cycles.

4.7.2.2 Powder reuse assessment and Complementary mechanical characterisation

Since the high-nitrogen powder blend was used for the optimisation of the PBF-LB/M process parameters (see Section 4.4), as well as for the fabrication of the specimens intended for impact toughness tests (see Section 4.6.3) and tensile tests (see Section 4.6.5), a further powder characterisation was carried out in terms of particle size distribution (PSD) and oxygen content. The aim of this analysis was to assess the possible degradation of the powder after exposure to the PBF-LB/M

process, by comparing its condition with that of the virgin, unprocessed powder. Based on the data reported in Table 4.22, it can be observed that the powder used to manufacture the pillars for the HCF fatigue tests and the corresponding tensile specimens still retained suitable characteristics in terms of PSD, oxygen, nitrogen, carbon and sulfur contents. In particular, no significant variations were detected with respect to the initial virgin powder condition, indicating that the powder did not undergo substantial degradation during the previous PBF-LB/M processing steps.

Table 4.22 Comparison between the particle size distributions and chemical composition of virgin powders never processed by PBF-LB/M and powders after PBF-LB/M processing. The graph reports both the frequency and cumulative volume distributions. The first sub-table summarizes the corresponding particle size distribution parameters, D10, D50 and D90, together with the cumulative volume fractions within selected size intervals. The second sub-table reports the measured contents of O, N, C and S.

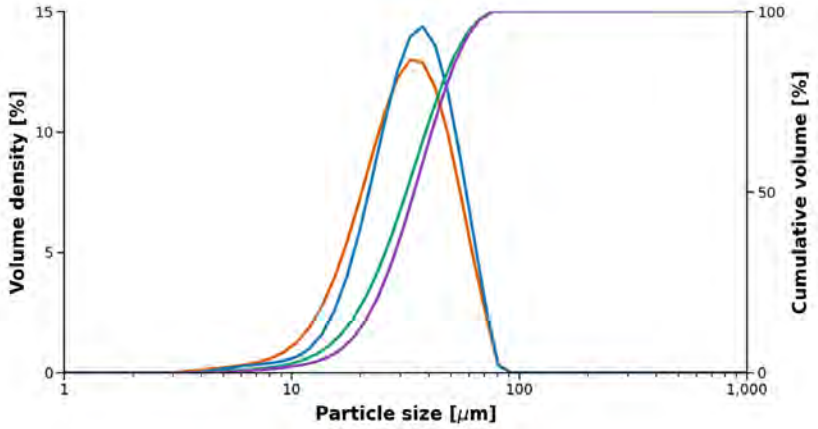

Sample	Curve identification	Particle size distribution parameters			Selected size ranges	
		D10 [μm]	D50 [μm]	D90 [μm]	Range [μm]	Volume fraction [%]
Virgin powders never processed by PBF-LB/M		16.1	31.9	54.3	0–20	18.21
					20–63	77.80
					20–75	81.49
Powders after PBF-LB/M processing		18.8	34.5	56.1	0–20	12.28
					20–63	83.90
					20–75	87.41

Sample	O [wt.%]	N [wt.%]	C [wt.%]	S [wt.%]
Virgin powders never processed by PBF-LB/M	0.02750 ± 0.00031	0.479 ± 0.0030	0.0205 ± 0.00118	0.000843 ± 0.000147
Powders after PBF-LB/M processing	0.02910 ± 0.00016	0.450 ± 0.0003	0.0183 ± 0.00115	0.001230 ± 0.000129

Tensile tests were carried out on material belonging to the same production job from which the specimens intended for HCF fatigue tests were obtained; these data are reported in Table 4.23.

The tensile tests were performed at room temperature using an Instron 3384 machine equipped with a 25 kN load cell. Strain was acquired by means of a digital image correlation system (VIC-2D 2009 software), using a digital extensometer, on flat dog-bone sub-size tensile specimens according to the ASTM E8 geometry [135]. The tests were performed at room temperature by imposing a strain rate of 1 s^{-1} [131].

Profilometry-based Indentation Plastometry (PIP) tests, performed using the Plastometrex PLX-Benchtop system, a proprietary non-destructive mechanical characterization method developed by Plastometrex [136], were performed samples produced in the same manufacturing jobs used to obtain the samples intended for tensile and HCF fatigue testing.

4.7.2.3 HCF Specimen Preparation and Applied Heat Treatment

In particular, for both the tensile tests and the HCF tests, the specimens were obtained from pillars with dimensions of 100 × 12 × 20 mm, built by PBF-LB/M in both horizontal and vertical orientations with respect to the *Z*-axis of the machine. The pillars were subjected to a solution heat treatment at 1080 °C for 35 min according to the conditions reported in sub-section 4.5.2.6, followed by water cooling. Subsequently, a stress-relief treatment at 200 °C for 2 h was performed in order to limit possible distortions during the subsequent electrical discharge machining used to obtain both the tensile specimens and those intended for HCF testing. The tensile and HCF specimens were then surface-prepared using the abrasive paper sequence 320, 600, 1200 and 2500 grit, as shown in Figure 4.66.

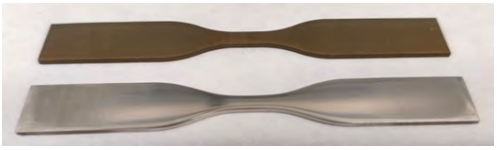

Fig. 4.66 Representative HCF specimen obtained by electrical discharge machining from a PBF-LB/M pillar. The upper specimen shows the as-cut condition after EDM, whereas the lower specimen shows the surface condition after preparation using the abrasive paper sequence 320, 600, 1200 and 2500 grit.

The geometry of the tensile and HCF specimens is shown in Figures 4.67a) and 4.67b).

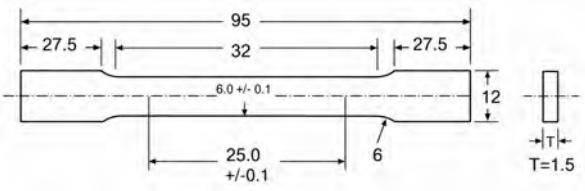

a) Geometry of the tensile specimen.

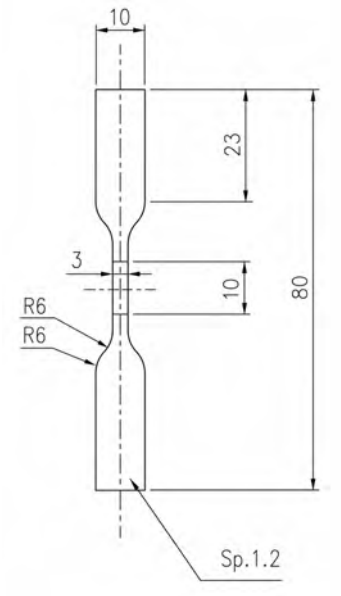

b) Geometry of the HCF fatigue specimen.

Fig. 4.67 Geometry of the specimens used for mechanical characterization: (a) tensile specimen and (b) HCF fatigue specimen.

4.7.3 Tensile characterization of the HCF specimen production job

The results of the tensile tests, reported in Table 4.23, therefore make it possible to associate the cyclic response of the HCF specimens with a framework of the static mechanical properties of the material processed and post-treated under the same conditions.

Table 4.23 Summary of tensile test results for PBF-LB/M UNS S32760 specimens produced from a blend of high-nitrogen powders, heat treated at 1080°C for 35 min, and tested on flat dog-bone sub-size tensile specimens according to the ASTM E8 geometry [135]. Two specimen groups are reported, corresponding to the horizontal and vertical build directions. The reported average austenite values were determined by XRD. Additional tensile parameters, including the Hollomon strain-hardening exponent n (Eq. 4.8), derived from tensile-curve analysis, are reported in the lower sub-table.

ID	Build direction	HT state	HT time	Austenite [vol.%] on plane	Test temp.	A_0 [mm^2]	$R_{p0.2}$ [MPa]	R_m [MPa]	A_{gt} [%]	A_t [%]	Z [%]
H06-a	Horiz.	1080°C	35 min	plane xy: 61.4 ± 1.1 plane zy: 61.7 ± 2.1	22°C	8.48	622	854	17.1	23.0	37.8
H06-b						7.92	648	908	17.7	25.0	39.4
H06-c						8.06	607	891	18.1	24.0	44.9
H06-d						8.35	649	922	18.9	25.0	49.0
V06-a	Vert.			plane xy: 59.5 ± 2.4 plane zy: 60.5 ± 2.7		8.21	610	882	18.0	28.0	38.0
V06-b						7.69	594	817	16.9	21.0	40.3
V06-c						8.20	591	826	17.5	24.0	41.6
V06-d						7.79	750	948	17.0	24.0	40.8

ID	n	Poisson	W [MJ/m^3] up to $R_{p0.2}$	W [MJ/m^3] up to R_m	W [MJ/m^3] up to A_{gt}
H06-a	0.134	0.48	1.1	10.4	34.0
H06-b	0.143	0.53	1.4	12.1	21.4
H06-c	0.147	0.53	1.2	12.3	22.3
H06-d	0.146	0.52	1.4	13.0	23.1
V06-a	0.146	0.49	1.3	10.8	30.7
V06-b	0.155	0.57	1.2	10.5	26.2
V06-c	0.159	0.54	1.0	10.9	18.8
V06-d	0.114	0.56	1.1	9.7	23.2

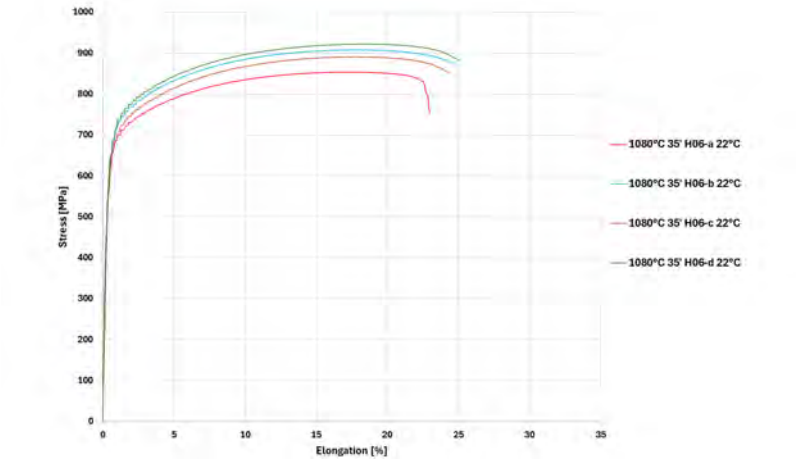

(a) PBF-LB/M UNS S32760 specimens produced from a high-nitrogen powder blend. The specimens were manufactured with horizontal orientation relative to the build-direction axis (Z) of the PBF-LB/M system and tested at 22°C.

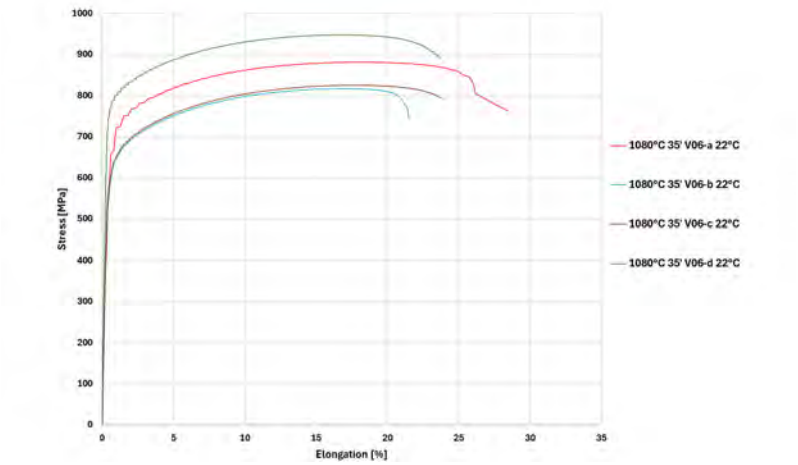

(b) PBF-LB/M UNS S32760 specimens produced from a high-nitrogen powder blend. The specimens were manufactured with vertical orientation relative to the build-direction axis (Z) of the PBF-LB/M system and tested at 22°C.

Fig. 4.68 Tensile test of PBF-LB/M UNS S32760 specimens produced from a high-nitrogen powder blend, built in the horizontal and vertical orientation, and tested at 22°C. The data corresponding to the individual curves are reported in Table 4.23.

4.7.3.1 Specimens built in the horizontal orientation

Overall, the specimens built in the horizontal orientation show a rather homogeneous mechanical response.

The $R_{p0.2}$ values range between 607 and 649 MPa, with an average value of approximately 632 MPa, whereas R_m varies between 854 and 922 MPa, with an average of approximately 894 MPa. In this group, specimen H06-a represents the most critical condition, showing the lowest R_m and Z values. To support the interpretation of this behaviour, the fracture surface of specimen H06-a was analysed by SEM and is reported in Figure 4.69. The fracture surface reveals the presence of several defect-related features, including lack-of-fusion regions containing partially or completely unmelted metallic powder particles, confirming the process-induced origin of these discontinuities. In contrast, areas not directly affected by lack-of-fusion defects show a more ductile fracture morphology, characterised by plastic deformation features and dimple-like microvoid coalescence. Therefore, the presence of extended lack-of-fusion defects may have contributed to the reduced R_m and reduction of area Z measured for this specimen.

The uniform elongation A_{gt} ranges between 17.1 and 18.9%, while the total elongation A_t lies between 23.0 and 25.0%. The reduction of area Z, ranging between 37.8 and 49.0%, further confirms a good capacity for localised deformation before fracture.

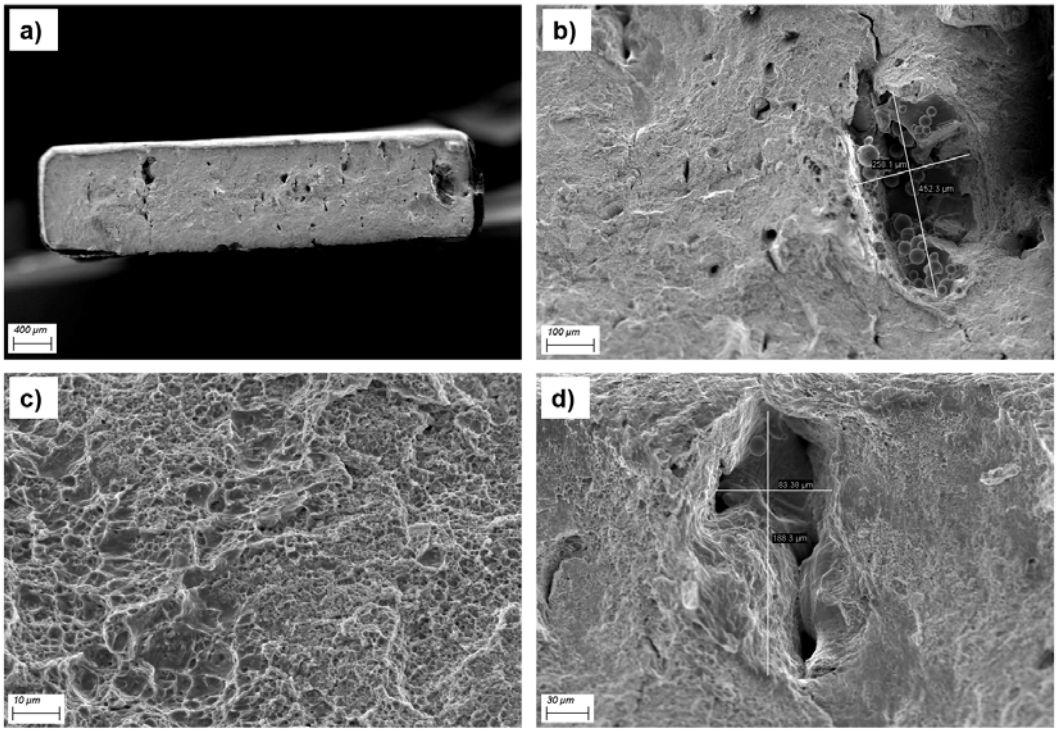

Fig. 4.69 SEM fracture surface of tensile specimen H06-a, selected as representative of the most critical horizontal tensile condition. Image (a) shows a general overview of the fracture surface, where several defect-related features can be observed. Images (b) and (d) highlight lack-of-fusion defects; in these regions, partially or completely unmelted metallic powder particles are still visible inside the cavities, confirming the process-induced origin of the discontinuities. Image (c) shows a region not directly affected by lack-of-fusion defects, where a ductile fracture morphology with plastic deformation features and dimple-like microvoid coalescence can be observed. Overall, the presence of extended lack-of-fusion defects may have contributed to the lower R_m and reduction of area Z measured for this specimen.

4.7.3.2 Specimens built in the vertical orientation

For the specimens built in the vertical orientation, the values are more scattered. In particular, specimen V06-b represents one of the most critical conditions found, showing the lowest R_m and A_t values within the vertical group; its fracture surface is reported in Figure 4.70 to support the interpretation of the possible influence of lack-of-fusion defects on the tensile response. Considering all specimens V06-a, V06-b, V06-c and V06-d, $R_{p0.2}$ varies between 591 and 750 MPa, with an average value of approximately 636 MPa.

However, specimen V06-d shows a significantly higher value than the other three specimens, which are instead concentrated between 591 and 610 MPa. The same behaviour is observed for R_m, which varies between 817 and 948 MPa, with V06-d again characterised by the maximum value. This improved tensile response can be related to the absence of extended lack-of-fusion defects on the fracture surface, as shown in Figure 4.71. In contrast to the other specimens, where lack-of-fusion defects appear to play a more critical role, specimen V06-d mainly exhibits only small isolated pores, suggesting a less severe defect population and, consequently, a lower detrimental effect on the measured tensile properties. Excluding this specimen, the values of the vertical specimens are more homogeneous and slightly lower than those of the horizontal specimens in terms of ultimate tensile strength. The uniform elongation of the vertical specimens nevertheless remains comparable to that of the horizontal specimens, with values ranging between 16.9 and 18.0%, whereas A_t varies between 21.0 and 28.0%. The reduction of area ranges between 38.0 and 41.6%, apart from variations that are still limited, indicating an overall stable plastic response.

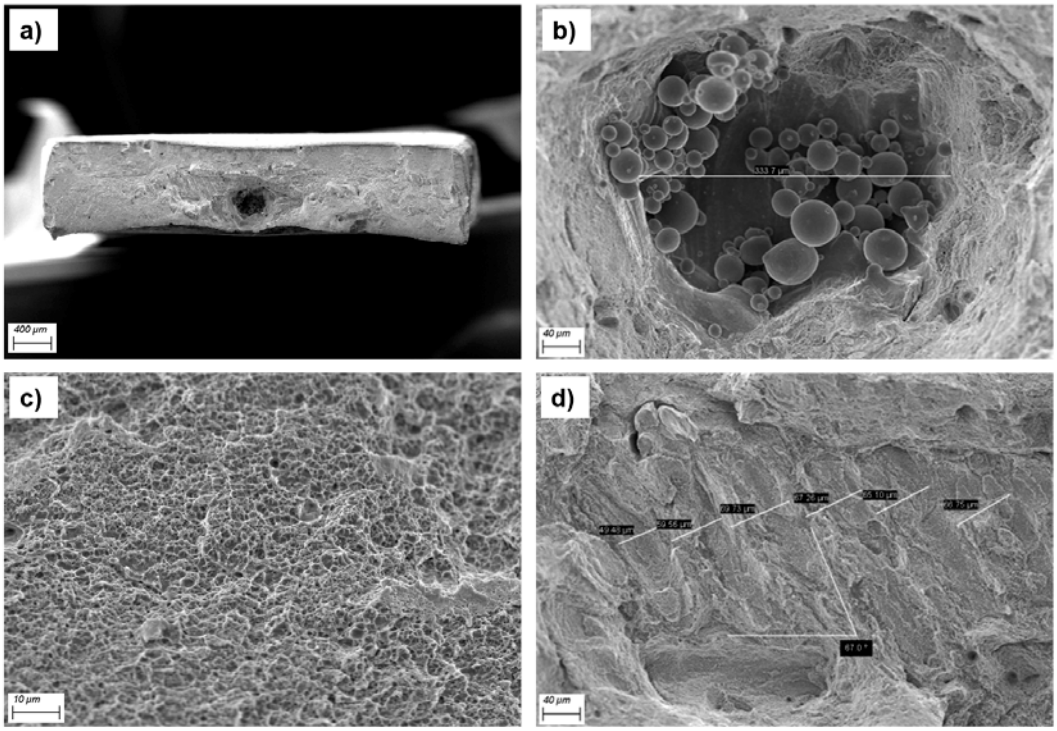

Fig. 4.70 SEM fracture surface of tensile specimen V06-b, selected as representative of one of the most critical vertical tensile conditions. Image (a) shows a general overview of the fracture surface, where a large defect-related region is visible. Image (b) highlights a lack-of-fusion defect containing partially or completely unmelted metallic powder particles, confirming the process-induced origin of the discontinuity. Image (c) shows a region not directly affected by lack-of-fusion defects, where a ductile fracture morphology characterised by plastic deformation and dimple-like microvoid coalescence can be observed. Image (d) reveals the overlap of adjacent laser scan tracks on the fracture surface, with a characteristic inclination angle of approximately 67°, consistent with the scan strategy adopted during PBF-LB/M processing. Overall, the presence of extended lack-of-fusion defects may have contributed to the lower tensile performance observed for this specimen.

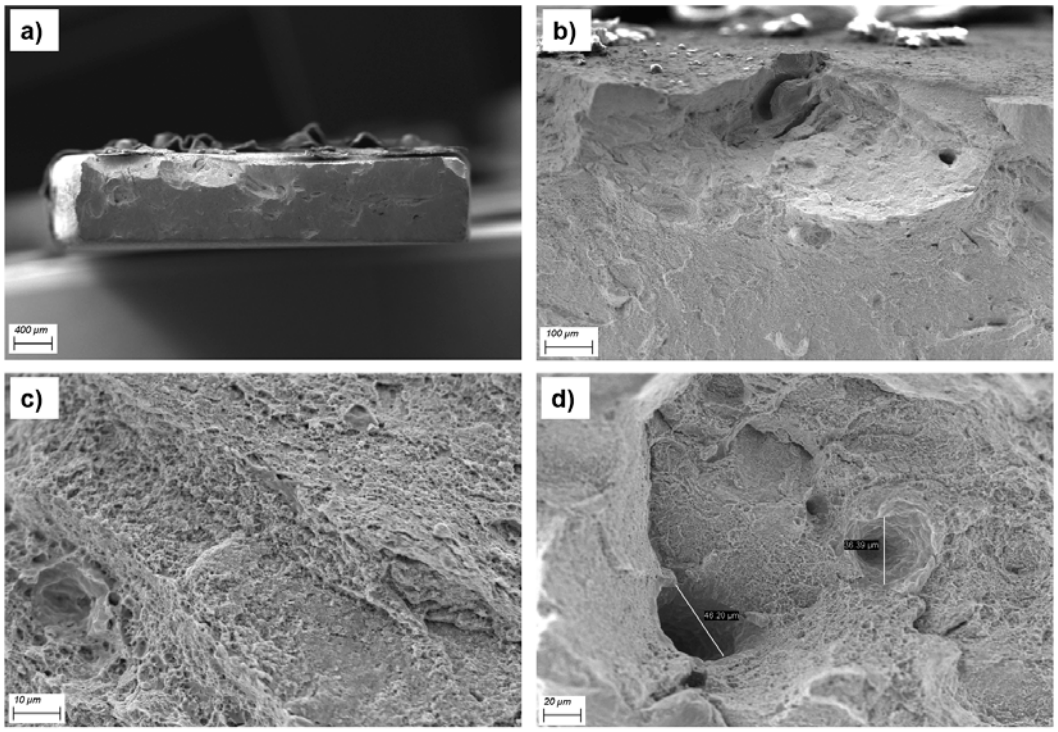

Fig. 4.71 SEM fracture surface of tensile specimen V06-d, showing the absence of extended lack-of-fusion defects and the presence of only limited isolated porosity. Image (a) provides a general overview of the fracture surface, where no extended lack-of-fusion defects can be observed. Image (b) highlights a defect located close to the external surface of the specimen, which likely acted as a preferential fracture nucleation site. Image (c) shows a region not directly affected by defects, where ductile fracture features associated with plastic deformation and dimple-like microvoid coalescence are visible; the morphology appears locally influenced by the different planes and layers generated during the PBF-LB/M process. Image (d) shows isolated pores on the fracture surface, representative of typical porosity defects associated with PBF-LB/M processing.

4.7.3.3 Analysis of the strain-hardening exponent n

The analysis of the strain-hardening exponent n highlights limited differences between the two orientations. In the horizontal specimens, n varies between 0.134 and 0.147, with an average value of approximately 0.143. In the vertical specimens, the values range between 0.114 and 0.159, with an average also equal to approximately 0.144. The presence of the lowest value for V06-d, equal to 0.114, is consistent with the higher $R_{p0.2}$ value measured on the same specimen, suggesting a lower strain-hardening capacity after yielding. Excluding V06-d, the vertical specimens show slightly higher n values, ranging between 0.146 and 0.159, indicating a strain-hardening capacity at least comparable, if not slightly more favourable, than that of the horizontal specimens.

The comparison with the data previously obtained on the cylindrical vertical specimens reported in Table 4.21 must be carried out with caution, since the two series differ in specimen geometry and strain measurement methodology. The specimens in Table 4.23 are flat ASTM E8 [135] specimens measured by VIC, whereas the data in Table 4.21 derive from cylindrical specimens tested with an extensometer. Limiting the comparison to the vertical specimens heat-treated at 1080 °C, the average $R_{p0.2}$ values are nevertheless of the same order of magnitude: approximately 636 MPa for the flat V06 specimens and approximately 653 MPa for the cylindrical V04–V06 specimens. Therefore, in terms of yield strength, no substantial differences emerge, except for a higher scatter in the flat specimens of the V06 group.

More evident differences instead emerge for R_m, A_t and Z. In the cylindrical vertical specimens heat-treated at 1080 °C, R_m is approximately 976–979 MPa, whereas in the flat vertical V06 specimens it varies between 817 and 948 MPa. Similarly, the total elongation of the cylindrical specimens reaches 32.4–33.6%, whereas in the flat V06 specimens it ranges between 21.0 and 28.0%. The reduction of area is also higher in the cylindrical specimens, equal to 53.4–62.5%, compared with 38.0–41.6% for the V06 specimens. These differences can be attributed to the different geometry, the different stressed volume, the different strain acquisition method and the higher sensitivity of flat specimens to the presence of defects, which, as stated and highlighted in Figure 4.70 and Figure 4.71 , characterise this job, as well as to edge effects and strain localisation.

Conversely, the parameter n is substantially comparable between the two series. The cylindrical vertical specimens heat-treated at 1080 °C show n values equal to 0.147–0.149, whereas the flat V06 specimens show values ranging between 0.146 and 0.159 for three specimens out of four, with only one lower value equal to 0.114. This suggests that the intrinsic strain-hardening capacity of the microstructure heat-treated at 1080 °C is fairly reproducible.

In summary, the H06 and V06 specimens belonging to the same job as the HCF specimens confirm that the heat treatment at 1080 °C for 35 min allows adequate static properties to be obtained, with $R_{p0.2}$ values around 600–650 MPa, ultimate tensile strength generally higher than 800 MPa and significant ductility. The tensile response is overall comparable between the horizontal and vertical orientations, although the vertical specimens show greater scatter, particularly for $R_{p0.2}$ and R_m.

However, the interpretation of the results must necessarily take into account the defect population observed in the available specimens, as highlighted in Figure 4.69 and Figure 4.70. The tensile data obtained on the same job provide the static reference necessary to interpret the cyclic behaviour in the presence of process-induced defects.

Compared with the previous cylindrical vertical specimens (see Table 4.21), the flat V06 specimens (see Table 4.23) show similar values of yield strength and strain-hardening exponent, but lower values of ultimate tensile strength, total elongation and reduction of area. This difference does not necessarily indicate a different intrinsic metallurgical quality of the material, but may reflect the combined effect of specimen geometry, measurement method and the higher sensitivity of flat specimens to PBF-LB/M defectiveness, particularly to the presence of lack of fusion.

4.7.4 High-cycle fatigue behaviour of PBF-LB/M UNS S32760 specimens affected by lack-of-fusion defects

Overall, the fatigue test results reported in Table 4.24 and Figure 4.72 highlight a significant scatter in fatigue life, which is typical of PBF-LB/M components in the presence of process-induced defects.
The lateral surfaces of selected HCF specimens were analysed in order to evaluate the role of surface and near-surface defects in fatigue crack initiation. As shown in Figure 4.73, particular attention was focused on the presence of lack-of-fusion defects on the specimen surface and on the possible occurrence of fatigue-related surface features, such as intrusions and extrusions, after cyclic loading.

Representative fracture surfaces of selected HCF specimens were investigated by SEM in order to assess the role of process-induced defects in fatigue crack initiation and propagation. The analysed specimens correspond to vertically built samples tested at different stress levels and fatigue lives, as reported in Figures 4.74–4.79.

The scatter becomes particularly evident when specimens tested at nominally similar load levels exhibit markedly different fatigue lives, as shown in Figure 4.73. This behaviour suggests that the HCF response is not controlled exclusively by the applied stress level, but also by the size, morphology, position and orientation of lack-of-fusion defects with respect to the loading direction. Indeed, in the HCF regime, the crack initiation stage represents a relevant fraction of the total life, as clearly highlighted in Figure 4.75 for the propagation extension; the presence of pre-existing defects reduces or partially eliminates this stage, causing the fatigue life to be dominated by the propagation of cracks originating from discontinuities already present within the volume or close to the surface, as observable in Figure 4.73 and Figure 4.75.

Table 4.24 HCF fatigue test data for PBF-LB/M UNS S32760 specimens produced from a high-nitrogen powder blend and built in the horizontal and vertical orientations. The specimens are reported in decreasing order of applied load. Green cells indicate run-out specimens, which reached 10^7 cycles without failure.

Horizontal orientation				**Vertical orientation**			
Specimen	**Load [MPa]**	**Cycles**	**Outcome**	**Specimen**	**Load [MPa]**	**Cycles**	**Outcome**
02-H-d	590	231 354	Failure	01-V-b	685	117 560	Failure
01-H-c	580	661 901	Failure	01-V-c	665	48 481	Failure
01-H-e	570	624 255	Failure	01-V-d	645	194 740	Failure
02-H-c	570	157 886	Failure	01-V-e	635	1 947 165	Failure
01-H-a	565	10^7	Run-out	02-V-b	625	91 548	Failure
02-H-e	565	141 662	Failure	02-V-c	625	92 782	Failure
01-H-d	560	6 149 010	Failure	02-V-d	625	104 547	Failure
02-H-a	550	134 861	Failure	02-V-e	600	111 034	Failure
02-H-b	550	10^7	Run-out	01-V-a	600	105 322	Failure
03-H-c	550	201 838	Failure	03-V-b	580	45 831	Failure
01-H-b	520	10^7	Run-out	03-V-c	540	1 247 256	Failure
				03-V-e	520	255 630	Failure
				02-V-a	520	150 482	Failure
				03-V-d	500	10^7	Run-out
				03-V-a	500	10^7	Run-out

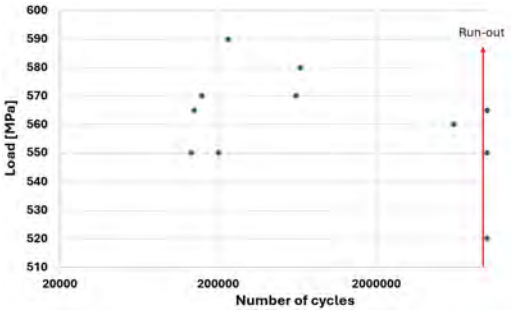

(a) HCF fatigue test results for horizontally built PBF-LB/M UNS S32760 specimens. The graph reports the applied load as a function of the number of cycles to failure; run-out specimens reached 10^7 cycles without failure.

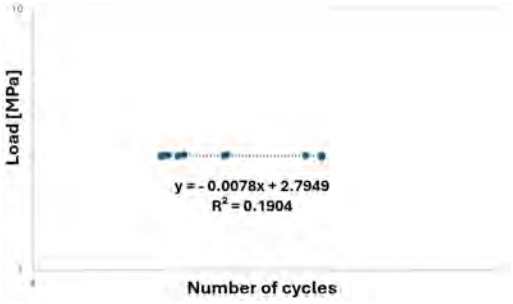

(b) Regression analysis of the HCF data for horizontally built specimens. The graph reports the fitted trend, the corresponding equation and the coefficient of determination R^2.

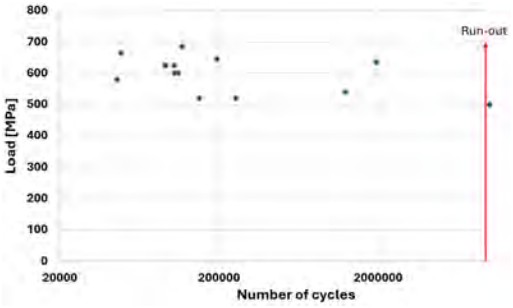

(c) HCF fatigue test results for vertically built PBF-LB/M UNS S32760 specimens. The graph reports the applied load as a function of the number of cycles to failure; run-out specimens reached 10^7 cycles without failure.

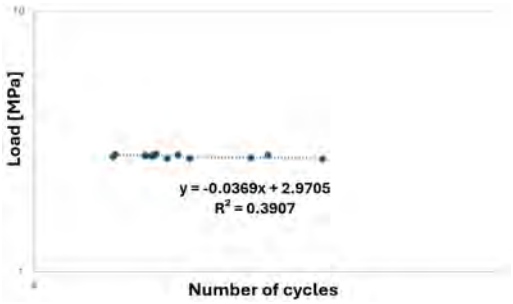

(d) Regression analysis of the HCF data for vertically built specimens. The graph reports the fitted trend, the corresponding equation and the coefficient of determination R^2.

Fig. 4.72 HCF fatigue test results for PBF-LB/M UNS S32760 specimens produced from a high-nitrogen powder blend and built in the horizontal and vertical orientations relative to the build-direction axis of the PBF-LB/M system. The experimental data are shown together with the corresponding regression plots, including fitted equations and R^2 values. Run-out specimens reached 10^7 cycles without failure.

4.7.4.1 HCF specimens built in the vertical orientation

For the specimens built in the vertical orientation, a general tendency towards a reduction in the number of cycles to failure with increasing applied load is observed. The specimens tested at higher levels, between 645 and 685 MPa, show relatively limited lives, ranging from approximately 4.8×10^4 to 1.9×10^5 cycles. In particular, specimen 01-V-c, tested at 665 MPa, failed after 48481 cycles, whereas specimen 01-V-b, tested at 685 MPa, reached 117560 cycles, as also shown in Figure 4.74. At 645 MPa, specimen 01-V-d showed a life of 194740 cycles. These results would suggest that, in the presence of PBF-LB/M defects, even moderate variations in the load level can produce a significant variation in fatigue life, although the scatter associated with the defect population remains highly relevant.

A particularly critical behaviour is observed in the vertical specimens tested at 625 MPa, as shown in Figure 4.75, for which three specimens failed within a very narrow interval, between approximately 9.1×10^4 and 1.0×10^5 cycles. This repeatability suggests that, for this specific combination of orientation, load level and defect population, fatigue damage was governed by defects comparable in terms of severity. Conversely, at lower loads, the scatter increases significantly. At 520 MPa, for example, values of 150482 and 255630 cycles were obtained, whereas at 500 MPa two specimens reached 10^7 cycles without failure. The latter can be considered as run-out specimens and indicate that, for the vertical orientation, the experimental survival limit under the investigated conditions is located around 500 MPa, at least for the specimens in which the critical defects were not sufficiently severe to induce failure before reaching the test limit.

4.7.4.2 HCF specimens built in the horizontal orientation

In the case of the specimens built in the horizontal orientation, the experimental response appears even more scattered. Some specimens reached 10^7 cycles even at relatively high load levels, such as 565 MPa for specimen 01-H-a, 550 MPa for specimen 02-H-b and 520 MPa for specimen 01-H-b. However, at the same load level of 550 MPa, other specimens showed early failure, such as 02-H-a at 134861 cycles and 03-H-c at 201838 cycles. This result is particularly significant because it demonstrates that, in the presence of lack of fusion, the concept of a nominal fatigue limit becomes strongly dependent on defect statistics. In other words, at

the same nominal stress, a specimen may behave as a run-out or fail after a few hundred thousand cycles depending on the presence of a critical defect in the most highly stressed region. This interpretation is supported by the SEM fracture surfaces reported in Figure 4.77, where specimens 02-H-a and 03-H-c show defect-related crack initiation regions located at or very close to the specimen surface. The same figure also reports specimen 01-H-d, which failed only after approximately 6.1×10^6 cycles at 560 MPa. In this case, the critical defect is located within the internal volume of the specimen, suggesting that not only the size and extension of the defect, but also its position with respect to the surface, strongly affects the fatigue life.

For the horizontal orientation, the failures observed between 565 and 590 MPa show lives ranging from approximately 1.4×10^5 to 6.6×10^5 cycles, with the exception of specimen 01-H-d, which at 560 MPa reached approximately 6.1×10^6 cycles before failure. This behaviour confirms the strong variability of the fatigue response, compatible with a non-uniform distribution of lack-of-fusion defects. The presence of a run-out specimen at 565 MPa and of specimens failed at similar or lower loads highlights that the severity of the critical defect can prevail over the effect of the nominal load, especially when the defect population is not controlled or not homogeneously distributed. Further evidence is provided by the fracture surfaces shown in Figure 4.78, which include specimens 02-H-e, 02-H-c and 01-H-c, tested at 565, 570 and 580 MPa, respectively. These specimens failed within the same lifetime range described above, and their fracture surfaces reveal defect-related regions and local discontinuities consistent with lack-of-fusion-induced crack initiation. Overall, the SEM observations confirm that the fatigue response of horizontally built specimens is governed by a combined effect of nominal stress level, defect size, defect morphology and defect location.

4.7.4.3 Comparison of HCF Specimens Built in Vertical and Horizontal Orientations

The comparison between vertical and horizontal orientation does not allow a clear superiority of one configuration over the other to be identified, due to the high scatter and the presence of run-outs at different load levels. However, some considerations can be made. The vertical specimens show systematic failures at high and intermediate loads, with run-outs observed only at 500 MPa. The horizontal specimens, instead, show run-outs also at 550–565 MPa, but at the same time premature failures

at the same load level. This would suggest that the horizontal orientation may, in some cases, provide a more favourable response, but only when the defect population does not include critical discontinuities unfavourably oriented with respect to the applied stress field. In the presence of lack of fusion, indeed, fatigue life is strongly controlled by the interaction between defect and build orientation, rather than by the specimen direction alone.

From a microstructural and defect-related point of view, lack-of-fusion defects represent particularly detrimental discontinuities for fatigue, since they are often characterised by an irregular morphology, high internal roughness and reduced local radii of curvature. These features promote local stress intensification and make such defects preferential crack initiation sites. Moreover, if the defects are oriented nearly perpendicular to the loading direction, their effect becomes even more severe, since the projected area of the defect with respect to the plane of maximum stress increases. This aspect is particularly relevant in PBF-LB/M materials, in which the defect distribution may be strongly anisotropic and correlated with the scanning strategy, the overlap between tracks, interlayer remelting and the growth direction [134].

The comparison between the tensile properties reported in Table 4.23 and the load levels used in the HCF tests reported in Table 4.24 highlights that the maximum stresses applied during fatigue lie within a significant range with respect to the yield strength of the material. For the horizontal specimens, the fatigue loads, mainly between 520 and 590 MPa, are close to, but generally lower than, the average $R_{p0.2}$ value measured on the H06 specimens. For the vertical specimens, instead, some load levels applied during fatigue, up to 685 MPa, are comparable to or higher than the average $R_{p0.2}$ value of the V06 specimens, although specimen V06-d shows a higher yield strength. This aspect is relevant because it indicates that, under some conditions, the fatigue response may be influenced not only by the elastic-cyclic regime, but also by the possible activation of local plasticity in correspondence with lack-of-fusion defects.

The presence of run-out specimens up to 10^7 cycles indicates that the material, when free from critical defects in the stressed section, can nevertheless sustain relatively high cyclic loads. However, the premature failure observed in other specimens at similar loads highlights that the HCF resistance of the component cannot be evaluated only on the basis of the nominal microstructure or static properties. For

structural applications, the fatigue design of PBF-LB/M UNS S32760 components must therefore explicitly consider the residual defect population.

The vertical specimens show run-outs at 500 MPa, whereas the horizontal specimens reach 10^7 cycles also at higher loads, up to 565 MPa; however, premature failures at comparable load levels confirm that the presence of a critical defect can dominate the response. Stereo-microscope analyses performed on the HCF specimens revealed the presence of defects with an average size of 46.05 ± 27.76 μm, further supporting the role of local defectiveness in controlling the fatigue behaviour. Therefore, the optimisation of the fatigue resistance of UNS S32760 steel specimens produced by PBF-LB/M requires not only the control of the chemical composition of the starting powder and of the microstructure through a suitable heat treatment, but above all the correct selection of process parameters, the verification of the maintenance condition of the PBF-LB/M system, an appropriate scanning strategy, and possible post-processing treatments aimed at reducing the residual internal defect population, such as HIP.

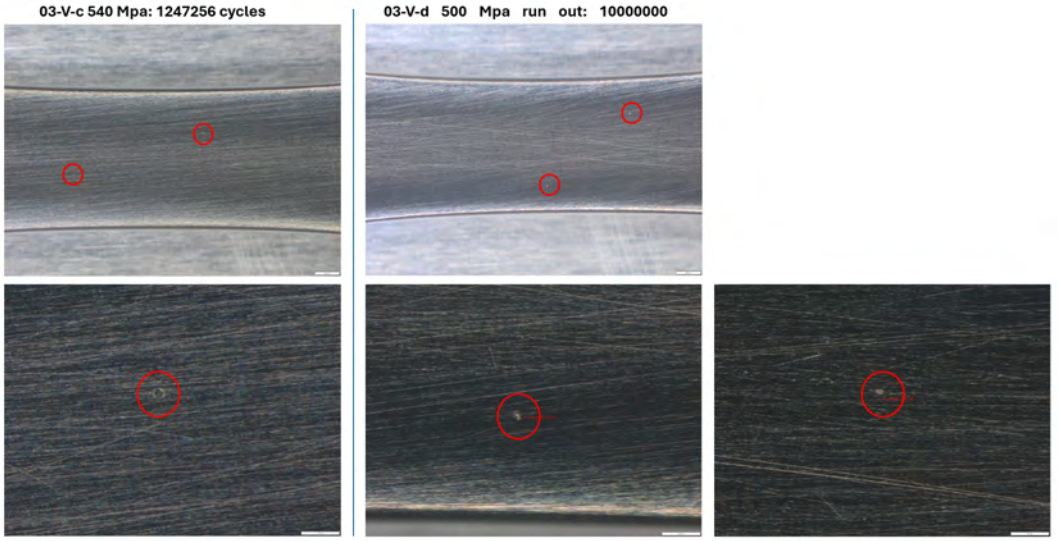

Fig. 4.73 Stereo-microscope observations of surface defects detected on selected HCF specimens. The images highlight the presence of surface and near-surface discontinuities, mainly attributable to lack-of-fusion defects, which can act as preferential crack nucleation sites under cyclic loading. The comparison between fractured and run-out specimens further supports the dominant role of the defect population in controlling the fatigue response of the investigated PBF-LB/M UNS S32760 samples.

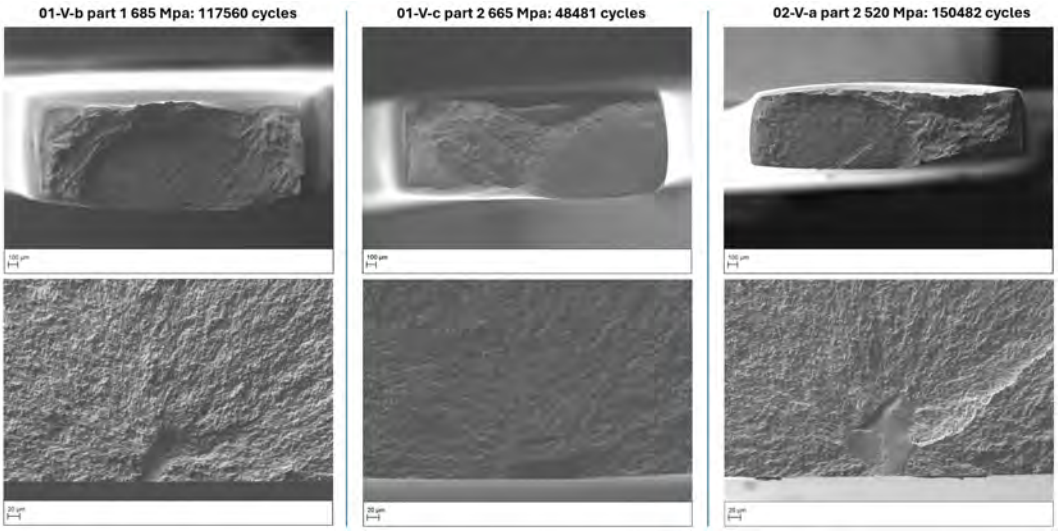

Fig. 4.74 SEM fracture surfaces of vertically built LPBF UNS S32760 HCF specimens. The figure reports representative fracture surfaces of specimen 01-V-b, tested at 685 MPa and failed after 117560 cycles; specimen 01-V-c, tested at 665 MPa and failed after 48481 cycles; and specimen 02-V-a, tested at 520 MPa and failed after 150482 cycles. The images show the overall fracture morphology and higher-magnification details of defect-related regions, highlighting the role of lack-of-fusion defects and local discontinuities in fatigue crack initiation.

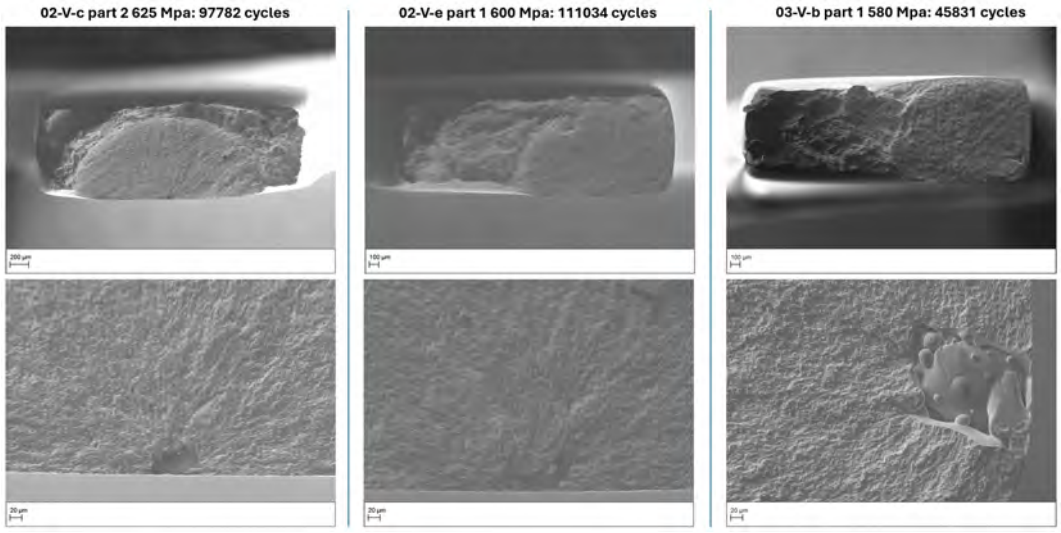

Fig. 4.75 SEM fracture surfaces of vertically built LPBF UNS S32760 HCF specimens. The figure reports representative fracture surfaces of specimen 02-V-c, tested at 625 MPa and failed after 92782 cycles; specimen 02-V-e, tested at 600 MPa and failed after 111034 cycles; and specimen 03-V-b, tested at 580 MPa and failed after 45831 cycles. The fracture surfaces reveal the presence of defect-related fracture regions, including lack-of-fusion features and partially unmelted powder particles, which may have promoted premature fatigue failure.

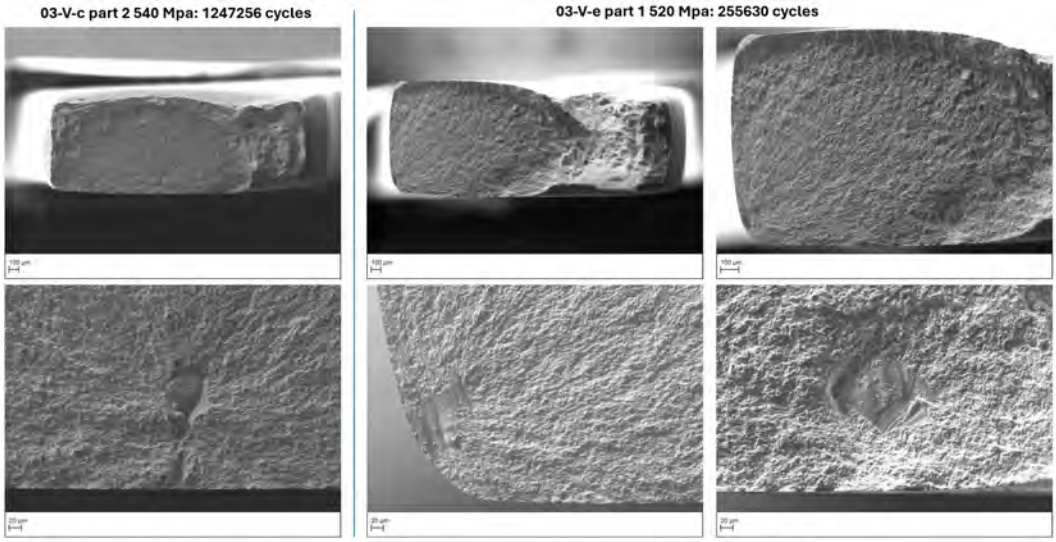

Fig. 4.76 SEM fracture surfaces of vertically built LPBF UNS S32760 HCF specimens. The figure reports representative fracture surfaces of specimen 03-V-c, tested at 540 MPa and failed after 1247256 cycles, and specimen 03-V-e, tested at 520 MPa and failed after 255630 cycles. The images show both the macroscopic fracture morphology and local defect-related features, indicating that fatigue crack initiation was strongly affected by the presence, size and location of process-induced defects.

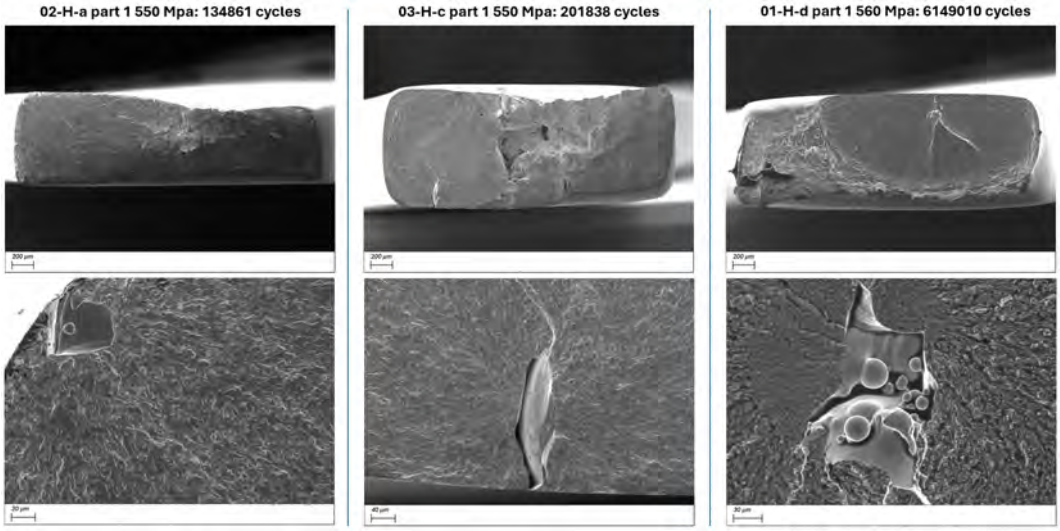

Fig. 4.77 SEM fracture surfaces of horizontally built PBF-LB/M UNS S32760 HCF specimens. The figure reports representative fracture surfaces of specimen 02-H-a, tested at 550 MPa and failed after 134861 cycles; specimen 03-H-c, tested at 550 MPa and failed after 201838 cycles; and specimen 01-H-d, tested at 560 MPa and failed after 6149010 cycles. The images show the overall fracture morphology and higher-magnification details of defect-related regions, highlighting the role of lack-of-fusion defects and local discontinuities in fatigue crack initiation. In particular, the comparison indicates that the fatigue life is not governed only by the size and extension of the critical defect, but also by its location with respect to the specimen surface. For specimens 02-H-a and 03-H-c, the defect-related crack initiation regions are located at or very close to the surface, favouring premature failure after a relatively low number of cycles. Conversely, in specimen 01-H-d, the critical defect is located within the internal volume of the specimen, leading to a delayed failure despite a comparable applied stress level. This evidence confirms the strong influence of both defect size and defect position on the fatigue response of horizontally built specimens.

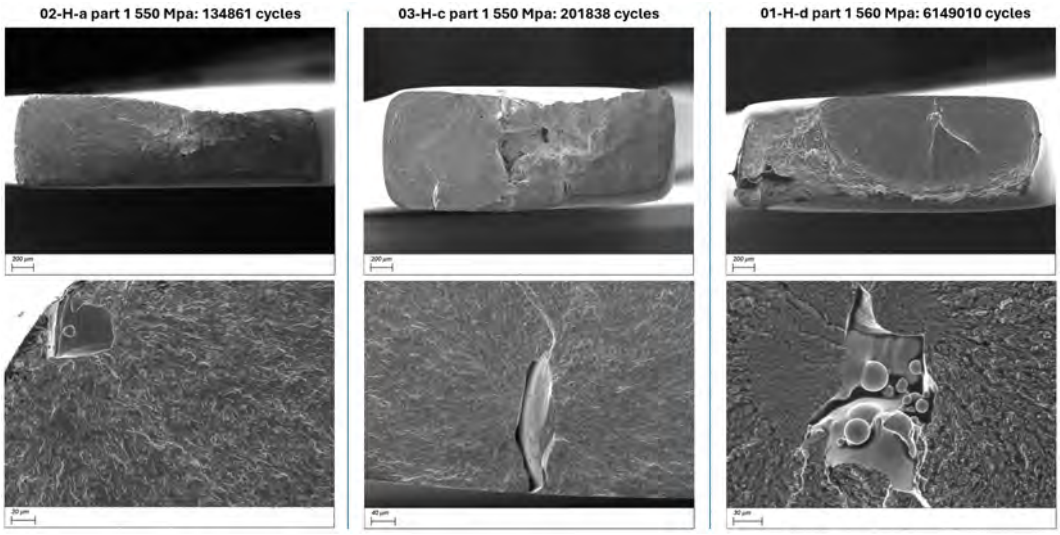

Fig. 4.78 SEM fracture surfaces of horizontally built PBF-LB/M UNS S32760 HCF specimens. The figure reports representative fracture surfaces of specimen 02-H-e, tested at 565 MPa and failed after 141662 cycles; specimen 02-H-c, tested at 570 MPa and failed after 157886 cycles; and specimen 01-H-c, tested at 580 MPa and failed after 661901 cycles. The images show the overall fracture morphology and higher-magnification details of defect-related regions, highlighting the role of lack-of-fusion defects and local discontinuities in fatigue crack initiation.

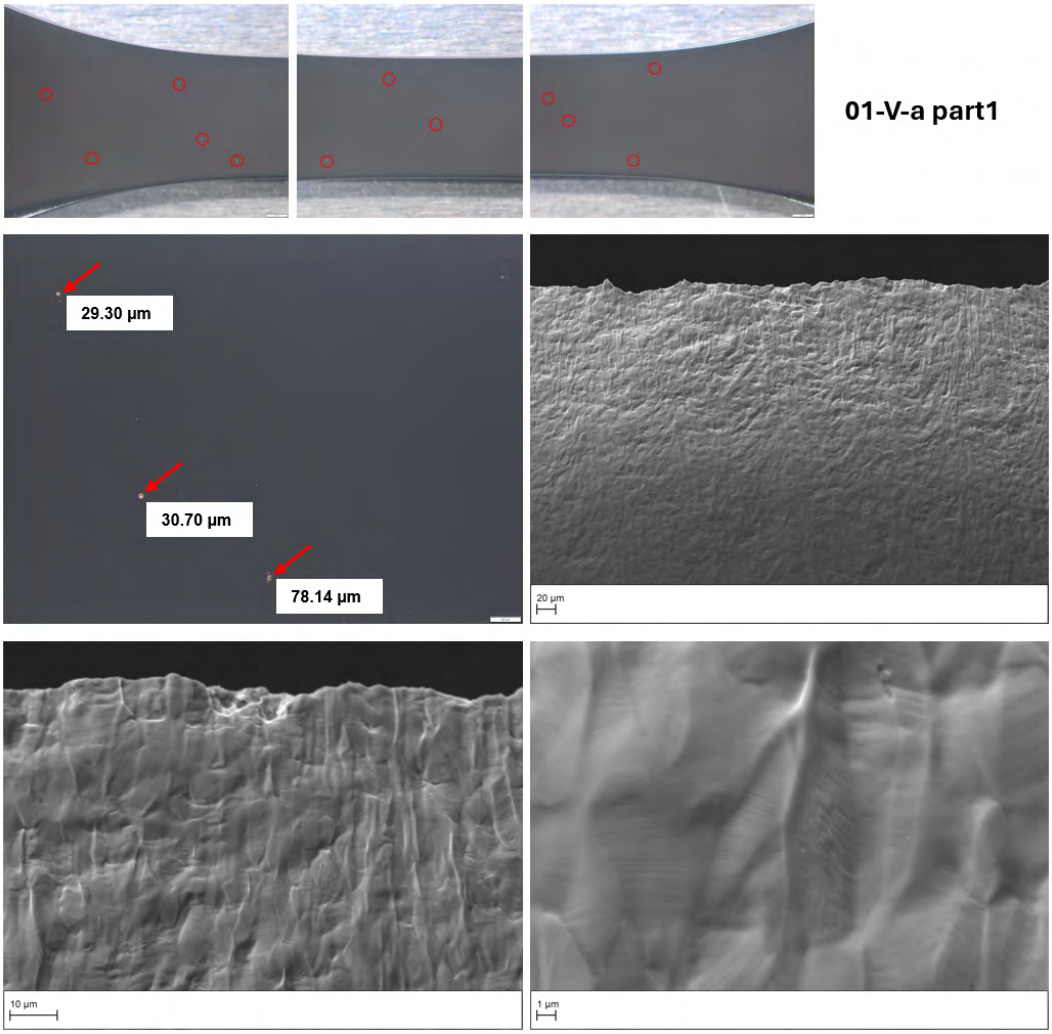

Fig. 4.79 Lateral surface of HCF specimen 01-V-a, superficially prepared up to colloidal silica polishing before fatigue testing and observed by SEM after fracture. Surface and near-surface lack-of-fusion defects are highlighted by red circles and arrows. The absence of evident intrusions and extrusions in the region below the fracture surface indicates that the reduced fatigue performance is mainly attributable to lack-of-fusion defects rather than to a fatigue damage mechanism governed by surface slip localization. These defects can act as preferential crack nucleation sites and dominate the fatigue response, preventing a clear assessment of the intrinsic microstructural contribution to crack initiation.

4.7.5 FE-SEM and EBSD analyses

FE-SEM and EBSD analyses were carried out in the region beneath the primary crack of specimen 02-H-d, tested in HCF at 590 MPa and failed after 231354 cycles. As reported in Figures 4.80–4.82, the aim was to correlate the fatigue crack path with the local microstructure, phase distribution and strain localisation features, as well as to provide a comparative assessment of the austenite content with respect to the values obtained by image analysis of optical micrographs and by XRD measurements.

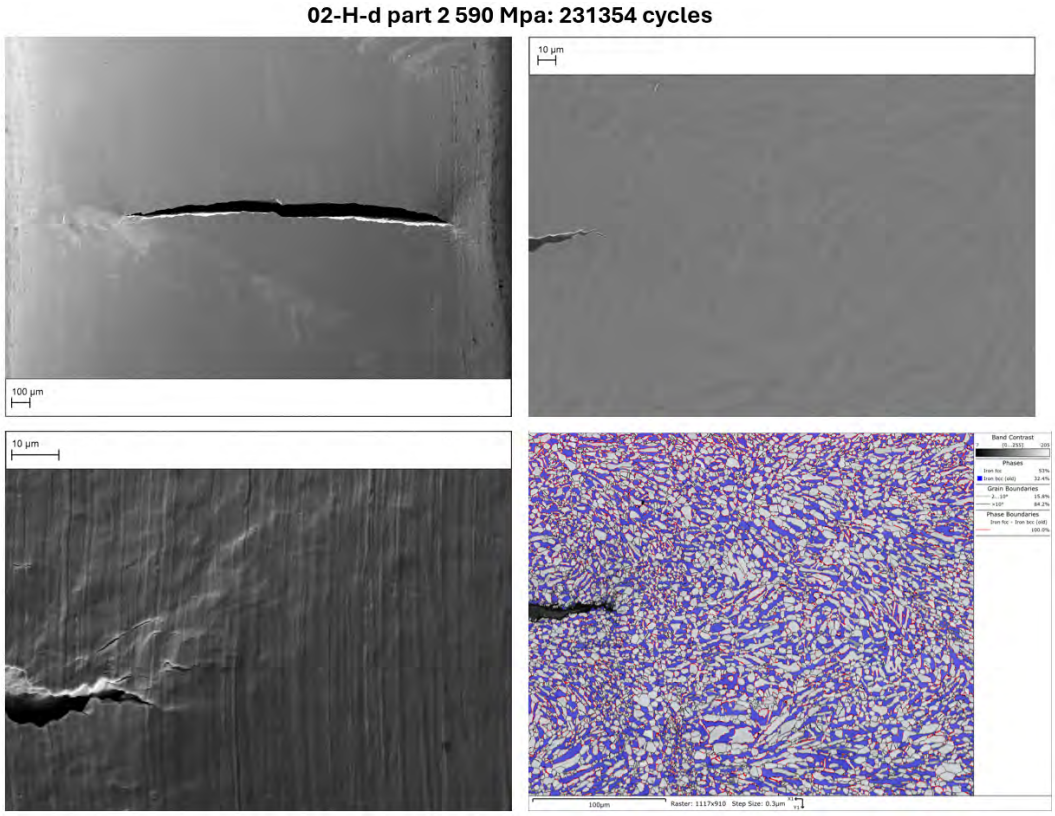

Fig. 4.80 FE-SEM overview of a secondary crack located beneath the primary fracture surface of HCF specimen 02-H-d, tested at 590 MPa and failed after 231354 cycles. The corresponding EBSD phase map acquired below the crack highlights the local interaction between fatigue crack propagation and the duplex ferritic-austenitic microstructure. The EBSD analysis indicates an austenite fraction of approximately 53 vol.%, shown in white, and a ferrite fraction of approximately 32 vol.%, shown in blue.

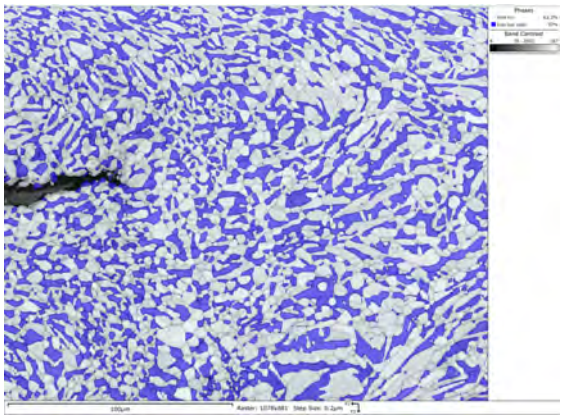

(a) The map EBSD phase map shows the ferritic and austenitic phase distribution in the region affected by fatigue crack propagation. The phase quantification obtained from the EBSD map indicates an austenite fraction of approximately 62.2% and a ferrite fraction of approximately 37.0%.

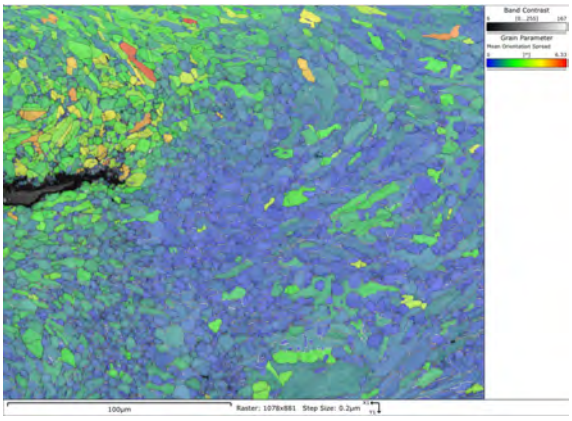

(b) EBSD Mean Orientation Spread (MOS) map acquired in the same region beneath the primary crack of HCF specimen 02-H-d. The map highlights the grain-scale orientation spread and provides information on local lattice curvature and deformation heterogeneity. Higher MOS values are mainly observed near the crack path and in selected microstructural regions, suggesting local strain accumulation associated with fatigue crack propagation and interaction with the duplex ferritic-austenitic microstructure.

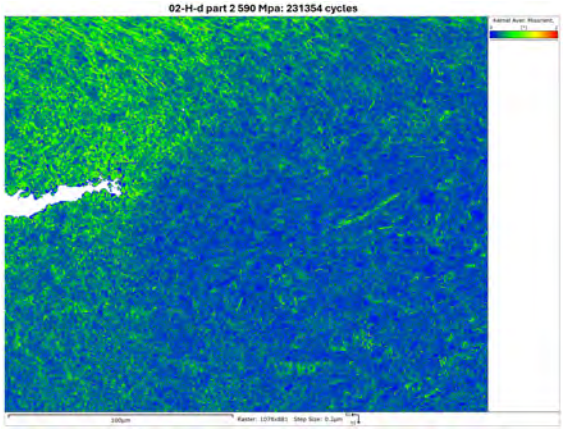

(c) Kernel Average Misorientation (KAM) map acquired beneath the primary crack of HCF specimen 02-H-d. The map shows the local misorientation distribution in the region affected by fatigue crack propagation, providing information on strain localisation associated with the duplex microstructure. The higher KAM values are mainly concentrated in the vicinity of the crack and in locally deformed regions, indicating the accumulation of plastic strain during fatigue loading.

Fig. 4.81 EBSD-based analysis beneath the primary crack of HCF specimen 02-H-d, tested at 590 MPa and failed after 231354 cycles. The figure reports: (a) the EBSD phase map, showing the local distribution of austenite and ferrite and the corresponding EBSD-derived phase fractions; (b) the Mean Orientation Spread (MOS) map, used to evaluate grain-scale orientation gradients and deformation heterogeneity; and (c) the Kernel Average Misorientation (KAM) map, used to assess local misorientation and strain localisation near the crack path.

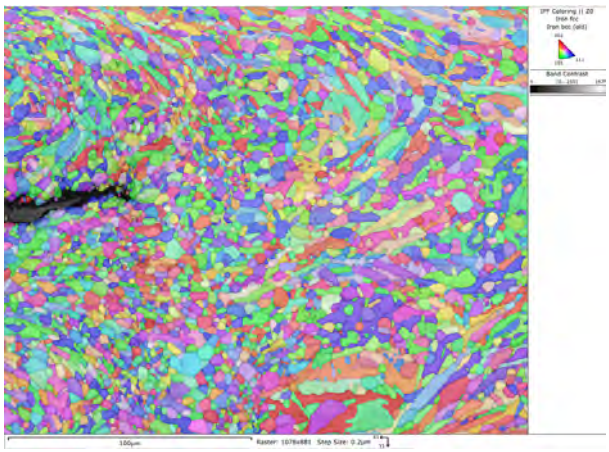

(a) IPF-Z_0 map, where Z_0 indicates the sample/reference direction normal to the EBSD acquisition plane.

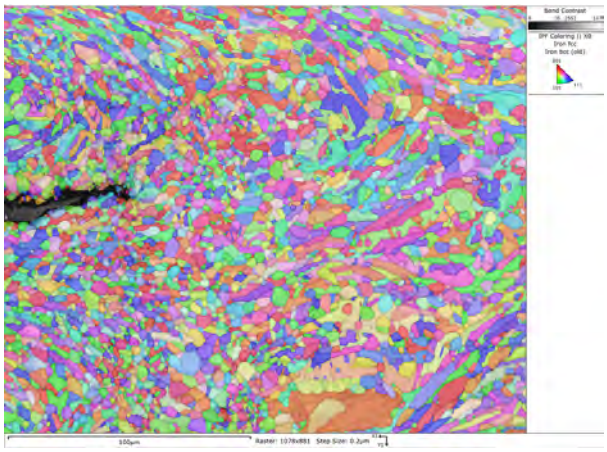

(b) IPF-X_0 map, where X_0 corresponds to one in-plane direction of the EBSD scan reference frame.

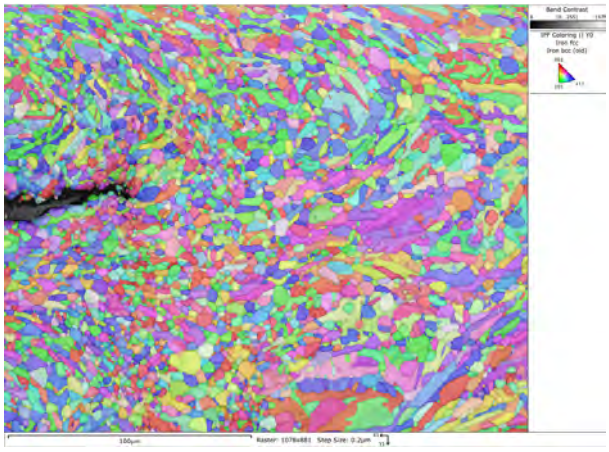

(c) IPF-Y_0 map, where Y_0 corresponds to the second in-plane direction of the EBSD scan reference frame.

Fig. 4.82 EBSD inverse pole figure (IPF) maps acquired beneath a secondary crack located below the primary fracture surface of HCF specimen 02-H-d, tested at 590 MPa and failed after 231354 cycles. The crystallographic orientation distribution is reported according to the Z_0, X_0, and Y_0 reference directions defined during EBSD acquisition in AZtec. Since the EBSD reference frame does not coincide with the LPBF build coordinate system, the relation between the two systems is explicitly stated: for the investigated ZY cross-section of the horizontally oriented specimen, the LPBF build direction Z_{LPBF} corresponds to the EBSD Y_0 direction. Accordingly, the IPF map coloured with respect to Y_0 is the most relevant for evaluating orientation features associated with the LPBF build direction, while the three IPF maps together allow the relationship between fatigue crack path, grain orientation, and duplex phase morphology to be assessed.

4.7.6 Correlative EBSD and Nanoindentation Analysis

A correlative EBSD and nanoindentation approach was adopted to assess the possible relationship between the local phase distribution and the micromechanical response of the HCF 02-V sample. A selected area of the XY section plane was first characterized by EBSD using a step size of 0.1 µm, in order to resolve the spatial arrangement of the austenitic and ferritic phases. Instrumented nanoindentation measurements were then performed on the same region using a Hysitron TI 950 system (Bruker, Billerica, United States). A Berkovich tip was used, and the distance between adjacent indents was fixed at 1.2 µm. The tests were carried out in load-control mode, with a maximum applied force of 2.5 mN maintained for 0.1 s. The EBSD phase map and the corresponding nanoindentation-derived modulus and hardness maps are shown in Figure 4.83.

The nanoindentation maps revealed a certain spatial variability in both indentation modulus and hardness. The modulus showed a relatively broad distribution, with most values concentrated around the central portion of the measured range, whereas hardness exhibited a narrower distribution centred close to 5 GPa, with a tail extending towards higher values. This scatter may be associated with the coexistence of the two phases, the position of each indent with respect to phase boundaries, local crystallographic orientation effects, and additional microstructural contributions that cannot be fully separated from the mechanical maps alone.

However, no marked difference in hardness or indentation modulus was identified between the austenitic and ferritic regions. This result is likely related to the very fine microstructure of the PBF-LB/M samples after heat treatment at 1080 °C for 35 min. Due to the small characteristic size of the phases, the volume probed beneath a nominally ferritic indent may also include austenite, and vice versa. This phase mixing within the indentation-affected volume can reduce the measurable contrast between the two phases, leading to partially overlapping mechanical responses.

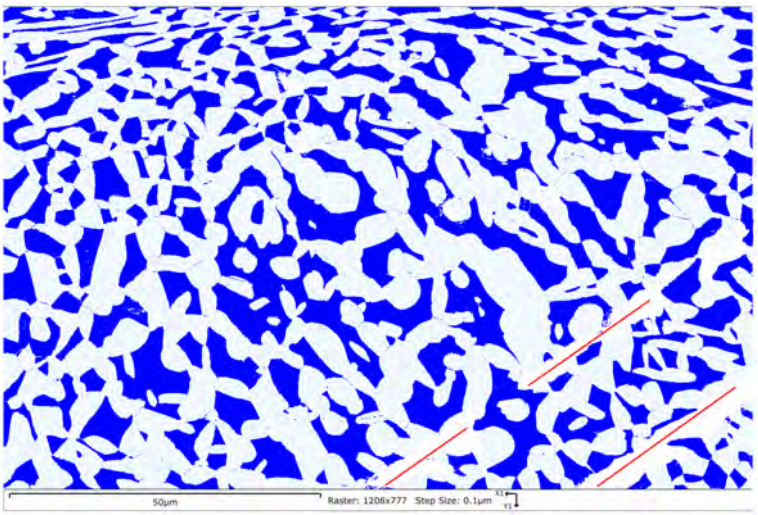

(a) EBSD phase map of the investigated area, showing the spatial distribution of the austenitic phase, represented in white/light cyan, and the ferritic phase, represented in blue. Image-based phase quantification indicated an austenite fraction of 58.4% and a ferrite fraction of 35.5%. The red oblique lines indicate artificial reference marks used to relocate the nanoindentation region and were not considered as microstructural features during phase quantification.

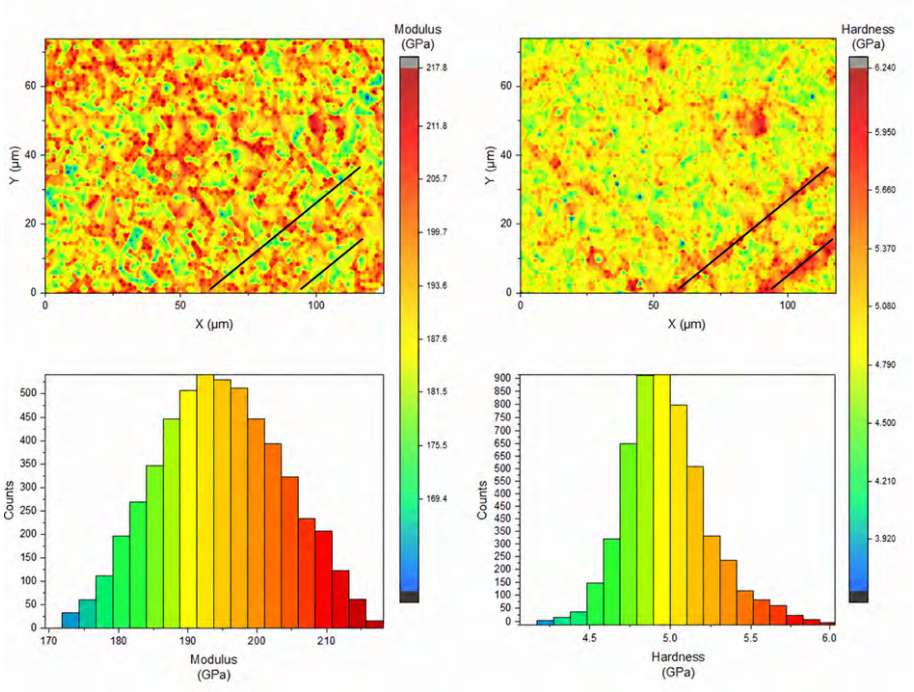

(b) Spatial maps and corresponding statistical distributions of indentation modulus and hardness obtained from the nanoindentation grid acquired in the same region shown in (a). The black oblique lines identify the reference marks and the affected regions were excluded from the mechanical analysis to avoid artefacts in the phase-resolved interpretation.

Fig. 4.83 Correlative EBSD and nanoindentation analysis performed on the same region of the investigated duplex microstructure. The oblique reference marks, highlighted in red in the EBSD map and in black in the nanoindentation maps, were used for spatial alignment between the two analyses and were excluded from the quantitative evaluation of the phase-dependent mechanical response.

4.7.7 Profilometry-based Indentation Plastometry (PIP) tests

4.7.7.1 PIP Measurement strategy and Sampling Locations

Measurements were carried out on the remaining portions of the H06 and V06 pillars, corresponding respectively to the horizontal and vertical build orientations, while maintaining a surface finish level comparable to that adopted for the tensile specimens. The results are reported in Table 4.25 and Table 4.26. The main objective of the analysis was to verify the possible presence of local variations in mechanical properties at different positions of the sample, with particular attention to the possible occurrence of gradients along the building direction, as shown in Figure 4.84. In addition, PIP tests were used to compare with the results obtained from conventional tensile tests carried out on samples extracted from the same pillars, whose results are reported in Table 4.23.

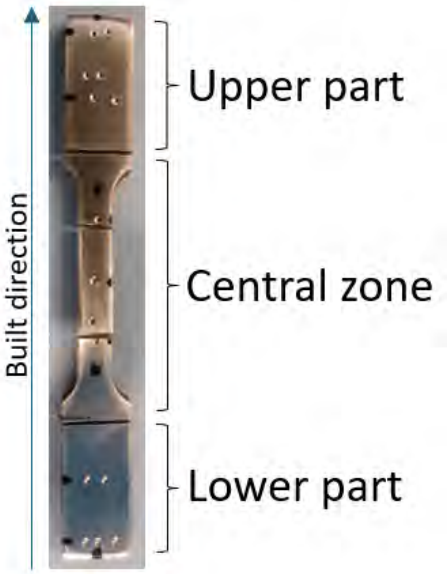

Fig. 4.84 Representative locations of the Profilometry-based Indentation Plastometry (PIP) measurements performed on a vertically built PBF-LB/M UNS S32760 specimen heat treated at 1080 °C for 35 min. The investigated areas were divided into lower part, central zone and upper part along the build direction, in order to assess possible local variations of the mechanical properties as a function of the distance from the build plate. Note: the cuts near some of the indentations were made after the analysis was performed.

Table 4.25 Summary of Profilometry-based Indentation Plastometry (PIP) results for PBF-LB/M UNS S32760 specimens built in the horizontal orientation. The table reports the values of $R_{p0.2}$, R_m, Necking strain and Brinell hardness. The central region of the specimen is highlighted separately to evaluate possible property variations along the investigated section.

Horizontal orientation						
ID	$R_{p0.2}$ **[MPa]**	R_m **[MPa]**	R_m **interval min. [MPa]**	R_m **interval max. [MPa]**	**Necking strain [%]**	**Brinell hardness [F/D^2 30]**
06-H-part1-02	649 ± 58	1073	1052	1110	16	299
06-H-part1-03	550 ± 72	1071	1040	1122	15	300
06-H-part1-04	558 ± 50	1081	1061	1120	17	282
06-H-part1-05	564 ± 50	1063	1040	1114	18	283
06-H-part1-08	601 ± 47	1051	1025	1092	17	282
06-H-central-01	720 ± 40	994	973	1015	16	299
06-H-central-02	687 ± 39	1005	981	1034	17	300
06-H-central-03	624 ± 51	1032	1004	1061	16	283
06-H-part2-01	569 ± 63	1046	1019	1083	15	282
06-H-part2-02	566 ± 50	1068	1048	1108	16	283
06-H-part2-03	591 ± 56	1048	1023	1071	14	299
06-H-part2-04	470 ± 61	1082	1053	1109	14	283
06-H-part2-05	555 ± 75	1066	1039	1091	14	300
Average value	593 ± 55	**1052**	**1028**	**1087**	16 ± 1	290 ± 9
Average value only central	677 ± 43	**1010**	**986**	**1037**	16 ± 1	294 ± 10

Table 4.26 Summary of Profilometry-based Indentation Plastometry (PIP) results for PBF-LB/M UNS S32760 specimens built in the vertical orientation. The table reports the values of $R_{p0.2}$, R_m, Necking strain, Brinell hardness and the distance from bottom to top of the investigated position. The central region of the specimen is highlighted separately to evaluate possible property variations along the build direction.

Vertical orientation							
ID	$R_{p0.2}$ **[MPa]**	R_m **[MPa]**	R_m **interval min. [MPa]**	R_m **interval max. [MPa]**	**Necking strain [%]**	**Brinell hardness [F/D^2 30]**	**Distance from bottom to top [mm]**
06-V-lower-01	595 ± 59	1039	1012	1064	14	300	3
06-V-lower-02	641 ± 40	1030	1012	1048	15	299	3
06-V-lower-03	562 ± 51	1066	1046	1110	16	283	15
06-V-lower-04	514 ± 75	1074	1049	1135	16	282	15
06-V-central-01	702 ± 37	995	979	1042	21	299	41
06-V-central-02	671 ± 51	1004	985	1069	19	300	48
06-V-central-03	639 ± 44	1027	1005	1052	16	300	59
06-V-upper-01	508 ± 57	1071	1042	1095	13	282	79
06-V-upper-02	625 ± 54	1025	1001	1075	17	300	79
06-V-upper-03	586 ± 62	1034	1009	1059	13	283	91
06-V-upper-04	618 ± 47	1037	1013	1093	17	281	91
06-V-upper-05	541 ± 60	1067	1045	1135	17	283	84
06-V-upper-06	559 ± 61	1062	1034	1111	17	283	84
Average value	597 ± 54	**1041**	**1018**	**1084**	16 ± 2	290 ± 9	–
Average value only central	671 ± 44	**1009**	**990**	**1054**	19 ± 3	300 ± 1	–

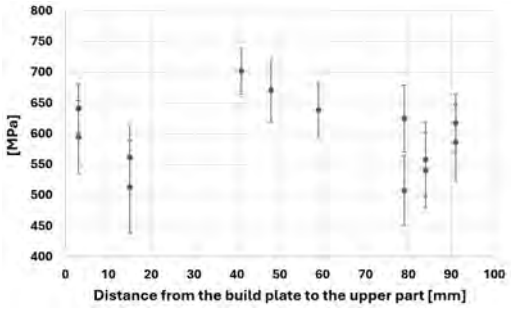

(a) $R_{p0.2}$ values as a function of the distance from the bottom part of the vertically built specimen.

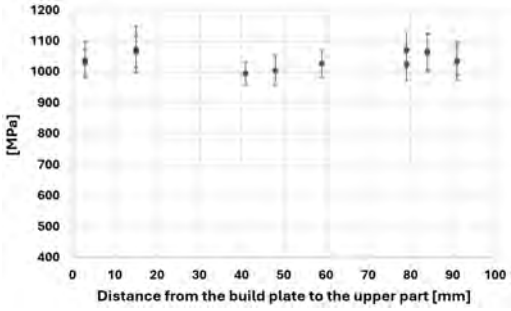

(b) R_m values as a function of the distance from the bottom part of the vertically built specimen.

Fig. 4.85 PIP-derived tensile properties as a function of the distance from the bottom part of vertically built PBF-LB/M UNS S32760 specimens. The graphs report the evolution of $R_{p0.2}$ and R_m along the build direction, allowing the evaluation of possible property variations with respect to the build height.

4.7.7.2 Spatial Variation of PIP-Derived Mechanical Properties

The PIP data obtained from the vertical specimens do not show a clearly significant and systematic variation in the mechanical properties as a function of the distance from the base of the build plate, as highlighted by the graphs in Figure 4.85.

The values of $R_{p0.2}$, R_m, Necking strain and Brinell hardness show a certain degree of local scatter, but they do not follow a monotonic increasing or decreasing trend along the build axis. For $R_{p0.2}$, values ranging from 508 to 702 MPa are observed, with an overall average of 597 ± 54 MPa. The central region shows, on average, higher values, equal to 671 ± 44 MPa; however, this increase does not continue towards the upper part of the specimen. This suggests a local variation rather than a true gradient along the build direction.

R_m also does not show a clear dependence on the distance from the base. The values range between 995 and 1074 MPa, with an average of approximately 1041 MPa. Moreover, the central region, although showing higher values of $R_{p0.2}$, presents R_m values slightly lower than the overall average, confirming the absence of a direct correlation between build height and ultimate tensile strength.

The Necking strain shows, on average, higher values in the central region, equal to $19 \pm 3\%$, compared with the overall average of $16 \pm 2\%$. However, also in this case, the trend is not progressive along the height of the specimen. Similarly, the Brinell hardness is higher and more uniform in the central region, with values equal to 300 ± 1, although high values are also present in other positions.

Overall, the results indicate that the observed differences are more likely attributable to local variations in the microstructure, phase distribution, texture or defect population, rather than to a defined mechanical gradient along the build axis. Therefore, based on the available data, the vertical specimens do not show a significant variation in the properties measured by PIP as a function of the distance from the base of the build plate. Similarly, also for the specimens built in the horizontal orientation, no significant differences emerge along the specimen, confirming a substantial homogeneity of the properties measured in the different analysed regions. Furthermore, considering the central PIP values, no significant differences emerge between horizontal and vertical specimens, since $R_{p0.2}$ and R_m are practically comparable in the two orientations.

4.7.7.3 Comparison Between PIP and Conventional Tensile Testing

Using only the average values obtained from the central region for the PIP tests, the comparison with the conventional tensile tests reported in Table 4.23 highlights good consistency for $R_{p0.2}$, whereas more pronounced differences emerge for R_m.

For the horizontal specimens, the conventional tensile tests reported in Table 4.23 provide an average $R_{p0.2}$ value of approximately 632 MPa, whereas the average PIP value for the central region is equal to 677 ± 43 MPa. The difference is therefore moderate and of the order of approximately 45 MPa, being compatible with the local nature of the PIP measurement and with the experimental scatter of the data.

For R_m, instead, the difference is more evident: the conventional tensile test provides an average value of approximately 894 MPa, whereas PIP returns a central average value of 1010 MPa. In this case, PIP therefore tends to overestimate the ultimate tensile strength compared with the macroscopic tensile test.

A similar behaviour is observed for the vertical specimens. The average $R_{p0.2}$ value obtained from the conventional tensile tests is approximately 636 MPa, whereas the average PIP value for the central region is equal to 671 ± 44 MPa. Also in this case, the difference is limited. However, it should be considered that specimen V06-d shows a $R_{p0.2}$ value significantly higher than the other vertical specimens; excluding this value, the average of the conventional vertical specimens decreases to approximately 598 MPa, thus increasing the deviation with respect to the PIP data. For R_m, the conventional tensile test provides an average value of approximately 868 MPa, whereas PIP returns 1009 MPa, confirming, also for the vertical orientation, a tendency of the PIP method to provide higher ultimate tensile strength values.

With regard to deformation, the comparison must be interpreted with caution, since the Necking strain parameter obtained from PIP is not directly equivalent to the total elongation A_t measured in the tensile test. However, it is more comparable with the uniform elongation A_{gt}. In the horizontal specimens, the average A_{gt} value from tensile testing is approximately 18%, whereas PIP provides a central Necking strain of $16 \pm 1\%$. In the vertical specimens, the average A_{gt} is approximately 17%, whereas PIP returns $19 \pm 3\%$. Therefore, in terms of uniform deformation, the two methods provide overall comparable values.

Overall, the comparison indicates that the PIP method returns $R_{p0.2}$ values that are reasonably consistent with those obtained from conventional tensile tests, whereas

it tends to provide higher R_m values. This difference can be attributed to the different nature of the two tests: conventional tensile testing measures the macroscopic response of the entire gauge volume of the specimen, which is influenced by geometry, defects and strain localisation, whereas PIP provides a local estimate of the mechanical properties through an inverse approach based on the indentation imprint. Moreover, it is necessary to consider that the algorithms used by the PIP software to derive $R_{p0.2}$ and R_m were mainly validated on metallic materials produced by conventional processing routes. Their application to steels produced by PBF-LB/M, and in particular to duplex or super duplex steels characterised by a peculiar dual-phase microstructure, anisotropy, possible local gradients and process-intrinsic defectiveness associated with additive manufacturing, may therefore introduce deviations from the values obtained through conventional tensile testing.

4.8 Corrosion testing

4.8.1 Introduction

The corrosion behaviour of UNS S32760 super duplex stainless steel was investigated in order to assess the effect of nitrogen content, and post-process heat treatment on resistance to localized corrosion. Particular attention was devoted to comparing conventionally manufactured materials with PBF-LB/M specimens produced from low- and high-nitrogen powders, in both as-built and heat-treated conditions. Since pitting corrosion in duplex and super duplex stainless steels is strongly governed by phase balance, elemental partitioning, microstructural heterogeneity, and the possible formation of secondary phases, the corrosion response was interpreted in relation to the previously characterized metallurgical features.

Two complementary ferric-chloride immersion tests were performed according to ASTM G48. Method A was used as a screening test to evaluate pitting susceptibility at 50 °C after 24 h of exposure, with additional extended-immersion tests carried out on the conditions that successfully passed the initial assessment. Method E was subsequently adopted to determine the critical pitting temperature (CPT) of the most corrosion-resistant conditions. The experimental results were discussed in terms of mass loss, visual and microscopic evidence of pitting, phase-resolved chemical composition, $PREN_W$, Cr_{eq}/Ni_{eq} ratio, and the influence of heat treatment on microstructural homogenization.

4.8.2 Materials and Methods

4.8.2.1 Test according to ASTM G48 Method A

The corrosion test was performed in accordance with ASTM G48, Method A [137] on seven different specimen categories of UNS S32760 steel as follow: sample obtained from a commercial threaded bar; sample obtained from forged bar material; sample manufactured by PBF-LB/M process from low-nitrogen powders, examined in the as-built condition and after heat treatment at 1020 °C and 1080 °C for 35 min; sample manufactured by PBF-LB/M from high-nitrogen powders, examined in the as-built condition and after heat treatment at 1080 °C for 35 min.
The specimens measuring $20 \times 10 \times 4$ mm (± 0.5 mm), sectioned by machining from

the ends of notched Charpy impact sample according to the layout in Figure 4.86 and wet polished as per standard requirements, were immersed in a ferric-chloride solution at 50 °C with a concentration of 6wt% $FeCl_3$, prepared immediately prior to testing. Due to safety restriction applied on the laboratory used during this research the pickling phase required by Norsok M630 standard [126] (see the reference to acceptance criteria on test results) as been waived and replaced by an accurate cleaning procedure described in the following section.

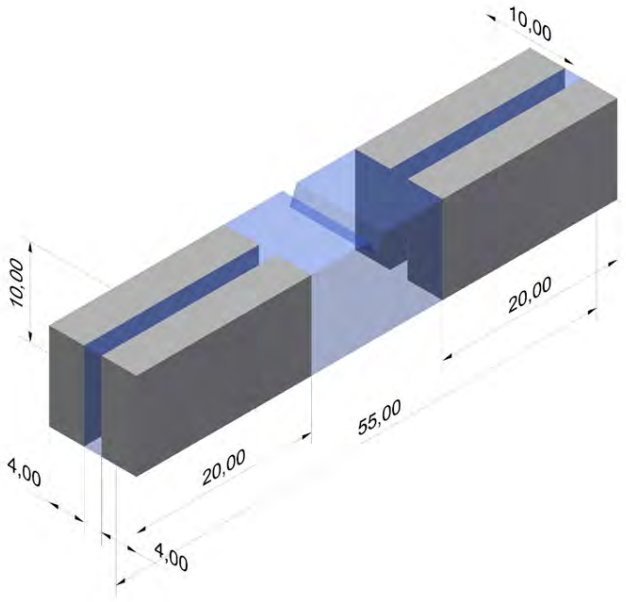

Fig. 4.86 Schematic illustration of the extraction procedure adopted to obtain corrosion-test specimens from the ends of notched Charpy impact samples. The extracted specimens measured $20 \times 10 \times 4$ mm (± 0.5 mm) and were obtained by machining from the extremities of the notched Charpy probes, yielding four corrosion-test specimens from each Charpy sample. These specimens were subsequently used for corrosion testing performed in accordance with ASTM G48, Method A and Method E.

In accordance with ASTM G48, Method A, a minimum solution volume of ≥ 5 mL cm^{-2} must be provided. For the present set of four specimens, the total exposed area was ≈ 25 cm^2, implying a minimum required volume of 125 mL. We used 600 mL of ferric-chloride solution in a 1 L beaker, which exceeds the specification by a factor of 4.8 and thus adequately satisfies the standard while limiting concentration drift and ensuring proper solution exchange around the samples.

Temperature control was provided by a thermostatic bath (ArgoLab, model WB 22 PUMP, with an integrated recirculation pump) used to heat the beaker containing the test solution. For each set of four samples, the temperature of the solution in the proximity of the samples was also monitored with a type K thermocouple and recorded using a Sefram 9816B data logger with an acquisition frequency of 1 Hz. The instrumentation setup, shown in Figure 4.87, allows the specimens to be positioned inside the beaker at an inclination of 45°, while minimizing the contact area with the supporting fixture.

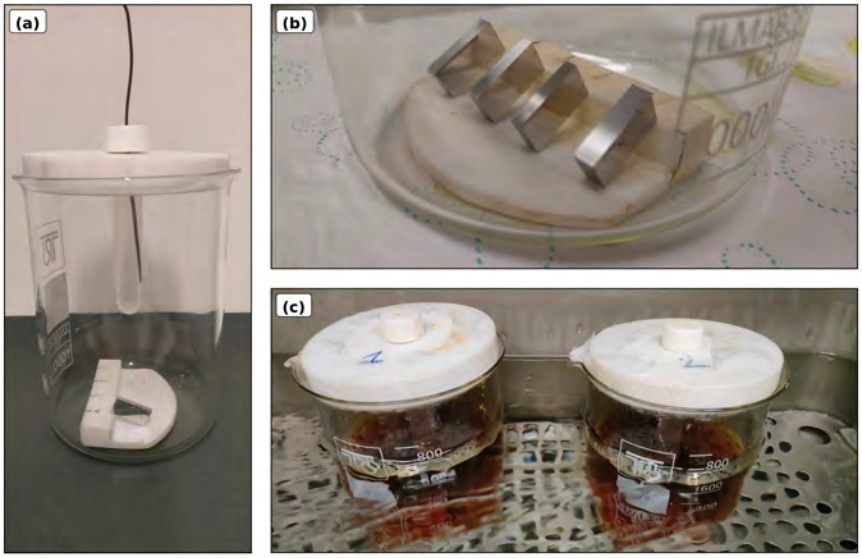

Fig. 4.87 Experimental setup adopted for the ASTM G48 Method A ferric-chloride immersion tests. (a) Positioning of the K-type thermocouple used for temperature monitoring in the prossimity of the specimens; the thermocouple was inserted into a test tube filled with distilled water, which was in turn immersed in the ferric-chloride solution. (b) Arrangement of the four test specimens inside the 1 L beker on a dedicated support, with an inclination of 45° and the largest face exposed to the solution, so as to minimize the contact area between the samples and the supports. (c) Bekers are immersed in the thermostatic bath used to control the test temperature.

Each specimen underwent a standardized pre-weigh cleaning: an ultrasonic bath in acetone for 5 min followed by drying with filtered compressed air. The mass was measured with a five-decimal-place analytical balance (Sartorius, model CPA225D-0CE), whereas the surface area of each specimen was calculated after measuring the dimensions measured with a caliper with an accuracy of 0,01mm.
The ASTM G48 specifies a minimum surface finish of 120 grit and evaluates cor-

rosion solely by mass loss with a low-magnification (20X) for pitting visual check, without microstructural assessment. Because we were also interested in pit initiation and growth within the primary phases, a parallel microstructural evaluation was implemented. Accordingly, one face of each specimen was polished to a metallographic wet finishing using the sequence 100, 180, 400, 800, 1200 and 2400 grit, followed by a colloidal-silica final polish, while the remaining five faces were prepared to 1200 grit to remain compliant with the standard. This approach preserves conformity with ASTM G48 method A and, at the same time, enables high-fidelity microstructural characterization of pitting.
At the end of the prescribed corrosion-exposure period, specimens were rinsed, cleaned, and weighed to quantify mass loss attributable to pitting. To ensure repeatability and comparability across specimens, a fixed cleaning protocol was applied:

1. Rinse in deionized water (1 min) to remove residual ferric-chloride solution.
2. Mechanical cleaning with a soft nylon-bristle brush to dislodge corrosion products from pits and from the external surface.
3. Ultrasonic cleaning in acetone bath for 5 min to remove loosened residues.
4. Drying with filtered compressed air to eliminate solvent and particulates.
5. Mass measurement with the analytical balance.

The clean, dry, and weigh cycle was repeated as needed until the recorded mass stabilized within the balance resolution, thereby minimizing artifacts associated with adherent corrosion products and enabling a reliable comparison among specimens. ASTM G48 does not establish a universal acceptance criterion for Method A. Rather, it defines the test procedure and the method for identifying and reporting pitting, whereas the pass/fail threshold must be specified in the technical agreement between the purchaser and the supplier. The ASTM G48 method A further indicates that mass losses ≥ 0.0001 g/cm^2 may be indicative of pitting or crevice corrosion; however, visual examination remains mandatory, meaning that mass loss alone is not sufficient to establish a pass outcome.

The acceptance criteria for passing the test were assessed in accordance with Norsok M630 [126], which specifies, for base material (acceptance criteria stated for weld area are less severe), an immersion period of 24 h, and are as follows:

1. The specimen shall exhibit no pits with a depth 25 µm on its surfaces, and no visible pitting shall be detected at 20× magnification.

2. The mass loss shall be lower than 0.0004 g/cm²

After mass-loss assessment, the designated face of each specimen was electrolytically etched in a sodium hydroxide solution to reveal the metallurgical microstructure and identify the phase in which pitting preferentially initiated.
For specimen types that pass the acceptance criteria after the 24 h immersion test, a further exposure in order to assess whether pitting would develop at longer immersion times. The 6wt% $FeCl_3$ solution was renewed after each inspection, performed at 48 h, 72 h, 96 h, 144 h, and 312 h.

4.8.2.2 Test according to ASTM G48 Method E

Only those specimens that had successfully passed the 24h ASTM G48 Method A test, were subsequently tested in accordance with ASTM G48 Method E after a new polishing for the determination of the Critical Pitting Temperature (CPT) [137]. Unlike Method A, Method E employs an acidified ferric chloride solution containing approximately 6 wt% $FeCl_3$ and 1 wt% HCl, thereby increasing the severity of the corrosive environment and enabling identification of the lowest temperature at which stable pitting is initiated.
The initial test temperature was selected on the basis of the empirical relationship provided by the referenced standard [137], which correlates the critical pitting temperature (CPT) with the chemical composition of the alloy. In particular, the estimated CPT is expressed as a function of the alloying element contents, expressed in weight percent, as follows:

$$\text{CPT}\ (^{\circ}\text{C}) = 2.5\,\%\text{Cr} + 7.6\,\%\text{Mo} + 31.9\,\%\text{N} - 41 \tag{4.9}$$

The starting test temperature was chosen as the nearest multiple of 5 °C to the estimated value, within the allowable range of 0–85 °C, and was subsequently adjusted stepwise according to the observed corrosion response.
In this experimental campaign, specimens with the same geometry as those used for Method A were adopted, together with the same solution volume and the same

temperature-monitoring setup, shown in Figure 4.87. After each test conducted at a given temperature, the specimens were removed, subjected to a new surface preparation procedure analogous to that adopted for Method A, and then re-exposed in fresh solution, which was renewed at every temperature step, in order to ensure reproducible testing conditions and to minimize any effects arising from surface alteration, local changes in solution chemistry, or accumulation of corrosion products. Cleaning, drying, and weighing were performed according to the same protocol described for Method A. Each test temperature was evaluated twice in order to confirm the reproducibility of the experimental findings. Moreover, as a more conservative criterion than that commonly adopted in standard practice, pits located at the specimen edges were also included in the final assessment. Accordingly, a given test condition was considered as successfully passed only when no pitting was detected over the entire specimen surface, including the edges.

4.8.3 Results of ASTM G48 Method A

4.8.3.1 Short-Term ASTM G48 Method A results

The results of the ASTM G48 Method A corrosion test, expressed in terms of overall mass loss after 24 h of immersion at 50 °C are reported in Table 4.27, revealed marked differences among the seven specimen types investigated.

Table 4.27 Total exposed area and global mass loss at 50°C after different exposure times during ASTM G48 Method A testing for UNS S32760 samples. For each sample type, the reported exposed area is the overall exposed area, obtained by summing the exposed areas of the four tested specimens. Likewise, the reported mass loss is the overall mass loss, obtained by summing the mass losses of the same four specimens. Blank celles in the table indicate that the corresponding test was not conducted.

UNS S32760 sample type	Area [cm^2]	Global mass loss [g/cm^2] at 50°C					
		24 h	48 h	72 h	96 h	144 h	312 h
Threaded bar	25.5	0	0	0	0	0	0
Forged sample	25.7	0.00651					
PBF-LB/M as-built low nitrogen	24.4	0.03936					
PBF-LB/M 1020°C×35' low nitrogen	25.3	0	0	0	0	0	0. 00001
PBF-LB/M 1080°C×35' low nitrogen	25.6	0	0	0	0	0	0
PBF-LB/M as-built high nitrogen	24.6	0.02881					
PBF-LB/M 1080°C×35' high nitrogen	25.2	0	0	0	0	0	0

In particular, the PBF-LB/M specimens produced from low-nitrogen powders and subsequently heat treated at 1020 °C for 35 min exhibited zero mass loss despite the presence of sigma phase, as documented in Figure 4.88. Optical micrographs of the etched area reveal the microstructure of the heat-treated material and confirm that, although sigma phase was present, no pits or preferential pit nucleation sites were observed, even in regions where sigma phase was located.
The same absence of mass loss was also observed for the PBF-LB/M specimens heat treated at 1080 °C for 35 min, for the specimen machined from threaded bar, and for the PBF-LB/M specimen produced from high-nitrogen powders in the heat-treated condition.

In contrast, measurable mass loss was observed for the forged specimen and for the as-built PBF-LB/M specimens produced from high- and low-nitrogen powders, amounting to 0.00651, 0.02881, and 0.03936 g/cm^2, respectively. Among these conditions, the forged material showed the mildest attack, while the as-built PBF-LB/M specimen produced from low-nitrogen powders exhibited the most severe

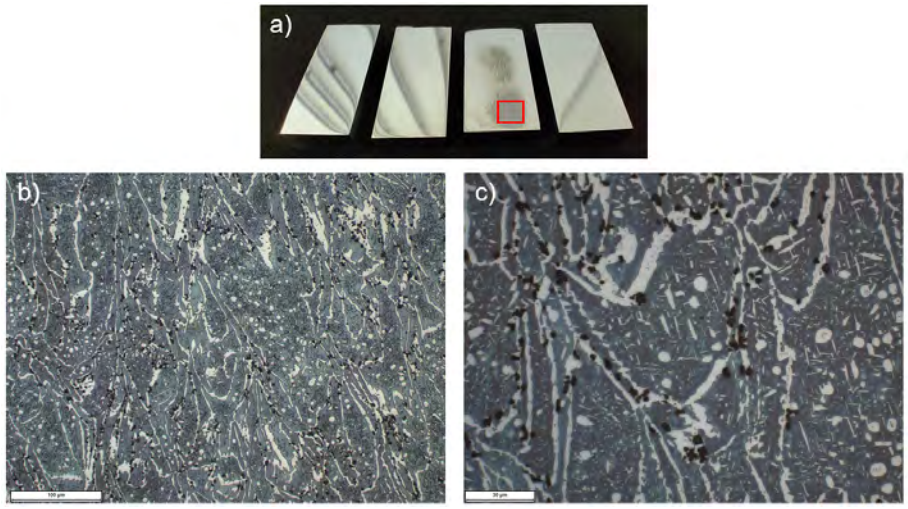

Fig. 4.88 PBF-LB/M specimens produced from low-nitrogen powders and subsequently heat treated at 1020 °C for 35 min. Despite the presence of sigma phase (black spot), this condition showed complete resistance to pitting attack after 24 h of exposure to ferric-chloride solution at 50 °C. a) Macroscopic appearance of the four specimens after testing. The second specimen from the right was electrolytically etched, highlighted by the red box, to reveal the microstructure within the selected surface region. (b, c) Optical micrographs of the etched area, showing the microstructure of the heat-treated material (austenite in white and ferrite in blue) and confirming that, although sigma phase was present, no pits or preferential pit nucleation sites were observed, including in areas where sigma phase was located.

degradation. The as-built PBF-LB/M material produced from high-nitrogen powders showed an intermediate response. This ranking is also supported by the macroscopic appearance of the specimen surfaces shown in Figure 4.91, from which a progressive increase in the severity and extent of corrosion damage can be observed, moving from the forged condition to the as-built PBF-LB/M condition produced from high-nitrogen powders and finally to the as-built PBF-LB/M condition produced from low-nitrogen powders. In the latter case, the attacked surface is characterized by a larger number of pits, whereas in the intermediate condition, corresponding to the UNS S32760 specimen produced from high-nitrogen powders, the pits are fewer in number but appear to have undergone greater growth and widening.

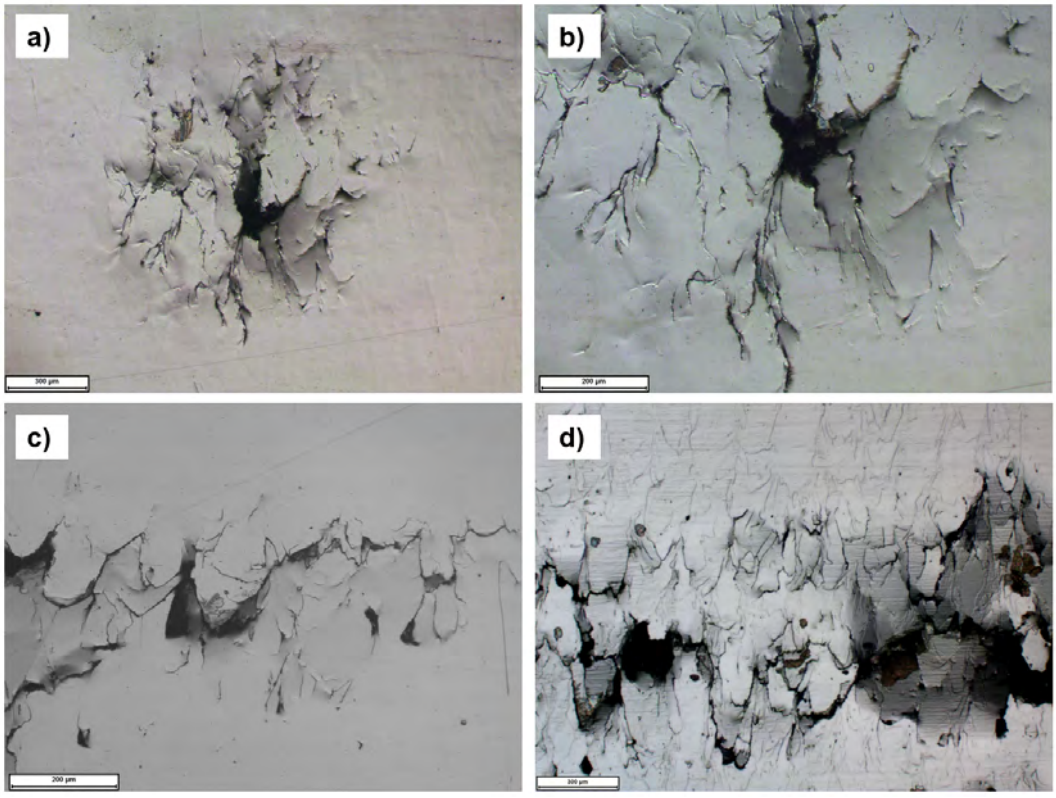

Fig. 4.89 Optical micrographs showing the corrosion morphology of the PBF-LB/M as-built low-nitrogen UNS S32760 sample after 24 h of ASTM G48 Method A exposure. (a) Origin of pit initiation. (b) Higher-magnification view of the region shown in (a), highlighting that corrosion nucleates and grows preferentially along the PBF-LB/M melt-pool boundaries. (c) Further evolution of the localized attack along the melt-pool structure. (d) Extended corrosion damage developing along the melt pools, both in terms of lateral propagation on the observation plane and penetration in depth.

4.8.3.2 Corrosion morphology and Microstructural interpretation

A more detailed interpretation of the lower pitting resistance exhibited by the as-built PBF-LB/M conditions can be derived from the corrosion morphologies shown in Figures 4.89 and 4.90. In both the low-nitrogen and high-nitrogen materials, pit initiation is consistently observed at or very close to the PBF-LB/M melt-pool boundaries, after which the attack propagates preferentially along the same melt-pool network, both laterally on the observation plane and in depth. This recurrent morphology indicates that the as-built state contains microstructural features intrinsically

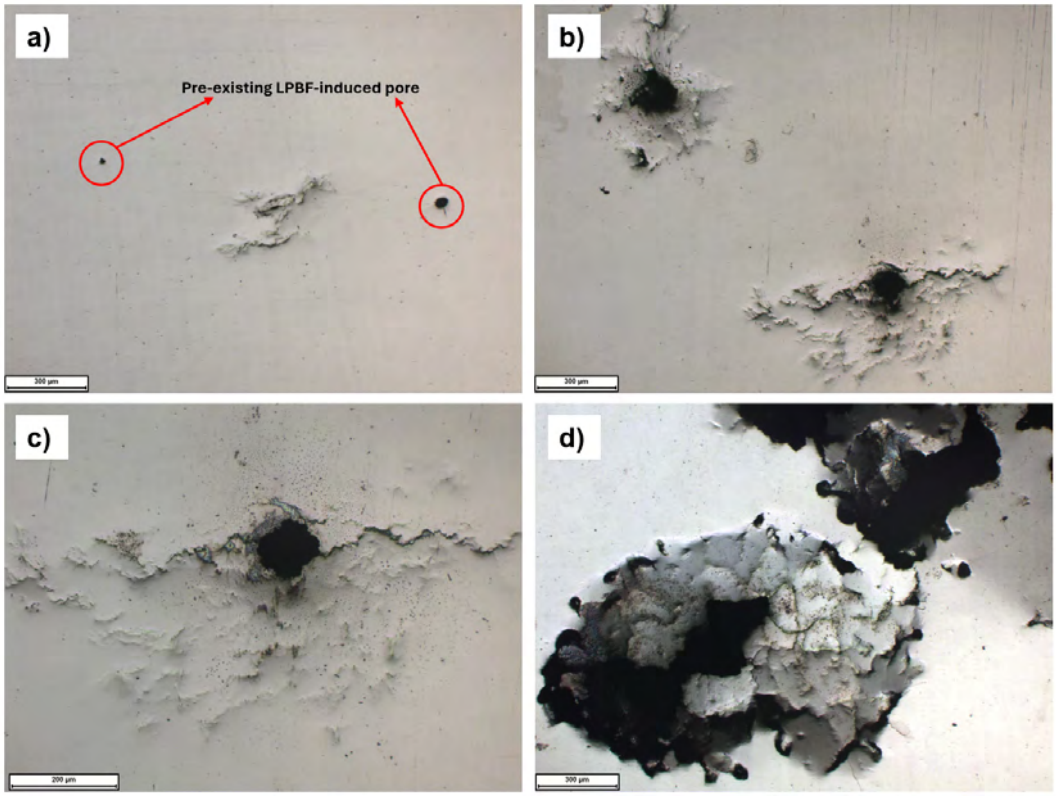

Fig. 4.90 Optical micrographs showing the corrosion morphology of the PBF-LB/M as-built high-nitrogen UNS S32760 sample after 24 h of ASTM G48 Method A exposure. (a) Central pit-initiation site, with pre-existing PBF-LB/M-induced pores visible in the surrounding area. (b) Corrosion nucleation and growth preferentially developing along the PBF-LB/M melt-pool boundary. (c) Higher-magnification view of the pit shown in (b). (d) Extended corrosion damage propagating along the melt-pool structure, both in terms of in-plane extension and penetration in depth.

detrimental to corrosion resistance, with the melt-pool architecture acting as the preferential path for passive-film breakdown and localized corrosion growth.

This behavior can reasonably be attributed to the heterogeneous microstructure inherited from the rapid solidification conditions of PBF-LB/M [138]. In particular, the melt-pool boundaries are likely associated with the combined effects of microsegregation and electrochemical heterogeneity. Such heterogeneities can generate local differences in pitting resistance, making the melt-pool border chemically and electrochemically less stable than the surrounding matrix.

This interpretation is well supported by Figure 4.89, where the sequence of micrographs documents the transition from pit initiation to extended corrosion

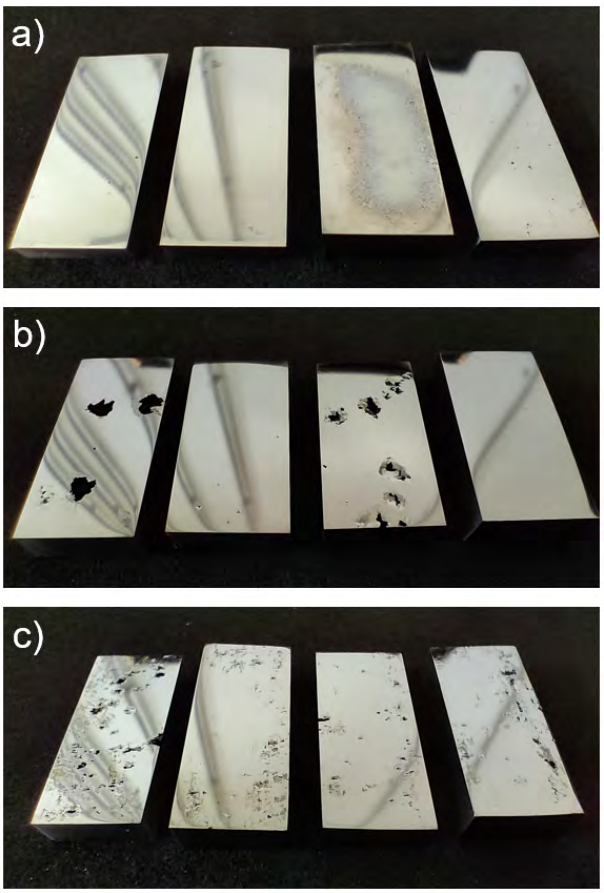

Fig. 4.91 Macroscopic appearance of the UNS S32760 specimen surfaces after 24 h of exposure at 50°C during ASTM G48 Method A testing: (a) Forged sample, (b) PBF-LB/M as-built high nitrogen, and (c) PBF-LB/M as-built low nitrogen. The observed surface condition is consistent with the measured global mass loss reported in Table 4.27.

propagation along the melt-pool structure. A comparable evolution is also observed in the high-nitrogen as-built condition shown in Figure 4.90. Particularly significant is panel (a) of Figure 4.90, where pre-existing PBF-LB/M-induced pores are visible in the vicinity of the attacked region. Despite their presence, these pores do not appear to act as the primary pitting initiation sites; instead, corrosion still nucleates preferentially at the melt-pool boundary. This observation indicates that isolated pre-existing porosity alone is not sufficient to explain the corrosion morphology and that melt-pool-related microstructural heterogeneity is the dominant factor governing the early stages of localized attack.

Within this framework, the beneficial effect of post-process heat treatment can be rationalized not only by the increase in austenite fraction, but also by the progressive reduction in microsegregation, local phase unbalance, and electrochemical discontinuities associated with the as-built melt-pool structure. By promoting chemical homogenization and microstructural rebalancing, heat treatment strongly reduces the preferential corrosion paths characteristic of the as-built condition, thereby leading to the marked improvement in pitting corrosion resistance observed experimentally.

4.8.3.3 NORSOK M-630 Assessment and Extended-exposure behaviour

A comparison between the two PBF-LB/M materials in the as-built condition, produced from powders with different nitrogen contents, further shows that the material manufactured from high-nitrogen powders, characterized by the presence of approximately 20 vol% austenite, experienced a lower mass loss than that produced from low-nitrogen powders, namely 0.0288 versus 0.0394 g/cm^2, the latter being fully ferritic in the as-built state. This result suggests that the presence of an austenite fraction in the as-built condition exerts a beneficial effect on pitting resistance, although it is not, by itself, sufficient to ensure complete test passing in the absence of an appropriate heat treatment. This observation is consistent with the well-established role of nitrogen in enhancing localized corrosion resistance in duplex and super duplex stainless steels [138, 139].

With regard to the conventionally processed materials, the specimen machined from threaded bar exhibited the best performance, with complete absence of both mass loss and pitting, whereas the forged specimen showed an intermediate behavior. Although the mass loss measured for the forged specimen, 0.0065 g/cm^2, was substantially lower than recorded for the PBF-LB/M materials in the as-built state, it nevertheless indicates a lower resistance to localized corrosion than for the threaded bar and for the appropriately heat-treated PBF-LB/M conditions. This suggests that, even in conventionally manufactured materials, the thermomechanical history and the final microstructure significantly affect the response to the ASTM G48 Method A test [137].

Finally, when the acceptance criterion defined according to NORSOK M-630 [126] is considered, namely absence of pitting and a mass loss lower than 0.0004 g/cm^2, only the specimens exhibiting zero mass loss can be regarded as fully compliant. Conversely, the PBF-LB/M materials in the as-built state, both with low and high

nitrogen content, as well as the forged material, must be considered non-compliant, as they exhibited mass losses far above the admissible threshold, in addition to the presence of pits with a depth exceeding 25 μm.
For the specimens that, after 24 h of immersion, had passed the test without any evidence of pitting and without appreciable mass variation, the exposure was further prolonged. The test was interrupted after 312 h of immersion. The results obtained from the extended-exposure tests are reported in Table 4.27.

In particular, the specimens produced by PBF-LB/M from both low- and high-nitrogen powders and subsequently heat treated at 1080 °C for 35 min, as well as the specimen machined from commercial threaded bar, maintained zero mass loss up to 312 h of immersion. This result confirms that, for these conditions, the absence of pitting observed after 24 h does not merely represent an initial or transient behaviour, but rather reflects substantial stability of the passive film even under more severe and prolonged exposure conditions.

Of particular interest is the behaviour of the material produced by PBF-LB/M from low-nitrogen powders and heat treated at 1020 °C for 35 min. Although this condition was characterized by the strong presence of sigma phase, it exhibited an extremely limited mass variation, equal to 0.00001 g/cm^2, only after 312 h of immersion. This value is well below the threshold of 0.0004 g/cm^2 adopted as the acceptance criterion and therefore indicates that, even over very long exposure times, the material retains a substantially high resistance to localized corrosion. More specifically, the slight mass loss detected only after 312 h appears to be governed primarily by pre-existing morphological defects, particularly porosity intrinsic to the PBF-LB/M process, rather than by a generalized deterioration in corrosion resistance attributable exclusively to the presence of sigma phase, as shown in Figure 4.92.

From an interpretative standpoint, these results show that post-process heat treatment not only enables the material to pass the ASTM G48 Method A test under the standard 24 h exposure condition, but also confers significant robustness to the corrosion response over prolonged exposure times. In other words, the heat-treated materials do not merely exhibit a marginal passive behavior, but rather a sufficiently stable resistance capable of preventing, or at least markedly delaying, pit initiation and propagation during extended exposure in $FeCl_3$ solution at 50 °C.

The fact that the condition heat treated at 1020 °C for 35 min, despite the presence of sigma phase, exhibited a behavior comparable to that of the other fully resistant

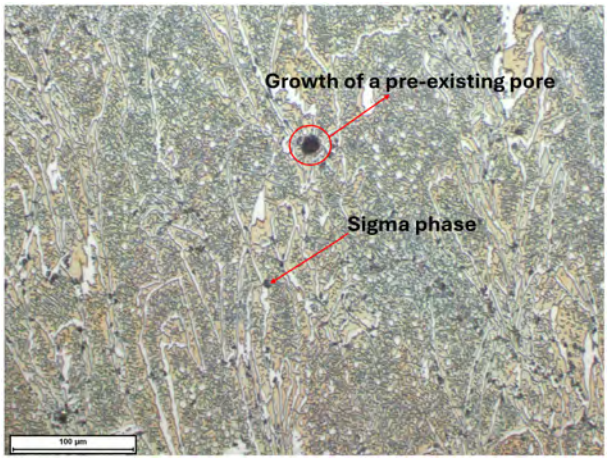

Fig. 4.92 Optical micrograph of the localized surface damage associated with the slight mass loss detected only after 312 h of immersion in the PBF-LB/M material produced from low-nitrogen powders and heat treated at 1020 °C for 35 min. The attack appears to have originated from the enlargement of a pre-existing pore-related defect, rather than by a generalized reduction in corrosion resistance caused exclusively by the presence of sigma phase.

conditions further suggests that, in the present case, the possible detrimental effect of sigma phase on pitting resistance was secondary with respect to the overall benefit induced by heat treatment in terms of microstructural rebalancing. More specifically, the slight mass loss detected only after 312 h appears to be governed primarily by morphological defects intrinsic to the PBF-LB/M process, rather than a generalized degradation in corrosion resistance attributable exclusively to sigma phase presence effect.

Overall, the results of the extended-exposure tests indicate that the specimens that had initially passed the 24 h test retained a behaviour largely consistent with the adopted acceptance criterion even at longer exposure times. This further supports the interpretation that the combination of appropriate heat treatment and a sufficiently homogeneous microstructure represents the key factor not only for passing the standard ASTM G48 Method A test, but also for ensuring good long-term stability of pitting corrosion resistance.

4.8.4 Results of test according to ASTM G48 Method E

In accordance to the ASTM G48 Method E pass/fail criterion, the results reported in Table 4.28 clearly reveal a markedly differentiated behaviour among the various microstructural conditions investigated. At each test temperature, both positive outcomes, corresponding to the absence of pitting, and negative outcomes, associated with the occurrence of localized attack, were repeated twice in order to validate the reproducibility of the experimental result.

Table 4.28 Results of the ASTM G48 Method E tests carried out on the investigated specimens at different test temperatures. Green cells indicate test passed, whereas red cells indicate test failed, with the corresponding average mass loss reported in g/cm^2. Blank cells correspond to temperatures not investigated for the specific sample condition. LN = low nitrogen; HN = high nitrogen.

UNS S32760 Sample type	ASTM G48 Method E test temperature										
	35°C	40°C	45°C	50°C	55°C	60°C	65°C	70°C	75°C	80°C	85°C
Threaded bar										0.00285	0.0084
PBF-LB/M 1020°C×35' LN		0.00001	0.00007	0.00023	0.00035	0.00312	0.00477				
PBF-LB/M 1080°C×35' LN								0.00110	0.00493		
PBF-LB/M 1080°C×35' HN											
Test passed without pitting/corrosion											
Test failed: pitting/corrosion observed											

4.8.4.1 Bulk-Composition-Based CPT estimates and Nitrogen effect

The test results clearly show that the pitting resistance of the different investigated samples does not depend solely on the average chemical composition reported in Table 4.29, but rather results from the combined effect of the overall content of the key elements governing passivity and the final microstructure induced by the heat treatment, including the partitioning of the alloying elements between ferrite and austenite, as highlighted in Table 4.30, as well as the possible presence of deleterious secondary phases such as sigma phase. Based on the average chemical composition, the theoretical CPT values calculated by means of the empirical relationship reported in ASTM G48 Method E [137] (Eq. 4.9), and listed in Table 4.31, show a preliminary ranking reasonably consistent with that expected for super duplex stainless steels [139].

Table 4.29 Average chemical composition of UNS S32760 samples, all values are reported in wt.%. The concentrations of Si, Cr, Mn, Fe, Ni, Cu, Mo, and W were determined by EDS (Oxford Ultim Max), and quantification was performed using AZtecLive software. Carbon and sulfur were measured by LECO CS 744 analyzer, whereas oxygen and nitrogen were measured by LECO ONH 836. The concentrations of light elements were used as constrained values during EDS quantification.

UNS S32760 sample type	Si	Cr	Mn	Fe	Ni	Cu	Mo	W	O	N	C	S
Threaded bar	0.4	26.3	1.0	60.1	7.6	0.6	3.6	0.7	0.00463	0.271	0.0333	0.001110
Forged sample	0.5	25.7	0.9	60.9	7.1	0.6	3.6	0.5	0.0101	0.264	0.0200	0.000958
PBF-LB/M 1020°C×35' low nitrogen	0.4	25.8	0.7	61.3	7.6	0.7	3.1	0.4	0.03785	0.140	0.0217	0.001170
PBF-LB/M 1080°C×35' low nitrogen	0.4	25.1	0.7	61.0	7.8	0.8	3.3	0.8	0.03785	0.140	0.0217	0.001170
PBF-LB/M 1080°C×35' high nitrogen	0.5	25.3	0.7	60.8	7.3	0.6	3.7	0.7	0.03047	0.400	0.0214	0.000849

Table 4.30 Phase-resolved elemental partitioning of UNS S32760 samples, reported in wt.%. For each element, the values measured in austenite (A) and ferrite (F) are reported separately. The concentrations of Si, Cr, Mn, Fe, Ni, Cu, Mo, and W were determined by EDS (Oxford Ultim Max). The concentrations of light elements were used as constrained values during EDS quantification.

	Si		Cr		Mn		Fe		Ni		Cu		Mo		W	
UNS S32760 sample type	A	F	A	F	A	F	A	F	A	F	A	F	A	F	A	F
Threaded bar	0.3	0.4	25.0	27.6	1.4	0.5	60.6	59.5	9.0	6.2	0.6	0.5	2.9	4.3	0.7	0.7
Forged sample	0.4	0.5	24.7	26.7	0.8	0.9	61.8	60.0	8.3	5.9	0.7	0.5	2.9	4.3	0.3	0.7
PBF-LB/M 1020°C×35' low nitrogen	0.3	0.5	23.8	27.8	0.8	0.6	62.3	60.4	9.2	6.0	0.8	0.6	2.5	3.6	0.2	0.5
PBF-LB/M 1080°C×35' low nitrogen	0.4	0.5	23.3	26.8	0.7	0.6	61.9	60.0	9.4	6.3	0.8	0.8	2.6	4.0	0.7	0.8
PBF-LB/M 1080°C×35' high nitrogen	0.3	0.6	24.6	26.1	0.7	0.6	61.1	60.6	8.5	6.2	0.8	0.5	3.0	4.3	0.5	0.8

Table 4.31 Comparison between theoretical and experimental critical pitting temperature (CPT) values of UNS S32760 samples.

UNS S32760 sample type	Theoretical CPT [°C]	Experimental CPT [°C]
Threaded bar	60.8	80
PBF-LB/M 1020°C×35' low nitrogen	51.5	40
PBF-LB/M 1080°C×35' low nitrogen	51.3	70
PBF-LB/M 1080°C×35' high nitrogen	63.1	≥ 85

The comparison between the chemical composition measured on powder cross sections, reported in Table 4.5, and that obtained after PBF-LB/M processing, reported in Table 4.29, indicates that the overall alloy chemistry was largely retained during manufacturing. With the exception of nitrogen, which was discussed separately, the main alloying elements remained within a relatively narrow compositional range. Silicon, manganese and iron showed only minor variations with respect to the starting powder, suggesting that the laser-based process did not induce marked compositional changes in these elements.

A slight decrease in chromium content was observed after PBF-LB/M processing. The powder cross sections showed an average Cr concentration of 26.67 ± 0.06 wt.%, whereas the low-nitrogen PBF-LB/M samples exhibited values between 25.1 and 25.8 wt.%. A comparable value was also measured in the high-nitrogen PBF-LB/M condition, equal to 25.3 wt.%. This variation remains limited in magnitude and should not be interpreted as evidence of a substantial chromium loss during processing. Rather, it may be related to local chemical heterogeneity, EDS quantification uncertainty, the normalization procedure adopted for the bulk samples, and slight compositional fluctuations in the initial feedstock used for powder production.

Nickel showed the opposite trend, increasing from 6.55 ± 0.60 wt.% in the powder cross sections to approximately 7.3–7.8 wt.% in the PBF-LB/M samples. Since significant nickel volatilization or uptake is not expected under the present processing conditions, this apparent enrichment is more plausibly associated with the relative variation of the other alloying elements within the normalized EDS dataset. Copper remained close to the powder composition, although slightly lower values were measured after PBF-LB/M processing, ranging from 0.6 to 0.8 wt.% compared with 0.90 ± 0.07 wt.% in the powder.

The Mo and W did not show evidence of systematic depletion. Molybdenum remained between 3.1 and 3.7 wt.%, compared with 3.28 ± 0.14 wt.% in the powder, whereas tungsten ranged from 0.4 to 0.8 wt.%, compared with 0.84 ± 0.08 wt.%. The larger scatter observed for W, particularly in the 1020 °C $\times$ 35 min low-nitrogen condition, should be considered with caution because of its low concentration and the intrinsic limitations of EDS quantification for minor alloying elements.

Overall, the compositional comparison does not reveal any pronounced alteration of the UNS S32760 metallic alloying-element balance after PBF-LB/M processing. The observed differences are moderate and mainly involve Cr, Ni and Cu, whereas

Si, Mn, Fe, Mo and W remain broadly comparable to the starting powder. Therefore, the microstructural and mechanical differences observed among the investigated PBF-LB/M conditions should be primarily ascribed to nitrogen content, thermal history, phase balance and heat-treatment response, rather than to major changes in the metallic alloy composition.

In particular, the PBF-LB/M sample heat treated at 1080 °C × 35 min with high nitrogen content exhibits the highest theoretical value (63.1 °C). This distribution directly reflects the weight of the three elements included in the standard formulation, namely Cr, Mo, and N, and especially the very pronounced role of nitrogen, whose coefficient in Eq. 4.9 is particularly high. From this perspective, the result obtained for the high-nitrogen PBF-LB/M sample treated at 1080 °C is fully consistent with its nitrogen content of 0.400 wt.%, markedly higher than that of the other samples. The higher nitrogen content, together with the similarly high Mo content (3.7 wt.%), is therefore expected to improve resistance to localized corrosion [139]. Several mechanisms have been proposed in the literature to account for the beneficial effect of nitrogen on corrosion resistance. Experimental evidence indicates that nitrogen tends to enrich beneath the passive film and at anodic dissolution sites. Moreover, some authors have suggested that nitrogen dissolution may, through its interaction with hydrogen, promote the formation of NH_4^+ ions. The generation of these ions would result in a local increase in pH, thus establishing conditions that are more favorable for repassivation [140].

Similarly, the threaded-bar material benefits from the combination of the highest Cr content of the entire series (26.3 wt.%), an Mo content of 3.6 wt.%, and still relatively high nitrogen content (0.271 wt.%), thus making it theoretically one of the most corrosion-resistant materials. The forged material, although not included in the Method E experimental campaign reported in the Table 4.28, exhibits an overall composition similar to that of the threaded bar, although slightly less favorable in terms of Cr and N, which justifies its slightly lower theoretical CPT value.

4.8.4.2 Microstructural origin of the Bulk-Compositional and Experimental CPT discrepancy

However, the comparison between theoretical CPT and experimental CPT unequivocally shows that average composition alone is not sufficient to describe the actual behavior of the materials. The most significant case is represented by the two low-

nitrogen PBF-LB/M samples, which, despite exhibiting nearly identical theoretical CPT values (∼51 °C), show profoundly different experimental behavior: the sample treated at 1020 °C × 35 min exhibits an experimental CPT of 40 °C, whereas the sample treated at 1080 °C × 35 min reaches a CPT of 70 °C. This discrepancy demonstrates that, at constant nominal composition, the response to localized corrosion is strongly governed by the microstructural evolution induced by heat treatment, which, in the case of the lower-temperature treatment, do not allow the dissolution of of deleterious sigma phase (and other intermetallic phases, see Table 3.2) previously present, and therefore cannot be interpreted exclusively on the basis of the bulk chemical composition of the material.

4.8.4.3 Phase-resolved chemical parameters and Localized corrosion resistance

In this respect, Table 4.30, which reports the partitioning of the alloying elements between austenite and ferrite, provides particularly important information. In all the investigated conditions, the expected behavior for duplex and super duplex stainless steels is observed, with Cr, Mo, and W preferentially partitioning to ferrite and Ni enriched in austenite [139]. However, the extent of such partitioning varies significantly from one sample to another and very likely plays a key role in the different corrosion responses. In the two low-nitrogen PBF-LB/M samples, austenite is in fact relatively depleted in Cr and Mo with respect to ferrite. In particular, in the sample treated at 1020 °C, austenite contains 23.8 wt.% Cr and 2.5 wt.% Mo, whereas ferrite reaches 27.8 wt.% Cr and 3.6 wt.% Mo; in the sample treated at 1080 °C, austenite contains 23.3 wt.% Cr and 2.6 wt.% Mo, compared with 26.8 wt.% Cr and 4.0 wt.% Mo in ferrite. This marked imbalance suggests a strong local heterogeneity in passivation potential between the two phases and, consequently, a greater susceptibility to pitting initiation in the less noble regions, most likely within austenite or at interphase.

The low-nitrogen PBF-LB/M sample treated at 1020 °C × 35 min represents the most critical condition. Despite a theoretical CPT of 51.5 °C, it fails experimentally already at 40 °C, thus exhibiting a pitting resistance far lower than that predicted by the simple ASTM formulation in Eq. 4.9. This behavior is consistent with the presence of sigma phase, already identified by microstructural analyses, which likely represents the most detrimental factor. Indeed, sigma precipitation causes local

depletion of the surrounding matrix in Cr, together with a greater difference in the concentration of this element between the austenitic and ferritic phases, as observed in Table 4.30, and in Mo, thereby reducing localized corrosion resistance in the adjacent regions. In this case, the deleterious effect of sigma phase appears to prevail over the benefit expected on the basis of the nominal material composition.

By contrast, the high-nitrogen PBF-LB/M sample treated at 1080 °C, which exhibited the best experimental behavior with no pitting observed up to 85 °C, presents a more favorable condition. While maintaining the typical duplex phase balance (austenite phase $\sim$ 55 % vol), it shows an austenite phase that is less depleted in Cr and Mo than that of the low-nitrogen PBF-LB/M samples, with values of 24.6 wt.% Cr and 3.0 wt.% Mo, whereas ferrite contains 26.1 wt.% Cr and 4.3 wt.% Mo. The smaller Cr difference between the two phases, together with the higher overall nitrogen content, suggests a condition of better chemical balance and therefore a reduction in the local heterogeneities responsible for passive-film destabilization. This is fully consistent with the fact that this sample exhibited an experimental CPT above the highest investigated temperature and therefore a pitting resistance higher than that of both the conventional threaded-bar material and the low-nitrogen PBF-LB/M samples.

The threaded-bar material represents a particularly interesting case, since it shows good qualitative agreement between theoretical prediction and experimental behavior. Indeed, despite a theoretical CPT of 60.8 °C, the material experimentally reached a CPT of 80 °C, ranking among the best-performing conditions. This behavior suggests that, in addition to its favorable chemical composition, the microstructure of the conventional material is characterized by a more balanced phase distribution and a lower level of morphological defects than that of the PBF-LB/M-produced samples.

A further level of interpretation of the localized corrosion behavior can be obtained from the analysis of the $PREN_W$, Cr_{eq}, Ni_{eq}, and Cr_{eq}/Ni_{eq} ratio values determined separately in austenite and ferrite, as reported in Table 4.32. These parameters make it possible to relate the local chemistry of the two phases more directly to the experimental CPT values obtained by ASTM G48 Method E, thus overcoming the limitations inherent in an assessment based only on the overall average chemical composition of the steel.

Table 4.32 Phase-resolved $PREN_W$ (Equation 3.1b, with K=16), Cr_{eq} (Equation 3.2a), and Ni_{eq} (Equation 3.2b) values of UNS S32760 samples. The values measured in austenite (A) and ferrite (F) are reported, together with the Cr_{eq}/Ni_{eq} on chemistry average ratio.

	$PREN_W$		Cr_{eq}		Ni_{eq}		Cr_{eq}/Ni_{eq}
UNS S32760 sample type	**A**	**F**	**A**	**F**	**A**	**F**	**Ratio**
Threaded bar	39.9	47.4	28.8	33.1	19.1	15.8	1.77
Forged sample	38.9	46.5	28.3	32.4	17.5	15.1	1.86
PBF-LB/M 1020°C×35' low nitrogen	34.7	42.9	26.9	32.5	14.7	11.4	2.28
PBF-LB/M 1080°C×35' low nitrogen	35.2	43.6	27.0	32.1	14.9	11.8	2.22
PBF-LB/M 1080°C×35' high nitrogen	41.8	48.0	28.5	31.8	21.8	19.3	1.47

First, the $PREN_W$ values calculated for the individual phases show, for all the investigated conditions, the expected behavior for super duplex stainless steels, with ferrite systematically exhibiting higher values than austenite, in agreement with what has been reported in the literature as a function of heat-treatment temperature [139]. This is fully consistent with the well-known tendency of Cr, Mo, and W to partition preferentially into the ferritic phase. However, although ferrite always exhibits the highest $PREN_W$, the experimental behavior in terms of CPT is not governed solely by the maximum value reached by one of the two phases, but rather by the overall phase balance, by the difference in local nobility, and by the microstructural quality of the material [139].

From this standpoint, the PBF-LB/M 1080°C×35' high nitrogen sample, which exhibited the best experimental response with a CPT of at least 85 °C, also shows the most favorable combination of phase-related parameters. In particular, it exhibits the highest $PREN_W$ value in austenite (41.8) and one of the highest values in ferrite (48.0). This condition is particularly significant, because it suggests that not only the ferritic phase, but also the austenitic phase, possesses very high intrinsic pitting resistance. In other words, the phase traditionally considered more vulnerable [91, 139] is not strongly penalized in this case, and this likely contributes to increasing the experimental CPT to values above the highest investigated limit. This result is consistent with the higher nitrogen content of the material, which increases both the overall PREN and the stability of austenite, thereby contributing to a more favorable combination of local corrosion resistance and microstructural balance.

The threaded bar material, for which an experimental CPT of 80 °C was measured, also shows high $PREN_W$ values in both phases, namely 39.9 in austenite and 47.4 in ferrite. Although the austenitic $PREN_W$ is lower than that of the high-nitrogen PBF-LB/M sample, it remains sufficiently high to guarantee excellent resistance to localized corrosion.

By contrast, the two PBF-LB/M low nitrogen samples heat treated at 1020°C×35' and 1080°C×35' exhibit significantly lower $PREN_W$ values, especially in the austenitic phase. In the sample treated at 1020°C×35', austenite exhibits a $PREN_W$ value of 34.7, whereas ferrite reaches 42.9; in the sample treated at 1080°C×35', the corresponding values are 35.2 and 43.6. These data indicate that, in both conditions, the austenitic phase is locally less resistant than that observed in the threaded-bar material and, above all, in the high-nitrogen PBF-LB/M material. This aspect is particularly relevant, because pitting tends to initiate preferentially in the less noble regions or in areas affected by strong compositional gradients between one phase and the other. Consequently, the lower $PREN_W$ of austenite in the low-nitrogen samples constitutes a first strong indication of their greater susceptibility to localized corrosion.

The comparison between the two low-nitrogen samples is, however, particularly instructive. Despite the fact that the $PREN_W$ values in the two phases are very similar, their experimental behavior in terms of CPT is drastically different: 40 °C for the material treated at 1020°C×35' versus 70 °C for the one treated at 1080°C×35'. This result clearly demonstrates that phase-specific $PREN_W$, although a very useful parameter, is not in itself sufficient to describe the actual behavior of the material unless it is accompanied by microstructural evaluation. In the sample treated at 1020°C, the presence of sigma phase constitutes a strongly detrimental factor, capable of lowering the CPT well below the value suggested by the chemical parameters alone. Sigma precipitation causes local depletion of Cr and Mo in the surrounding matrix and therefore introduces preferential sites for pitting initiation, partially canceling the benefit expected on the basis of the nominal PREN of the phases.

This interpretation is also directly supported by the corrosion morphology observed after ASTM G48 Method E testing. As shown in Figure 4.93, corresponding to the PBF-LB/M low-nitrogen sample treated at 1020°C×35' and tested at 65 °C, localized attack appears to nucleate in correspondence with sigma phase. This observation is fully consistent with the strongly detrimental role of sigma precipitation,

which locally depletes the adjacent matrix in Cr and Mo and thereby promotes passive-film breakdown and pit initiation.

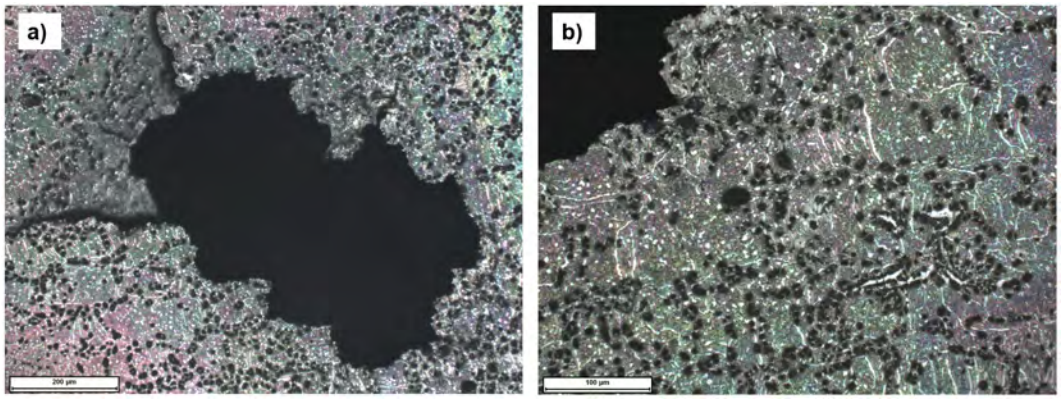

Fig. 4.93 Optical micrographs of localized corrosion in the PBF-LB/M low-nitrogen UNS S32760 sample heat treated at 1020°C×35' and tested according to ASTM G48 Method E at 65 °C. (a) Pit morphology showing that localized corrosion may have nucleated from sigma phase. (b) Higher-magnification view of the same region.

The combined interpretation of the Cr_{eq} and Ni_{eq} values reported in Table 4.32 provides further insight. The low-nitrogen samples treated at 1020°C and 1080°C show the highest average Cr_{eq}/Ni_{eq} ratios, namely 2.28 and 2.22, respectively. Such a high ratio indicates a stronger ferrite-promoting tendency of the system, consistent with ferrite stabilization and with a lower ability to sustain a sufficiently developed and chemically robust austenitic fraction. This aspect is in good agreement with their lower pitting resistance, particularly in the sample treated at 1020°C, where the combination of low Ni_{eq}, low nitrogen content, and the presence of sigma phase determines the most critical condition of the entire series tested in accordance with ASTM G48 Method E.

By contrast, although the PBF-LB/M low-nitrogen sample treated at 1080°C×35' exhibits a significantly improved corrosion resistance, with an experimental CPT of 70 °C, localized attack can still be observed at specific microstructural sites. As shown in Figure 4.94, pit nucleation appears to occur preferentially within the austenitic phase or at the ferrite/austenite interphase regions. This behavior is in good agreement with the phase-resolved $PREN_W$ values discussed above, since austenite represents the phase with the lower intrinsic pitting resistance in this condition. Therefore, although the suppression of sigma phase markedly improves the corrosion

response, the persistence of local chemical imbalance between ferrite and austenite remains sufficient to define preferential sites for pit nucleation.

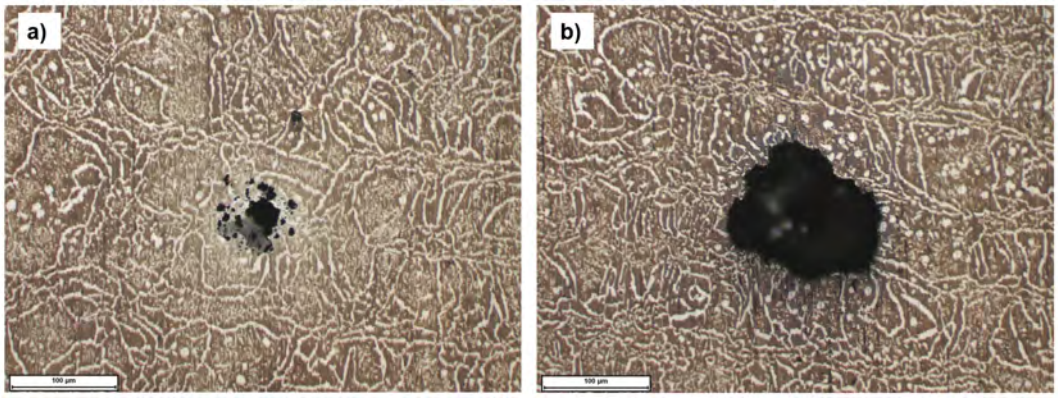

Fig. 4.94 Optical micrographs of localized corrosion in the PBF-LB/M low-nitrogen UNS S32760 sample heat treated at 1080°C×35' and tested according to ASTM G48 Method E at 70 °C. (a) Pit morphology at the experimental CPT condition showing that pit nucleation occurs preferentially within the austenitic phase or at the ferrite/austenite interface, consistently with the lower $PREN_W$ of austenite. (b) Higher-magnification view.

Conversely, the PBF-LB/M 1080°C×35' high nitrogen sample, which exhibits the best experimental behavior, also shows the lowest Cr_{eq}/Ni_{eq} ratio of the entire series, equal to 1.47. This value reflects a system that is more balanced from the ferrite/austenite standpoint, with a significantly higher Ni_{eq} in both phases and especially in austenite (21.8), consistently with the strong austenite-stabilizing effect exerted by nitrogen. From a metallurgical standpoint, this result suggests that the high nitrogen content not only increased the theoretical PREN, but also promoted the formation of a more balanced and chemically less heterogeneous microstructure, with a consequent increase in passive-film stability and resistance to pitting initiation.

The threaded bar material shows an intermediate yet very favorable condition, with a Cr_{eq}/Ni_{eq} ratio equal to 1.77. This value, lower than that of the low-nitrogen samples but higher than that of the high-nitrogen sample, is in perfect agreement with the observed experimental behavior, with the threaded-bar material reaching a high CPT, although lower than that of the high-nitrogen PBF-LB/M sample treated at 1080°C. The forged sample, although not included in the Method E experimental campaign reported in the results table, also shows $PREN_W$ values and a Cr_{eq}/Ni_{eq} ratio (1.86) very close to those of the threaded-bar material. This suggests that, in the absence of significant microstructural defects, the forged material could be expected

to show pitting resistance intermediate between that of the conventional materials and that of the appropriately heat-treated low-nitrogen PBF-LB/M samples.

Overall, the analysis of the phase-related parameters demonstrates that the experimentally measured pitting resistance does not simply depend on the average $PREN_W$ of the material, but is strongly influenced by three main aspects: *i*) the absolute $PREN_W$ value of the most vulnerable phase, generally austenite; *ii*) the degree of chemical imbalance between ferrite and austenite; and *iii*) the Cr_{eq}/Ni_{eq} ratio, as a synthetic indicator of the ferrite-promoting tendency of the system and therefore of the level of microstructural rebalance that can be achieved. From this perspective, the PBF-LB/M high nitrogen sample treated at 1080 °C represents the optimal condition, in which high austenitic $PREN_W$, low Cr_{eq}/Ni_{eq} ratio, and good microstructural homogeneity cooperate in maximizing CPT. Conversely, the PBF-LB/M low nitrogen sample treated at 1020 °C represents the least favorable condition, in which low austenitic $PREN_W$, high Cr_{eq}/Ni_{eq} ratio, and the presence of sigma phase act jointly to drastically reduce resistance to localized corrosion.

Chapter 5

Conclusions

5.1 Main Scientific Contributions

This research work demonstrated the feasibility of an integrated process chain for the production of super duplex stainless steel UNS S32760 powders from process waste and their subsequent transformation into components by PBF-LB/M. The adopted approach made it possible to establish a continuous link across the whole production route, starting from powder production by a vacuum inert gas atomizer in a close-coupled configuration, followed by the optimisation of PBF-LB/M process parameters, post-process heat treatment, and final qualification in terms of microstructural assessment, mechanical properties, and corrosion resistance. This approach confirms that the production of metallic powders from industrial waste can represent a technically viable strategy to reduce the environmental impact associated with the manufacturing of high-performance components, while maintaining adequate control over the characteristics required for additive manufacturing applications.

5.1.1 Integrated Waste-to-Powder Route: Atomization Optimisation and Sustainability

The analysis of the gas atomization process highlighted the key role of CFD modelling in defining the operating window to be adopted. The simulation of the gas-jet fluid dynamic field, integrated with targeted experimental trials, made it possible to correlate the atomization pressure with plume morphology, process stability, particle size distribution, debris formation, and gas consumption. In this way, the number of experimental trials required could be reduced, directing the campaign towards the most promising conditions for maximising the yield in the 20–63 μm particle-size fraction, which is of interest for the PBF-LB/M process. CFD simulation does not replace experimental validation; rather, it reduces the degree of empiricism involved in process development, limiting the material and time required for process refinement, and reducing the use of energy and technical gases during the optimisation stage. For the PSI Hermiga 100/10 VIGA close-coupled gas atomization system used in this work, an argon pressure of 40 bar represented the most favourable compromise between stable atomization, yield in the PBF-LB/M-relevant 20–63 μm particle-size fraction, powder quality, and gas consumption.

The carbon footprint evaluation confirmed the interest of the waste-to-powder production route. The direct conversion of waste into atomized powders reduces the need for conventional primary or secondary raw materials and enables the valorisation of a material with a high content of alloying elements, such as Cr, Mo, Ni, W. This aspect is particularly relevant for super duplex stainless steels, in which the cost and environmental impact of the raw material are strongly influenced by the presence of strategic elements with high economic value. The possibility of obtaining processable powders from UNS S32760 waste therefore contributes to the development of a more circular supply chain for the production of high-performance components, with potential environmental and economic advantages.

5.1.2 Process-Gas Composition, Nitrogen Enrichment, and Nitrogen Retention During PBF-LB/M

The composition of the process gases used during atomization proved to be not only a fluid dynamic parameter, but also a factor with significant metallurgical influence. In particular, the use of nitrogen in the melting chamber promoted nitrogen absorption in the molten metal, according to the expected behaviour associated with nitrogen solubility as a function of partial pressure. Compared with the starting material used as atomization feedstock, characterised by a nitrogen content of approximately 0.268 ± 0.004 wt.%, the use of nitrogen both in the melting chamber and as atomization gas led to an increase of approximately 0.210 wt.%, bringing the nitrogen content of the high-nitrogen powders to values close to 0.479 wt.%. This increase corresponds to a relative enrichment of approximately 80% with respect to the initial feedstock. The use of nitrogen only as atomization gas, instead, showed a much more limited effect on the final nitrogen content, probably due to the extremely short interaction times between the gas and the metallic droplets during solidification.

Moreover, the use of nitrogen as atomization gas promoted a higher particle true density, reducing the tendency to form intraparticle porosity, characterised by an average diameter of approximately 183.7 ± 33.8 nm, associated with argon entrapment.

It therefore follows that, in order to significantly increase the nitrogen content of UNS S32760 powders, it was necessary to use nitrogen also as the atmosphere in the melting chamber.

The increase in nitrogen content directly affected the microstructure of the atomized powders. Powders produced with nitrogen in the melting chamber showed the presence of austenite already in the as-atomized condition, whereas powders obtained under low-nitrogen conditions were characterised only by the ferritic phase, or in any case by an austenite fraction below the quantification limit of the XRD technique and SEM observations. However, the austenite fraction detected in the high-nitrogen powders was not independent of particle size, but increased with increasing particle size, consistently with the lower cooling rates and longer residence times at high temperature experienced by coarser droplets during solidification. In the particle-size fraction of interest for PBF-LB/M, equal to 20–63 μm, the austenite content in the high-nitrogen powders was approximately in the range of 25–30 vol.%.

This result is of particular interest for super duplex stainless steels processed by PBF-LB/M, since nitrogen is a strong austenite stabiliser and contributes both to the ferrite-austenite balance and to resistance to localised corrosion.

The subsequent transformation by PBF-LB/M showed that the nitrogen content of the powders is not entirely retained in the consolidated component. In the case of high-nitrogen powders, the initial powder mixture in the 20–63 µm fraction exhibited an average nitrogen content of 0.479 ± 0.003 wt.%, whereas the as-built PBF-LB/M specimen produced with the optimised parameters, corresponding to an HED of 66.7 J/mm³, showed a nitrogen content of 0.400 ± 0.002 wt.%. Transformation by PBF-LB/M therefore caused an absolute nitrogen reduction of approximately 0.079 wt.%, corresponding to a relative loss of about 16.5% with respect to the initial powder content. Despite this depletion, the consolidated material still retained a nitrogen content significantly higher than that of the initial atomization feedstock, equal to 0.268 ± 0.004 wt.%, confirming the effectiveness of using nitrogen-enriched powders to compensate for the loss occurring during laser melting.

It is also relevant to observe that, at the selected HED of 66.7 $\mathrm{J\,mm^{-3}}$, the nitrogen decrease was of comparable absolute magnitude for the low-nitrogen and high-nitrogen powder blends. The low-nitrogen powders decreased from approximately 0.206 wt.% to 0.140 wt.%, corresponding to a relative nitrogen reduction of approximately 32.0%. By comparison, the high-nitrogen powder mixture decreased from 0.479 ± 0.003 wt.% to 0.400 ± 0.002 wt.%, corresponding to a relative reduction of approximately 16.5%.

Therefore, although the nitrogen decrease occurred within the same order of magnitude for both powder blends, its relative impact was greater for the low-nitrogen material because of its lower initial nitrogen content. This indicates that nitrogen depletion is strongly influenced by the thermal history associated with laser melting and solidification, whereas the initial powder composition remains decisive in determining the nitrogen level retained in the final component. Consequently, the use of high-nitrogen powders remains strategically advantageous, since it enables a higher nitrogen level to be retained in the final component even after the depletion induced by PBF-LB/M processing. Notably, this nitrogen depletion occurred despite the use of a flowing nitrogen atmosphere during PBF-LB/M processing, indicating that the nitrogen-containing process environment alone was not sufficient to ensure complete nitrogen retention during laser melting and solidification.

This phenomenon makes it even more important to start from powders with a high nitrogen content, since only in this way is it possible to maintain, in the PBF-LB/M component, a nitrogen level sufficient to promote austenite formation and to sustain the performance typically required for a super duplex stainless steel. The high-nitrogen powders favoured the presence of an austenite fraction already in the as-built condition, whereas the low-nitrogen powders led to predominantly ferritic microstructures, confirming the central role of powder chemistry in controlling the metallurgical response of the PBF-LB/M material.

5.1.3 Heat Treatment, Microstructural Rebalancing, and Mechanical Performance

The post-process heat treatment was confirmed to be essential for restoring, in the components, a duplex microstructure suitable for service. The heat-treatment results showed that the selection of 1080 °C for 35 min should not be interpreted as the condition providing only the highest austenite fraction. The treatment at 1020 °C for 35 min, although promoting a fine microstructure, was associated with the presence of sigma phase, estimated at approximately 1.5 vol.%, and therefore did not represent the most favourable condition from an overall metallurgical point of view. Conversely, the treatment at 1080 °C for 35 min provided the best compromise among dissolution of deleterious phases, ferrite-austenite rebalancing, and preservation of a microstructure compatible with application requirements. The analysed micrographs show that the nitrogen content of the powders strongly influences the microstructure obtained after heat treatment: specimens produced from low-nitrogen powders exhibit a ferritic-austenitic dual-phase microstructure that is still markedly anisotropic, whereas those produced from high-nitrogen powders show a finer, more homogeneous, and clearly more isotropic microstructure, with a significantly higher average austenite fraction.

The mechanical tests confirmed that the most balanced overall condition was obtained after heat treatment at 1080 °C for 35 min. The as-built state exhibited high strength values, but was penalised by insufficient ductility and toughness, consistently with the predominantly ferritic microstructure and with the presence of defects typical of the PBF-LB/M process. By rebalancing the phases, the heat treatment instead made it possible to reduce the excessive brittleness of the as-built state and to obtain

a better balance among strength, ductility, and toughness. In particular, for the low-temperature Charpy tests, the condition treated at 1080 °C for 35 min proved to be the most effective among those investigated and the only one, for the low-nitrogen horizontal specimens, fully compliant with the toughness requirements specified by NORSOK M-630. The tensile tests performed on specimens treated at 1080 °C for 35 min also showed adequate static properties, with yield strength values in the range of 600–650 MPa, ultimate tensile strength generally above 800 MPa, and significant ductility.

5.1.4 Corrosion Qualification and Recommended Powder-to-Component Route

The corrosion tests further highlighted the combined importance of heat treatment and nitrogen content. In the ASTM G48 Method A tests, the PBF-LB/M specimens heat-treated at 1080 °C for 35 min, produced from both low-nitrogen and high-nitrogen powders, showed no mass loss up to 312 h of immersion, indicating remarkable stability of the passive film even under prolonged exposure conditions. Conversely, the as-built specimens showed a non-compliant response, with mass loss and pit formation, confirming that optimisation of PBF-LB/M parameters alone is not sufficient to guarantee the corrosion resistance required for severe applications.

The results obtained by ASTM G48 Method E indicated that the best resistance to localised corrosion was achieved by the PBF-LB/M specimens produced from high-nitrogen powders and treated at 1080 °C for 35 min. This condition showed the highest experimental CPT value, equal to at least 85 °C, higher than that of the low-nitrogen PBF-LB/M specimens treated at the same temperature. This behaviour can be attributed to the higher residual nitrogen content in the component, to the more favourable distribution of the austenitic phase, and to the finer and more isotropic microstructure. The comparison between the low-nitrogen specimens treated at 1020 °C and at 1080 °C further confirms that, for the same nominal composition, pitting resistance is strongly governed by the final microstructure and by the presence or absence of deleterious intermetallic phases.

Overall, this research demonstrates that the sustainable production of UNS S32760 powders from process waste, followed by PBF-LB/M and by an appropriately selected heat treatment, can lead to components with mechanical properties and

corrosion resistance compatible with the requirements for applications in chloride-containing environments. The most promising route identified involves the use of nitrogen in the melting chamber during atomization, the production of high-nitrogen powders, transformation by optimised PBF-LB/M parameters, and final heat treatment at 1080 °C for 35 min. This combination makes it possible to compensate for nitrogen loss during additive manufacturing, promote the restoration of a more balanced duplex microstructure, improve microstructural isotropy, and obtain a more robust response from both the mechanical and localised corrosion resistance standpoints.

5.2 Implications for Industrial Implementation

The results provide an industrially oriented guideline for the implementation of waste-derived UNS S32760 powders in PBF-LB/M. The proposed route is based on the controlled integration of feedstock selection, gas atomization, powder qualification, PBF-LB/M parameter optimisation, heat treatment, and performance assessment. From this perspective, qualification should not rely on a single parameter, such as density or austenite fraction, but should include powder chemistry, nitrogen retention, defect population, phase balance, mechanical behaviour, and corrosion resistance.

The atomization pressure of 40 bar identified in this work should be considered specific to the PSI Hermiga 100/10 VIGA close-coupled system, its annular slit nozzle geometry, the adopted melt-delivery conditions, and the investigated UNS S32760 feedstock. It should therefore not be interpreted as a universal operating value for all VIGA systems. Nevertheless, the methodology adopted in this work, based on CFD-assisted operating-window definition followed by focused experimental validation, is directly transferable to industrial-scale atomization systems.

Similarly, the PBF-LB/M parameter set identified using the Aconity Mini 3D system, including the selected HED of 66.7 J/mm^3, should be considered a useful starting point rather than a directly transferable industrial recipe. Different PBF-LB/M systems may exhibit substantial differences in laser-spot diameter, optical configuration, recoating system, layer thickness, gas-flow arrangement, scan strategy, and thermal conditions. Therefore, a dedicated parameter-optimization campaign remains necessary whenever the powder is transferred to a different PBF-LB/M system.

By contrast, the solution treatment at 1080 °C for 35 min is primarily based on the metallurgical response of UNS S32760 rather than on the specific gas atomizer or PBF-LB/M machine used in this work. It therefore represents a more transferable reference condition. Nevertheless, its application at industrial scale should be validated for the specific component geometry, wall thickness, furnace thermal uniformity, loading configuration, and quenching conditions.

5.3 Limitations of the Present Study and Future Research Directions

5.3.1 Scale-Up of the Waste-to-Powder Route

The present study provides a technically grounded proof of feasibility for the complete waste-to-powder-to-component route. However, the PSI Hermiga 100/10 system installed at the Alessandria campus of Politecnico di Torino represents an intermediate-scale VIGA plant between a purely laboratory-scale apparatus and a fully industrial production unit. Consequently, significant differences may arise during transfer to larger industrial atomization systems, including changes in melt mass, thermal inertia, nozzle geometry, gas recirculation, gas consumption, melt-flow control, and particle-collection efficiency.

Future work should therefore focus on the recalibration of the atomization parameters for industrial-scale systems, supported by further CFD analyses and validation trials. The pressure, gas-to-metal ratio, superheat, melt-chamber overpressure, nozzle configuration, and gas-recirculation strategy should be reassessed as a function of the scale and design of the industrial plant.

A relevant development would be the use of UNS S32760 machining chips as feedstock. Such material is generally more widely available than non-compliant components, but introduces additional challenges related to lubricant contamination, washing efficiency, possible surface oxidation, and handling. Future research should therefore assess suitable washing and de-oiling procedures, quantify residual contamination after cleaning, and investigate chip compaction before charging the atomization crucible. Increasing the bulk density of the chip charge could enable a larger mass of material to be introduced into the crucible and improve melting

efficiency and overall process yield. A dedicated life-cycle assessment should evaluate the environmental burden associated with chip collection, cleaning, compaction, melting, atomization, sieving, and powder qualification.

5.3.2 Transferability of PBF-LB/M Processing and Heat Treatment

The selected PBF-LB/M parameters should be validated on additional machine platforms and for geometries more representative of industrial components. Particular attention should be given to the effect of machine-specific hardware, gas-flow conditions, scan strategy, build orientation, and thermal history on density, nitrogen retention, microstructure, and defect population. The selected HED may serve as an initial reference, but it cannot replace machine-specific process optimisation.

The heat-treatment route should also be validated on components with different thicknesses and thermal masses. Although 1080°C for 35 min represented the most favourable practical compromise within the present study, industrial implementation requires verification of temperature uniformity, heating rate, soaking time, quenching rate, and the final phase balance in the actual component geometry.

5.3.3 Further Microstructural, Corrosion, and Fracture-Mechanics Investigations

Further research should clarify the mechanisms responsible for nitrogen depletion during PBF-LB/M. In particular, the individual contributions of melt-pool evaporation, spatter generation, gas–metal mass transfer, and powder reuse should be quantified. The evolution of nitrogen content during repeated powder recycling cycles should also be evaluated, since industrial PBF-LB/M production normally involves multiple powder-reuse operations.

Further corrosion work should extend the present ASTM G48 testing through electrochemical characterisation, crevice-corrosion evaluation, and testing under service-representative chloride-containing environments. In parallel, fatigue investigations should be repeated on specimens produced under conditions specifically

optimised to minimise lack-of-fusion defects, including the possible application of hot isostatic pressing and controlled surface-finishing routes.

Finally, the tensile tests performed at -46°C provided direct values of $R_{p0.2}$, R_m, and E under the temperature conditions relevant to possible future fracture-mechanics testing. These data represent a useful basis for the design of low-temperature CTOD tests, but do not replace direct fracture-toughness measurements. Future CTOD investigations should assess crack-initiation resistance and defect tolerance in relation to build orientation, heat-treatment condition, and microstructural state. Such work would be particularly relevant for applications in which fracture-mechanics qualification is required, including severe-service oil-and-gas and selected nuclear applications.

References

[1] P. Samal and J. Newkirk, editors. *ASM Handbook, Volume 7: Powder Metallurgy*, volume 7 of *ASM Handbook*. ASM International, 2015.

[2] Metal Powder Industries Federation (MPIF). Industry facts. https://www.mpif.org/Resources/IndustryFacts.aspx, 2025. Accessed on August 2025.

[3] World Steel Association. World steel in figures 2024. https://www.worldsteel.org/data/world-steel-in-figures/world-steel-in-figures-2024, 2025. Accessed on August 2025.

[4] Isaac Chang and Yuyuan Zhao, editors. *Advances in Powder Metallurgy: Properties, Processing and Applications*. Woodhead Publishing Series in Metals and Surface Engineering. Woodhead Publishing, Oxford, 2013. eBook ISBN: 9780857098900.

[5] Mohsen Attaran. The rise of 3-D printing: The advantages of additive manufacturing over traditional manufacturing. *Business horizons*, 60(5):677–688, 2017.

[6] Damir Godec, Joamin Gonzalez-Gutierrez, Axel Nordin, Eujin Pei, and Julia Ureña Alcázar, editors. *A Guide to Additive Manufacturing*. Springer International Publishing, 2022.

[7] Ian Gibson, David Rosen, Brent Stucker, Mahyar Khorasani, David Rosen, Brent Stucker, and Mahyar Khorasani. *Additive manufacturing technologies*, volume 17. Springer, 2021.

[8] ISO and ASTM. ISO/ASTM 52900:2021, Additive manufacturing — General principles — Fundamentals and vocabulary. Available at: https://www.iso.org/obp/ui/#!iso:std:74514:en, 2021.

[9] Markus Ramsperger and Simon Eichler. Electron beam based additive manufacturing of alloy 247 for turbine engine application: from research towards industrialization. *Metallurgical and Materials Transactions A*, 54(5):1730–1743, 2023.

[10] Gopala Rao Thellaputta, Pulcharu Subhash Chandra, and CSP Rao. Machinability of nickel based superalloys: a review. *Materials Today: Proceedings*, 4(2):3712–3721, 2017.

[11] Mark Armstrong, Hamid Mehrabi, and Nida Naveed. An overview of modern metal additive manufacturing technology. *Journal of Manufacturing Processes*, 84:1001–1029, 2022.

[12] Paul Gradl, Darren C Tinker, Alison Park, Omar R Mireles, Marissa Garcia, Ryan Wilkerson, and Christopher Mckinney. Robust metal additive manufacturing process selection and development for aerospace components. *Journal of Materials Engineering and Performance*, 31(8):6013–6044, 2022.

[13] Shubhavardhan Ramadurga Narasimharaju, Wenhan Zeng, Tian Long See, Zicheng Zhu, Paul Scott, Xiangqian Jiang, and Shan Lou. A comprehensive review on laser powder bed fusion of steels: Processing, microstructure, defects and control methods, mechanical properties, current challenges and future trends. *Journal of Manufacturing Processes*, 75:375–414, 2022.

[14] Silvia Vock, Burghardt Klöden, Alexander Kirchner, Thomas Weißgärber, and Bernd Kieback. Powders for powder bed fusion: a review. *Progress in Additive Manufacturing*, 4(4):383–397, 2019.

[15] ISO, ASTM, and CEN (European Committee for Standardization). EN ISO/ASTM 52928:2024, Additive manufacturing of metals — Feedstock materials — Powder life cycle management (ISO/ASTM 52928:2024). Available at: https://compass.astm.org/, 2024.

[16] Patrick Pradel, Zicheng Zhu, Richard Bibb, and James Moultrie. Complexity is not for free: the impact of component complexity on additive manufacturing build time. 2017.

[17] Bradley Howell Jared, Brad Boyce, Corbett Chandler Battaile, Hojun Lim, Hy D Tran, Joshua Robbins, Brett W Clark, and Teddy D Blacker. Complexity Isn't Necessarily Free: Opportunities and Challenges in Additive manufacturing. 2015.

[18] Richard Rothfelder, Florian Nahr, Lova Chechik, Dominic Bartels, and Michael Schmidt. A brief history of the progress of laser powder bed fusion of metals in europe. *Journal of Manufacturing Science and Engineering*, 145(10):100801, 2023.

[19] Wilhelm Meiners, Konrad Wissenbach, and Andres Gasser. Selective laser sintering at melting temperature, 2001. Priority: DE 19649865 C1 ("Verfahren zur Herstellung eines Formkörpers"), filed 1996-12-02; published 1998-02-12. Family includes US 6,215,093 B1.

[20] Mohan Jiao, Hongyu Long, Buwei Xiao, Xiaoyu Liang, and Feng Lin. Electron beam powder bed fusion additive manufacturing: A comprehensive review and its development in china. *Additive Manufacturing Frontiers*, 3(4):200177, 2024.

[21] Laura ET Mathias, Vitor E Pinotti, Bruna F Batistão, Nicolas Rojas-Arias, Gustavo Figueira, Angelo F Andreoli, and Piter Gargarella. Metal powder as feedstock for laser-based additive manufacturing: From production to powder modification. *Journal of Materials Research*, 39(1):19–47, 2024.

[22] Ethan M Sullivan, Saman Sharif Hedås, Mattias Jerhamre Engström, and Greta Lindwall. Effect of powder particle size distribution and contouring on build quality in electron beam powder bed fusion of a medium-c hot-work tool steel. *The International Journal of Advanced Manufacturing Technology*, 128(7):2953–2967, 2023.

[23] Thywill Cephas Dzogbewu. Additive manufacturing of tial-based alloys. *Manufacturing Review*, 7:35, 2020.

[24] Reinhold Wartbichler, Tobias Maiwald-Immer, Fabian Pürstl, and Helmut Clemens. Laser powder bed fusion of intermetallic titanium aluminide alloys using a novel process chamber heating system: a study on feasibility and microstructural optimization for creep performance. *Metals*, 12(12):2087, 2022.

[25] Jonathan B Baker. Market definition: An analytical overview. *Antitrust LJ*, 74:129, 2007.

[26] Wohlers Associates. 3D Printing and Additive Manufacturing Global state of the Industry. https://wohlersassociates.com/product/wr2025/, 2025. Accessed on August 2025.

[27] Maximilian Munsch and Eric Wycisk Matthias Schmidt-Lehr. Predicting the metal additive manufacturing market and breaking the hype cycle. *Metal AM*, 06 2024.

[28] MarketsandMarkets. 3D Printing Metals Market by Metal Type, Form, Technology, End-use Industry, and Region – Global Forecast to 2030. https://www.marketsandmarkets.com/Market-Reports/3d-printing-metal-market-34714085.html, 2025. Accessed on August 2025.

[29] IDTechEx. Metal Additive Manufacturing 2025–2035: Technologies, Players, and Market Outlook. https://www.idtechex.com/en/research-report/metal-additive-manufacturing/1097, 2025. Accessed on August 22, 2025.

[30] Mordor Intelligence. Powder Bed Fusion Process 3D Printer Market Size & Share Analysis - Growth Trends & Forecasts (2025 - 2030). https://www.mordorintelligence.com/industry-reports/powder-bed-fusion-process-3d-printer-market, 2025. Accessed on August 22, 2025.

[31] TechNavio. Metal Powder Bed Fusion Market 2024–2028. https://www.researchandmarkets.com/reports/5835909/metal-powder-bed-fusion-marketrela2-5561294, 2024. Accessed on August 22, 2025.

[32] Global Industry Analysts, Inc. Metal Powder Bed Fusion - Global Strategic Business Report. https://www.researchandmarkets.com/reports/6006979/metal-powder-bed-fusion-global-strategicrela0-5835909, 2025. Accessed on August 22, 2025.

[33] ISO, ASTM, and CEN (European Committee for Standardization). BS ISO/ASTM DIS 52908: Additive manufacturing of metals — Finished part properties — Post-processing, inspection and testing of parts produced by powder bed fusion. Available at: https://compass.astm.org/, 2025.

[34] ISO, ASTM, and CEN (European Committee for Standardization). EN ISO/ASTM 52909:2024, Additive manufacturing of metals — Finished part properties — Orientation and location dependence of mechanical properties for metal parts (ISO/ASTM 52909:2024). Available at: https://compass.astm.org/, 2024.

[35] ISO, ASTM, and CEN (European Committee for Standardization). EN ISO/ASTM 52904:2024, Additive manufacturing of metals — Process characteristics and performance — Metal powder bed fusion process to meet critical applications (ISO/ASTM 52904:2024). Available at: https://compass.astm.org/, 2024.

[36] AMPOWER GmbH & Co. KG. AMPOWER Report 2025 on Additive Manufacturing. https://additive-manufacturing-report.com/report-2025/, 2025. Accessed on August 25, 2025.

[37] Salomé Sanchez, Peter Smith, Zhengkai Xu, Gabriele Gaspard, Christopher J Hyde, Wessel W Wits, Ian A Ashcroft, Hao Chen, and Adam T Clare. Powder bed fusion of nickel-based superalloys: A review. *International Journal of Machine Tools and Manufacture*, 165:103729, 2021.

[38] Sheng Cao, Yichao Zou, Chao Voon Samuel Lim, and Xinhua Wu. Review of laser powder bed fusion (lpbf) fabricated Ti-6Al-4V: process, post-process treatment, microstructure, and property. *Light: Advanced Manufacturing*, 2(3):313–332, 2021.

[39] Xin Wang, Dongyun Zhang, Ang Li, Denghao Yi, and Tianci Li. A review on traditional processes and laser powder bed fusion of aluminum alloy microstructures, mechanical properties, costs, and applications. *Materials*, 17(11):2553, 2024.

[40] 360iResearch. Gas Atomized Metal Powder Market by Material Composition (Aluminum, Copper Alloy, Nickel Alloy), Application Technology (Additive Manufacturing, Cold Spraying, Laser Cladding), End Use Sector, Particle Size Distribution, Powder Classification - Global Forecast 2025–2030. https://www.researchandmarkets.com/reports/6120603/gas-atomized-metal-powder-market-materialrela1-6006979, August 2025. Accessed on August 22, 2025.

[41] H. Henein, V. Uhlenwinkel, and U. Fritsching. *Metal Sprays and Spray Deposition*. Springer International Publishing, 2017.

[42] H. Liu. *Science and Engineering of Droplets:: Fundamentals and Applications*. WILLIAM ANDREW PUBLISHING, LLC Norwich, New York, U.S.A., 1999.

[43] A.J. Yule and J.J. Dunkley. *Atomization of Melts: For Powder Production and Spray Deposition*. Oxford series on advanced manufacturing. Clarendon Press, 1994.

[44] Oleg D Neikov, NA Yefimov, and Stanislav Naboychenko. *Handbook of non-ferrous metal powders: technologies and applications*. Elsevier, 2009.

[45] Junfeng Wang, Min Xia, Jialun Wu, and Changchun Ge. Nozzle clogging in vacuum induction melting gas atomization: Influence of the delivery-tube and nozzle coupling. *Archives of Metallurgy and Materials*, pages 1359–1370, 2022.

[46] Junfeng Wang, Min Xia, Jialun Wu, and Changchun Ge. Nozzle clogging in vacuum induction melting gas atomisation: influence of gas pressure and melt orifice diameter coupling. *Powder Metallurgy*, 66(4):281–294, 2023.

[47] Junfeng Wang, Min Xia, Jialun Wu, Xian Jian, and Changchun Ge. Precise control of atomization initial stage to address nozzle clogging issue in the vacuum induction-melting gas atomization process. *Journal of Materials Research and Technology*, 30:1505–1517, 2024.

[48] Norman Dombrowski and WR Johns. The aerodynamic instability and disintegration of viscous liquid sheets. *Chemical Engineering Science*, 18(3):203–214, 1963.

[49] Hong-Wu Ouyang, CHEN Xin, and Bai-yun Huang. Influence of melt superheat on breakup process of close-coupled gas atomization. *Transactions of Nonferrous Metals Society of China*, 17(5):967–973, 2007.

[50] Mohamed S El-Genk and Hamed H Saber. Minimum thickness of a flowing down liquid film on a vertical surface. *International Journal of Heat and Mass Transfer*, 44(15):2809–2825, 2001.

[51] PK Senecal, David P Schmidt, Idriss Nouar, Christopher J Rutland, Rolf D Reitz, and ML Corradini. Modeling high-speed viscous liquid sheet atomization. *International journal of multiphase flow*, 25(6-7):1073–1097, 1999.

[52] Martin Dopler. *Prediction of Particle Sizes of Gas-Atomized Metal Powders*. PhD thesis, University of Leoben, 2017.

[53] Nicola Zeoli. *Multiphase modelling of the characteristics of close coupled gas atomization*. PhD thesis, Aston University, Jun. 2011.

[54] GM Faeth, L-P Hsiang, and P-K Wu. Structure and breakup properties of sprays. *International Journal of Multiphase Flow*, 21:99–127, 1995.

[55] Sheikhali M Sheikhaliev, Andrey V Beryukhov, and John J Dunkley. Powder manufacturing and processing: Metal droplet's deformation and break-up by a gas stream. In *European Congress and Exhibition on Powder Metallurgy. European PM Conference Proceedings*, volume 1, page 1. The European Powder Metallurgy Association, 2004.

[56] W-H Chou and GM Faeth. Temporal properties of secondary drop breakup in the bag breakup regime. *International journal of multiphase flow*, 24(6):889–912, 1998.

[57] Ernesto Urionabarrenetxea, José Manuel Martín, Alejo Avello, and Alejandro Rivas. Simulation and validation of the gas flow in close-coupled gas atomisation process: Influence of the inlet gas pressure and the throat width of the supersonic gas nozzle. *Powder Technology*, 407:117688, 2022.

[58] Alexander Ariyoshi Zerwas, Flavia Costa da Silva, Roberto Guardani, Lydia Achelis, and Udo Fritsching. Impact of the gas atomizer nozzle configuration on metal powder production for additive manufacturing. *Powder Technology*, 443:119974, 2024.

[59] Steven P Mates and Gary S Settles. A study of liquid metal atomization using close-coupled nozzles, part 1: Gas dynamic behavior. *Atomization and Sprays*, 15(1), 2005.

[60] C Feng Gao, Z Yu Xiao, H Ping Zou, Z Qiang Liu, Jin Chen, S Kui Li, and D Tong Zhang. Characterization of spherical alsi10mg powder produced by double-nozzle gas atomization using different parameters. *Trans. Nonferrous Met. Soc. China*, 29(2):374–384, 2019.

[61] J-P Roth, I Šulák, Z Chlup, J Fischer-Bühner, U Krupp, and K Jahns. The dispersion-strengthening effect of tin evoked by in situ nitridation of nicu-based alloy 400 during gas atomization for laser powder bed fusion. *Materials Science and Engineering: A*, 893:146129, 2024.

[62] Chengsong Cui, Felix Stern, Nils Ellendt, Volker Uhlenwinkel, Matthias Steinbacher, Jochen Tenkamp, Frank Walther, and Rainer Fechte-Heinen. Gas atomization of duplex stainless steel powder for laser powder bed fusion. *Materials*, 16(1):435, 2023.

[63] Peng Wang, Jing Li, Xin Wang, Bo-Rui Du, Shi-Yuan Shen, Xue-Yuan Ge, and Miao-Hui Wang. Impact mechanism of gas temperature in metal powder production via gas atomization. *Chinese Physics B*, 30(5):054702, 2021.

[64] A. Lawley. *Atomization: The Production of Metal Powders*. Monographs in P/M series. Metal Powder Industries Federation, 1992.

[65] Federico Simone Gobber, Paolo C Priarone, Antonio Pennacchio, and Marco Actis Grande. Effect of inert gas pressure on the properties and carbon footprint of uns s32760 powders made from waste materials by gas atomization. *Journal of Materials Research and Technology*, 33:8814–8828, 2024.

[66] Ernesto Urionabarrenetxea, Alejo Avello, Alejandro Rivas, and José Manuel Martín. Experimental study of the influence of operational and geometric variables on the powders produced by close-coupled gas atomisation. *Materials & Design*, 199:109441, 2021.

[67] Jason Ting, Michael W Peretti, and William B Eisen. The effect of wake-closure phenomenon on gas atomization performance. *Materials Science and Engineering: A*, 326(1):110–121, 2002.

[68] P. Lacombe, B. Baroux, and G. Béranger, editors. *Stainless Steels*. Les Éditions de Physique, Les Ulis, France, 1993. Based on the proceedings of the 1989 Spring School organized by CNRS, SF2M and CACEM.

[69] J.R. Davis, editor. *Stainless Steels*. ASM Specialty Handbook. ASM International, 1994.

[70] Marina Knyazeva and Michael Pohl. Duplex steels: part i: genesis, formation, structure. *Metallography, Microstructure, and Analysis*, 2(2):113–121, 2013.

[71] Robert Gunn. *Duplex stainless steels: microstructure, properties and applications*. Elsevier, 1997.

[72] European Commission, Joint Research Centre (JRC). Critical and strategic materials (rmis). https://rmis.jrc.ec.europa.eu/eu-critical-raw-materials, 2025.

[73] European Parliament and Council of the European Union. Regulation (eu) 2024/1252 establishing a framework for ensuring a secure and sustainable supply of critical raw materials and amending regulations (eu) no 168/2013, (eu) 2018/858, (eu) 2018/1724 and (eu) 2019/1020. *Official Journal of the European Union*, 3 May 2024. http://data.europa.eu/eli/reg/2024/1252/oj, May 2024. Adopted on 11 April 2024; published on 3 May 2024; in force since 23 May 2024.

[74] James Chater. Duplex: massive improvement. Featured Story; online version.

[75] Industry Experts. Duplex stainless steel – a global market overview. https://www.researchandmarkets.com/reports/6022806/duplex-stainless-steel-global-market-overview, November 2024. Accessed on November 2025.

[76] Robert N. Gunn, editor. *Duplex Stainless Steels: Microstructure, properties and applications*. Abington Publishing, Cambridge, England, 1997.

[77] Weir Material Ltd. MDS 12804/00/01, Issue E, December 1991. Material data sheet.

[78] ASTM International. ASTM A240/A240M-26, Standard Specification for Chromium and Chromium-Nickel Stainless Steel Plate, Sheet, and Strip for Pressure Vessels and for General Applications. Available at: https://compass.astm.org/content-search/?content=A240

[79] J. Charles and S. Bernhardsson, editors. *Duplex Stainless Steels '91*, volume 1. Les Éditions de Physique, Les Ulis, France, 1991. Proceedings of the conference held in Beaune, Bourgogne, France, 28–30 October 1991.

[80] J. Charles and S. Bernhardsson, editors. *Duplex Stainless Steels '91*, volume 2. Les Éditions de Physique, Les Ulis, France, 1991. Proceedings of the conference held in Beaune, Bourgogne, France, 28–30 October 1991.

[81] Iris Alvarez-Armas and Suzanne Degallaix-Moreuil. *Duplex stainless steels*. John Wiley & Sons, 2013.

[82] S Atamert and JE King. Sigma-phase formation and its prevention in duplex stainless steels. *Journal of materials science letters*, 12(14):1144–1147, 1993.

[83] Leonidas Gargalis, Leonidas Karavias, Joachim S Graff, Spyros Diplas, Elias P Koumoulos, and Evangelia K Karaxi. A comparative investigation of duplex and super duplex stainless steels processed through laser powder bed fusion. *Metals*, 13(11):1897, 2023.

[84] Johannes Kunz, Autchariya Boontanom, Simone Herzog, Piyada Suwanpinij, Anke Kaletsch, and Christoph Broeckmann. Influence of hot isostatic pressing post-treatment on the microstructure and mechanical behavior of standard and super duplex stainless steel produced by laser powder bed fusion. *Materials Science and Engineering: A*, 794:139806, 2020.

[85] D Jiang, Nick Birbilis, CR Hutchinson, and M Brameld. On the microstructure and electrochemical properties of additively manufactured duplex stainless steels produced using laser-powder bed fusion. *Corrosion*, 76(9):871–883, 2020.

[86] Karl P Davidson and Sarat B Singamneni. Metallographic evaluation of duplex stainless steel powders processed by selective laser melting. *Rapid Prototyping Journal*, 23(6):1146–1163, 2017.

[87] Kamran Saeidi, Sajid Alvi, Frantisek Lofaj, Valeri Ivanov Petkov, and Farid Akhtar. Advanced mechanical strength in post heat treated slm 2507 at room and high temperature promoted by hard/ductile sigma precipitates. *Metals*, 9(2):199, 2019.

[88] F. Shang, X. Chen, Z. Wang, Z. Ji, F. Ming, S. Ren, and X. Qu. The microstructure, mechanical properties, and corrosion resistance of UNS S32707 hyper-duplex stainless steel processed by selective laser melting. *Metals*, 9(2):1012, 2019.

[89] Ali Mulhi, Shirin Dehgahi, Prashant Waghmare, and Ahmed J Qureshi. Process parameter optimization of 2507 super duplex stainless steel additively manufactured by the laser powder bed fusion technique. *Metals*, 13(4):725, 2023.

[90] Saleh Sabah Alturaihi, Nicolae Serban, Ion Cinca, ML Angelescu, and IV Balkan. Influence of solution treatment temperature on microstructural and mechanical properties of hot rolled uns s32760/f55 super duplex stainless steel (sdss). *UPB Sci. Bull. Ser. B*, 83, 2021.

[91] Yanjun Guo, Jincheng Hu, Jin Li, Laizhu Jiang, Tianwei Liu, and Yanping Wu. Effect of annealing temperature on the mechanical and corrosion behavior of a newly developed novel lean duplex stainless steel. *Materials*, 7(9):6604–6619, 2014.

[92] Zhiqiang Zhang, Hongyang Jing, Lianyong Xu, Yongdian Han, Lei Zhao, Xiaoqing Lv, and Jianyang Zhang. The impact of annealing temperature on improving microstructure and toughness of electron beam welded duplex stainless steel. *Journal of Manufacturing Processes*, 31:568–582, 2018.

[93] Di Zhang, Aobo Liu, Bangzhao Yin, and Peng Wen. Additive manufacturing of duplex stainless steels-a critical review. *Journal of Manufacturing Processes*, 73:496–517, 2022.

[94] Maria Laura Gatto, Alberto Santoni, Eleonora Santecchia, Stefano Spigarelli, Fabrizio Fiori, Paolo Mengucci, and Marcello Cabibbo. The potential of duplex stainless steel processed by laser powder bed fusion for biomedical applications: A review. *Metals*, 13(5):949, 2023.

[95] Feng Shang, Xiaoqiu Chen, Zhiyong Wang, Zuchun Ji, Fei Ming, Shubin Ren, and Xuanhui Qu. The microstructure, mechanical properties, and corrosion resistance of UNS s32707 hyper-duplex stainless steel processed by selective laser melting. *Metals*, 9(9):1012, 2019.

[96] AD Iams, JS Keist, and TA Palmer. Formation of austenite in additively manufactured and post-processed duplex stainless steel alloys. *Metallurgical and Materials Transactions A*, 51(2):982–999, 2020.

[97] Andrew M Mullis, Duncan J Borman, et al. CFD modelling of Close-Coupled Gas Atomisation (CCGA) process by employing the euler-lagrange approach to understand melt flow instabilities. *Chemical Engineering Science*, 295:120205, 2024.

[98] Daniel Beckers, Nils Ellendt, Udo Fritsching, and Volker Uhlenwinkel. Impact of process flow conditions on particle morphology in metal powder production via gas atomization. *Advanced Powder Technology*, 31(1):300–311, 2020.

[99] H. K. Versteeg and W. Malalasekera. *An Introduction to Computational Fluid Dynamics: The Finite Volume Method*. Pearson, Harlow, UK, 2nd edition, 2007.

[100] Jinsong Hua, Federico Simone Gobber, Marco Actis Grande, Dag Mortensen, and Jan Ove Odden. A numerical modeling framework for predicting the effects of operational parameters on particle size distribution in the gas atomization process for nickel-silicon alloys. *Powder Technology*, 435:119408, 2024.

[101] RAHMİ Ünal. Investigation on metal powder production efficiency of new convergent divergent nozzle in close coupled gas atomisation. *Powder Metallurgy*, 50(4):302–306, 2007.

[102] E. Urionabarrenetxea, J. M. Martín, and A. Avello. Influence of some geometric features of the atomisation chamber on particle agglomeration and satellite formation during gas atomisation. In *Euro PM 2019 congr exhib.*, 2019.

[103] Ibrahim S Jawahir and Ryan Bradley. Technological elements of circular economy and the principles of 6r-based closed-loop material flow in sustainable manufacturing. *Procedia Cirp*, 40:103–108, 2016.

[104] JR Duflou, K Wegener, AE Tekkaya, M Hauschild, F Bleicher, J Yan, and B Hendrickx. Efficiently preserving material resources in manufacturing: Industrial symbiosis revisited. *CIRP Annals*, 73(2):695–721, 2024.

[105] Ces Selector. Update 1, 17.2.0. the UK: Granta Design Limited, 2017. Available at: https://scholar.google.com/scholar?q=+author:Selector%20Ces.

[106] G. Hammond and C. Jones. Embodied carbon – the inventory of carbon and energy (ice), annex b: How to account for recycling. BG 10/2011, BSRIA, 2011.

[107] ASTM International. ASTM E1019-24: Standard Test Methods for Determination of Carbon, Sulfur, Nitrogen, and Oxygen in Steel, Iron, Nickel, and Cobalt Alloys by Combustion and Inert Gas Fusion Techniques. Available at: https://www.astm.org/e1019-24.html, 2024.

[108] ASTM International. ASTM B213-25, Standard Test Methods for Flow Rate of Metal Powders Using the Hall Flowmeter Funnel. Available at: https://compass.astm.org/content-search/?content=ASTM%20B213&stype=A, 2025.

[109] ASTM International. ASTM B964-25, Standard Test Methods for Flow Rate of Metal Powders Using the Carney Funnel. Available at: https://compass.astm.org/content-search/?content=ASTM%20B964&stype=A&page=0, 2025.

[110] GM Janowski, FS Biancaniello, and SD Ridder. Beneficial effects of nitrogen atomization on an austenitic stainless steel. *Metallurgical Transactions A*, 23(12):3263–3272, 1992.

[111] Jyrki Pitkälä, Lauri Holappa, and Ari Jokilaakso. A study of the effect of alloying elements and temperature on nitrogen solubility in industrial stainless steelmaking. *Metallurgical and materials transactions B*, 53(4):2364–2376, 2022.

[112] L Becker, J Boes, J Lentz, C Cui, V Uhlenwinkel, M Steinbacher, R Fechte-Heinen, W Theisen, and S Weber. Quantification of extremely small-structured ferritic-austenitic phase fractions in stainless steels manufactured by laser powder bed fusion. *Materialia*, 22:101393, 2022.

[113] MA Ribeiro Miranda, José Marcos Sasaki, Sérgio Souto Maior Tavares, HFG De Abreu, and JM Neto. The use of x-ray diffraction, microscopy, and magnetic measurements for analysing microstructural features of a duplex stainless steel. *Materials characterization*, 54(4-5):387–393, 2005.

[114] Vahid A Hosseini, Sten Wessman, Kjell Hurtig, and Leif Karlsson. Nitrogen loss and effects on microstructure in multipass tig welding of a super duplex stainless steel. *Materials & design*, 98:88–97, 2016.

[115] Geon-Woo Baek, Sung-Jae Jo, Sourabh Kumar Soni, Jong Un Moon, May Likha Lwin, Yong Rai Kim, Rae Cheol Kang, Sung Soo Park, Dae-Hyeon Kim, and Soon-Jik Hong. Influence of gas type on microstructure and characteristics of super duplex stainless steel alloy powders prepared via gas atomization. *Journal of Materials Research and Technology*, 38:5476–5485, 2025.

[116] S Hertzman and J Charles. On the effect of nitrogen on duplex stainless steels. *Revue de Métallurgie*, 108(7-8):413–425, 2011.

[117] Klara Trydell, Kjell-Arne Persson, Nuria Fuertes, Erwan Siewert, Nakhleh Hussary, Michael Pfreuntner, Per Bengtsson, Paul Janiak, Ravi Vishnu, and Mette Frodigh. Ferrite fraction in duplex stainless steel welded with a novel plasma arc torch. *Welding in the World*, 67(3):805–817, 2023.

[118] Kostas Migiakis and GD Papadimitriou. Effect of nitrogen and nickel on the microstructure and mechanical properties of plasma welded uns s32760 super-duplex stainless steels. *Journal of Materials Science*, 44(23):6372–6383, 2009.

[119] Aconity3D. AconityMINI. https://aconity3d.com/products/aconity-mini/, 2025. Accessed on August 2025.

[120] Shubhavardhan Ramadurga Narasimharaju, Wenhan Zeng, Tian Long See, Zicheng Zhu, Paul Scott, Xiangqian Jiang, and Shan Lou. A comprehensive review on laser powder bed fusion of steels: Processing, microstructure, defects and control methods, mechanical properties, current challenges and future trends. *Journal of Manufacturing Processes*, 75:375–414, 2022.

[121] Di Zhang, Aobo Liu, Bangzhao Yin, and Peng Wen. Additive manufacturing of duplex stainless steels-a critical review. *Journal of Manufacturing Processes*, 73:496–517, 2022.

[122] Roxy Peck, Chris Olsen, and Jay L. Devore. *Introduction to Statistics and Data Analysis*. Brooks/Cole, Cengage Learning, 3 edition, 2008.

[123] Paolo Ferro, Franco Bonollo, and Giulio Timelli. Sigma phase precipitation modelling in a uns s32760 superduplex stainless steel. *La Metallurgia Italiana*, 2012.

[124] Fuad Khoshnaw, Cornelia Marinescu, Ancuta Sofronia, Cornel Munteanu, Maria Marcu, Laura Eugenia Barbulescu, Cristina Ciobota, Elisabeta Mirela Cojocaru, Speranta Tanasescu, and Alexandru Paraschiv. Microstructural and thermoanalytical characterization of super duplex stainless steel-uns s32760-f55. *Materials Today Communications*, 28:102644, 2021.

[125] AJ Ramirez, John C Lippold, and Sérgio Duarte Brandi. The relationship between chromium nitride and secondary austenite precipitation in duplex stainless steels. *Metallurgical and materials transactions A*, 34(8):1575–1597, 2003.

[126] Standards Norway. NORSOK Standard M-630: Material data sheets for piping. Available at: https://www.standard.no/, October 2013. Issued by Standards Norway.

[127] DIN Deutsches Institut für Normung e.V. E DIN 50125:2016-04: Testing of metallic materials — tensile test pieces, April 2016. Draft standard (Entwurf).

[128] Karlsruher Institut für Technologie, Institut für Technische Physik. Technical drawing of threaded round tensile specimen, 4 mm diameter, m6x1 thread, 22 mm gauge length, 45 mm overall length, June 2012. Technical drawing dated 28.06.2012; drawing file "Rundzug D4 M6.idw".

[129] ASTM International. ASTM E23-25: Standard Test Methods for Notched Bar Impact Testing of Metallic Materials. Available at: https://compass.astm.org/, 2025.

[130] Luca Annovazzi. Prove di impatto: come la qualità del provino influenza il risultato finale. Master's thesis, Politecnico di Milano, 2014.

[131] Victor Barbosa de Souza, Rodinei Lopes, Paulo Feliciano Soares Filho, and Heraldo Silva da Costa Mattos. Strain rate sensitivity analysis of duplex and superduplex steels in tensile tests. *Materials Research*, 23(3):e20190482, 2020.

[132] BSI, CEN, and ISO. BS EN ISO 6892-1:2019, Metallic materials — Tensile testing — Part 1: Method of test at room temperature. Available at: https://bsol-bsigroup-com.ezproxy.biblio.polito.it/Search/Search?searchKey=bs+en+iso+6892-1%3A2019&OriginPage=Header+Search+Box&autoSuggestion=true, 2019.

[133] ASTM International. ASTM A370-24a: Standard Test Methods and Definitions for Mechanical Testing of Steel Products. Available at: https://compass.astm.org/, 2024.

[134] Iris Raffeis, Uwe Vroomen, Frank Adjei-Kyeremeh, Dennis Großmann, Horst Hammelrath, Elmar Westhoff, Sebastian Bremen, D Boscolo Bozza, and Andreas Bührig-Polaczek. Comparative investigations into microstructural and mechanical properties of as-cast and laser powder bed fusion (lpbf) fabricated duplex steel (1.4517). *Materialwissenschaft und Werkstofftechnik*, 51(4):432–444, 2020.

[135] ASTM International. ASTM E8/E8M-25, Standard Test Methods for Tension Testing of Metallic Materials, 2025. Available at: https://compass.astm.org/content-access?contentCode=ASTM%7CE0008_E0008M-25%7Cen-US.

[136] Plastometrex. PLX-Benchtop Mechanical Testing Product. Available at: https://www.plastometrex.com/products/plx-benchtop, 2026. Accessed: 2026-04-28.

[137] ASTM International. ASTM G48-11 (reapproved 2020): Standard Test Methods for Pitting and Crevice Corrosion Resistance of Stainless Steels and Related Alloys by Use of Ferric Chloride Solution. Available at: https://www.astm.org/g0048-11r20e01.html, 2020.

[138] Zbigniew Brytan, Mengistu Dagnaw, Jana Bidulská, Róbert Bidulskỳ, and Mohd Ridha Muhamad. Post-processing effect on the corrosion resistance of super duplex stainless steel produced by laser powder bed fusion. *Materials*, 17(12):2807, 2024.

[139] Hua Tan, Yiming Jiang, Bo Deng, Tao Sun, Juliang Xu, and Jin Li. Effect of annealing temperature on the pitting corrosion resistance of super duplex stainless steel uns s32750. *Materials Characterization*, 60(9):1049–1054, 2009.

[140] RFA Jargelius-Pettersson, J Flyg, and S Wessman. The influence of nitrogen alloying on the pitting and crevice corrosion of austenitic and duplex stainless steels. In *Materials science forum*, volume 318, pages 489–494. Trans Tech Publ, 1999.